

Molecular fluorescence near metallic interfaces

Submitted by

Piers Andrew

*to the University of Exeter
as a thesis for the degree of
Doctor of Philosophy
in the Faculty of Science*

September 1998

This thesis is available for Library use on the understanding that it is copyright material and that no quotation from the thesis may be published without proper acknowledgement.

I certify that all the material in this thesis which is not my own work has been identified and that no material is included for which a degree has previously been conferred upon me

Dedicated to Mum and Dad, for being the best parents ever.

Abstract

The spontaneous emission rate of an emitter is not a fixed property, but instead depends on the local electromagnetic mode density, since this determines the availability of the external decay channels for the excited emitter. Manipulation of the electromagnetic modes to which an emitter can couple to gives control over the emission process, potentially leading to improvements in the efficiency and directionality of light emitting devices such as polymer LEDs and diode lasers. In this thesis, a series of studies are presented which examine the fluorescence emission from dye molecules placed above a metallic interface, the simplest possible modification of the free-space mode density.

The spontaneous emission rate and radiation pattern of a monolayer of Eu^{3+} ions positioned above a planar silver mirror are investigated as a function of the Eu^{3+} ion-metal separation and good agreement is found with a theoretical model.

The effect of perturbing the interface by corrugation of the surface profile is then studied by replacing the planar mirror by silver gratings of various pitches and depths. The spontaneous emission rate distance dependence found for a planar interface is not affected by small amplitude corrugations, but significant deviations from the planar behaviour occur for deeper gratings. For the deepest gratings considered, there is also evidence for the existence of different dipole sites above the grating surface.

The angular distribution of the emission is also perturbed by the grating structure, since the usually non-radiative surface modes excited by the dye molecules can scatter from the corrugation giving rise to sharp re-radiated emission peaks. The dependence of these emission peaks on the sample structure was studied, and the dispersion of the modes determined.

Contents

ABSTRACT	1
LIST OF FIGURES	7
ABBREVIATIONS	15
ACKNOWLEDGEMENTS	16
CHAPTER 1 INTRODUCTION	18
CHAPTER 2 CONTROLLING SPONTANEOUS EMISSION	21
2.1 Introduction	21
2.2 Photonic band gap structures	24
2.3 Microcavities	27
2.4 Fluorescence above interfaces	32
2.4.1. The Marburg experiments	33
2.4.2 After Drexhage	37
2.4.3 The Exeter experiments	40
2.5 Summary	44
CHAPTER 3 ELECTROMAGNETIC SURFACE MODES	45
3.1 Introduction	45
3.2 Surface-plasmon polaritons.	46
3.2.1 The surface-plasmon polariton dispersion relation	47
3.2.2 Propagation length of the SPP	51
3.2.3 Penetration depth of the SPP fields	52
3.2.4 The SPP dispersion curve for a free-electron metal	53
3.2.5 Effect of a dielectric overlayer on SPP dispersion	56

3.3 Waveguide modes	58
3.3.1 The asymmetric slab waveguide	61
3.3.2 TE guided modes	65
3.3.3 TM guided modes	68
3.4 Coupling to surface modes	70
3.4.1 Prism coupling techniques	72
3.4.2 Grating coupling techniques	75
3.4.3 Coupling SPP modes to light	78
3.5 Electromagnetic theory of gratings	79
3.5.1 The Chandezon method	80
3.5.2 Reflectivity of grating structures	82
3.6 Summary	89
CHAPTER 4 LANGMUIR-BLODGETT FILM DEPOSITION	91
4.1 Introduction	91
4.1.1 Historical context	92
4.2 Langmuir monolayers	94
4.2.1 LB materials	96
4.2.2 Surface pressure-area isotherms	97
4.2.3 Measurement of surface pressure	100
4.3 Film deposition.	101
4.3.1 The Langmuir-Blodgett technique	101
4.3.2 Transfer ratios	103
4.3.3 The Horizontal transfer technique	104
4.4 LB deposition apparatus	105
4.4.1 The Langmuir-Blodgett trough	106
4.4.2 The ultra-pure water system	107
4.5 Experimental procedure	108
4.5.1 The clean room	108
4.5.2 Substrate preparation	110
4.5.3 Solution preparation	112
4.5.4 Film deposition	113
4.5.5 Choice of dipping parameters	115
4.6 Fluorescent LB monolayers	117

4.6.1 Required dye properties	117
4.6.2 Choice of fluorophore	120
4.6.3 Synthesis of the Eu^{3+} complex	122
4.6.4 Properties of the Eu^{3+} complex	124
4.7 Summary	129
CHAPTER 5 SURFACE-PLASMON ENERGY GAPS AND PHOTOABSORPTION	130
5.1 Introduction	130
5.2 Sample preparation and characterisation	132
5.2.1 Reflectivity measurements	132
5.3 Experimental	135
5.4 Results	137
5.4.1 Experimental data	137
5.5 Analysis	139
5.5.1 Theoretical modelling	143
5.5.2 Gap optimisation	145
5.6 Summary	150
CHAPTER 6 FLUORESCENCE ABOVE A PLANAR MIRROR	152
6.1 Introduction	152
6.2 Sample design and fabrication	153
6.3 Excited state lifetime measurements	156
6.3.1 Experimental technique	156
6.3.2 Results	159
6.4 Theoretical analysis	164
6.4.1 Dipole emission above a planar mirror	165
6.4.2 Assumptions of the model	168
6.4.3 Modelling the lifetime data	170
6.4.4 Discussion	174
6.5 Radiation pattern measurements	179
6.5.1 Experimental technique	179
6.5.2 Results	182

6.5.3 Electric dipole radiation patterns _____	183
6.5.4 Magnetic dipole emission _____	188
6.5.5 Modelling radiation patterns _____	190
6.6 Spectral measurements _____	195
6.7 Summary _____	197
CHAPTER 7 FLUORESCENCE ABOVE CORRUGATED SURFACES _____	199
7.1 Introduction _____	199
7.1.1 Grating induced perturbations _____	200
7.1.2 Previous studies _____	202
7.2 Grating fabrication _____	204
7.2.1 Substrate preparation _____	205
7.2.2 Exposure and development _____	207
7.2.3 Post-treatment _____	210
7.2.4 Fast atom etching _____	211
7.2.5 LB deposition _____	212
7.3 Long pitch grating measurements _____	215
7.3.1 Characterisation _____	215
7.3.2 Lifetime measurements _____	217
7.3.3 Radiation pattern measurements _____	220
7.3.4 Distance dependence of radiation patterns _____	226
7.3.5 Azimuthal dependence of radiation patterns _____	230
7.3.6 Summary for long pitch gratings _____	234
7.4 Short pitch grating measurements _____	235
7.4.1 Design and characterisation of samples _____	236
7.4.2 Lifetime measurements _____	239
7.4.3 20nm amplitude gratings _____	239
7.4.4 30nm amplitude gratings _____	240
7.4.5 40nm amplitude gratings _____	241
7.4.6 68nm amplitude gratings _____	242
7.4.7 75nm amplitude gratings _____	244
7.4.8 130nm amplitude gratings _____	246
7.4.9 Radiation pattern measurements _____	251
7.4.10 Discussion of short pitch grating results _____	256

7.5 Summary	259
CHAPTER 8 CONCLUSIONS AND FUTURE WORK	260
8.1 Absorption of light	260
8.2 Emission of light	261
8.2.1 Planar interfaces	261
8.2.2 Corrugated interfaces	262
8.3 Future work	264
8.4 Publications	266
REFERENCES	267
APPENDIX A MAGNETIC DIPOLE RADIATION PATTERNS	279

List of figures

Figure 2.1	The experimental geometry studied by Drexhage.	34
Figure 2.2	Interference of the direct wave from a dipole source and the wave reflected from a planar mirror.	37
Figure 3.1	The incident, reflected and transmitted fields associated with a TM polarised electromagnetic wave incident upon a planar interface.	48
Figure 3.2	The field and charge distributions associated with the SPP mode.	50
Figure 3.3	The SPP dispersion curve for a free-electron metal surface.	55
Figure 3.4	Geometry of a metal surface coated by a dielectric overlayer of thickness d .	57
Figure 3.5	Reflection and refraction of light at a planar boundary between two media of different dielectric constant.	59
Figure 3.6	A planar dielectric slab waveguide, clad asymmetrically with air and metal.	61
Figure 3.7	Mode field profiles $E(y)$ of the waveguide of <i>figure 3.6</i> for various values of the tangential wavevector β .	63
Figure 3.8	The field profiles of the first three TE and TM guided modes for the asymmetric metal-clad waveguide shown in <i>figure 3.6</i> .	70
Figure 3.9	Dispersion curve for light propagation in a prism of index n with evanescent coupling to the SPP modes of a metal-air interface close to the base of the prism.	73
Figure 3.10	Prism ATR geometries; (a) the Otto configuration and (b) the Kretschmann configuration.	74

Figure 3.11	The SPP dispersion curve for a metallic grating surface corrugated with a single harmonic component of pitch λ_g .	77
Figure 3.12	The multilayer grating geometry and associated coordinate system.	80
Figure 3.13	Theoretically generated reflectivity curves for TM-polarised light of wavelength 632.8nm incident upon a sinusoidal grating of pitch 800nm near the -1 SPR.	84
Figure 3.14	Theoretically generated reflectivity curves for TM-polarised light of wavelength 632.8nm incident upon a sinusoidal grating of pitch 800nm near the +2 SPR.	85
Figure 3.15	The effect of the second harmonic component a_2 on the -1 SPR.	87
Figure 3.16	The effect of the second harmonic component a_2 on the +2 SPR.	88
Table 4.1	Results of the elemental analysis carried out on the europium complex.	124
Figure 4.1	The molecular structure of 22-tricosenoic acid.	96
Figure 4.2	The surface pressure/area isotherm for a Langmuir film of 22-tricosenoic acid on a water subphase at 20°C .	97
Figure 4.3	Compression of a long chain fatty acid Langmuir film on a water subphase illustrating the (a) gas phase, (b) liquid phase and (c) solid phase.	99
Figure 4.4	The Wilhelmy plate and the forces acting upon it.	100
Figure 4.5	Langmuir-Blodgett film transfer on the (a) downstroke, (b) upstroke.	102
Figure 4.6	The structure of (a) x-type, (b) y-type and (c) z-type Langmuir-Blodgett multilayer films.	103
Figure 4.7	The horizontal film transfer technique.	105

Figure 4.8	The Langmuir-Blodgett trough in cross-section.	106
Figure 4.9	The europium complex, N-hexadecyl pyridinium tetrakis (1,3-diphenyl-1,3-propandionato) europium (III).	121
Figure 4.10	The fluorescence emission spectrum of a monolayer of N-hexadecyl pyridinium tetrakis (1,3-diphenyl-1,3-propandionato) europium (III) under UV excitation at $337nm$.	127
Figure 4.11	The time dependence of the $614nm$ emission from a monolayer of the europium complex deposited on a control sample.	128
Figure 5.1	The experimental set-up used to measure the angle-dependent reflectivity.	133
Figure 5.2	Angle-dependent reflectivity of the dye-coated SPP energy gap grating at $488nm$ for TM polarised incident light.	134
Figure 5.3	The experimental arrangement used to measure the angle-dependent excitation spectrum of the sample.	136
Figure 5.4	Photoluminescence from the dye layer on the SPP energy gap grating as a function of the angle of incidence and wavelength of TM polarised incident light.	138
Figure 5.5	Normalised absorption spectrum for the SPP energy gap sample.	140
Figure 5.6	Theoretical plot of the reflectivity of the energy gap grating sample as a function of the angle of incidence and wavelength of an incident beam of TM polarised light.	141
Figure 5.7	The absorption spectrum and SPP dispersion of the energy gap sample plotted on the same axes.	142

Figure 5.8	The absorption spectrum and SPP dispersion of the control sample plotted on the same axes.	143
Figure 5.9	Numerical modelling to show the effect of increasing the amplitude of the second harmonic component of the grating profile on the normalised absorption spectrum of a dye coated grating	147
Figure 5.10	Numerical modelling to show the effect of varying the phase of the second harmonic of the grating profile with respect to the fundamental on the normalised absorption spectrum of a dye-coated grating	148
Figure 5.11	Numerical modelling to show the effect of varying the dye layer thickness on the normalised absorption spectrum of a dye-coated grating.	150
Table 6.1	The parameters used to model the experimentally measured distance dependence of the Eu^{3+} lifetime.	173
Table 6.2	The parameters used to obtain the theoretically modelled radiation pattern dependencies of <i>figure 6.10</i> .	186
Table 6.3	The values taken by l_1 , l_2 and δ for the three different electric dipole orientations. The dipole emission is taken to have a maximum intensity of unity.	192
Figure 6.1	A plan view of the 0 to 60 spacer layer sample, showing the two step fabrication process.	155
Figure 6.2	The experimental configuration used to measure excited state lifetimes.	157
Figure 6.3	Fluorescence decay curves for Eu^{3+} ions located (a) 83nm and (b) 218nm distant from a silver mirror, together with the single exponential fits.	159
Figure 6.4	The experimentally measured excited state lifetime of the Eu^{3+} complex in front of a silver mirror as a function of the ion-metal separation.	161

Figure 6.5	The geometry used in the dipole decay rate calculation, (a) perpendicular dipole, (b) parallel dipole.	166
Figure 6.6	The distance dependence of the 5D_0 lifetime of Eu^{3+} ions located in front of a silver mirror.	173
Figure 6.7	The contribution to the decay rate of a parallel oriented dipole above a mirror as a function of the normalised wavevector u and the dipole-mirror separation distance.	175
Figure 6.8	The contribution to the decay rate of a perpendicularly oriented dipole above a silver mirror as a function of the normalised wavevector u and the dipole-mirror separation distance.	176
Figure 6.9	The experimental configuration used to make the radiation pattern measurements.	180
Figure 6.10	Radiation patterns of the 614nm Eu^{3+} electric dipole emission.	184-186
Figure 6.11	Comparison of the normalised radiation patterns measured for the electric and magnetic dipole Eu^{3+} emission.	189
Figure 6.12	The three different dipole orientations.	191
Figure 6.13	The double-interface geometry for calculation of radiation patterns.	193
Figure 6.14	Emission spectra for the Eu^{3+} /mirror system for a variety of ion/mirror separations.	195
Figure 6.15	The emission spectra measured for an ion/mirror separation of 412nm at emission angles of 0° and 70° .	196
Table 7.1	Parameters used to obtain the fit in <i>figure 7.2</i> .	216
Table 7.2	The fit parameters obtained from reflectivity measurements for the short pitch gratings used.	238

Figure 7.1	The interferometer used for grating fabrication.	207
Figure 7.2	Angle-dependent reflectivity of the 800.1 nm pitch grating for TM polarised incident light of wavelength 632.8 nm.	216
Figure 7.3	The experimentally measured lifetime of the Eu^{3+} complex above a silver grating of pitch 800.1 nm as a function of the ion/metal separation.	218
Figure 7.4	Fluorescence decay curves for Eu^{3+} ions located 24 and 72 spacer layers distant from the 800.1 nm pitch silver grating, together with the single exponential fits.	219
Figure 7.5	Radiation patterns of the 60 and 180 spacer layer regions of the 800.1 nm pitch grating sample, for p-polarised and s-polarised emission.	222-223
Figure 7.6	The p-polarised radiation pattern for the 222 spacer layer region of the 800.1 nm pitch grating sample.	225
Figure 7.7	The dependence of the mode dispersion on the spacer layer thickness for the 800.1 nm pitch grating sample.	227
Figure 7.8	The data from <i>figure 7.7</i> re-plotted on expanded axes to show the nature of the scattering processes giving rise to the observed emission peaks.	229
Figure 7.9	The k-space map for a grating with $G < k_0$.	230
Figure 7.10	The measured azimuthal angle dependence of the peak SPP emission obtained from the 800.1 nm pitch grating sample.	232
Figure 7.11	The azimuthal emission data of <i>figure 7.10</i> re-plotted to determine the validity the proposed mode scattering mechanism.	233
Figure 7.12	Reflectivity of two of the 400 nm pitch gratings for TM-polarised incident light ($\lambda=612\text{nm}$). (a) Grating 1 ($a_0\sim 17\text{nm}$), and (b) Grating 11 ($a_0\sim 75\text{nm}$).	237

Figure 7.13	The lifetime of the Eu^{3+} ions above a silver grating of amplitude $\sim 20\text{nm}$ as a function of the ion-metal separation.	240
Figure 7.14	The lifetime of the Eu^{3+} ions above a silver grating of amplitude $\sim 30\text{nm}$ as a function of the ion-metal separation.	241
Figure 7.15	The lifetime of the Eu^{3+} ions above a silver grating of amplitude $\sim 40\text{nm}$ as a function of the ion-metal separation.	242
Figure 7.16	The lifetime of the Eu^{3+} ions above a silver grating of amplitude $\sim 68\text{nm}$ as a function of the ion-metal separation.	243
Figure 7.17	The Eu^{3+} ion excited state lifetime distance dependence for a planar interface and two different depth grating structures.	244
Figure 7.18	The lifetime of the Eu^{3+} ions above a silver grating of amplitude $\sim 75\text{nm}$ as a function of the ion-metal separation.	245
Figure 7.19	Fluorescence decay curves for Eu^{3+} ions located 32 spacer layers above (a) a grating of pitch 415nm and amplitude 75nm , and (b) a planar interface, together with the single exponential fits.	245
Figure 7.20	The fluorescence decay of Eu^{3+} ions located 32 spacer layers above a grating of pitch 415nm and amplitude 130nm , together with a single exponential fit.	247
Figure 7.21	The fluorescence decay of Eu^{3+} ions located 32 spacer layers above the planar region of the 130nm amplitude grating sample, together with a single exponential fit.	248

- Figure 7.22** The “lifetime” of the Eu^{3+} ions above a silver grating of amplitude $\sim 130\text{nm}$ as a function of the ion-metal separation. **249**
- Figure 7.23** The fraction of the fluorescence decay corresponding to the long lifetime component for the 130nm amplitude grating sample. **250**
- Figure 7.24** Radiation patterns of the 104 spacer layer region of the 30nm and 68nm amplitude grating samples, for p-polarised emission and s-polarised emissions. **252-253**
- Figure 7.25** The p-polarised radiation patterns for the 4 spacer layer thick regions of the short pitch grating samples. **255**

Abbreviations

ATR	Attenuated total reflection
CPS	Chance, Prock and Silbey
HMDS	1,1,1,3,3,3-hexamethyldisilazane
HPLC	High performance liquid chromatography
LB	Langmuir-Blodgett
LED	Light emitting diode
PBG	Photonic band gap
PMT	Photomultiplier tube
PSD	Phase-sensitive detectors
PTFE	Polytetrafluoroethene
Q	Quality factor
QED	Quantum electrodynamics
RF	Radio frequency
RO	Reverse osmosis
SpE	Spontaneous emission
SPP	Surface-plasmon polariton
SPR	Surface-plasmon resonance
StE	Stimulated emission
TE	Transverse electric
TM	Transverse magnetic
TOC	Total organic carbon

Acknowledgements

I'd like to thank all those people, who through their help, kindness and friendship made this thesis possible. Firstly, I am indebted to my supervisor, Bill Barnes. Without his enthusiasm, insight and not inconsiderable coding skills, I'd still be trying to take data in vain. Thanks Bill, hope you find your jumper! I'd also like to thank Roy Sambles, who was always willing to wrestle with tricky problems, and whose curiosity and unique insight has been a continual inspiration. A big thank-you goes to Kevin Welford, my external supervisor who helped to fund this work through a CASE award from DRA Malvern in association with the EPSRC.

It's customary at this point to direct a few remarks to those fellow denizens and ex-denizens of the Basement who do so much to make the lab such a stimulating place to do a Ph.D. It's been a positive pleasure to have spent the last three or four years working with them. Particular thanks go to Rich, a fellow LB sufferer who managed to escape, a connoisseur of fine curries and all-round top bloke. Cheers for all the help mate. Thanks also to Alan, who has been a good friend for more years than I care to remember and is always a willing accomplice in unofficial experimentation in or out of the lab. Now, where's that iodine... An honourable mention goes to Phil for his entertaining clean-room antics, and who carries the LB torch forward into the next generation, the mad fool. Thanks for all your help Phil. I'd be very remiss if I didn't mention Mikey J somewhere here. Notable for his encyclopaedic knowledge of quotes from a certain *subset* of films and his skills, such as they are, on the füssball table, he's done much to inject a certain levity to the basement, for which I'm eternally grateful. Thanks to Emma¹ for many hours of philosophical discussion (and gossip) in saloon bars, her good taste in beers and for being an all-round good egg. It's an awfully long time since that third year project now! A nod of the head and a tilt of the cap go to Chris who knows all about lifes' rich tapestry and how best to soil it. I'm sure my vocabulary has expanded greatly in the time I've known him. Thanks also to Steve "Chris"

Kitson and his *entirely* blue wardrobe for all the help he gave me in the early stages of the work. Ben “Lucky” Hodder deserves a special mention for his prowess on the guitar and willingness to use 3kV power supplies when a PP9 would do. Glad that you’re still here mate! Thought you could “scam” a mention Pete? Doh! Many thanks in chronological order go to: the “newest” boys, Nobu, Nathan “Nate-dog” Smith, and Jon; the “new” boys, Benny “Nice!” Hallam, Alastair “Smutty” Hibbins and Martin “Saucester” Salt; the “old” boys, Mike “Connery” Linehan, Nick “Out-there” Wanstall, Dom, Rich W, Robin, Matt, Nick C, Rob, Alfredo and Marc; and of course to those fixed stars in the firmament, Fuzi and Lizhen, Bill P, Geoff Bradberry and Trevor Preist.

Thanks to Pete Cann, a true wizard in the workshop, who knew better than I what designs would work, what wouldn’t and how to make an A-1 job of them all, for all of the equipment you’ve made and fixed for me. Oh and for the *excellent* cheesecakes, which he deserves wider recognition for.

To Dave Jarvis for many evaporations.

To the members of the Mechanical and Electronic workshops for their help at one time or another.

To Barry and John “Crossword” Meakin in stores.

To Margaret, Liz and Val and the other secretarial staff.

To Professor John Inkson for the use of departmental resources.

To Debbie and Ben, Mich, my fellow rocket scientist and Martin for being such convivial companions.

To Em, for all her love and support, during times both good and bad ☺

Finally, a special thank-you to my Mum, Dad and brother Theo for all their love, encouragement and support over the last 25 years.

Chapter 1

Introduction

There is currently much interest in the possibility of controlling the optical properties of light emitting species by modification of the nature and availability of the electromagnetic modes to which the emitter can couple. A molecule can only de-excite by the emission of a photon, for example, if a mode exists with the correct energy. The mode density can be altered by changing the boundary conditions for the electromagnetic field, and the simplest possible alteration of the electromagnetic density of states is caused by the introduction of a planar mirror interface. In this thesis, the fluorescence emission from a monolayer of a Eu^{3+} complex above such a metallic interface is studied, and the perturbation caused by corrugating this interface is investigated by replacing the planar interface with a diffraction grating.

The effect of a planar interface on the emission from a dye molecule positioned above it is determined by the proximity of the molecule to the metal surface. When the molecule is close to the metal, the primary decay mechanism is the excitation of non-radiative surface-plasmon polariton (SPP) modes at the interface, and the fluorescence emission from the dye is strongly quenched by energy transfer to the surface. As the molecule is moved further away from the metal, the coupling to the surface mode decreases, and it is the interference between the direct and reflected field from the interface that determines the nature of the emission; in effect the dipole is driven by its own reflected field. This leads to the observation of oscillations in the spontaneous emission rate as a function of the molecule-mirror separation, and modification of the angular distribution of the emitted radiation.

If the planar mirror is replaced by a diffraction grating, scattering processes also have to be taken into account to determine the overall response

of the system. The most obvious effect of the corrugation is the scattering of the normally non-radiative surface modes such as the SPP, coupling them to photons and thus giving rise to sharp peaks in the radiation pattern. It may also be possible for the fields emitted by the molecule to scatter from the corrugation, thus changing the planar interference condition and hence affecting the spontaneous emission rate.

It is the aim of this thesis to investigate these processes and to determine how the emission of a dye monolayer above a metallic grating surface is perturbed by the presence of a corrugated interface.

The remainder of this thesis is divided into seven chapters. Chapter 2 contains a review of the literature relating to the control of spontaneous emission by the manipulation of the electromagnetic density of states, and introduces the concepts relevant to the study of fluorescence above interfaces. The results of earlier investigations carried out by previous workers at the University of Exeter are also detailed.

Because of the importance of the surface modes of a metallic interface in determining the optical response of dye molecules located nearby, chapter 3 is devoted to a detailed discussion of the nature and properties of the modes concerned, namely the SPP. Because the structures studied also include a dielectric spacer layer, guided modes can be supported in addition to the SPP, and their relevance is also discussed.

Experimentally, it is not a trivial task to construct samples which contain dye molecules spaced less than optical wavelength away from a metal interface, and in chapter 4 the method used to fabricate such samples, the Langmuir-Blodgett technique, is introduced. The requirements made of the fluorescent dye material are also discussed, and the synthesis of an appropriate dye detailed.

The first experimental results are presented in chapter 5, which highlight the importance of the coupling between the dye molecules and the SPP modes of the interface. In this study, however, it is the absorption process, and not the emission process which is examined. Experimental results are presented demonstrating that energy gaps which prohibit the propagation of SPPs may be used to control the absorption properties of such molecules. Experimental data is compared with theoretical predictions, and numerical modelling presented to

show how the effect of the gap on the absorption may be optimised by a suitable choice of the grating profile.

In chapter 6, the fluorescence emission of a dye monolayer above a planar metallic interface is addressed experimentally, and both the spontaneous emission rate and the angular dependence of the emission are studied as a function of the dye-metal separation. Good agreement with theoretical predictions is found in both cases. It is shown that the radiation patterns measured for the 614nm and 592nm Eu^{3+} ion emission have substantially different angular dependencies because of their respective origin from electric and magnetic dipole transitions. This chapter paves the way for the investigation of the perturbation caused by corrugation of the interface.

This topic is addressed in chapter 7, where fluorescence emission above a corrugated surface is studied by replacing the planar interface of chapter 6 by a metallic diffraction grating. A variety of grating profiles are examined, and the effect of increasing the amplitude of the corrugation on the spontaneous emission rate addressed.

The conclusions of the work, and directions for future study are presented in chapter 8.

Chapter 2

Controlling spontaneous emission

2.1 Introduction

In this chapter, the prospect of controlling the spontaneous emission of luminescent species such as atoms or molecules by changing the local optical environment will be discussed.

The emission (luminescence) and absorption of light by such an entity depends to a large extent on its electronic configuration, since it is the electrons which primarily interact with incident radiation in the optical region of the electromagnetic spectrum. Consider for simplicity a two level atom with a single optical transition involving the ground state and an excited state of a bound electron. This electron, initially in the ground state, may be promoted to the excited state by the absorption of a photon of suitable energy (equal to the energy difference between the two levels). The excited atom may then revert to the ground state in a luminescent decay process by the re-emission of a photon of the same energy. This decay process is known as spontaneous emission (SpE) to distinguish it from the phenomenon of stimulated emission (StE). The spontaneous emission of light by an atom can be characterised by the spectrum of the luminescence, the lifetime of the excited state, and by the spatial distribution of the emitted radiation, known as the *radiation pattern*.

These properties are all dependent on the nature of the emitting species, or more precisely, by the energy levels involved in the transition. The spectral distribution of the emission depends upon the energy differences between available energy levels, whilst the lifetime of the emission is inversely related to the transition rate of the process. This is given by Fermi's Golden rule, and is thus related to the wavefunctions of the initial and final states of the transition.

The radiation pattern of the emitter will depend upon the electronic charge distributions of these initial and final states since these determine the representation of the source in a multipole expansion. The simplest possible source behaves as an electric dipole, and for systems where the emission wavelength is much greater than the source dimensions, this is usually the dominant term. If this transition is forbidden then the source may radiate as a magnetic dipole, electric quadrupole or other higher order multipolar emitter. These will all have different angular radiation patterns and so it is possible to distinguish the character of a transition by the spatial distribution of the emission.

There is currently much interest in the possibility of controlling or tailoring these radiative characteristics to suit particular device applications. An important example is the elimination of unwanted spontaneous emission in semiconductor lasers. Control over this principal loss mechanism could lead to the fabrication of low-noise and potentially zero-threshold light emitters [*De Martini and Jacobovitz (1988), Yablonovitch (1987)*]. Alteration of the spectral and spatial emission of fluorescent species also can be used to optimise polymer LED display devices [*Dodabalapur (1997)*].

One way to tailor spontaneous emission to suit a given application is to modify the molecular structure of the emitter, so that the resulting alteration of the electronic energy levels give rise to the change desired. This essentially chemical approach can only go so far in attaining the desired level of control since it is difficult to affect all three defining motifs of spontaneous emission at once, in the required manner.

A second, complementary, and perhaps more versatile method of effecting change in the radiative characteristics of a material arises not from control of the *electronic* states of the emitter itself as in the previous approach, but from control of the *photonic* states of the material within which the emitter is embedded. This possibility was first noted by *Purcell (1946)* in relation to the relaxation of nuclear spins, but the relevance to optical processes went relatively unnoticed until the pioneering work of *Drexhage (1974)*. By controlling the optical environment of the emitter, it is possible to change the electromagnetic modes which the emitter can couple to, thus affecting the radiative properties of the system. This is not only of interest for device

applications; the resulting alteration of the matter-radiation interaction has important consequences for understanding the nature of fundamental optical processes [Fearn *et al.* (1995)].

It can be seen that both these approaches are important in affecting spontaneous emission by applying Fermi's Golden rule to an electric dipole emitter [Fermi (1932)]

$$\Gamma(\omega) = \frac{\pi}{2\hbar^2} \left| \langle \phi_i^* | H | \phi_f \rangle \right|^2 \rho(\omega). \quad (2.1)$$

Here, $\Gamma(\omega)$ is the transition rate (*i.e.* spontaneous emission rate) of the dipole, the modulus term is the matrix element for the electronic transition, H is the electric dipole operator and $\rho(\omega)$ is the density of electromagnetic modes with frequency ω . Altering the electronic energy levels of the emitter results in a change in the transition matrix element, whilst altering the electromagnetic density of states results in a change in $\rho(\omega)$, both of which lead to a variation in the decay rate.

The essence of controlling the spontaneous emission rate lies in the understanding that an excited emitter can only decay *via* the emission of a photon if there is an electromagnetic mode available with the right energy and wavevector. If there is no such mode available then the emitter cannot de-excite radiatively, with the result that the lifetime of the excited state is increased. The emission spectrum will reflect this through the appearance of gaps in broadband spectra. Conversely, if the density of electromagnetic modes is increased above the free-space density then the decay rate can be enhanced, leading to a decrease in the lifetime of the excited state. The radiation pattern of the emission can also be influenced by controlling the spatial distribution of the allowed modes, thus channelling the emission into predetermined propagation directions. The emission characteristics are thus significantly altered by the nature and availability of the electromagnetic states of the host medium.

These depend to some extent upon the refractive index of the medium since this determines how many optical modes can occupy a given volume, thus affecting the mode density. This effect can be understood in a heuristic way by considering the reduction in wavelength of light from λ_0 to λ_0/n upon

entering a dielectric of index n . The number of modes per unit volume will thus increase by a factor of n^3 , indicating that the density of electromagnetic modes should have a similar dependence. The dependence of the spontaneous emission rate of emitters on the refractive index of the host has been reported by *Rikken and Kessener (1995)*. In this study, the lifetime of europium ions was measured in solutions of different refractive index, and good agreement with a local field theory was found. In a similar study, *Snoeks et al. (1995)* measured the lifetime of erbium ions implanted under the surface of a glass slide as a function of the refractive index of solvents covering the slide, again matching theory. *Lavallard et al. (1996)* examined a slightly different system; that of dye molecules in micellar solution, and also found variation in the excited state lifetime with the index of the solution.

The term photonic is often used to emphasise the idea that photons propagating within a medium have a density of states and a band structure, and can thus be described in a similar manner to electrons propagating in a crystal lattice. This analogy is most perfectly revealed in photonic band gap (PBG) materials – materials fabricated with an artificial superlattice structure to be periodic on the scale of the wavelength of light. These materials can exhibit photonic stop bands, band edges and even defect modes; all reminiscent of the behaviour of electrons in a semiconductor material.

Broadly speaking there are two parallel avenues of research which are being investigated with reference to the control of the emission and propagation of light. These are the use of PBG materials as mentioned above, and the use of Fabry-Pérot microcavities to constrain optical fields, thus altering the electromagnetic mode density. Both of these approaches will be briefly discussed in the following sections, before the simplest possible modification of photonic states possible, that introduced by a planar interface, is discussed in detail.

2.2 Photonic band gap structures

The simplest possible structure that possesses a photonic band gap is the quarter-wave dielectric stack. As the name suggests, this consists of

alternate $\lambda/4$ thick planar layers of high and low index refractive dielectric material, forming a one-dimensional periodic lattice. Light incident on the structure normal to the layers will be Bragg scattered by the index modulation, resulting in the creation of backward travelling waves. If the optical wavevector is half of the Bragg vector of the lattice, these counterpropagating waves will interfere constructively to form a standing optical field within the structure. There are two possible locations of the standing wave field with respect to the lattice; the field maxima may coincide with the centre of the high index medium or with the centre of the low index medium. These two field configurations will have identical wavevectors, but since on average they experience different refractive indices they will have different frequencies ($k=2\pi n_{\text{ave}}/\lambda$). The high frequency mode will thus have electric field maxima in the low index layers, whilst the low frequency mode has field maxima in the high index layers. This leads to the formation of a band gap; waves with frequencies between the two standing wave values (*i.e.* within the gap) interfere destructively on scattering, and are thus damped. This is the simplest example of a photonic band gap. If light is normally incident upon this multilayer stack within the gap region it will be reflected, and because dielectrics have low losses, these structures are often used as high-reflectivity mirrors or filters.

If the light is not incident on the stack normally, then the scattering vector is no longer parallel to the wavevector of the light, which results in a shift of the gap centre to higher frequencies. A corollary of this is that the reflectivity of a multilayer dielectric mirror falls off as the angle of incidence increases for a given wavelength.

The idea of controlling light using the principles learnt from the one-dimensional multilayer stack was extended to three dimensions by *Yablonovitch (1987)* and *John (1987)*, who proposed the concept of a *photonic crystal*. A photonic crystal is a material which possesses a full photonic band gap, *i.e.* a material with a frequency stop band for electromagnetic waves over *all* propagation directions and polarisations. Within this gap region there are no optical modes, and hence no zero-point fluctuations [*Yablonovitch (1993)*]. This has important consequences for the inhibition of spontaneous emission. If the emission frequency of a species lies within the gap, emission cannot take place

and the lifetime of the emitting state is thus infinite, in the absence of other decay mechanisms [Martorell and Lawandy (1990)]. Other optical processes may be similarly affected; for instance, the resonant dipole-dipole interaction within a periodic dielectric structure has been investigated theoretically by Kurizki and Genack (1988). In this study it was predicted that significant changes would occur in the non-radiative energy transfer rate from one species to another for transitions within the gap region. This effect could be used to control co-operative emission processes within lasing media for example.

Although the photonic energy gaps are the subject of great theoretical and experimental interest, they are not the only features of PBG materials that suggest potential applications. The band edge modes are potentially useful since they correspond to standing waves and not propagating waves, whilst the introduction of defects within photonic crystals can lead to the formation of donor and acceptor states within the gap itself.

Because the band edge modes are stationary modes, the corresponding optical fields are highly localised within the structure, and have a periodic nature. The resulting increased interaction between light and matter could be of use in the enhancement of non-linear optics phenomena, particularly those involving the periodic poling of crystals. Plotting the band structure of the gap region further reveals that the band edges are flat, implying that the density of k-states per unit frequency interval is very large. This has implications for the design of efficient laser diodes, which could benefit from the enhanced emission possible at the band edge [Tocci et al. (1996)].

The analogy with semiconductor materials is extended by the existence of photonic donor and acceptor modes, created by the presence of defects in the lattice structure [Yablonovitch et al. (1991a)]. These highly localised modes have energies within the gap, and are effectively high-Q microcavities due to the presence of the surrounding PBG material. Such defect modes could be used to fabricate monomode microlaser devices, or even low-loss waveguide structures [Foresi et al. (1997)].

Fabrication of a material that exhibits a photonic band gap extending over all propagation directions requires the structure to be periodic on the scale of the optical wavelength in all three spatial dimensions. The technical difficulty involved in actually manufacturing such a structure has meant that most effort to

date has been directed at the production of microwave photonic crystals, where the required periodicity is much larger [*Sievenpiper et al. (1996)*]. A further complication is that, to be complete, the gap must exist for both orthogonal polarisations of the electromagnetic field, a condition that has no parallel in the electronic analogue.

The first genuine photonic crystal with a full gap was designed by *Yablonovitch et al. (1991b)* and demonstrated in the microwave regime. This feat has not yet been achieved in the visible, although pseudo-gaps have been reported for several colloidal structures [*Míguez et al. (1997)* and *Vlasov et al. (1997)*]. Various ingenious methods have been proposed to manufacture a full PBG crystal, most notably by *Yablonovitch (1993)*, but since a full gap is not necessarily needed, the colloidal approach is generating much interest. This is due to the way in which a suspension of spheres can spontaneously *self-assemble* to form an artificial crystal. The crystal structure itself can be determined by the use of template-driven epitaxy, allowing the creation of both fcc and bcc structures [*van Blaaderen et al. (1997)*]. Recently, inhibition of the spontaneous emission of a dye was demonstrated using a dye-doped colloidal crystal [*Petrov et al. (1998)*]. Both changes in the emission spectrum and lifetime of the dye were observed, and were attributed to the photonic band gap of the lattice structure. This situation has been considered theoretically by *Suzuki and Yu (1995)* who calculated the emission rate of electric dipoles in fcc photonic crystals.

Further information on photonic crystals can be found in *J. Opt. Soc. Am. B 10,2 (1993)*; a special edition of the journal devoted to materials which are periodic on the scale of the wavelength of light.

2.3 Microcavities

The other structure commonly used to influence the spontaneous emission of atoms and molecules is the microcavity. As the name suggests the microcavity is simply a Fabry-Pérot cavity with a lateral dimension commensurate with the wavelength of light, typically sub-micron.

The photonic mode spectrum and density of states within the microcavity are both determined by the boundary conditions imposed on the electromagnetic field by the cavity walls. As a result, only those optical modes whose wavelength is a multiple of half the cavity width can be supported within the cavity, in much the same way that an organ pipe has certain fundamental acoustic modes. This discretisation of the electromagnetic mode spectrum alters the energy density associated with the electromagnetic field within the cavity, since only certain frequency photons are allowed to propagate. The zero-point vacuum fluctuations of the field (*virtual photons*) within the cavity are thus limited to the set of allowed frequencies dictated by the cavity dimensions. The cavity has only one (TM) mode for light of wavelength less than half the cavity width. This condition is known as the $\lambda/2$ cutoff. For the case of two conducting parallel plates, the resulting decrease in energy density from the free-space value leads to the existence of an attractive force between the two plates. This phenomenon is known as the Casimir effect [Casimir and Polder (1948), Casimir (1948)].

The spectrum of discrete cavity modes can be used to explain the effect of the cavity on the spontaneous emission of species contained within. Consider the case where the energy of the excited state is such that the photons it emits are prohibited from propagating within the cavity, *i.e.* the cavity is beneath cutoff. In this case, the excited state cannot decay by the emission of a photon since there is no available mode for the photon. In the absence of other non-radiative de-excitation routes, the decay of the state is forbidden and thus the lifetime of the excited state is lengthened. Alternatively, if the cavity is tuned by varying the cavity width, the optical transition can be brought into resonance with a cavity mode and the emission is correspondingly enhanced.

Quantum mechanically, spontaneous emission can be viewed as the emission of a photon from a species stimulated by vacuum fluctuations. These fluctuations are dependent on the mode structure in the vicinity of the emitter; if there are no modes, then there can be no fluctuations and thus the emission from the emitter cannot be stimulated. The converse argument holds true; at a band edge, the increased density of states per unit frequency interval leads to the existence of more virtual photons, thus enhancing the emission of the

source. The virtual photon description poses interesting questions about the dynamical nature of the emission process. If a cavity wall is removed, it takes a finite time for the emitter to detect the change, this time being given by the transit time for a photon to propagate to the emitter site from outside the cavity [*Fearn et al. (1995)*]. Cavities provide an excellent testing ground for the quantum mechanical description of light and matter, and this has led to the development of the field of cavity quantum electrodynamics (QED), reviewed in the article by *Hinds (1991)*.

When the optical fields within the cavity become very well confined, *i.e.* when the Q of the cavity is high, the coupling between the atom and the cavity modes dominates over the losses. In this strong coupling regime spontaneous emission is reversible and is characterised by the periodic exchange of energy between the atom and the cavity modes. The effect of the cavity is no longer a simple perturbation to the behaviour of the atom, but instead, it is more correct to consider the atom and the field as a single entity. Their behaviour can then be described as an entanglement between a state consisting of an excited atom and an unoccupied cavity mode, and a state consisting of an unexcited atom with a single photon in the cavity mode. The reversible spontaneous emission can be observed as a variation in the photon occupation in the cavity due to the resonant exchange of energy between the atom and cavity, a phenomenon known as *Rabi* oscillation [*Haken and Wolf (1994)*]. Depending on the pump power and number of atoms in the observation volume, oscillations can be observed which correspond to higher order photon occupation within the cavity mode [*Brune et al. (1996)*]. Similar entanglements of atoms and photons have been predicted for photonic crystals [*John and Wang (1990)*]. If the coupling between atom and cavity is strong enough, it is possible that the cavity modes will be split, leading to the observation of Rabi splitting [*Heinzen et al. (1987)*].

The first experimental demonstration of the inhibition of spontaneous emission in a cavity was achieved in the far infra-red, using an atomic beam travelling through a Fabry-Pérot cavity tuned below cutoff [*Hulet et al. (1981)*]. In this experiment, the extension of the lifetime of a beam of cesium atoms excited into a Rydberg state was observed. This was attributed to the absence of virtual photons within the cavity able to stimulate the 130nm transition

required to de-excite the atoms. This demonstration was later scaled to near-optical wavelengths by *Jhe et al. (1987)* who inhibited the $3.3\mu\text{m}$ transition of cesium atoms in a similar experiment.

Experiments in the optical regime have been more ambiguous due to the problem of locating emitters at precise positions within sub-wavelength scale microcavity structures. The resulting distribution of emitters leads to a smearing out of the desired inhibition effects. Early studies observed both the enhancement and inhibition of the spontaneous emission rate of dyes contained within on and off resonance cavities respectively. The geometries used in these studies were planar microcavities, either containing dye solutions [*De Martini et al. (1987)* and *(1991)*], or assembled monolayers of a dye [*Suzuki et al. (1991)*]. The poorly defined emitter position within these cavities, however, made it difficult to theoretically model the results obtained.

More involved experiments were carried out by the AT&T group, who studied semiconductor Fabry-Pérot microcavities implanted with erbium ions ($\lambda=1.54\mu\text{m}$). By fabricating a series of cavities of differing length, they were able to sweep from below cutoff to above cutoff for the first cavity mode and observe the change in the lifetime which resulted [*Hunt et al. (1995)*]. In related experiments, the radiation pattern from these cavities was measured and found to agree with a classical theory [*Schubert et al. (1992)*].

Similar experiments have been carried out by *Rigneault et al. (1997)* and *Robert et al. (1998)* who used ion implantation to fabricate dielectric microcavities containing erbium and praseodymium ions as emitters. They measured the emission of power into the various guided modes of the microcavity to show that the spontaneous emission rate was independent of the mode structure for weakly reflecting mirrors. In the microcavity used, the power emitted into the bound modes of the cavity simply detracted from the amount of power radiated from the cavity, leading to no overall change in emission rate.

The planar microcavity is not the only microcavity geometry that has been investigated. By drawing a neodymium-doped fibre down to sub-micron diameters and coating with gold, *Zbinden et al. (1995)* were able to create cylindrical microcavities and measured a 40% reduction in the lifetime of the excited Nd^{3+} ions contained within.

Theoretically, the spontaneous emission from species contained within planar microcavities has been treated both quantum mechanically and classically with identical results – the equivalence of these approaches has been proved by *Yeung and Gustafson (1996)*. Authors who have adopted quantum mechanical treatments include *Dutra and Knight (1996)*, *Philpott (1973)* and *Björk et al. (1991)*. Several different classical approaches have been made, most notably using Hertz vectors [*Chance et al. (1978)*] or using Green's functions [*Tomaš and Lenac (1993)*]. The advantage of the classical approach is that the effects of absorption within the system can be modelled simply, which is not trivial in the quantum mechanical case.

In effect, the microcavity approach is similar to the inclusion of high Q defect modes into a PBG structure. If a defect corresponding to a phase slip of $\lambda/4$ is introduced into the centre of a Bragg stack, the structure resembles that of a Fabry-Pérot cavity. Indeed, the optical behaviour changes from a mirror to a notch filter [*Yablonovitch (1992)*]. The transition from an isolated defect mode to a network of impurities within a dielectric stack was modelled by *Stanley et al. (1993)*.

Most of the microcavities reported in the literature have made use of dielectric mirrors to form the cavity walls. This stems from the low-losses that these mirrors have in the visible regime, in contrast with metallic mirrors. This advantage is offset to some extent by the strong angle dependence of the reflectivity of dielectric stack mirrors. Whilst the reflectivity at normal incidence may be as high as 99.9% for a given wavelength, this has usually fallen by a factor of two at 30° to the normal. This leads to poor field confinement and the effect on the spontaneous emission of emitters within the cavity is consequently degraded. Metallic mirrors, however, have very good reflectivities over a large angle range giving good confinement of the optical fields. Possible ways to use metal mirrors in optical microcavities, whilst avoiding the inherent losses, will be discussed later in this thesis.

Spontaneous emission above a planar interface will be considered in the following sections. This subject is of considerable interest both theoretically and experimentally because of the simplicity of the geometry, and the relevance it has to many important physical systems.

2.4 Fluorescence above interfaces

Of all the structures used to demonstrate the alteration of the spontaneous emission by geometrical means, the simplest is a planar reflecting interface, *i.e.* a mirror. Although the optical field confinement provided by the mirror is weaker than in previous cases, the principles involved are similar, and thus the underlying physics can be investigated in a facile manner. This has led to a wealth of work investigating the behaviour of fluorescent emitters above planar mirrors, most notably that of Drexhage and co-workers. The research carried out by this group has been reviewed in the article by *Drexhage (1974)*.

The first work examining the emission from a dye layer near an interface was carried out by *Selényi (1911), (1938) and (1939)*, who observed wide angle interference patterns in the emitted fluorescence. He attributed this to interference between the direct rays from the dye layer and the reflected rays from the interface. Furthermore, he correctly deduced from these observations that the emission from the dye molecules was electric dipole in nature. Further experimental progress was limited due to difficulties in achieving the thinner films necessary to make systematic studies of the effect of the interface on the emission. A general theory of the wide-angle interference phenomena observed by Selényi was subsequently proposed by *Doermann and Halpern (1939)*, though this was considered unnecessarily sophisticated by Selényi:

“In reality, the experiment in question is a simple one that can be performed in half a day at the utmost, and it can also be clearly explained in a few lines and without any mathematical formulae.” *Selényi (1939)*.

This work was continued by Drexhage and other members of Kuhn’s group at Marburg in the 1960’s, using an improved technique that allowed the temporal dependence of the emission from *monomolecular* dye layers to be investigated. This work will be discussed in detail because it forms the basis of modern research into the effect an interface has on the emission of molecules nearby, and so is the ideal introduction to the work contained in this thesis.

2.4.1. The Marburg experiments

In a series of elegant experiments, Drexhage investigated the absorption and emission of light by a layer of dye molecules situated in close proximity to the surface of a metal. The use of the Langmuir-Blodgett technique to deposit monomolecular layers represented a great advance over previous investigations. This allowed the formation of a single *monolayer* of dye molecules separated by a precise distance from the metal; effectively the ideal test-bed to study the effect of the interface. The resolution of this technique is only limited by the length of the molecule deposited, which in Drexhage's case was only 2.6 nm .

The experiments carried out fell into two groups, the first to investigate the absorption of light by dye molecules, and the second to investigate the emission properties of the molecules. Both sets of experiments could be carried out using similar samples. The experimental geometry is shown in *figure 2.1* and consisted of a series of monolayers of fatty acid molecules deposited using the Langmuir-Blodgett technique onto a silver mirror to form a transparent spacer layer. Depending upon the number of monolayers deposited, this spacer layer could be fabricated with a variable, but precise, thickness ranging from 2.6 nm to over 600 nm . A monolayer of dye molecules was then deposited on top of this assembly to complete the sample. The fabrication of samples using the Langmuir-Blodgett technique will be discussed in more detail in chapter 4.

(a) Absorption of light

In these experiments, the dye molecules were effectively used as a probe of the local optical field intensity within the structure. The dye molecules (in this case a cyanine derivative) were excited by light normally incident upon the structure from above. The light reflected from the mirror interfered with the incident light to create a standing optical wave. Depending upon their position within this standing wave field, the dye molecules could absorb energy from the field and this was subsequently re-emitted as fluorescence. The intensity of the fluorescence emitted by a dye is proportional to the amount of energy absorbed.

Since for weakly absorbing species, the absorption depends linearly upon the square of the local field E^2 , the fluorescence intensity is a direct measure of the local field strength.

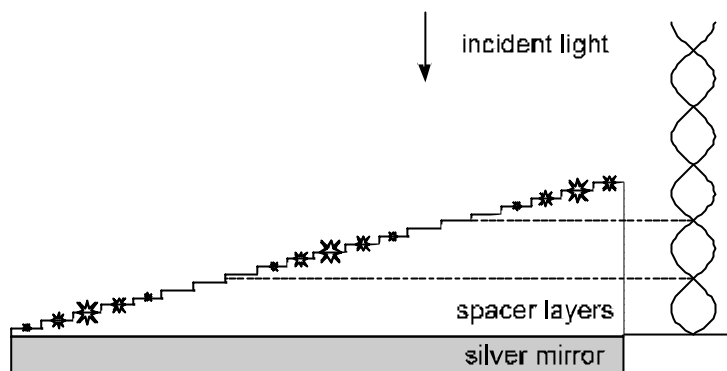


Figure 2.1 The experimental geometry studied by Drexhage, consisting of a “staircase” structure of spacer layers deposited on a mirror, capped by a monolayer of fluorescent dye. When light is incident upon this system, a standing light wave forms in front of the mirror which is able to excite fluorescence from the dye at field antinodes. Conversely, there is no fluorescence at distances corresponding to nodes. (Adapted from *Bücher et al. (1967)*.)

When the dye layer was situated at nodes of the optical field, the fluorescence observed was very weak. Conversely, when the molecules were situated at field antinodes the fluorescence was much stronger, as expected. By measuring the intensity of the fluorescence from the dye molecules as a function of dye-metal distance, Drexhage was able to map out the field profile throughout the sample. While the positions of the nodes were found to agree with a simple formula, the positions of the antinodes did not [*Drexhage (1974)*]. The origin of the discrepancy is that the fluorescence emitted by the dye is subject to the same interference effects as the pump wave. Because the absorption and emission wavelengths of the dye are different, the corresponding interference conditions are also different, leading to a complicated distance dependence. The effect of this interference on the emission process will be the subject of the next section.

The fluorescent probe technique outlined above was subsequently used by *Drexhage (1970)* to investigate the evanescent light field which exists

beyond the interface between high and low refractive index materials. By measuring the fluorescence from a monolayer of dye positioned at different distances from such an interface, he was able to show that the strength of the evanescent field does fall off exponentially.

(b) The emission of light

The emission of light above a reflecting interface is influenced in a similar way to the absorption of light, as was hinted in the previous section. Instead of considering the effect the interface has on the density of electromagnetic states in the vicinity of the molecule, however, it makes more sense in this scenario to adopt a classical approach. In this model, the dye molecule is treated as a dipole oscillator radiating into the half space above the mirror interface. The field above the mirror is thus composed of two components, the direct emission from the molecule, and the reflected field from the mirror. The oscillation of the dipole is then modified by the reflected field at the dipole site. Depending on the phase change accumulated on the round trip from the mirror, this field can drive the dipole in phase, or out of phase, leading to an enhancement or inhibition of the radiative rate. This is manifested as a variation in the lifetime of the dipole excited state as a function of distance from the mirror.

In order to demonstrate this, Drexhage measured the excited state lifetime of a fluorescent dye containing a Eu^{3+} ion as a function of the dye/metal separation distance [*Drexhage et al. (1966)*]. Two distinct regimes were found. Above a separation of about 30nm , the lifetime displayed oscillations with distance as expected, due to the interference effect of the reflected field. As the separation increased these oscillations decreased in amplitude. This implies that the reflected field is less intense at the dipole site for large molecule/mirror distances, a reasonable inference since the field originates from a dipole source. For separations smaller than 30nm it was found that the lifetime of the dye decreased rapidly with distance, suggesting that the dipole was being quenched very strongly by the presence of the metal in some way.

Using a theory based on the interference of the direct and reflected fields it was possible to explain the experimental results when the metal and molecule were well separated, but not the rapid quenching of the emission due to energy

transfer to the metal. A full theoretical treatment of the phenomenon of fluorescence in front of a mirror was given in a series of papers by Chance, Prock and Silbey (CPS), and summarised in the review article *Chance, Prock and Silbey (1978)*.

In their classical model, which treats the dipole as a simple harmonic oscillator, driven by the reflected field and damped by radiative emission, the quenching was seen to result from non-radiative transfer of energy to the metal surface. This is achieved mainly through the excitation of surface-plasmon polariton (SPP) modes, which propagate along the metal surface. These bound surface modes provide an extra non-radiative decay channel for the excited molecules, which decreases the lifetime of the excited state significantly. A full description of the SPP and other related modes will be given in chapter 3 because of their importance in the decay of excited molecules near metal interfaces. It will be seen that light can not normally couple to these modes, and it is necessary to provide extra momentum to achieve this. The near field of the dipole *can* provide this extra momentum because of the curvature of the wavefronts. The strength of coupling to the mode is thus determined by the degree of overlap of the dipole near field with the metal surface.

The SPP is not the only decay channel opened up by the proximity of the metal surface. As the molecule-metal separation decreases below about 10nm other physical processes can occur, such as the direct excitation of electron-hole pairs and the loss of energy to Joule heating in the metal [*Ford and Weber (1984)*]. In fact, at such small length scales these processes, rather than excitation of the SPP mode, dominate the damping of the dipole.

The radiation pattern of the emission is also affected by the presence of the mirror. This can be seen by consideration of *figure 2.2*. The emission in any given direction arises from a direct wave from the dipole and a reflected wave from the mirror. These two waves will interfere, and depending upon the path difference, this interference will give rise to maxima and minima in the angle dependent emission from the system. The exact radiation pattern observed will depend upon a number of factors, such as the orientation and nature of the dipole, the distance of the dipole away from the interface, and the polarisation of the light. These were neglected in the discussion of the lifetime dependence of

the emission, but as we shall see in chapter 6, these factors all have to be taken into account.

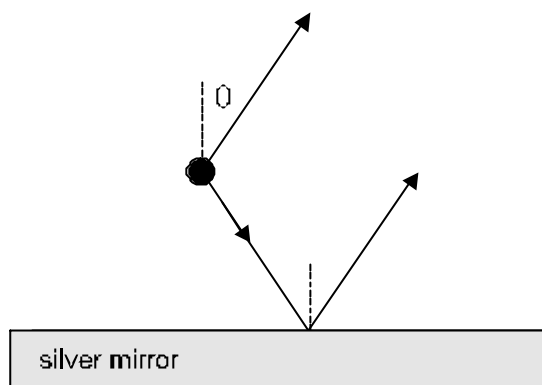


Figure 2.2 Interference of the direct wave from a dipole source and the wave reflected from a planar mirror.

After the pioneering work of Drexhage, there was much interest in the nature of the de-excitation processes involved in the decay of molecules near interfaces. The remainder of the chapter is therefore devoted to a discussion of some of the more important research subsequently carried out in this field. More comprehensive information can be found in the review articles by *Waldeck et al. (1985)* and *Barnes (1998)*.

2.4.2 After Drexhage

Much of the work carried out immediately after Drexhage's investigations was concerned with trying to understand the nature of the energy transfer to the metal for small dye/metal distances.

Using the CPS theory, *Weber and Eagen (1979)* showed theoretically that the power lost to the SPP mode was an exponential function of the dye/metal separation. If they included the loss due to other non-radiative processes, it was found that the peak coupling to the SPP mode was achieved at separations of the order 10-100nm, depending on the system. To demonstrate that dye molecules *could* de-excite via the generation of SPPs they carried out an experiment using a high index prism coated with optically thin silver. This silver film was placed in contact with a solution of a highly

fluorescent dye, rhodamine 6G. The dye was excited using a laser light incident from within the prism, and fluorescence was observed within the prism, characteristic of the re-radiation of SPPs propagating at the liquid/silver interface. The use of a prism was required to allow the SPP modes to couple to radiation since the SPP is a non-radiative mode for an unperturbed planar interface. Other methods of achieving coupling between SPPs and light are discussed in chapter 3. This phenomenon was also observed in experiments carried out by *Benner et al. (1979)*.

More quantitative results were obtained by *Pockrand et al. (1980)* who used the Langmuir-Blodgett technique to investigate the distance-dependence of molecule-SPP coupling. To achieve this, a thin silver film was evaporated onto the base of a prism followed by the deposition of a sequence of fatty acid spacer layers to create a “staircase” arrangement. This structure was capped with a monolayer of dye and more fatty acid layers to create a constant thickness structure. The dye molecules were excited by light incident from the air side of the structure, and fluorescence observed within the prism. As in the Weber and Eagen experiment, this fluorescence was the result of dye molecules de-exciting by generating SPPs at the silver/LB interface. Since the silver film was thin, these SPPs could couple to radiation modes in the prism, leading to the observation of narrow lobes in the radiation pattern. By monitoring the intensity of this SPP outcoupled light as a function of the spacer layer thickness, Pockrand was able to plot the distance dependence of the coupling. The optimum coupling distance for the system, *i.e.* the distance needed to obtain maximum intensity of prism coupled light, was found to be 18nm . At smaller separations, the coupling to SPPs was much reduced, highlighting the dominance of other decay mechanisms in this regime.

Similar experiments were carried out by *Lukosz and Kunz (1979)* who used a variable thickness air gap rather than a staircase structure to vary the molecule/metal separation. Again, it was found that SPP excitation was the most important decay channel for separations in the range of 10 to 50nm .

All the experiments mentioned so far were designed to investigate the role of the SPP in the decay of excited molecules. There has been a wealth of experiments investigating the energy transfer to metals by other competing mechanisms, but all suffer from experimental difficulties because of the small

distance scales involved. Within experimental error, however, all seem to validate the classical model given by Chance, Prock and Silbey, which predicts a $1/d^3$ dependence on the emission rate [Whitmore *et al.* (1982), Daffesthofer *et al.* (1995)]. An example of this type of study is the work of Crossen *et al.* (1993). By spin casting polymeric materials, they were able to deposit spacer layers onto aluminium mirrors with a thickness resolution of $\sim 1\text{nm}$, up to total thicknesses of about 6nm . Using this technique they studied the lifetime and emission spectra of monolayers of rhodamine spaced at different distances from the metal. The broadened spectra and shortened lifetimes observed were attributed to the excitation of electron-hole pairs in the metal.

Adams *et al.* (1980) investigated the luminescence lifetime of condensed nitrogen films on silver surfaces and found agreement with classical theory for the distance regime $3\text{-}1000\text{nm}$. They later considered the effect of corrugating the planar mirror interface to form a diffraction grating [Adams *et al.* (1982)]. In this study, the deposition of nitrogen films up to 200nm in thickness allowed the excitation of guided modes as well as SPPs. Scattering from the diffraction grating then allowed these modes to couple to radiation, resulting in the observation of peaks in the angle-dependent emission. Plotting the angular position of the peaks as a function of layer thickness revealed the characteristic dispersion of the modes, confirming the origin of the emission maxima. No lifetime data was reported however, and so the effect of the corrugation on the emission rate of the species was still uncertain. The use of a grating to scatter non-radiative surface modes such as the SPP and thus couple them to photons was first reported by Knoll *et al.* (1981) who spaced dye molecules from a silver grating using the Langmuir-Blodgett technique.

Subsequently, Holland and Hall reported on the enhanced fluorescence of dye molecules situated above planar waveguiding structures, and attributed the increase to the interaction between the molecules and the enhanced fields of the guided modes [Holland and Hall (1985)]. In their original paper, it was uncertain as to whether the fluorescence increase arose from the enhancement of the incident field, or the enhancement of the molecular emission. It is likely that both were involved due to the poor optical quality of their samples, which could have resulted in roughness scattering of the bound modes. (In a truly flat sample, the bound modes could not scatter and so the energy would be lost to

the substrate). The data was reanalysed in a subsequent paper, which included an adaptation of the CPS theory [Sullivan and Hall (1997)]. The impetus for this work was the possibility of increasing the sensitivity of chemical sensors through the enhancement in emission made possible by molecule-surface mode interaction. The enhancement reported upon in their previous research, which partly relied upon roughness scattering, was improved by deliberate corrugation of the waveguide, thus allowing the direct re-radiation of bound surface modes [Sullivan *et al.* (1994)].

2.4.3 The Exeter experiments

Very recently, research has been carried out on the fluorescence of dye molecules deposited directly onto metallic grating structures. Particular attention was paid to the importance of the SPP mode in determining the radiation pattern of the emission. The work, carried out by Kitson and co-workers, has four distinct components. The first two relate to the enhancement of the absorption and emission properties of the dye molecules by interaction with the SPP modes of the interface, whilst the second two investigate the effect of SPP band gaps.

Initially, an increase in the absorption of the dye molecules was demonstrated by pumping them *via* the enhanced fields of the SPP mode [Kitson *et al.* (1996a)]. This was achieved by varying the angle of incidence of a pump beam at the grating surface and observing the fluorescence of the dye molecules. When the SPP mode was resonantly excited *via* grating coupling, the intensity of fluorescence from the dye was found to increase by up to ten times the off-resonant value. This increase is due to the highly enhanced fields of the SPP mode, which effectively concentrate the energy of the pump beam in the vicinity of the dye molecules. In this way, the absorption cross-section of the dye molecules is increased by the SPP-molecule interaction. This has possible applications in enhancing the rate of photochemical reactions [Goncher *et al.* (1984)] or increasing the intensity of Raman scattering [Giergiel *et al.* (1988)].

The same interaction can occur in the emission process also. When the excited dye molecules decay, the dominant route is the excitation of SPP

modes at the metal interface. If the interface is flat, then the modes are bound to the surface, and their energy is lost as heat to the metal. If, however, the metal surface is corrugated, then the SPP can scatter from the periodicity and couple to radiation. In this way, energy which would otherwise be lost can be recouped as a useful optical emission. To demonstrate this, the fluorescence from dye coated metal gratings was measured as a function of angle for a fixed pump angle [Kitson *et al.* (1996b)]. Peaks were observed in the angular emission which corresponded to the scattering and re-radiation of SPP modes generated by the de-excitation of dye molecules. This scattered SPP emission was typically an order of magnitude more intense than the direct emission from the dye, and had an angular width of about 2°. Studies of the wavelength, polarisation and azimuthal dependence of the enhanced emission were made; all of which confirmed the origin of this SPP re-radiation. The enhanced emission in certain directions has possible uses in sensor applications

Just as periodic dielectrics can exhibit photonic band gaps, corrugated metal surfaces can display band gaps for SPPs in an analogous fashion [Barnes *et al.* (1995), (1996)]. The underlying physical processes are the same, but because the SPP is a surface mode, propagation only has to be inhibited in a plane to create a full gap. Corrugating a surface to form a grating with sub-micron periodicity is relatively simple, and so the study of SPP band gaps provides an easy way of investigating PBG effects without the complexity of fabricating three-dimensionally periodic crystals.

In order to observe the effect of an SPP band gap on the interaction between SPPs and dye molecules, two different experiments were performed. In the first experiment, the coupling between *excited* dye molecules and SPPs was perturbed by the introduction of a gap in the SPP dispersion. By measuring the fluorescent emission from a grating sample which possessed an SPP band gap in the emission spectrum of the dye, Kitson *et al.* (1995) were able to demonstrate that the SPP decay channel had been blocked. The gap was observed as a reduction in the SPP re-radiation intensity for those wavelengths corresponding to the gap region, indicating that the coupling to those modes was diminished.

In the second experiment, described fully in chapter 5, the coupling of SPPs to dye molecules was perturbed by the presence of an SPP band gap for

wavelengths corresponding to the absorption spectrum of the dye. It was observed that the enhanced absorption mediated by the SPP–molecule interaction was absent for wavelengths corresponding the gap region [Andrew *et al.* (1997)]. This was caused by the removal of the SPP excitation channel by the blocking of relevant energy modes. In this way, a gap was introduced into the absorption spectrum of the dye/grating system. In both of these SPP energy gap experiments, an enhancement of the SPP-molecule interaction was observed in the band edge regions, as expected from mode density considerations. This resulted in an increase in the fluorescence emission from the system.

To achieve a full gap for SPP modes requires more than a single corrugation of the surface since the modes are only blocked from propagating within a small azimuthal angle range normal to the grating grooves [Barnes *et al.* (1997)]. By using a hexagonally textured grating surface, Kitson *et al.* (1996c, 1996d) demonstrated that SPP propagation could be blocked in *all* azimuthal directions for a given frequency range, so producing a full SPP band gap. The SPP decay channel is thus completely removed for fluorescent emitters above such a metallic surface.

As mentioned previously, dielectric mirrors are often used in microcavity structures to avoid the “inherent” losses that metals exhibit at optical wavelengths. Since for many applications this loss is almost exclusively due to the excitation of SPPs at metal-dielectric interfaces, the use of corrugated surfaces could allow dielectric stacks to be replaced with metal mirrors in microcavities. This is desirable because, unlike dielectric stacks, metals exhibit high reflectivity over large angle ranges. In addition, the penetration depth of optical fields into metals is much smaller than it is for dielectric stacks. The result is that metallic microcavities exhibit much greater optical confinement than cavities made from dielectric mirrors, and consequently have a greater effect upon spontaneous emission. The use of metals is also required for devices with electrodes, such as electroluminescent polymer LEDs in order to inject electrons into the light-emitting layer. Any means of reducing the optical losses in such a situation is desirable.

As a preliminary investigation, the mode structure of a metallic microcavity with a singly corrugated mirror interface has been measured by

Kitson et al. (1998). An SPP band gap was observed beneath the cut-off for cavity waveguide modes, implying that for at least one propagation direction there were no electromagnetic modes within the cavity. Work is currently in progress to fabricate metallic microcavities with hexagonally textured mirrors to inhibit modes in all directions. The resulting structure is thus a hybrid between a microcavity and a PBG crystal. The aim of these investigations is to fabricate a cavity with a full SPP band gap coincident in frequency with the cut-off for the lowest order TE mode. Emitters radiating at this frequency can thus only couple to the TE mode, and since it is at cut-off, the emission will be enhanced (the mode is a standing wave). Another consequence of the standing wave nature of this TE mode is that the emission from the structure will occur in a direction normal to the top mirror, a desirable result for most devices.

Although many works have reported the alteration of radiation patterns by corrugation of the interface, principally by the scattering of bound surface modes, there have been no experimental reports of decay rate modifications. Despite this, there have been a considerable number of theoretical predictions about the decay rate modification obtained in the presence of a corrugated interface. Notable amongst these are the studies of Leung and co-workers [*Leung et al. (1987a, 1987b, 1988, 1989)*]. In these papers, the CPS theory was extended to include the effect of a sinusoidal interface profile. By assuming small depth-to-pitch ratios, *i.e.* weak profile modulations, and considering normal incidence of the dipole fields only ($k_{||}=0$), it was predicted that morphology dependent resonances should be observable, leading to significant changes in the decay rate. The enhancements in decay rate predicted for these resonances, typically two orders of magnitude greater than the planar interface rate, are all the more surprising considering the weakness of the proposed modulation (typically a sinusoid with pitch 500nm and amplitude $\sim 0.1\text{nm}$). It is likely that these remarkable effects will depend strongly on the assumptions made, and will vanish, or be much reduced, for a more rigorous model. The assumption that only the $k_{||}=0$ term is important, for example, is not even true in the case of a planar interface. It will be seen in chapter 6 that for a planar interface, a summation has to be made over a large range of $k_{||}$ values to obtain realistic results for the decay rate of dipoles ($k_{||}$ is the in-plane momentum component of the dipole field).

Investigating the decay rate of emitters in close proximity to a corrugated interface will form a large part of the experimental work reported in this thesis. The gratings considered have large depth-to-pitch ratios, and so the theory described above is not expected to be valid since it is only a perturbation of the planar interface result. Nevertheless, deeper gratings should show more interesting behaviour than shallow gratings because of the increase in the intensity of scattered fields, and the greater dissimilarity in the local environment of dipoles displaced laterally across a grating groove.

2.5 Summary

In this chapter, the control of spontaneous emission by alteration of the local electromagnetic mode density has been reviewed. Particular attention has been paid to the modification of molecular fluorescence resulting from the proximity of a reflecting interface. In this context, the pioneering work of Drexhage has been discussed, together with the advances made by subsequent investigators. These studies are of interest because they form the motivation for the work contained in this thesis.

The significance of the SPP mode as a decay channel for excited molecules above metal mirrors has been highlighted. Together with waveguide modes, SPPs are the most important decay mechanism for the structures considered in this thesis, and so the following chapter will be devoted to a discussion of their properties.

Chapter 3

Electromagnetic surface modes

3.1 Introduction

An excited atom or molecule located in free space will eventually relax back to its ground state *via* the emission of a photon (discounting for the time being the possibility of internal non-radiative relaxation). In this situation there have been no limitations placed on the nature of the emission of the molecule. If, however, the molecule is placed above an interface, or embedded within a multilayer system, the boundary conditions for the radiated field are significantly altered, and there is the possibility of relaxation not *just* by the emission of photons, but also by the excitation of electromagnetic surface modes. Indeed, if the molecule-interface separation is small compared with the emission wavelength, then the excitation of surface modes will be the dominant decay mechanism. In this case the emission of the molecule will be determined mainly by the nature of the surface modes available and the strength of coupling to these modes.

In light of the important contribution that these modes make to the emission characteristics of excited species, this chapter will be devoted to a discussion of their physical origin and the nature of their propagation and dispersion. Since these modes are found to be non-radiative, the problem of coupling light into these modes will also be addressed. Several different layered structures will be considered, which are typical of samples fabricated in later chapters of this thesis and the surface modes they support will be discussed. Initially we will concentrate on the mode supported by a simple planar metal/dielectric interface, the surface-plasmon polariton (SPP), derive the relevant dispersion relation, and then consider the spatial extent of the fields associated with it. If a thick dielectric overlayer is added to the metal (of higher

refractive index than the surrounding medium) the structure may support guided electromagnetic modes as well as the SPP and we will consider what conditions are necessary to observe these modes.

3.2 Surface-plasmon polaritons.

The surface-plasmon polariton is a non-radiative electromagnetic mode which propagates along the interface between a metal and a dielectric medium. Essentially, the SPP is a result of the coupling between electromagnetic radiation and surface charge oscillations, and as such is a transverse magnetic (TM) mode. This is because there has to be a component of the electric field *normal* to the interface to generate the necessary surface polarisation charge. TM polarised light incident on an interface will satisfy this condition since the electric vector lies in the plane of incidence, whereas transverse electric (TE) polarised light will not since the electric vector is normal to the plane of incidence. As expected for a surface mode, the fields associated with the SPP are strongly localised at the interface (decaying exponentially into the bounding media) and are typically highly enhanced with respect to the incident light field. These properties make the SPP mode particularly sensitive to the optical parameters of the interfacial region, and many studies use the excitation of SPPs as a powerful surface-specific characterisation tool. This technique has been used extensively to measure the optical constants of metals [Weber and McCarthy (1975), Nash and Sambles (1995 and 1996)] as well as their surface roughness [Ræther (1988)]. Thin overlayers and adsorbates on metal surfaces have been studied in detail using SPPs by Ræther (1988) and Pockrand (1978). Probably the most widespread use of the SPP, however, is in sensing applications, where a *change* in the interface parameters is detected. Examples include the sensing of gases [Nylander *et al.* (1982)], biomaterials [Lawrence and Geddes (1997)] and organic condensates [Vukusic *et al.* (1992a)]. In a similar manner SPPs have been used to monitor electrochemical reactions by Jory *et al.* (1996). The highly enhanced fields of the mode also make it particularly suited to the study of non-linear optical phenomena, especially second harmonic generation [Schmidlin *et al.* (1989)] and Raman scattering

[*Giergiel et al. (1988)*]. Although these examples demonstrate the extensive use made of SPP techniques in applied physics applications, they also have a rôle to play in more fundamental investigations, see for example the elegant series of experiments carried out by *Groeneveld et al. (1990)*. In this study SPPs were excited in pump-probe measurements to observe the ultrafast relaxation of a hot electron plasma excited in a thin film.

The dispersion relation $\omega(k)$ for the SPP mode will now be derived and the implications this has for the coupling of incident light to the mode will be discussed.

3.2.1 The surface-plasmon polariton dispersion relation

Consider the interface between two isotropic media, both semi-infinite in extent. From Maxwell's equations it can be shown that the normal component of the electric displacement \mathbf{D} will be continuous across the interface. Furthermore, the constitutive relation linking \mathbf{D} and the electric field \mathbf{E} states that

$$\mathbf{D} = \epsilon \epsilon_0 \mathbf{E} \quad (3.1)$$

where ϵ_0 is the permittivity of free space and ϵ is the dielectric constant of the medium in question (in general, this will be complex). If the upper medium is a dielectric with positive real part of ϵ and the lower medium is a metal with negative real part of ϵ , then it can be seen from *equation (3.1)* that the normal component of \mathbf{E} will change direction as we cross the interface. It is this discontinuity in the normal \mathbf{E} field which creates a sheet of polarisation charge trapped at the interface. If the static fields of the preceding argument are replaced by time-dependent electromagnetic waves, the dispersion relation of the resultant surface charge oscillation can be derived. The following treatment is due to *Ræther (1988)*.

Figure 3.1 shows a TM electromagnetic wave incident at the interface between two semi-infinite non-magnetic media, the upper medium a dielectric with dielectric constant ϵ_2 and the lower medium a metal with dielectric constant ϵ_1 . The waves propagate in the x-y plane and as there is no z-dependence $\partial/\partial z = 0$. Because for a non-radiative surface mode solution only one

electromagnetic wave need exist in each medium, one of the fields in the dielectric can be set to zero – arbitrarily this is chosen to be \mathbf{E}_2^+ .

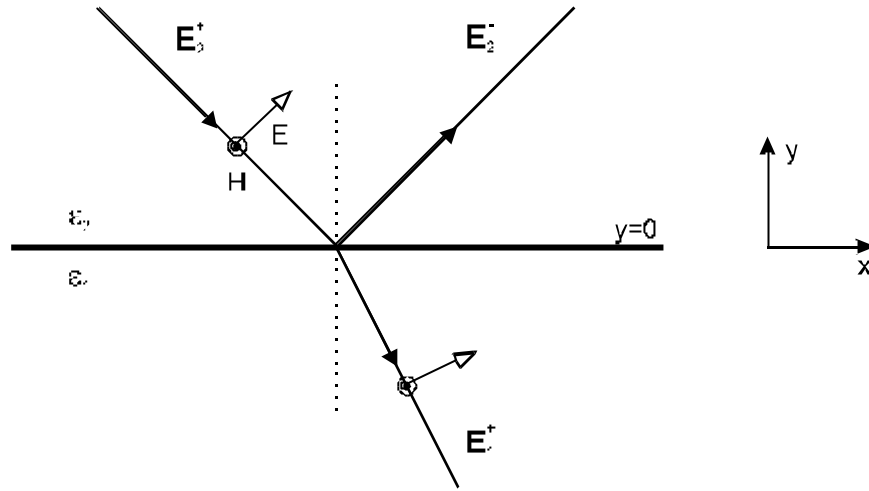


Figure 3.1 The incident, reflected and transmitted fields associated with a TM polarised electromagnetic wave incident upon a planar interface. The z-axis projects out of the plane of the page.

The fields in the upper and lower half-spaces can then be expressed in the following manner

$$y > 0 \quad \mathbf{E}_2 = [E_{x2}, E_{y2}, 0] \exp i(k_{x2}x + k_{y2}y - \omega t) \quad (3.2)$$

$$\mathbf{H}_2 = [0, 0, H_{z2}] \exp i(k_{x2}x + k_{y2}y - \omega t)$$

$$y < 0 \quad \mathbf{E}_1 = [E_{x1}, E_{y1}, 0] \exp i(k_{x1}x - k_{y1}y - \omega t) \quad (3.3)$$

$$\mathbf{H}_1 = [0, 0, H_{z1}] \exp i(k_{x1}x - k_{y1}y - \omega t)$$

where k_x and k_y are the tangential and normal components of the wavevector of the mode respectively. These fields must satisfy Maxwell's equations, and upon substitution into the curl equation

$$\nabla \times \mathbf{H} = \epsilon \epsilon_0 \frac{\partial \mathbf{E}}{\partial t} \quad (3.4)$$

the following expressions may be obtained

$$k_{y1} H_{z1} = \omega \epsilon_0 \epsilon_1 E_{x1} \quad (3.5)$$

$$k_{y2} H_{z2} = -\omega \epsilon_0 \epsilon_2 E_{x2}. \quad (3.6)$$

(Note that use is made of the identities $\partial/\partial y \equiv \pm ik_y$ and $\partial/\partial t \equiv -i\omega$)

The requirement from Maxwell's equations that the tangential components of the \mathbf{E} and \mathbf{H} fields should be continuous across the interface leads to the boundary conditions

$$E_{x1} = E_{x2} \quad (3.7)$$

$$H_{z1} = H_{z2}.$$

Equations (3.5), (3.6) and (3.7) can then be used to obtain

$$\frac{k_{y1}}{\epsilon_1} + \frac{k_{y2}}{\epsilon_2} = 0. \quad (3.8)$$

The boundary conditions in equation (3.7) also imply that

$$k_{x1} = k_{x2} = k_x$$

which is a statement of the conservation of momentum parallel to the interface. This is to be expected since the interface is translationally invariant. From the wave equation, the wavevector of an electromagnetic wave propagating in a medium of dielectric constant ϵ is given by

$$k^2 = \epsilon \left(\frac{\omega}{c} \right)^2 \quad k = \frac{2\pi}{\lambda} \quad (3.9)$$

where λ is the wavelength in the medium. In terms of the tangential and normal components of the wavevector

$$k_x^2 + k_{yi}^2 = \epsilon_i \left(\frac{\omega}{c} \right)^2 \quad i=1,2. \quad (3.10)$$

Equations (3.8) and (3.10) can then be rearranged to obtain the tangential component of the wavevector

$$k_x = \frac{\omega}{c} \sqrt{\frac{\epsilon_1 \epsilon_2}{\epsilon_1 + \epsilon_2}}. \quad (3.11)$$

This is the dispersion relation which describes the charge oscillation at the interface. The oscillation is longitudinal in nature, and has associated transverse and longitudinal electromagnetic fields with maxima at the surface $y=0$ and which decay exponentially away from the interface. These charge distributions and field profiles are illustrated in *figure 3.2*. It is the coupling between the surface charge oscillation and these electromagnetic fields which constitutes the SPP mode. The TM polarised nature of the mode thus becomes clear – since TE polarised light has no normal component of the electric field at the interface, it cannot generate the requisite surface charge, and hence cannot excite the mode.

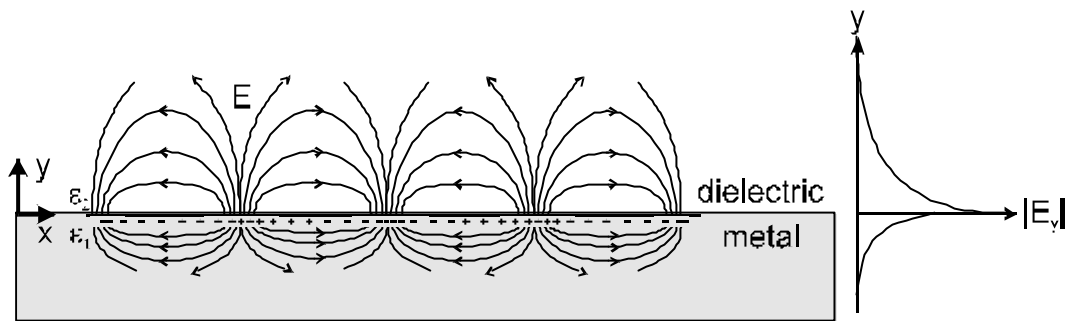


Figure 3.2 The field and charge distributions associated with the SPP mode.

Up to this point in the description of the SPP mode no limitations have been placed on the values that ϵ_1 and ϵ_2 may take, save that ϵ_1 describes a metal and ϵ_2 a dielectric. As a result, appropriate forms for the dielectric constant of the media are

$$\epsilon_1 = \epsilon'_1 + i\epsilon''_1 \quad \epsilon'_1 < 0 \quad (3.12)$$

$$\epsilon_2 > 1.$$

The imaginary term in the metal ϵ accounts for the scattering losses inherent in a *real* metal; the electrons can scatter from phonons, defects and also the surface. Medium 1 is thus a real metal, and medium 2 a loss-free dielectric. The SPP wavevector can then be written in the form $k_x = k'_x + ik''_x$, where the first term describes the propagation of the mode, and the second term the damping due to absorption in the metal. If the metal is good, that is, $|\epsilon'_1| \gg \epsilon''_1$, *equation 3.11* may be used to find the following expressions

$$k'_x = \frac{\omega}{c} \left(\frac{\epsilon'_1 \epsilon_2}{\epsilon'_1 + \epsilon_2} \right)^{1/2} \quad (3.13)$$

and

$$k''_x = \frac{\omega}{c} \left(\frac{\epsilon'_1 \epsilon_2}{\epsilon'_1 + \epsilon_2} \right)^{3/2} \frac{\epsilon''_1}{2(\epsilon'_1)^2}. \quad (3.14)$$

To describe a propagating mode, k'_x must be real, and *equation 3.13* shows that for $\epsilon'_1 < 0$ this is indeed the case as long as $|\epsilon'_1| > \epsilon_2$. If both of these conditions are satisfied then it is found from *equation 3.13* that $k'_x > \sqrt{\epsilon_2}(\omega/c)$. This means that the SPP mode *always* has a greater wavevector than a photon of the same frequency propagating in the adjacent dielectric. This has two important implications.

Because the energy and wavevector of a photon in the dielectric can never simultaneously match that of the SPP, no coupling is possible and the SPP mode is thus *non-radiative*. In order to excite an SPP at a planar interface using photons some means of augmenting the photon momentum is thus required (the momentum of a photon is linearly related to its wavevector). Several schemes to achieve this are detailed in *section 3.4*.

Since $k'_x > \sqrt{\epsilon_2}(\omega/c)$, inspection of *equation 3.10* shows that k_{yi} is always imaginary. This ensures that the fields associated with the SPP decay into the bounding media exponentially, as required. It is thus the enhanced momentum of the SPP mode that effectively ties it to the interface. In the following sections the spatial extent of the SPP fields will be considered.

3.2.2 Propagation length of the SPP

Introduction of an imaginary component to the SPP wavevector, k''_x , leads to an exponential decay in the intensity of the mode as it propagates along the interface between the metal and the dielectric. From *equation 3.2*, the fields associated with the SPP will fall off as $\exp(-k''_x x)$ and so the intensity will

fall off as $\exp(-2k_x''x)$. The distance over which the intensity falls off to 1/e of its initial level then given by $L = (2k_x'')^{-1}$ and thus

$$L = \frac{\lambda_0}{2\pi} \left(\frac{\epsilon_1' + \epsilon_2}{\epsilon_1' \epsilon_2} \right)^{3/2} \frac{(\epsilon_1')^2}{\epsilon_1''}. \quad (3.15)$$

The dielectric constant of silver at $\lambda_0=632.8nm$ is $\epsilon_{Ag} \approx (-17.6+0.7i)$ and it is found from *equation 3.15* that $L \approx 42nm$ for SPP propagation at a silver-air interface. Further into the infra-red, silver becomes a better metal and this figure improves dramatically. The energy lost by the SPP as it propagates along the interface is absorbed by the metal and gives rise to local heating. If the propagation length, L , of the mode is small this heating can be significant and leads to applications in measuring thermal non-linearities [*Sambles and Innes (1988)*]. More importantly, if the SPP mode encounters a surface corrugation with periodicity comparable to its wavelength and considerably less than its propagation length, it is possible for the mode to Bragg scatter from the surface and thus gain the extra momentum needed to couple to photons.

As was shown earlier, the SPP fields penetrate into the bounding media and in the next section the extent to which this occurs will be quantified.

3.2.3 Penetration depth of the SPP fields

The amplitudes of the fields associated with the SPP will decrease exponentially into the surrounding media because of the imaginary nature of the normal wavevector k_y . If the penetration depth of the fields is defined to be the distance normal to the interface over which the field strength falls to 1/e of the value at the interface the spatial extent of the electromagnetic fields associated with the SPP can be calculated. First, an expression for k_y is required. Substituting *equation 3.11* into *equation 3.10*, and assuming that $|\epsilon_1'| \gg \epsilon_1''$ yields

$$k_{yi} = \pm \frac{\omega}{c} \left(\frac{\epsilon_i'^2}{\epsilon_1' + \epsilon_2} \right)^{1/2} \quad i=1,2. \quad (3.16)$$

Note that the previous conditions $\epsilon'_1 < 0$ and $|\epsilon'_1| > \epsilon_2$, guarantee that k_{yi} is purely imaginary, as mentioned earlier. Since the fields fall off normal to the interface as $\exp(-|k_{yi}|y)$ the penetration depth is given by $\hat{y}_i = |k_{yi}|^{-1}$ and expressions for the field penetration into each medium can be found

$$\hat{y}_1 = \frac{\lambda_0}{2\pi} \left| \frac{\epsilon'_1 + \epsilon_2}{\epsilon_1'^2} \right|^{1/2} \quad (3.17)$$

$$\hat{y}_2 = \frac{\lambda_0}{2\pi} \left| \frac{\epsilon'_1 + \epsilon_2}{\epsilon_2^2} \right|^{1/2}. \quad (3.18)$$

Considering a silver-air interface and using the previously quoted values for the dielectric constant of silver at $\lambda_0=632.8nm$, it is found that $\hat{y}_1=25nm$ and $\hat{y}_2=434nm$. It can be seen from this that the fields associated with the SPP penetrate much further into the dielectric than into the metal. Consideration of the local field intensities thus shows that if a monolayer of dye molecules is located above the metal, interaction between the molecules and the SPP mode is possible and indeed likely for dye-metal separations less than the emission wavelength of the molecule.

3.2.4 The SPP dispersion curve for a free-electron metal

In this section the effect of describing the metal with a frequency-dependent dielectric constant is discussed and the consequence this has for the SPP dispersion curve illustrated. Before doing this it will be instructive to apply the results of the previous sections to the case of an interface between a dielectric and a perfect metal. A perfect metal will respond instantaneously to an applied electric field to cancel it, is loss-less and is thus characterised by a dielectric constant of the form $\epsilon = -\infty + 0.0i$. From *equation 3.15* it is found that the propagation length of an SPP at such an interface is infinite and *equation 3.17* shows that the \mathbf{E} field associated with the mode is totally excluded from the metal, as expected. Conversely, *equation 3.18* implies that the \mathbf{E} field is infinite in extent in the dielectric medium, which is atypical behaviour for a surface mode. In the limit of a perfect metal, however, the SPP

dispersion relation *equation 3.13* reduces to the form $k'_x = \sqrt{\epsilon_2}(\omega/c)$, which is identical to the dispersion relation of a photon propagating parallel to the interface in the dielectric above the metal. The behaviour of the SPP mode propagating at the interface of a perfect metal and a dielectric as detailed above is thus reminiscent of that of a photon and the mode is described as *light-like*.

To investigate the dispersion of the SPP mode for a more realistic system the frequency dependence of the dielectric constants of the media must be considered. For most loss-free dielectric media the dispersion of the dielectric constant is negligible in the visible region due to the lack of electronic resonances. The dielectric constant of such a material can thus be regarded as frequency independent. In the case of a metal, however, the dielectric constant is found to vary quite markedly with frequency throughout the visible region. This is a result of the response of the conduction electrons to an applied optical field. To obtain the frequency dependence of the dielectric constant of a metal in a simple fashion, the conduction electrons may be regarded as a gas of non-interacting particles within a lattice of positive ion cores. This *free-electron model* describes the behaviour of an ideal gas of electrons and by way of analogy the metal is thus known as an *ideal* metal. The metal is assumed to be loss-free and thus the imaginary part of the dielectric constant is set to zero. The real part of the dielectric constant is then given by

$$\epsilon(\omega) = 1 - \frac{\omega_p^2}{\omega^2} \quad (3.19)$$

where ω is the angular frequency of the radiation and ω_p is the *plasma frequency* of the metal. Consideration of the bulk longitudinal plasma oscillations of the electron gas for $k=0$ shows that

$$\omega_p = \sqrt{\frac{ne^2}{m\epsilon_0}} \quad (3.20)$$

where n is the free-electron density, e the electronic charge, m the electronic mass and ϵ_0 the permittivity of free space. The significance of the plasma frequency is understood when the nature of $\epsilon(\omega)$ from *equation 3.19* is investigated for frequencies above and below ω_p . When $\omega < \omega_p$, $\epsilon(\omega)$ is negative

and the response is thus metallic in nature. Note that as $\omega \rightarrow 0$ the response tends to that of a perfect metal (as $\omega \rightarrow 0$, $\varepsilon(\omega) \rightarrow -\infty$, assuming finite ω_p). If on the other hand $\omega > \omega_p$, $\varepsilon(\omega)$ is positive and the frequency of the applied field is too high for the electron gas to respond in a collective fashion. The resultant behaviour will then resemble that of a dielectric. The plasma frequency thus defines the metal-dielectric transition in the response of the material to applied optical fields.

To obtain the frequency dependent SPP dispersion curve for a free-electron metal/dielectric interface, the dielectric constant given in *equation 3.19* is substituted into the SPP dispersion relation *equation 3.20*. The resulting curve is illustrated in *figure 3.3* where it is plotted together with the dispersion of a photon propagating at grazing incidence in the dielectric medium. This line represents the maximum wavevector possible in the plane of the interface for a photon of a given frequency, and is known as the *light-line*.

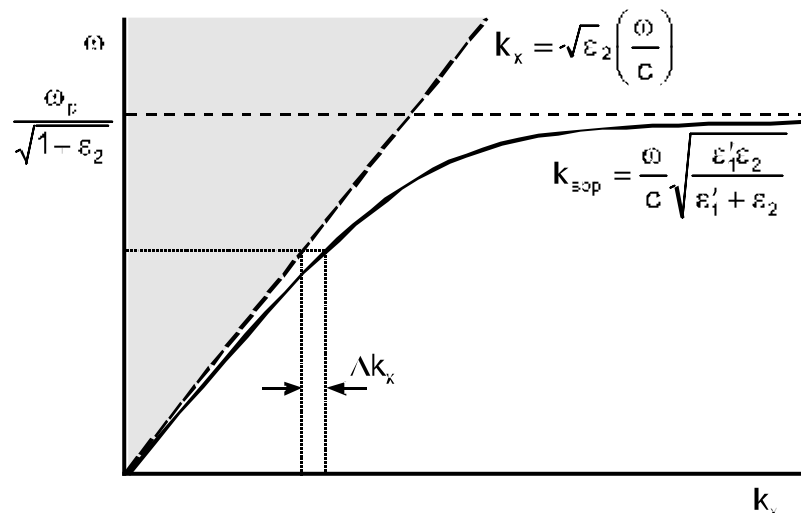


Figure 3.3 The SPP dispersion curve for a free-electron metal surface. The grey region represents the range of frequencies and wavevectors accessible to light propagating in the dielectric above the metal, and is bounded by the light-line.

As the frequency decreases, the SPP dispersion approaches the light line asymptotically from the high wavevector side. This reinforces the notion that the SPP mode becomes more light-like as the metal approximates a perfect

metal more closely. The non-radiative nature of the mode is also illustrated, as at no point does the SPP curve enter the grey shaded region which represents the range of frequencies and wavevectors accessible to light propagating in the dielectric medium. For a given energy the SPP mode always has slightly greater momentum than a photon of the same frequency in the dielectric, the mismatch being denoted as Δk in the figure. Note that in the limit of large wavevector, the frequency of the mode approaches the value $\omega_p / \sqrt{1 + \epsilon_2}$. This is known as the *asymptotic surface plasmon frequency* and for a silver-air interface corresponds to an energy of 3.6 eV, which is the UV region of the electromagnetic spectrum. As this limit is approached, both the phase velocity (ω/k) and the group velocity ($\partial\omega/\partial k$) of the mode tend to zero and so the SPP becomes a standing wave. The consequent 'flat-band' behaviour implies that the asymptotic surface plasmon has a large density of states per unit frequency interval in \mathbf{k} -space as compared to the mode at lower energies. If the energy of the asymptotic surface plasmon could be reduced to lie within the visible region of the spectrum this enhanced density of states could lead to increased molecule-SPP coupling.

3.2.5 Effect of a dielectric overlayer on SPP dispersion

In work described later in this thesis, the interaction between an excited dye molecule and a metal mirror is investigated as a function of the molecule-metal separation. To position these dye molecules a known distance above the metal surface, monolayers of a fatty acid are sequentially deposited onto the bare metal to form a transparent dielectric spacer layer. A monolayer of the dye molecules is then deposited on top of the dielectric. By varying the number of spacer monolayers deposited the overlayer thickness, and thus the dye-metal separation, can be controlled with molecular resolution.

One consequence of the presence of this dielectric overlayer is that, for fixed frequency, the dispersion curve of the SPP propagating along the metal surface is shifted to higher wavevectors. Consider the metal/dielectric/air structure shown in *figure 3.4*, where the dielectric layer thickness d is variable, $\epsilon_2 > 1$ and $\epsilon_3 = 1$.

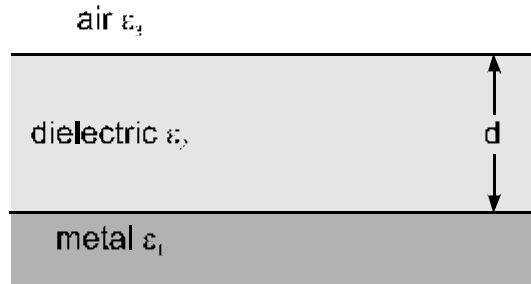


Figure 3.4 Geometry of a metal surface coated by a dielectric overlayer of thickness d .

In the limit that $d=0$, the geometry is that of a metal-air interface and the SPP wavevector is given by the single-interface dispersion relation (equation 3.13) as $(\omega/c)\sqrt{\epsilon_1/(\epsilon_1 + 1)}$. For $0 < d < \lambda$, the SPP electromagnetic fields exist in both the dielectric layer and the air half-space, and the exact SPP wavevector is necessarily given by a double interface solution [Pockrand (1978)]. It is obvious, however, that the SPP will have greater wavevector than in the metal-air case due to the higher permittivity of the dielectric overlayer. It is this shift in the wavevector of the SPP on addition of overlayers which is exploited in most sensing applications. In the limit that $d > \lambda$, the SPP electromagnetic fields lie almost completely within the dielectric and the SPP wavevector is again given by the single interface solution, this time with the dielectric constant of air replaced by that of the dielectric. It is thus seen that as the dielectric overlayer thickness is increased the wavevector of the SPP mode at the metal-dielectric interface increases from

$$\frac{\omega}{c} \sqrt{\frac{\epsilon_1}{\epsilon_1 + 1}} \quad \text{to} \quad \frac{\omega}{c} \sqrt{\frac{\epsilon_1 \epsilon_2}{\epsilon_1 + \epsilon_2}}$$

with the upper wavevector limit being reached asymptotically. This behaviour is known as the *thickness dispersion* of the SPP mode. If the thickness of the dielectric layer is increased further then the structure will become capable of supporting waveguide modes as well as the SPP. These modes are the subject of the next section.

3.3 Waveguide modes

Waveguide modes are the confined electromagnetic waves which exist in certain stratified media. A whole host of structures will support waveguide modes e.g. planar dielectric slabs, microspheres or cylindrical glass fibres, but the common characteristic is that they all have a *core* region, in which the mode propagates, and a *cladding* region, into which the electromagnetic fields associated with the mode decay exponentially. The ability of such structures to *guide* light efficiently is of immense value in the telecommunications industry, where waveguides in the form of optical fibres transmit signals hundreds of kilometres with huge bandwidth and negligible loss. A second use of waveguide structures is in the field of integrated optics, where optical components are incorporated into microelectronic circuits to produce monolithic optoelectronic devices. For a good general review of this area see *Tien (1977)*.

In the microwave regime metals have little loss and so hollow metal-clad waveguides can be used to guide radiation. The electromagnetic fields within the guide are confined by the metallic walls, since at microwave frequencies the penetration depth into the metal is small. In the optical region, however, metals exhibit much greater loss and this increases the attenuation of light propagating in metal-clad guides to unacceptable levels. To counter this, waveguides for optical radiation are commonly made from low-loss dielectric materials such as silica. In this case the optical fields are confined within the guide by the total internal reflection of light at the interface between a high refractive index core region and a low refractive index cladding region. An alternative method of guiding light relies upon Bragg reflection to confine the mode to the core region of a photonic crystal optical fibre [*Russell et al. (1998)*].

To obtain a full description of the properties of guided modes requires the solution of Maxwell's equations for the relevant guiding structure. Before attempting this, the physical basis of the guiding process will be investigated by examining the phenomenon of total internal reflection. It will be seen that the guiding of light is intimately related to the conservation of momentum of the guided light.

Consider light incident at the planar interface between two media characterised by their dielectric constants ϵ_1 and ϵ_2 , as shown in *figure 3.5*.

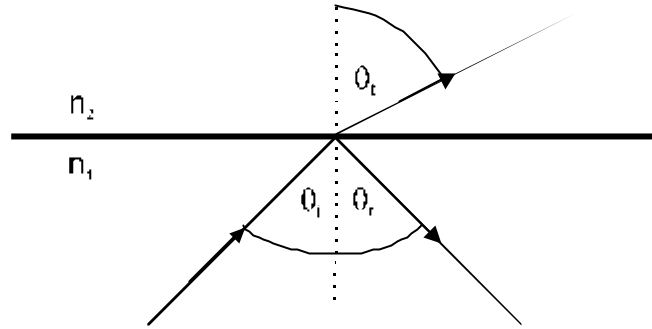


Figure 3.5 Reflection and refraction of light at a planar boundary between two media of different dielectric constant.

The direction of propagation of the reflected light in medium 1 and the refracted light in medium 2 can be obtained by considering the conservation of linear momentum for a photon of light incident in medium 1. A photon of wavevector \mathbf{k}_0 propagating in a vacuum has linear momentum

$$\mathbf{p} = \hbar\mathbf{k}_0 \quad |\mathbf{k}_0| = \frac{2\pi}{\lambda_0} \quad (3.21)$$

where λ_0 is the wavelength in vacuum. If the photon passes into a medium with refractive index $n (= \sqrt{\epsilon})$, its phase velocity will change from c to c/n and thus the wavelength in the medium will change to λ_0/n . This increases the wavevector from \mathbf{k}_0 to $n\mathbf{k}_0$ (generally $n>1$) and so the linear momentum of a photon propagating in a medium of refractive index n is given by

$$\mathbf{p} = n\hbar\mathbf{k}_0. \quad (3.22)$$

Neglecting the constant \hbar , the momentum of a photon of light is thus equivalent to its wavevector and these terms are often used synonymously.

Because of the translational invariance of the interface, the tangential component of the photon momentum will be conserved on reflection or transmission. Thus, for reflection

$$\begin{aligned} n_1\hbar k_0 \sin \theta_i &= n_1\hbar k_0 \sin \theta_r \\ \theta_i &= \theta_r \end{aligned} \quad (3.23)$$

and similarly for transmission

$$\begin{aligned} n_1 \hbar k_0 \sin \theta_i &= n_2 \hbar k_0 \sin \theta_t \\ n_1 \sin \theta_i &= n_2 \sin \theta_t \end{aligned} \quad (3.24)$$

which is of course, Snell's law describing the refraction of light across an interface.

If light is incident at the interface between high and low refractive index media from the high index side, there will be an angle of incidence θ_c beyond which the incident photon has a greater tangential momentum than is possible for a photon propagating in the low index medium. When this occurs light cannot propagate into the low index medium and thus must undergo *total internal reflection* back into the high index region to conserve tangential momentum. If a structure is made with a low/high/low index profile, light internally incident at an interface beyond the critical angle θ_c is confined to propagate solely within the high index medium, and so will be guided by it. This forms the basis of waveguiding in dielectric materials.

The critical angle θ_c occurs when the transmitted light in the low index medium has the maximum possible tangential momentum, *i.e.* it is propagating parallel to the interface. So with $n_1 > n_2$, *equation 3.24* yields

$$\theta_c = \arcsin\left(\frac{n_2}{n_1}\right). \quad (3.25)$$

Although light does not propagate into the low index medium for incidence beyond the critical angle, an optical field does exist beyond the interface. To conserve momentum this field has a tangential momentum component equal to that of the incident light in the high index medium, and since this exceeds the maximum possible momentum in the low index medium, the normal component is imaginary to conserve total momentum (*c.f. equation 3.10*). This gives an exponential decay of the fields away from the interface and so the field is evanescent and does not correspond to a propagating photon. It will be seen in *section 3.4* how the enhanced tangential momentum achieved in this manner gives a means of coupling to non-radiative modes such as the SPP.

The metal/dielectric/air structure shown in *figure 3.4* is typical of the samples studied experimentally in later chapters. If a monolayer of fluorescent molecules is deposited at the dielectric/air interface, interaction between the molecules and the SPP mode at the metal/dielectric interface is extremely likely. If the dielectric layer is thick enough to support waveguide modes then it is possible for the molecules to interact with these modes as well. In view of this, the next section is devoted to an examination of the properties of these modes, together with a derivation of their field profiles.

3.3.1 The asymmetric slab waveguide

The geometry which corresponds most closely to the experimental arrangement is that of a planar dielectric slab bounded on one side by air and on the other side by a metal, thus forming an asymmetrically clad waveguide. In the following analysis, the metal and air regions are considered to extend to infinity away from the slab in the y -direction, whilst the slab itself is infinite in extent in the x and z directions. This is illustrated in *figure 3.6*.

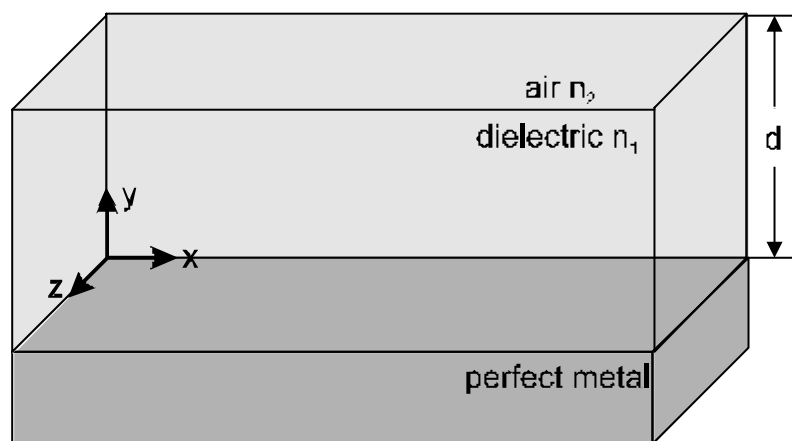


Figure 3.6 A planar dielectric slab waveguide, clad asymmetrically with air and metal showing the co-ordinate system used in the text.

The following analysis is adapted from the method outlined in *Yariv (1991)*; similar approaches can be found in many texts, see for example *Owyang (1981)*.

Allowed guided modes of the system will be solutions of the wave equation, which assuming simple harmonic time-dependence has the form

$$\nabla^2 \mathbf{E}(\mathbf{r}) + \omega^2 \epsilon \mu \mathbf{E}(\mathbf{r}) = 0$$

or

$$\nabla^2 \mathbf{H}(\mathbf{r}) + \omega^2 \epsilon \mu \mathbf{H}(\mathbf{r}) = 0$$

(3.26)

in a source-free region. Solutions will be chosen which correspond to waves propagating in the x-direction, *i.e.*

$$\mathbf{E}(\mathbf{r}, t) = \mathbf{E}(y, z) \exp i(\beta x - \omega t) \quad (3.27)$$

where β is the tangential wavevector of the mode, also known as the propagation constant. Substitution into *equation 3.26* yields

$$\left(\frac{\partial^2}{\partial y^2} + \frac{\partial^2}{\partial z^2} \right) \mathbf{E}(y, z) + [\omega^2 \epsilon \mu - \beta^2] \mathbf{E}(y, z) = 0. \quad (3.28)$$

Because the guide is presumed to extend to infinity in the z direction, it will be assumed that the fields have no z-dependence and so $\partial/\partial z=0$. To simplify matters the metal is assumed to be perfect and there will be no field penetration into the metallic substrate; the wave will only exist in the dielectric media. Using the relation $\omega^2 \epsilon \mu = n^2 k_0^2$, *equation 3.28* can thus be rewritten separately for the dielectric and air regions as follows

$$\frac{\partial^2}{\partial y^2} \mathbf{E}_1(y) + [n_1^2 k_0^2 - \beta^2] \mathbf{E}_1(y) = 0$$

(3.29)

$$\frac{\partial^2}{\partial y^2} \mathbf{E}_2(y) + [n_2^2 k_0^2 - \beta^2] \mathbf{E}_2(y) = 0.$$

Before solving these equations explicitly, the nature of the solutions at a given frequency ω will be considered as a function of the tangential wavevector β . Since the dielectric region has a higher refractive index than the air above it ($n_1 > n_2$), there are three separate regimes to consider.

For $\beta > n_1 k_0$, $(1/\mathbf{E})(\partial^2 \mathbf{E}/\partial y^2) > 0$ in the air and dielectric regions which implies that \mathbf{E} is exponential in form for both. This is to be expected since the

resulting mode has a higher wavevector than is possible for a propagating wave and an evanescent solution must result for all regions. A possible solution is depicted in *figure 3.7a*.

If $n_1 k_0 > \beta > n_2 k_0$, $(1/\mathbf{E})(\partial^2 \mathbf{E}/\partial y^2)$ is negative for the dielectric region and positive for the air region. This gives sinusoidal solutions for the dielectric region and exponential ones for the air region. Possible field distributions for this regime are illustrated in *figures 3.7b,c*. Since the energy carried by these modes is localised within (or near) the dielectric medium, they are called *guided modes*, and the dielectric region is known as the *guiding layer*. Note that an existence condition for these modes is that $n_1 > n_2$, *i.e.* the core region has a higher refractive index than the cladding region. This result is to be expected after the previous discussion of total internal reflection in the context of guiding light.

If $n_2 k_0 > \beta > 0$, $(1/\mathbf{E})(\partial^2 \mathbf{E}/\partial y^2)$ is negative everywhere, and now the field is sinusoidal in the air region as well as the dielectric region. Because of this the modes are not confined to the dielectric layer and are known as *radiative* or *leaky* modes. Again, possible field profiles are illustrated in *figure 3.7d*.

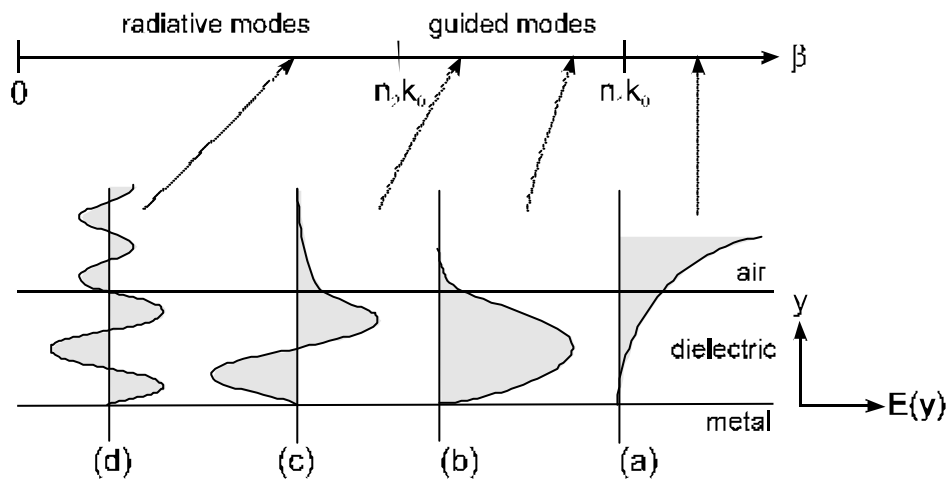


Figure 3.7 Mode field profiles $E(y)$ of the waveguide of *figure 3.6* shown for various values of the tangential wavevector β .

In this leaky regime β is a continuous variable which results in a continuum of available radiative modes, but for $n_1 k_0 > \beta > n_2 k_0$ there are only a

finite number of guided modes available, the number determined by the thickness of the guiding layer, the frequency of the radiation and the refractive indices of the layers involved. Solutions to the wave equation in the guided mode regime $n_1 k_0 > \beta > n_2 k_0$ will now be examined in more detail.

The derivation of the field profiles of the guided modes starts from Maxwell's curl equations, which assuming fields with time dependence of the form $\exp i\omega t$ can be written as

$$\nabla \times \mathbf{E}(\mathbf{r}) = -i\omega\mu\mu_0\mathbf{H}(\mathbf{r}) \quad \nabla \times \mathbf{H}(\mathbf{r}) = i\omega\epsilon\epsilon_0\mathbf{E}(\mathbf{r}). \quad (3.30)$$

For the guided modes

$$\mathbf{E}(\mathbf{r}) = \mathbf{E}(y) \exp -i\beta x \quad \mathbf{H}(\mathbf{r}) = \mathbf{H}(y) \exp -i\beta x \quad (3.31)$$

which on substitution into *equation 3.30* and separating into scalar components gives

$$\begin{aligned} \frac{\partial E_z}{\partial y} &= -i\omega\mu\mu_0 H_x, & \frac{\partial H_z}{\partial y} &= i\omega\epsilon\epsilon_0 E_x \\ \beta E_z &= -\omega\mu\mu_0 H_y, & \beta H_z &= \omega\epsilon\epsilon_0 E_y \\ i\beta E_y + \frac{\partial E_x}{\partial y} &= i\omega\mu\mu_0 H_z, & i\beta H_y + \frac{\partial H_x}{\partial y} &= -i\omega\epsilon\epsilon_0 E_z. \end{aligned} \quad (3.32)$$

These equations can be separated into two self-consistent sets, the first involving E_z , H_x and H_y only, the second involving H_z , E_x and E_y only. The electric field in the first set is confined to the transverse plane (normal to the direction of propagation) and so these equations describe TE modes, whereas in the second set it is the magnetic field which lies in the transverse plane and so those equations describe TM modes.

TE solutions can thus be specified totally by the sole electric field component E_z

$$H_x = \frac{i}{\omega\mu\mu_0} \frac{\partial E_z}{\partial y} \quad H_y = -\frac{\beta}{\omega\mu\mu_0} E_z \quad (3.33)$$

and the TM solutions similarly by the sole magnetic field component H_z

$$E_x = -\frac{i}{\omega\epsilon\epsilon_0} \frac{\partial H_z}{\partial y} \quad E_y = \frac{\beta}{\omega\epsilon\epsilon_0} H_z. \quad (3.34)$$

These two types of mode will be considered in turn.

3.3.2 TE guided modes

For the TE modes the electric field E_z component must satisfy the wave equations given in *equation 3.29*. A standing wave solution is required in the dielectric layer and will be of the general form

$$E_{z1}(y) = E^e \cos k_{y1}y + E^o \sin k_{y1}y \quad (3.35)$$

where $k_{y1}^2 = n_1^2 k_0^2 - \beta^2$. Note that the condition $n_1 k_0 > \beta$ ensures that k_{y1} is real. When $y=0$, the boundary condition that the tangential electric field is continuous across the metal-dielectric interface implies that $E_{z1}(0) = 0$ and so the fields in the dielectric layer are given by

$$\begin{aligned} E_{z1}(y) &= E^o \sin k_{y1}y \\ H_{x1}(y) &= \frac{ik_{y1}}{\omega\mu_1\mu_0} E^o \cos k_{y1}y \\ H_{y1}(y) &= -\frac{\beta}{\omega\mu_1\mu_0} E^o \sin k_{y1}y \end{aligned} \quad (3.36)$$

with the last two results arising from *equation 3.33*.

The fields in the air half-space must be evanescent to ensure that the mode is confined to the dielectric layer, and a suitable general solution for this region has the form

$$E_{z2}(y) = E^+ \exp -ik_{y2}(y-d) + E^- \exp ik_{y2}(y-d) \quad (3.37)$$

where $k_{y2}^2 = n_2^2 k_0^2 - \beta^2$. Note that in this case the condition $\beta > n_2 k_0$ ensures that k_{y2} is imaginary and hence $E_{z2}(y)$ is exponential and not oscillatory in nature.

To obtain finite fields as $y \rightarrow \infty$, $E^+ = 0$ and thus the fields in the air are given by

$$\begin{aligned} E_{z2}(y) &= E^- \exp ik_{y2}(y-d) \\ H_{x2}(y) &= -\frac{k_{y2}}{\omega\mu_2\mu_0} E^- \exp ik_{y2}(y-d) \\ H_{y2}(y) &= -\frac{\beta}{\omega\mu_2\mu_0} E^- \exp ik_{y2}(y-d) \end{aligned} \quad (3.38)$$

with the last two results obtained from *equation 3.33* as in the previous case.

When $y=d$, the tangential fields must be continuous across the dielectric-air interface, hence

$$\begin{aligned} E_{z1}(d) &= E_{z2}(d); & E^- &= E^0 \sin k_{y1}d \\ H_{x1}(d) &= H_{x2}(d); & -\frac{k_{y2}E^-}{\mu_2} &= \frac{ik_{y1}E^0}{\mu_1} \cos k_{y1}d \end{aligned}$$

Combining these two equations results in the relation

$$\frac{ik_{y1}}{\mu_1} + \frac{k_{y2}}{\mu_2} \tan k_{y1}d = 0 \quad (3.39)$$

which is the dispersion relation for the TE modes of the guide. Solutions to this equation are usually obtained by graphical means enabling the dispersion curve of the modes to be plotted, but exact solutions for special cases can be obtained explicitly.

Note from *equation 3.38* that the mode is radiative when k_{y2}^2 is positive and guided when k_{y2}^2 is negative. The condition $k_{y2}^2=0$ corresponds to the transition between these regimes and is known as the *cut-off*. Inspection of *equation 3.39* shows that at cut-off $\tan k_{y1}d \rightarrow -\infty$ and thus k_{y1} is restricted to the values

$$k_{ym1} = (2m+1) \frac{\pi}{2d} \quad m=0,1,2,\dots \quad (3.40)$$

The subscript m denotes the number of zero crossings of the $E_z(y)$ field profile within the guide and is known as the *order* of the mode. At cut-off, the tangential wavevector of the mode is the maximum sustainable in the air region ($\beta = n_2 k_0$), and thus in the air the fields take the form of a plane wave propagating along the interface. If the tangential wavevector increases past this point then the guided mode regime is entered: k_{y2} becomes imaginary (see *equation 3.10*) and the fields thus decay exponentially into the air. Note that as β increases further, the penetration depth of the mode into the air decreases (whilst still imaginary, k_{y2} increases with β). The mode is thus confined to the core region more completely as β gets larger.

The criterion that determines whether a mode is guided or not, $n_1 k_0 > \beta > n_2 k_0$, can be re-expressed in terms of the normal wavevector of the mode as

$$k_{y1}^2 \leq (n_1^2 - n_2^2) k_0^2. \quad (3.41)$$

A given mode will have the largest possible normal wavevector k_{y1} at cut-off since its tangential wavevector will then be at a minimum ($\beta = n_2 k_0$). Substituting this maximum value (given by *equation 3.40*) into *equation 3.41* and rearranging results in the inequality

$$d \geq \frac{2m+1}{\sqrt{n_1^2 - n_2^2}} \frac{\lambda_0}{4}. \quad (3.42)$$

This inequality puts a limit on the maximum number of guided modes supported by a waveguide of given thickness – modes can be supported up to order m , where m is the largest integer satisfying the inequality. Furthermore it can be seen that every TE mode has a thickness cut-off below which it cannot propagate. In the limit that $d=0$, the structure has no TE guided modes at all, as expected.

The field profiles of the bound TE modes are thus given by *equations 3.36* and *3.38*, with the normal wavevector at cut-off obtained from *equation 3.40*. TM modes of the waveguide will be treated in a similar manner in the following section.

3.3.3 TM guided modes

The TM mode solutions can be determined by consideration of the transverse component of the electric field, which for TM modes is E_x since $E_z=0$. This field component must satisfy *equation 3.29* and the solution for the dielectric layer, taking into account the boundary condition that $E_{x1}(0) = 0$, is

$$\begin{aligned} E_{x1}(y) &= E^0 \sin k_{y1} y \\ E_{y1}(y) &= -\frac{i\beta}{k_{y1}} E^0 \cos k_{y1} y \\ H_{z1}(y) &= -\frac{i\omega\epsilon_1\epsilon_0}{k_{y1}} E^0 \cos k_{y1} y \end{aligned} \quad (3.43)$$

Again, $k_{y1}^2 = n_1^2 k_0^2 - \beta^2$, and $n_1 k_0 > \beta$ guarantees that k_{y1} is real. The expressions for $E_{y1}(y)$ and $H_{z1}(y)$ come from manipulation of *equation 3.32*.

The fields of the guided modes are exponential in form in the air half-space, and if the exponentially increasing term in the general solution is disregarded as unphysical, the following profiles result

$$\begin{aligned} E_{x2}(y) &= E^- \exp ik_{y2}(y-d) \\ E_{y2}(y) &= \frac{\beta}{k_{y2}} E^- \exp ik_{y2}(y-d) \\ H_{z2}(y) &= \frac{\omega\epsilon_2\epsilon_0}{k_{y2}} E^- \exp ik_{y2}(y-d) \end{aligned} \quad (3.44)$$

Matching the tangential fields at the dielectric-air interface ($y=d$) yields

$$\begin{aligned} E_{x1}(d) &= E_{x2}(d); & E^- &= E^0 \sin k_{y1} d \\ H_{z1}(d) &= H_{z2}(d); & \frac{\epsilon_2}{k_{y2}} E^- &= -\frac{i\epsilon_1}{k_{y1}} E^0 \cos k_{y1} d. \end{aligned}$$

Dividing and rearranging these two expressions gives the result

$$\frac{k_{y2}}{\epsilon_2} + \frac{k_{y1}}{i\epsilon_1} \tan k_{y1}d = 0 \quad (3.45)$$

which is the dispersion relation for the TM modes of the guide. Again, at cut-off $k_{y2} = 0$, thus $\tan k_{y1}d = 0$ and the normal wavevector of the mode within the guide is restricted to the values

$$k_{ym1} = \frac{m\pi}{d} \quad m=0,1,2,\dots \quad (3.46)$$

Equation 3.41 may then be used to obtain the cut-off condition for the TM modes

$$d \geq \frac{m}{\sqrt{n_1^2 - n_2^2}} \frac{\lambda_0}{2}. \quad (3.47)$$

Again, this inequality limits the number of modes guided by a given structure, and also gives the thickness cut-off for any guided mode. In contrast to the TE case where there is a thickness cut-off below which no modes can propagate at all, it can be seen that the asymmetric guide will always support the lowest order TM mode, the TM_0 . This mode is in fact identical to the surface-plasmon polariton which propagates at the metal-dielectric interface as discussed in *section 3.2*, and so it is seen that the SPP mode is simply the lowest order TM mode of a metal-clad waveguide.

A derivation of the mode field profiles obtained for waveguides clad by non-perfect metals can be found in *Kaminow et al. (1974)*. The expressions which result are more complex than those derived here, but are essentially very similar in form.

The field profiles associated with the first three TE and TM guided modes are illustrated in *figure 3.8* for the case where the guide is slightly thicker than the mode cut-off thickness.

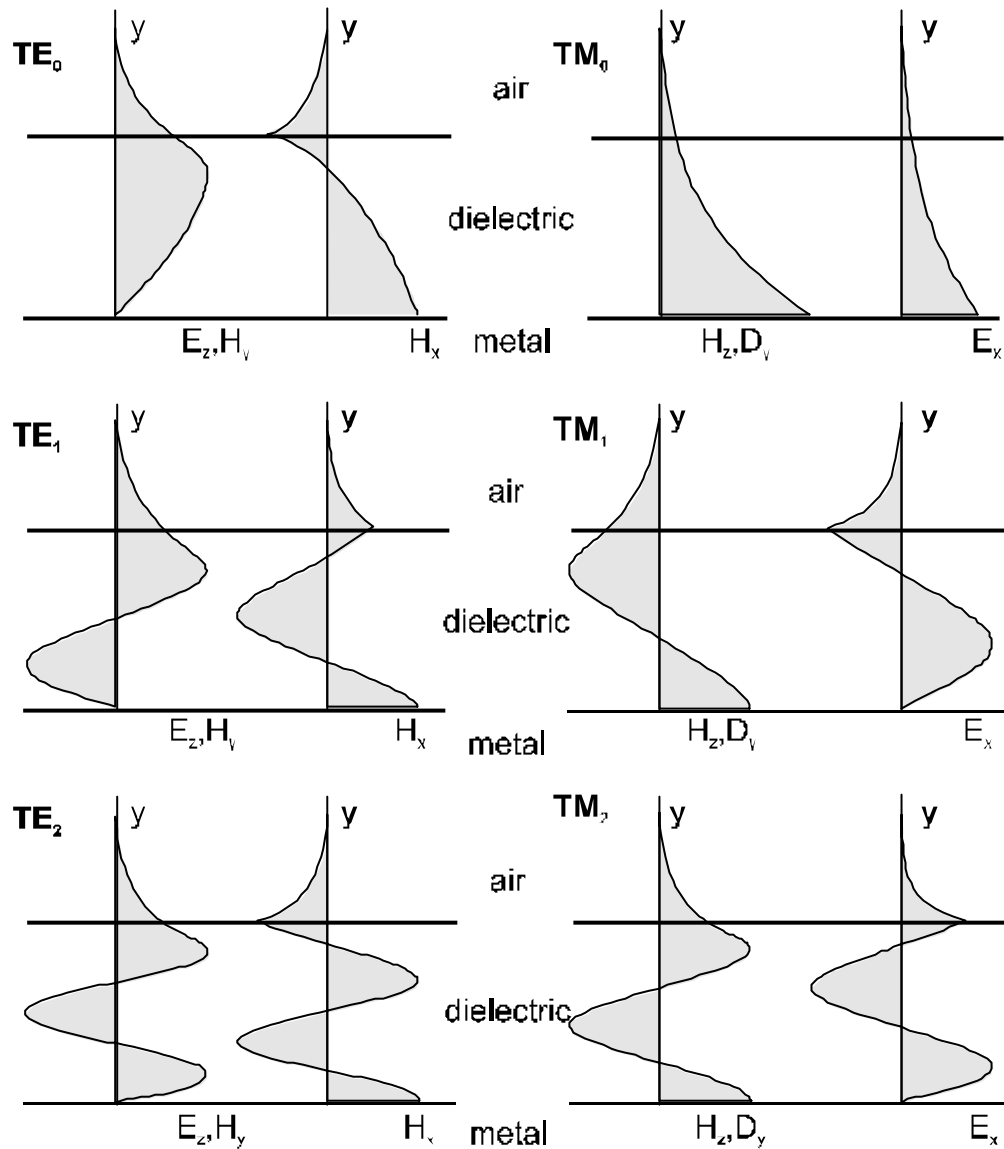


Figure 3.8 The field profiles of the first three TE and TM guided modes for the asymmetric metal-clad waveguide shown in *figure 3.6*.

3.4 Coupling to surface modes

In *sections 3.2* and *3.3* it was shown that both guided modes and the SPP mode at an interface are non-radiative, that is, they possess a greater tangential wavevector than a photon of the same frequency propagating in the adjacent dielectric medium. This momentum mismatch (see *figure 3.3*) means that light cannot be radiatively coupled to these modes directly and so some

means of enhancing the photon momentum is required. This can be achieved by modifying the surface environment, or less commonly by modifying the nature of the source of the incident radiation. Several methods exist which allow the direct radiative excitation of surface modes by alteration of the environment of the interface. The first method discussed utilises the phenomenon of attenuated total reflection (ATR) to enhance the momentum of incident photons, and is commonly known as *prism coupling*. The second method uses the scattering of photons from a rough surface to excite modes and is the basis of the *grating coupling* technique. In the following section these coupling techniques will be detailed and the use of surface plasmon resonance (SPR) as a surface characterisation tool described. For the sake of brevity only the coupling to SPPs will be considered although the techniques mentioned are equally applicable to the excitation of both guided modes and SPPs.

In the context of the work carried out in this thesis, however, there is an alternative method of exciting surface modes which does not require the surface geometry to be altered. An excited molecule in the vicinity of a surface can de-excite by coupling to surface modes such as the SPP directly. This is possible since the emission of light from molecules is in many cases characteristic of an electric dipole source. The emitted field of such a dipole has cylindrical symmetry and can be represented by a Fourier series of plane waves, which in the near-field ($d \ll \lambda_0$) includes evanescent high wavevector terms. Some of these will match the wavevector of the available surface modes and if the surface is close enough will thus allow coupling between the molecule and the mode. In the far-field of the dipole these evanescent fields have decayed away and, as expected, only the propagating plane wave component remains. In this regime, then, the molecule cannot excite surface modes. This molecule-surface interaction will be the subject of the bulk of the experimental work described in this thesis.

3.4.1 Prism coupling techniques

It was mentioned in *section 3.3* that light incident beyond the critical angle at the interface between high and low refractive index media is totally internally reflected since the tangential momentum of the light is too high to allow light to propagate in the lower index medium. The resulting evanescent optical field which exists in this medium has a tangential momentum equal to that of the incident light in the optically denser material. Because this exceeds the maximum momentum usually attainable in the lower refractive index medium, it is possible for light to radiatively couple to the SPP modes of a metal surface *via* this evanescent field. Coupling methods which utilise this phenomenon are thus known as attenuated total reflection (ATR) techniques.

Consider light propagating at angle θ to the normal of the bottom face of a prism of refractive index n . The tangential momentum of the light is $n\hbar k_0 \sin \theta$ and assuming that the dielectric adjacent to the metal is air ($\epsilon=1$), coupling to the SPP mode can be observed when

$$nk_0 \sin \theta = k_{\text{spp}} = k_0 \sqrt{\frac{\epsilon_{\text{metal}}}{\epsilon_{\text{metal}} + 1}}. \quad (3.48)$$

It is seen that SPPs can be excited when $n \sin \theta > 1$, *i.e.* $\theta > \theta_c$. Note that the proximity of the prism to the metal-air interface does affect the SPP dispersion and strictly speaking, the double interface result should be used [Ræther (1988)]. In practise, the perturbation introduced is small and so the single interface result given in *equation 3.11* is used. The effect of increasing the momentum of the incident light through the use of a prism is illustrated in the dispersion curve of *figure 3.9*.

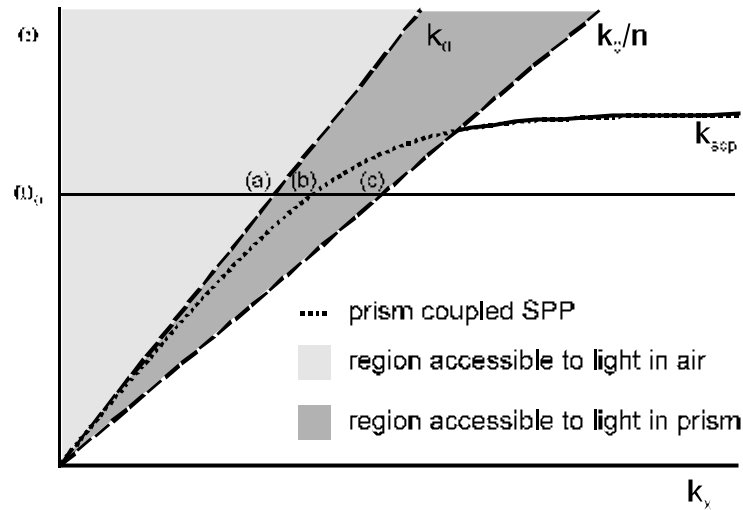


Figure 3.9 Dispersion curve for light propagation in a prism of index n with evanescent coupling to the SPP modes of a metal-air interface in close proximity to the base of the prism. For light of frequency ω_0 within the prism point (a) corresponds to the critical angle, point (b) to the excitation of SPPs by evanescent field coupling and (c) to the grazing incidence of light along the interface within the prism.

Coupling to SPP modes is most easily observed by monitoring the angle-dependent reflectivity of the prism-air interface. As the critical angle is approached the reflectivity increases as the intensity of the transmitted beam propagating in the air falls. At the critical angle the transmitted beam becomes evanescent and incident light is totally internally reflected; the reflectivity thus reaches a maximum of 1. Past this *critical edge* the SPP coupling condition *equation 3.48* may be satisfied. When this occurs, energy is absorbed from the incident beam and there is a dip in the reflectivity corresponding to the excitation of the SPP. When the coupling between the incident beam and the SPP is perfect, the reflectivity falls to zero. The feature observed in the reflectivity of an interface created by excitation of the SPP mode is known as a surface-plasmon resonance (SPR). The first intentional demonstration of the optical excitation of SPP modes used the ATR geometry shown in *figure 3.10a* and was due to *Otto (1968)*.

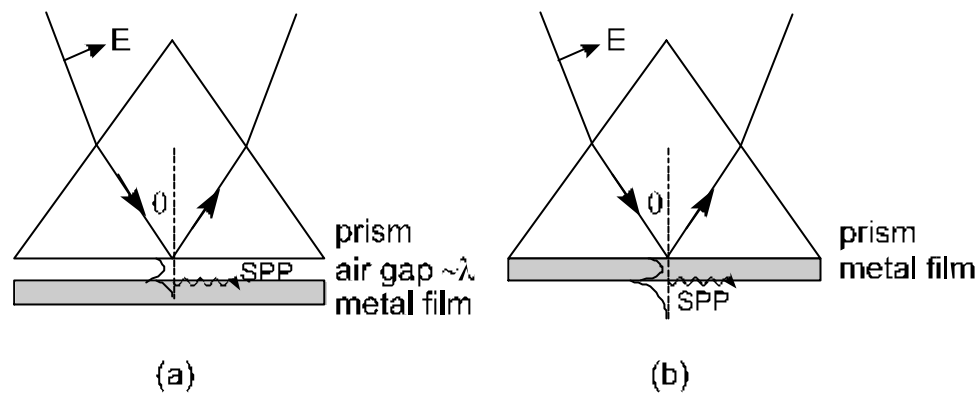


Figure 3.10 Prism ATR geometries; (a) the Otto configuration and (b) the Kretschmann configuration.

In the Otto configuration, a bulk metallic substrate is brought up to the base of a high-index prism. The evanescent field excited by a beam of light incident beyond the critical angle within the prism penetrates the air gap between the prism and the metal and can excite the SPP mode at the metal-air interface. The coupling strength to the mode is determined by the thickness of the air gap, and for optimum coupling this will be of the order of the wavelength of the radiation used. In the visible regime this is difficult to achieve since the required gap (typically $\sim 1\mu\text{m}$) is smaller than the average diameter of dust particles and extreme care has to be taken in sample preparation. This problem is less severe in the infra-red spectral region since the required air gap is commensurately larger and hence more easily attained. The main application of the Otto geometry is in the study of the surface modes of bulk materials, to which it is uniquely suited.

Soon after Otto demonstrated the optical excitation of SPPs using the ATR method described above, a refinement was made by Kretschmann and R  ther which avoids the use of an air gap entirely [Kretschmann and R  ther (1968)]. In this ATR configuration (see figure 3.10b) a thin metal film is deposited directly onto the base of a prism. The evanescent light field generated by an incident beam of light in the prism penetrates through the metal film and can excite SPPs at the metal-air interface on the far side of the film. The coupling strength to the SPP mode can be varied by changing the thickness of the metal film and for light of wavelength $\lambda_0=632.8\text{nm}$ incident upon a silver film, the optimum coupling is achieved when the thickness is $\sim 40\text{nm}$.

The advantage of the Kretschmann configuration is the ease with which suitable samples can be made. Using thermal evaporation techniques, thin films of metals can be deposited with nanometric precision, thus allowing great control of the SPP coupling conditions. By fitting experimental reflectivity data to theory curves derived from Fresnel's equations it is possible to obtain the optical constants and thickness of the metal film (or air gap thickness for the Otto geometry) thus allowing the optical characterisation of the sample. Note that an SPP mode can propagate along the prism-metal interface as well as the metal-air interface for the Kretschmann configuration. This mode, however, has too much momentum to be optically excited by light in the prism and so is not observed in ATR experiments (unless additional momentum is made available).

3.4.2 Grating coupling techniques

In 1902, Wood conducted a series of experiments in which the light from incandescent lamps was reflected from metallic ruled diffraction gratings [*Wood (1902)*]. The spectra thus created contained a series of anomalous discontinuities which he was unable to explain, expecting to see continuous spectra due to the nature of the light source. Rayleigh was able to show that some of the anomalies, characterised by cusps in the spectra, were created by diffracted orders becoming evanescent as they passed beyond the grating horizon. This led to an increase in the intensity of the propagating orders including the specular [*Rayleigh (1907)*]. A second set of anomalies which consisted of sharp dips in the spectra remained unexplained until Fano proposed that they indicated the excitation of TM-polarised surface modes [*Fano (1941)*]. It is these anomalies which correspond to the grating coupling of incident light to the SPP mode of a metallic grating surface. Due to the complexities involved in theoretically modelling the response of grating structures to electromagnetic radiation, however, detailed investigation of the phenomenon of grating coupling was neglected for many years. Interest in the interaction of light with diffraction gratings was only rekindled by the increasing importance of the integrated optics field and the realisation that grating structures could act as compact and efficient waveguide couplers. At the same

time advances in computing power led to the feasibility of numerically modelling the response of such systems, using techniques such as the differential formalism of *Chandezon et al. (1982)* which is described in *section 3.5*.

By corrugating the interface between two media, the translational symmetry of the surface is destroyed and hence the tangential momentum of light incident upon the surface need no longer be conserved. The periodicity associated with the corrugation of the surface profile allows light to be scattered by an integer number of grating vectors \mathbf{G} in the direction normal to that of the grating grooves since the grooves act as an array of scatterers. The grating vector associated with the surface is given by

$$\mathbf{G} = \frac{2\pi}{\lambda_g} \hat{\mathbf{n}} \quad (3.49)$$

where the grating profile is a perfect sinusoid with a pitch of λ_g and $\hat{\mathbf{n}}$ is a unit vector pointing in the direction normal to the grating grooves. A beam of light incident upon a grating surface is thus scattered into a series of diffracted orders in both reflection and transmission. If a diffracted order passes off beyond the grating horizon it may no longer propagate and instead becomes evanescent. The enhanced momentum associated with this evanescent order allows the incident radiation to couple to surface modes which exist beyond the light-line, such as the SPP. The coupling condition is then given by

$$\mathbf{k}_0 \sin \theta \pm m\mathbf{G} = \pm \mathbf{k}_{\text{spp}} \quad (3.50)$$

where $\mathbf{k}_0 \sin \theta$ is the in-plane wavevector of the incident light, m is an integer and \mathbf{k}_{spp} is the SPP wavevector. *Equation 3.50* shows that grating coupling exhibits some significant differences to the ATR excitation of SPP modes. It can be seen that if $|\mathbf{k}_0| \gg |\mathbf{G}|$, the SPP mode can be excited at more than one angle of incidence depending on the number m of scattering events that occur. Indeed SPPs can be excited which propagate in the opposite direction to the incident light if the in-plane momentum of the light is decreased far enough, a result impossible with ATR coupling. If the in-plane component of the wavevector of the incident light is not parallel to the grating vector, *i.e.* the grating is not in the classical mount, then the SPP excited will propagate at some angle to the

grating grooves, which is why unlike *equation 3.48* the grating coupling condition is a vector equation. The periodicity of the grating breaks the symmetry of the surface and so the azimuthal angle φ between the plane of incidence of the light and the normal to the groove direction must be defined. The classical mount then corresponds to the azimuth $\varphi=0$. The mechanism of grating coupling is depicted in *figure 3.11*, where the dispersion curve for SPPs propagating on a metallic diffraction grating surface is presented in the extended Brillouin zone representation. Note that light is assumed to be incident in the classical mount.

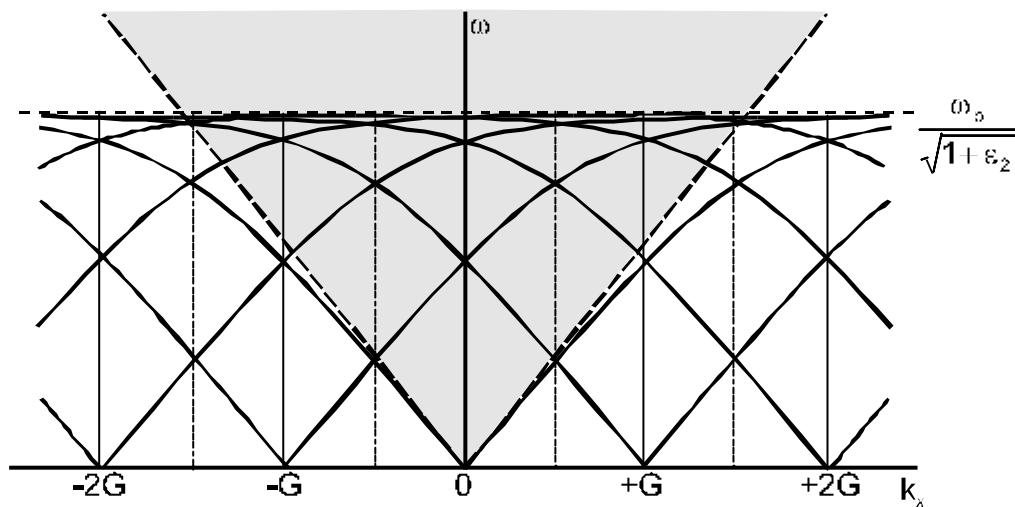


Figure 3.11 The SPP dispersion curve for a metallic grating surface corrugated with a single harmonic component of pitch λ_g . The shaded region between the two dashed light-lines represents the region accessible to incident photons and hence branches of the SPP dispersion curve scattered into this region can be radiatively excited.

Corrugating the surface affects the dispersion of the SPP mode by decreasing the planar SPP phase velocity for a given frequency [*Pockrand (1974)*], but for shallow gratings the planar SPP dispersion relation, *equation 3.11*, is a good approximation.

The coupling strength to the mode is determined by the amplitude of the grating profile since it is this which determines the intensity of the diffracted orders and hence how much power is available in the evanescent fields. This

point will be expanded upon in *section 3.5* where the theoretical modelling of the optical response of gratings will be reviewed.

Optical excitation of SPPs is also observed when the metal/dielectric interface is rough on the scale of the wavelength of light [*Ræther (1988)*]. This can be understood as a special case of grating coupling whereby the rough surface is represented by a Fourier series of harmonics with appropriate amplitudes and wavevectors. Some of these will be sufficient to satisfy *equation 3.50* and thus couple incident light to SPP modes.

In the preceding two sections the coupling of photons to the SPP mode has been considered and several mechanisms discussed to achieve this. Although these mechanisms are entirely different they share a common characteristic; the excitation of the mode is made possible by the extra momentum available when a propagating order becomes evanescent. In the case of a grating these orders are simply the diffracted orders, whereas in the case of ATR coupling geometries it is the transmitted order which becomes evanescent. A corollary of this is that a surface-plasmon resonance is always found just beyond the critical edge created when an order becomes evanescent.

3.4.3 Coupling SPP modes to light

It is worthwhile while discussing photon-SPP coupling to note that the inverse process can also occur, that is, SPPs travelling along a surface can undergo scattering into photons under appropriate conditions. This effect is particularly evident when the SPPs are generated by the de-excitation of fluorescent molecules placed above a metal film. If the metal film is corrugated these SPP modes can scatter from the grating, resulting in the emission of narrow angular lobes of light propagating in directions given by *equation 3.50* [*Adams et al. (1980)*]. This phenomenon is discussed in more detail in chapter 7. Similarly, if the metal film is evaporated onto the base of a high index prism then the SPPs propagating along the metal/air interface can emit light into the prism in directions given by *equation 3.48* via the evanescent field of the SPP mode [*Pockrand et al. (1980)*, *Weber and Eagen (1979)*].

This SPP-photon coupling also has a part to play in the measured reflectivity of dielectric/metal interfaces. The coupling acts as a radiative loss mechanism for the SPP mode, and if the coupling strength is high this radiative damping of the mode leads to a broad surface-plasmon resonance feature. The statement that the dip in reflectivity corresponding to SPR is caused by the loss of energy to the SPP mode can thus be seen as a simplification. In fact, it is the interference between the specular reflection from the metal and the re-radiation from the SPP mode that causes the dip in reflectivity. The mode is then perfectly coupled when the reflection and re-radiation are exactly equal since the re-radiated light is in antiphase with the reflection.

3.5 Electromagnetic theory of gratings

The optical response of an excited molecule in close proximity to a surface will depend to a large extent upon the reflectivity of that surface; it is the reflectivity that determines the strength of the reflected fields at the dipole site and hence the influence of the surface on the molecule. Measurement of the reflectivity of an interface will also be used to optically characterise the samples studied in this work, and so the development of a theoretical framework to model the reflectivity of a surface is of prime importance.

For planar interfaces this is relatively straightforward and is tackled in a similar manner to all problems in electromagnetism; solutions to Maxwell's equations are sought for each medium and the relevant boundary conditions applied. This approach results in the derivation of Fresnel's equations which can be recast in a matrix format to allow the response of multilayer structures to be calculated in a simple fashion [Berreman (1972), (1973)]. The theoretical reflectivity curves generated in this way can be then be fitted to experimental data to obtain the optical constants and layer thicknesses of a planar sample.

This technique can also be applied to grating structures but it is not trivial to apply the field-matching boundary conditions at non-planar interfaces. A number of theoretical approaches exist to master this problem; the one used in this work is the differential formalism of *Chandezon et al. (1982)*. Alternative methods, such as the integral technique, are discussed by *Maystre (1980)*. In

the following section, the Chandezon method is briefly described along with a discussion of the relevant refinements made in recent years.

3.5.1 The Chandezon method

The geometry of interest is illustrated in *figure 3.12*, which also describes the grating co-ordinate system used throughout this thesis. The structure consists of a series of corrugated layers, each with the same periodicity λ_g and oriented so that the grating vector lies along the x -direction. The i^{th} layer has thickness d_i , upper interface profile $a(x)$ and a complex permittivity given by ϵ_i . Light, assumed to consist of monochromatic plane waves, is incident upon the structure from within the top medium. The direction of propagation of the incident light is then defined by two angles θ and φ . The polar angle θ defines the angle between the wavevector and the normal to the substrate plane, and the azimuthal angle φ then defines the rotation of the plane of incidence from the positive x -direction.

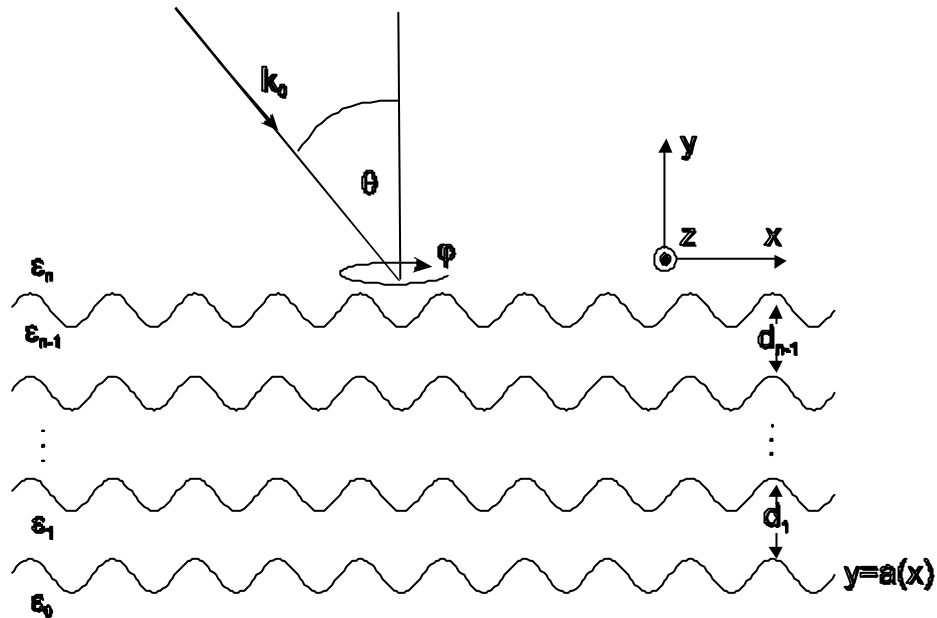


Figure 3.12 The multilayer grating geometry and associated co-ordinate system.

The crux of Chandezon's method is the application of a co-ordinate transformation to the problem so that the corrugated interfaces between layers become planar in the new curvilinear frame. The transformation used is

$$\begin{aligned} u &= x \\ v &= y - a(x) \\ w &= z. \end{aligned} \tag{3.51}$$

The corrugated interfaces thus become planes of constant v in the new frame, and the boundary conditions are thus simplified because the normal to the interface no longer oscillates as a function of x . The relevant boundary conditions are:

- (1) The tangential E and H fields are continuous across each interface.
- (2) The fields remain finite as $y \rightarrow \pm\infty$; this is known as the *outgoing wave condition*.

The next step is to express Maxwell's equations and the fields in the new curvilinear (u,v,w) co-ordinate frame, which is now the most mathematically complex part of the problem. This is achieved by expressing both the fields and Maxwell's equations as Fourier series expanded in terms of the wavevector in the u -direction. To numerically solve the problem these infinite series must be truncated at some point, which necessarily limits the number of scattered orders N considered in the calculation. The choice of N , known as the *truncation parameter*, is a compromise between the accuracy achieved for a given number of scattered orders (*i.e.* how well the series has converged) and the computation time required for that calculation. In general, the number of orders that need to be considered depends upon the depth to pitch ratio of the grating profile; the larger the ratio, the greater number of orders that need to be considered. In practise, the calculation is carried out with the smallest number of orders required to produce results that converge within the limits of precision of the numerical computation. For most gratings considered in this work, inclusion of orders up to $N=5$ was sufficient, but the deeper gratings studied in chapter 7 required a truncation parameter of $N=12$ to obtain convergent results.

The result of this truncation is a series of $4N+2$ linear differential equations, which form a single matrix eigenequation. The resulting eigenvectors

and eigenvalues are then sorted into evanescent and propagating fields and the matrix equation inverted to obtain the scattered field intensities.

The original Chandezon formalism as outlined above deals only with the diffraction of light incident in the classical mount ($\varphi=0$) from multilayer structures with a single sinusoidal modulation. The technique has since been extended to allow modelling of conical diffraction (where $\varphi \neq 0$) [Elston *et al.* (1991a,b)], conical diffraction from multilayer grating structures with arbitrary non-identical interfaces [Preist *et al.* (1995)], and the conical diffraction from uniaxial multilayer grating structures [Harris *et al.* (1996)]. The numerical stability of the calculation has also been improved by the implementation of scattering matrix techniques [Cotter *et al.* (1995)]. Further details can be found in Harris (1996).

A number of FORTRAN codes based on the Chandezon method and its extensions have been developed by co-workers, allowing numerical calculation of the reflectivity of grating structures to be carried out. In the following section these codes will be used to study the effect of the grating profile on the SPR features observed in the angle-dependent reflectivity of grating structures. This will demonstrate the sensitivity of the SPR to the parameters describing the grating surface, indicating that the optical characterisation of surface profiles is possible.

3.5.2 Reflectivity of grating structures

Whenever the coupling condition *equation 3.50* is satisfied, it is possible for incident light to excite the SPP mode propagating at the metallic grating surface. This results in the observation of SPR features in the angle-dependent reflectivity of the grating. These SPR features are usually labelled by the sign and number of the diffracted order which provides the coupling since, as mentioned in *section 3.4.2*, the SPP mode may be excited for more than one value of the in-plane wavevector of the incident light. The shape of the SPR features present depends strongly upon the grating profile since this determines the nature of the scattering of the incident light.

Experimentally, the gratings used in this work have been manufactured using a holographic technique (for details, see chapter 7), and due to non-

linearities in the fabrication process, it is unlikely that they will have a surface profile consisting of a single harmonic component. A useful way of modelling the surface profile of such a distorted grating is to represent it as a Fourier series, expanded in terms of the fundamental wavevector component G . This approach was first introduced by *Rosengart and Pockrand (1977)* to explain the form of +2 SPR features in the reflectivity of distorted gratings. In this formulation, the surface profile is given by

$$a(x) = a_0 \sin Gx + a_1 \sin(2Gx + \phi_1) + a_2 \sin(3Gx + \phi_2) + \dots \quad (3.52)$$

where the n^{th} Fourier component has an amplitude of a_{n-1} and a phase (with respect to the fundamental) of ϕ_{n-1} . The advantage of this description of the grating profile is that the scattering processes which influence the optical response of the grating can be attributed to particular Fourier components in the expansion, a fact that will be illustrated in the following section.

Because of the manufacturing technique used, the gratings used in this work are all non-blazed, that is to say, they are symmetric with respect to a rotation about the normal to the average grating plane of 180° . This limits the odd harmonics of the fundamental to phases of 0 or π , and the even harmonics of the fundamental to phases of $\pm \pi/2$. Generally only the first three terms in the Fourier expansion were required to describe the optical response of the gratings used in this work.

Initially the coupling of light to SPPs will be considered for an undistorted grating with only a single harmonic component in the surface profile. The perturbation induced by the inclusion of a second harmonic component in the profile will then be examined since this is usually the most significant distortion of a sinusoidal profile encountered.

Figure 3.13 shows the angle-dependent reflectivity calculated for TM-polarised light incident upon an undistorted silver grating in the vicinity of the -1 SPR for a number of grating amplitudes. There are two distinct groups of features to note. The first set is characterised by a cusp in the reflectivity at 12.1° which corresponds to the critical edge where the -1 diffracted order becomes evanescent. As this angle is approached, the power in the -1 order becomes redistributed amongst the other propagating orders, leading to the

increase in the specular reflectivity observed. Note that the greater the amplitude of the grating, the larger the step in the reflectivity observed since the efficiency (power) of the diffracted order increases with amplitude. The angular position of this critical edge depends *only* on the wavelength of the incident light and the pitch of the grating. Measurement of the critical angle thus allows an unambiguous determination of the grating pitch.

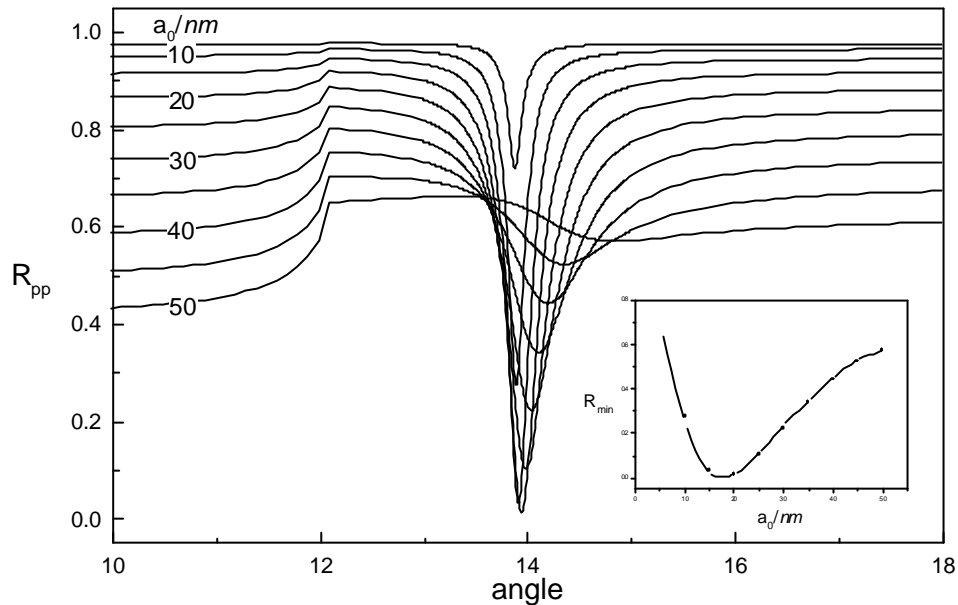


Figure 3.13 Theoretically generated reflectivity curves for TM-polarised light of wavelength 632.8nm incident upon a sinusoidal grating of pitch 800nm in the vicinity of the -1 SPR. The curves are calculated for a range of grating amplitudes from 5nm to 50nm and it is assumed that the grating is silver with $\epsilon = -17 + 0.7i$. The inset shows the variation in the minimum reflectivity with grating amplitude (taken from the main figure), showing the variation in coupling strength to the SPP mode.

The second notable feature occurs just beyond the critical edge when the incident light has enough momentum to excite the SPP mode by -G scattering from the grating. This -1 SPR is initially rather poorly coupled since there is little power scattered into the -1 evanescent order. As the grating amplitude increases, the strength of scattering increases and so the mode becomes more strongly coupled. The optimum coupling (minimum reflectivity) occurs for a

grating amplitude of about $18nm$. Beyond this point, the coupling strength to the SPP decreases with increasing amplitude. This can be understood by recognising that the SPP, once excited, can scatter by $+G$ from the grating and couple to light propagating in the same direction as the specular reflection. This radiative damping increases with grating amplitude and so for deep gratings the radiative damping will dominate the internal damping leading to an overcoupled mode. The dependence of the -1 SPR minimum reflectivity on the grating amplitude is illustrated in the inset to *figure 3.13*, and clearly shows the dependence of the SPP coupling strength on the grating amplitude.

Figure 3.14 shows the reflectivity of the same grating calculated for the region of the $+2$ SPR but with otherwise identical conditions. Again there are two groups of features to note. The small kink at 35.6° corresponds to the critical edge where the $+2$ diffracted order becomes evanescent. Note that the change in reflectivity at this critical edge is a great deal smaller than that observed when the -1 order becomes evanescent, even for the deepest gratings considered. This is because the $+2$ diffracted order arises from *two* consecutive $+G$ scatters and is thus less intense than the -1 diffracted order.

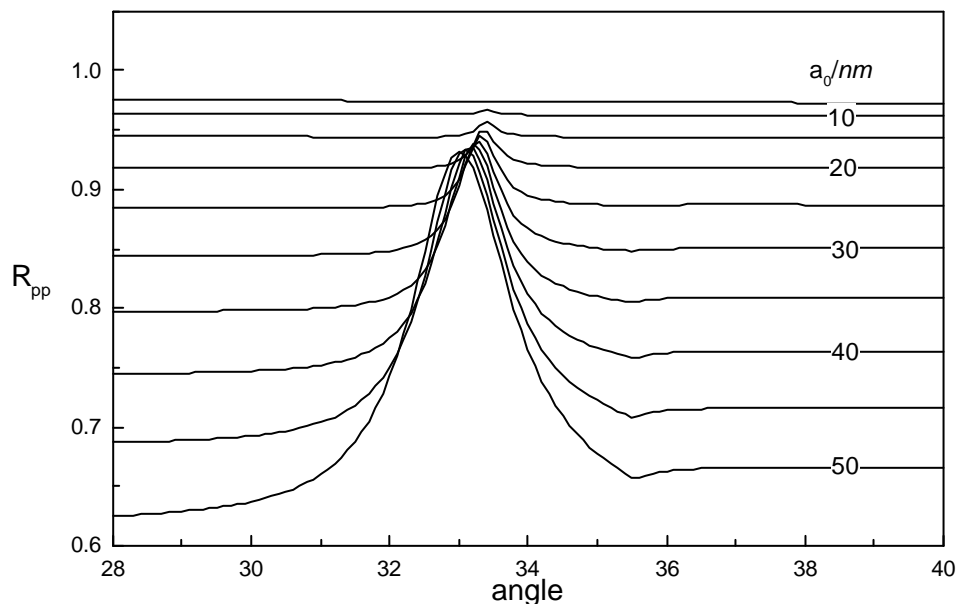


Figure 3.14 Theoretically generated reflectivity curves for TM-polarised light of wavelength $632.8nm$ incident upon a sinusoidal grating of pitch $800nm$ in the vicinity of the $+2$ SPR. The parameters are identical to those of *figure 3.13*.

The second feature observed in *figure 3.14* is the +2 SPR which corresponds to the excitation of the SPP mode *via* +2G scattering. In contrast with the first order coupling, the excitation of the SPP is observed here as a peak in the reflectivity as a function of angle. The increase in the reflectivity arises because the SPP scatters twice from the grating leading to an extra phase change of π . The re-radiation from the SPP is thus in phase with the specular reflection, leading to an increase in the reflectivity for the +2 SPR.

Note that for the shallow gratings, the second order features are much weaker than the first order features. This can be seen by comparison of *Figures 3.13* and *3.14*, which show how the coupling strength to the SPP mode varies for the -1 SPR and the +2 SPR respectively. This difference in behaviour can be explained by consideration of the intensity of the various diffracted orders from a shallow sinusoidal grating. It is observed that the ± 1 diffracted orders are more intense than the ± 2 and higher diffracted orders. This is expected since first order diffraction arises from the scattering of a photon by a single grating vector G , whereas second order diffraction is due to two single G scatters in succession; a far less probable event. It is thus inevitable that the ± 1 SPRs are more strongly coupled than the higher order SPR features in the reflectivity of the undistorted grating since there is more power available when the ± 1 diffracted orders becomes evanescent. This also explains the behaviour of the various critical edge features.

The effect of distorting the grating profile by adding a second harmonic will now be considered. This will significantly alter the reflectivity of the grating demonstrating the possibility of characterising the higher harmonics in the grating profile *via* reflectivity measurements. For a grating profile consisting of a fundamental and a second harmonic (experimentally, the most significant distortion), the physical effect of a phase $\phi_1 = +\pi/2$ is to flatten the grating peaks and sharpen the troughs, whilst the reverse is true for a phase of $\phi_1 = -\pi/2$. Profiles like the latter often arise from the etching of an initially sinusoidal grating in a fast atom beam, since the etch rate is a function of the angle of incidence of the beam.

Figure 3.15 shows the effect of adding a second harmonic component to the grating profile on the reflectivity in the vicinity of the -1 SPR. Theoretical reflectivity curves are plotted for an undistorted grating, and identical gratings distorted by a second harmonic with phases of $\phi_1 = \pm\pi/2$. It can be seen that although the distortion does affect the form of the -1 SPR by altering the wings of the resonance, it is only a minor perturbation.

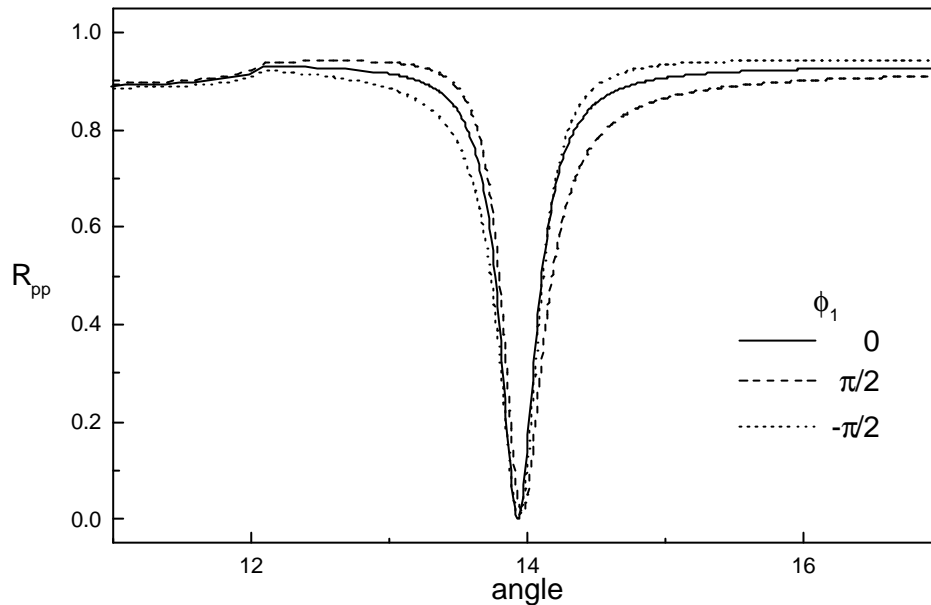


Figure 3.15 The effect of the second harmonic component a_1 on the -1 SPR. The solid line is a theoretically generated reflectivity curve for TM-polarised light of wavelength 632.8nm incident upon a sinusoidal grating of pitch 800nm and fundamental amplitude $a_0=18\text{nm}$. The broken lines are the corresponding curves for the same grating distorted by a second harmonic component of amplitude $a_1=4\text{nm}$ and phase of $\phi_1 = \pm\pi/2$. It is assumed that the grating is silver with $\epsilon = -17+0.7i$.

A far more significant change to the reflectivity is seen in the vicinity of the +2 SPR, as noted by *Bryan-Brown et al. (1993)*. This is illustrated in *figure 3.16* for identical gratings to those considered in *figure 3.15*. It can be seen that the small +2 SPR reflectivity maxima obtained for an undistorted profile becomes a deep reflectivity minima in the presence of a 2G profile component. Again the coupling in the wings of the resonance depends on the phase of the second

harmonic component; a discernible shoulder occurs on the side of the resonance nearest the critical edge for a phase of $+\pi/2$, and on the opposite side for a phase of $-\pi/2$. The sensitivity of the +2 SPR to the second harmonic component thus allows the size and phase of this harmonic to be accurately determined.

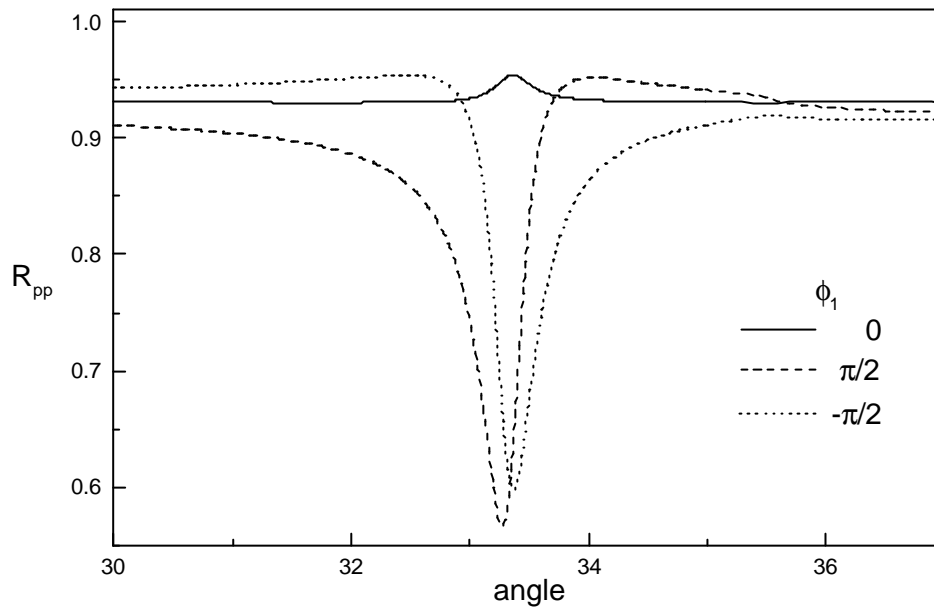


Figure 3.16 The effect of the second harmonic component a_1 on the +2 SPR. The solid line is a theoretically generated reflectivity curve for a sinusoidal grating whilst the broken lines are the corresponding curves for the distorted gratings. All parameters are identical to those used in *figure 3.15*.

Since the coupling to the SPP for the +2 SPR corresponds to a $2G$ scattering event, it follows that the resonance is a second-order process for an undistorted grating since light must scatter twice from the grating to match momentum, as mentioned earlier. The resultant coupling is thus much weaker than that for single G scatter events. The inclusion of a second harmonic component to the profile allows light to be directly scattered by $2G$ to excite the SPP. Because this scattering is direct, the coupling is much stronger, and since it results from a single grating scatter the re-radiated light from the SPP is out of phase with the specular reflection from the metal, leading to the observation of a reflectivity minima. The second harmonic component thus determines the

coupling to the +2 SPR in much the same way that the fundamental component affects the coupling to the -1 SPR.

In general, the $\pm n$ SPR feature is very sensitive to the nG Fourier component in the expansion of the surface profile. The expression of the grating profile as a Fourier series thus allows the accurate determination of each component in the profile by observation of the appropriate SPR feature. To experimentally characterise a given grating profile typically involves choosing a suitable wavelength for the incident light so that as many SPR features are observed as possible. The reflectivity measurement is thus sensitive to the greatest number of profile components, and the experimentally determined surface profile will thus be as complete as possible.

By fitting the experimental reflectivity data from a grating using the theoretical model of Chandezon, it is thus possible to characterise the optical constants *and* grating profile of the system accurately, which will be of vital importance in future chapters.

3.6 Summary

An excited molecule in close vicinity to a metallic interface is highly likely to decay back to its ground state *via* the excitation of the electromagnetic surface modes of the interface. In this chapter the surface modes that can propagate at the experimentally relevant interface between a metal and dielectric layer have been introduced. These modes comprise the surface-plasmon polariton (SPP) and a series of TM- and TE-polarised guided modes. While the SPP mode can exist even with a zero thickness dielectric overlayer, it was demonstrated that the guided modes can only exist above certain cut-off thicknesses. It was also shown that the SPP is simply the lowest order TM mode of a metal/dielectric/air waveguide. All of these modes are non-radiative and are bound to the surface region by virtue of the excess momentum they possess with respect to photons of light in the adjacent media. Various ways of directly radiatively coupling to these modes by enhancing the momentum of incident light have been discussed, as well as the possibility of excitation by fluorescent molecules located near to the interface. Finally, the Chandezon

technique for modelling the optical response of grating structures has been introduced, demonstrating the feasibility of the characterising the surface profile by reflectivity measurements.

Chapter 4

Langmuir-Blodgett film deposition

4.1 Introduction

One of the primary aims of this thesis will be to investigate the fluorescence of dye molecules situated less than an optical wavelength away from various mirror interfaces. To do this in a systematic fashion, it will be necessary to achieve sub-micron, and for preference, nanometric resolution in the location of the dye molecules with respect to the surface. In this chapter, a method of achieving this Lilliputian task will be described.

The ideal way to investigate the optical response of fluorescent emitters in a given geometry would be to study a single entity. In this case, it would be guaranteed that only a single optical environment is sampled, since there is only one emitter with a well-defined location to consider. This situation can be achieved by using ion-trapping techniques, see for example the work of *DeVoe and Brewer (1996)*. By trapping and laser cooling two barium ions, they were able to observe sub- and superradiant spontaneous emission from the two-ion system. Alternatively, it is possible to use near-field optical microscopy to investigate single molecule fluorescence processes [*Weiss et al. (1996)*]. Particular care would need to be taken, however, to ensure that the tip of the collection optics did not seriously perturb the system. The problem with these techniques is that they require sophisticated and thus costly apparatus, and this, together with their complexity, effectively precludes their use.

The only alternative to these single molecule methods is to perform averaging over an ensemble of emitters, rather than the time averaging the signal from a single emitter. In this case, a plane of emitters fixed at a given distance above a mirror interface is needed thus ensuring that all emitters have the same environment. The signal can then be acquired from all emitters rather than a single emitter, making measurements simple to perform.

In this chapter, we will discuss how layered structures can be fabricated in a relatively simple fashion using the Langmuir-Blodgett (LB) technique. This monomolecular layer deposition method allows the positioning of dye monolayers with nanometric precision above mirror interfaces. Previously, other studies of molecular fluorescence above mirrors have used a variety of sample fabrication techniques, which include spin deposition [Kitson *et al.* (1995)], evaporation [Kunz and Lukosz (1980)] and adsorption [Adams *et al.* (1980)]. Spin deposition and evaporation suffer from the problem that the films produced can be inhomogeneous and discontinuous, especially if the deposition of a few monolayers is required. Furthermore, evaporated films of dielectric material (required for transparent spacer layers) tend to be microscopically rough which causes unwanted light scattering and thus complicates the optical response. The adsorption of a matrix of condensed gas vapour on a sample is also problematic in that the experiments must be carried out at low temperature, typically in a cryostat.

The Langmuir-Blodgett technique suffers none of these disadvantages and is unique in providing an easy way of fabricating ordered and oriented molecular heterostructures of well-defined morphology. This technique was used by Drexhage (1974) in his study of fluorescence above interfaces, a task to which it is ideally suited. The basis of the Langmuir-Blodgett technique is that certain types of molecule will form a floating monomolecular layer when introduced onto a water surface. This insoluble monolayer can then be compressed until the molecules adopt a close-packed two-dimensional crystalline structure. If a suitable support is repeatedly passed through this compressed layer, a monolayer of molecules will be transferred to the substrate with each pass, leading to the deposition of a multilayer structure, known as a *Langmuir-Blodgett (LB) film*. The overall film thickness can obviously be determined with a resolution of a single monolayer.

4.1.1 Historical context

The first recorded observation of the use of monomolecular layers dates back to the 18th century BC, when the Babylonians were known to use the

spreading of oil on water as a method of divination. Another early application of the monolayer spreading technique is the ancient Japanese art form known as *sumi-nagashi*. In this technique, known in the 12th century AD, a colloidal suspension of sub-micron sized carbon particles and protein (*sumi*) is deposited onto a water surface. The addition of gelatin to this uniform layer causes the dye to flow (*nagashi*) into random patterns which can then be transferred onto paper or silk. This is the forerunner of the modern technique of *marbling*.

It has been known for centuries that oil spread on water can calm wave motion; the phenomenon was described by Pliny the elder. The first scientific investigation was carried out by *Franklin (1774)* who noted the phenomenal area that the oil could expand to cover on the water surface. *Rayleigh (1899)* proposed that such a film would expand until it was only a single molecule in thickness, and thought that if this was measured, a direct determination of the size of an organic molecule could be made. This was achieved by *Pockels (1891)*, who found a length of 2.2nm for stearic acid, which agrees well with modern measurements. Subsequently, Pockels measured the first surface pressure/area isotherm for a floating monolayer [*Pockels (1893)*], an important progression which will be discussed in a later section.

The subject was put on a sound theoretical footing by the work of Irving Langmuir. The adsorption of molecules at the interface between a liquid and a vapour was attributed to the unbalanced intermolecular forces found in the interfacial region. The imbalance results from the difference in bonding between the water molecules of the surface and those within the bulk [*Langmuir (1915)*]. Subsequent work revealed the oriented nature of molecules within the film, and Langmuir could then explain the basis upon which molecules were able to form films and which could not. In the process, he was able to determine the size and shape of many organic molecules together with their orientation at the water-air interface.

An important extension was made by Langmuir's co-worker Blodgett, who demonstrated the transfer of floating monolayers from the water surface onto a solid substrate [*Langmuir (1920)*, *Blodgett (1935)*]. Such transferred films are called Langmuir-Blodgett films in their joint honour.

Research in this field was then largely dormant until the 1960's, when Kuhn and his group commenced a series of investigations into energy transfer

in organised supermolecular structures [*Bücher et al. (1967)*, *Kuhn and Möbius (1971)*]. The work of Drexhage as described in chapter 2 was one branch of this concerted and prolific research effort. Interest in the technique was then rekindled due to its unique ability to form ordered and oriented multilayer structures. Areas of study which have subsequently utilised LB fabrication methods include non-linear optics, chemical sensing and investigations of molecular processes such as fluorescence and Raman scattering. Currently, the close resemblance of LB films to biological membranes has led to applications in interdisciplinary research; for example, the light-harvesting behaviour of proteins has been replicated in artificial structures [*Yamazaki et al. (1988)*, *Yonezawa et al. (1987)*].

The following chapter will briefly introduce the technique of Langmuir-Blodgett film fabrication, together with details of the manufacture of the fluorescent dye used in this work. More information on Langmuir-Blodgett films can be found in the classic text by *Gaines (1966)*. Recent reviews can be found in *Roberts (1990)* and *Petty (1996)*.

4.2 Langmuir monolayers

An important concept in any discussion of monolayers and their formation is that of the surface tension of a liquid interface. Molecules at the surface of a liquid differ from those of the bulk in that they are not surrounded on all sides by similar neighbours; they therefore experience an imbalance in intermolecular attraction. The result is a net inward attractive force on the surface molecules, which leads to the minimisation of the surface area of the liquid. Because the surface of a liquid will spontaneously contract, there is a free energy associated with it, *i.e.* work must be done to extend the surface (against the inward attractive forces of the bulk molecules). The free surface energy per unit area of the surface can be formally made equivalent to a force per unit length acting parallel to the surface, known as the surface tension. For water, this has a value of 73mNm^{-1} at 293K and atmospheric pressure.

If an insoluble and non-volatile material is placed on a water surface, it may behave in one of two fashions depending upon the surface tension. It

either will remain as a compact drop or will spread out to form a film; the exact behaviour is governed by the nature of the molecules spread on the surface. In order to form a film the attraction to water molecules must be greater than the mutual attraction. Two classes of compound serve to illustrate this point.

Consider first molecules such as the long chain alkanes, which have the general formula $\text{CH}_3(\text{CH}_2)_n\text{CH}_3$. These are insoluble in water because of the non-polar nature of the aliphatic chain and exhibit strong van der Waals attractive forces between chains. Consequently, when they are deposited on a water surface they do not spread out, but instead form a floating lenticular drop. If, however, a polar carboxylic acid group is substituted onto the end of the hydrocarbon chain to form an alcanoic acid (with the general formula $\text{CH}_3(\text{CH}_2)_n\text{CO}_2\text{H}$), this situation is changed dramatically. The acidic headgroup can form strong hydrogen bonds with water molecules and is thus very *hydrophilic*. The material will consequently spread out over a water surface to solvate the polar headgroup of each molecule. The molecules are stopped from fully dissolving by the *hydrophobic* aliphatic chain, and so remain at the water surface. On compression of this system, the headgroups remain solvated, while the tails are lifted clear of the water surface, thus forming an oriented monolayer.

It can be seen that to form such a layer, a molecule must have both a hydrophilic group and a hydrophobic group. Such molecules are known as *amphiphiles*, or surfactants, and the floating monolayers they form are called Langmuir films to distinguish them from films transferred onto a solid substrate. In an expanded form, the molecules interact minimally and the layer has little effect on the surface tension of the water. When compressed, however, the molecules exert a repulsive force on one another and so the surface tension of the film-covered surface is lower than that of pure water. It is useful in the context of Langmuir films to define a surface pressure Π ,

$$\Pi = \gamma_0 - \gamma \quad (4.1)$$

where γ_0 is the surface tension of pure water and γ is the surface tension of the film covered surface. Although water is the most usual subphase, many other

materials have been used, including certain hydrocarbons and mercury (!). From *equation 4.1*, it can be seen that the maximum possible surface pressure for a monolayer on a water surface at 293K is 73mNm^{-1} .

4.2.1 LB materials

The classic example of a family of compounds which are archetypal LB materials are the long chain carboxylic acids and their salts, commonly known as fatty acids. The carboxylic acid headgroup provides a hydrophilic moiety as mentioned in the previous section, whilst the aliphatic tail is hydrophobic, rendering them insoluble in water. Their film-forming ability depends largely on the length of the aliphatic chain; if the chain is too short, the molecule may be completely solvated leading to unstable films. The lower limit for obtaining an insoluble monolayer is reached with the 12-carbon member of the family, *n*-dodecanoic acid. As the chain length increases so do the attractive van der Waals forces between molecules which provide lateral cohesion; this leads to the formation of progressively more condensed monolayers.

A typical example of this class of compound is 22-tricosenoic acid, the molecular structure of which is illustrated in *figure 4.1*. This material has been studied widely because of its excellent film forming and film-transfer properties [Barnes and Sambles (1986)] and so was an obvious choice for use as a transparent spacer molecule.

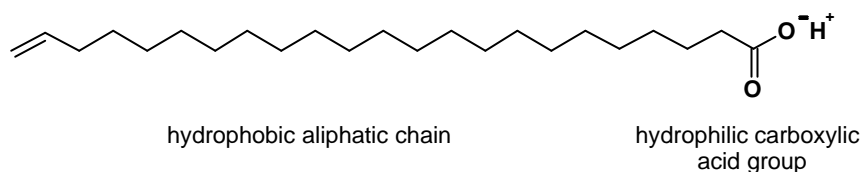


Figure 4.1 The molecular structure of 22-tricosenoic acid, depicting the amphiphilic nature of carboxylic acid molecules.

The structure differs little from the ideal template, an unsaturated double bond linking the terminal carbons of the aliphatic chain. Many other classes of compounds have been studied in the context of monolayer formation, most notably benzene derivatives, porphyrins, phthalocyanines, and naturally of

course, phospholipids. Further information on LB film-forming materials can be found in chapter 2 of *Roberts (1990)*.

4.2.2 Surface pressure-area isotherms

When a monolayer is laterally compressed on a water surface, it will undergo phase transitions due to the changing interactions between neighbouring molecules within the layer. These may be most clearly observed by measuring the surface pressure of the film-covered surface as a function of the film area, for a given temperature. This measurement, commonly known as an *isotherm*, can also be used to assess the quality of floating Langmuir films. The surface pressure, as defined in *equation 4.1*, is obtained by measuring the reduction in the surface tension of the film-covered surface as the available film area is reduced using a moving barrier. This will be discussed further in a following section.

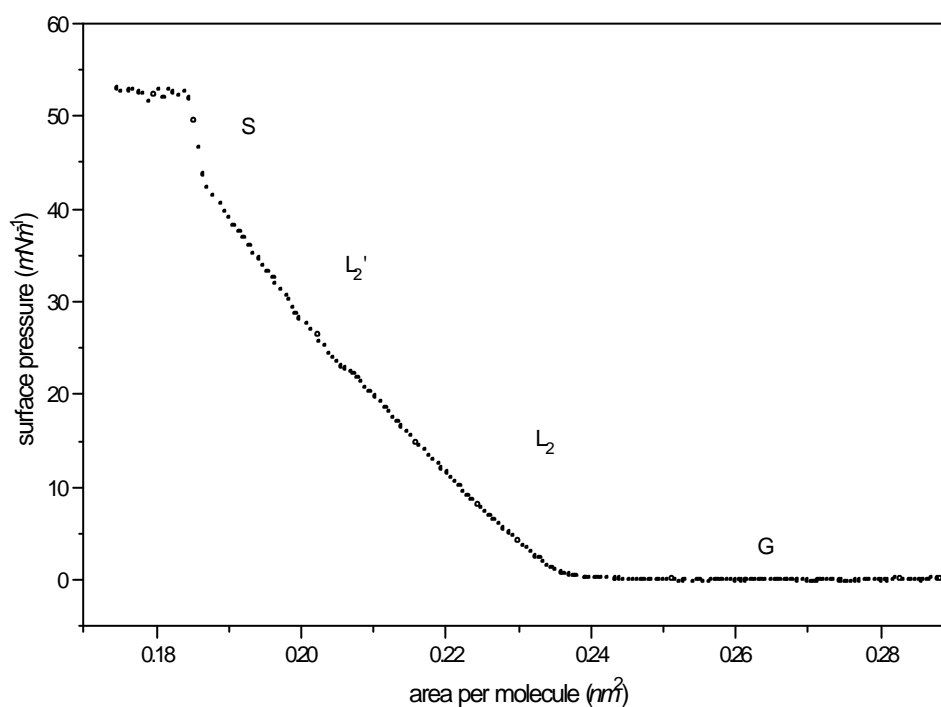


Figure 4.2 The surface pressure/area isotherm for a Langmuir film of 22-tricosenoic acid on a water subphase at 20°C. The gas (G), liquid-condensed (L₂, L₂') and solid (S) phases of the film are indicated.

Figure 4.2 shows the surface pressure-area isotherm for a monolayer of 22-tricosenoic acid on a water subphase at 20 °C. Note that instead of total film area, the abscissa has been scaled to show the more useful area *per molecule* instead. The form of this isotherm reveals much about the molecular arrangement at the water surface. It is evident that there are several distinct regions in the plot, corresponding to different phases of this two-dimensional system. These phases are analogous with the more common phases of three-dimensional systems, and denote different molecular behaviour at the interface.

When the film is uncompressed, the area per molecule is high, and molecular motion at the surface is essentially unhindered. The molecules are thus widely separated, and their behaviour is akin to that of a gas, albeit one restricted to two dimensions only. In this *gaseous* phase (G), the hydrocarbon tails of the molecules lie flat on the water and can adopt any orientation in the surface plane; this is illustrated in *figure 4.3a*. The surface pressure is zero, indicating that the surface tension is unchanged from that of pure water.

On compression, the area per molecule is decreased and the molecules begin to interact with one another. Free rotation of the hydrocarbon tails can no longer occur and clusters of molecules start to form. At this point, the surface pressure begins to rise, as shown by the “lift-off” in the isotherm. As the film area is reduced further, the hydrocarbon tails are gradually lifted away from the water surface, to which they are tethered by the solvated headgroups. These headgroups are not yet close-packed and the tails are randomly oriented making this phase the two-dimensional equivalent of a liquid. This is illustrated in *figure 4.3b*.

Whilst in this *liquid-expanded* phase (L_1), the monolayer is still compressible, and further reduction in the film area tends to force the headgroups closer together and align the hydrocarbon tails in a single direction. The formation of this condensed phase is marked by a rapid change in the gradient of the isotherm, after which the surface pressure increases approximately linearly. During this process, the tilt angle of the hydrocarbon tails away from the surface normal decreases in a continuous fashion. Several *liquid-condensed* metaphases are possible here, corresponding to different alignment of the molecular tails. For 22-tricosenoic acid, a transition occurs at $\Pi \sim 23 \text{ mNm}^{-1}$ between a phase (L_2) where the tails tilt toward the nearest

neighbour, and a higher-pressure phase (L_2') where the tails tilt toward the next nearest-neighbour [Shih *et al.* (1992)]. This is visible as a shoulder in the isotherm.

At a surface pressure of $\Pi=42\text{mNm}^{-1}$ there is a further abrupt change in gradient to a steeply sloping linear region. This is the result of a transition to the *solid* phase (S) where the molecules are arranged in a rigid two-dimensional array with closely packed head groups and normally oriented hydrocarbon tails; this is depicted in *figure 4.3c*. This pseudo-crystalline phase has a low compressibility and the area per molecule of $\sim 0.2\text{nm}^2$ is similar to the cross-sectional area of the carboxylic acid headgroup. These facts evince the close-packed nature of the molecules in this phase. Further compression leads to the collapse of the film due to buckling or overturning, whereby a bilayer starts to form from molecules forced out of the monolayer.

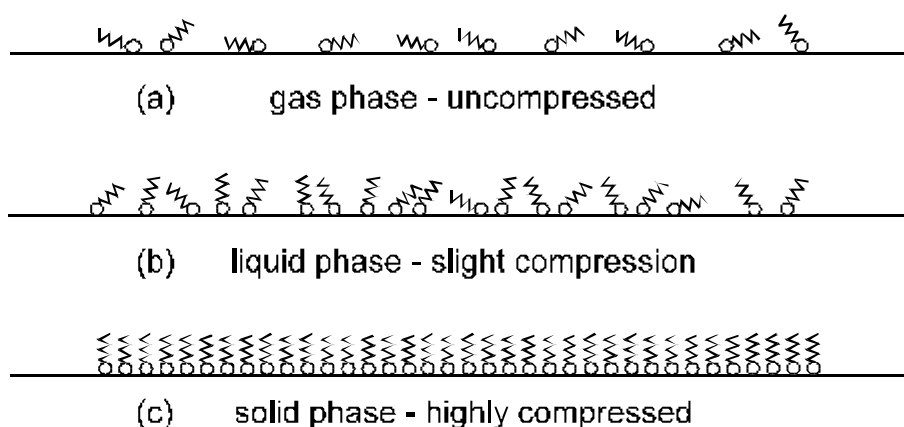


Figure 4.3 Compression of a long chain fatty acid Langmuir film on a water subphase illustrating the (a) gas phase, (b) liquid phase and (c) solid phase. The circles represent the carboxylic acid group, whilst the zigzag tail represents the aliphatic chain.

The actual situation is more complex than this description indicates, since depending on the precise temperature a host of different metaphases are possible, even for a simple molecule. By measuring isotherms at different temperatures, it is possible to construct the phase diagram for a given Langmuir film [Peterson (1992)]. It is also a simplification to assume that the Langmuir film consists of a single well-oriented monodomain; Brewster angle microscopy

reveals that the film consists of many randomly aligned smaller domains. These range in size from tens of micrometres to a few tenths of a millimetre depending on the exact formation conditions. If the molecules are tilted away from the normal, as they are in the liquid-condensed phases, the Langmuir film will be birefringent due to the different orientation of individual domains.

4.2.3 Measurement of surface pressure

In order to measure the isotherm of a Langmuir film a method was needed to determine the surface pressure of the monolayer. This was achieved using a device known as a Wilhelmy plate, although other methods are possible, see for example *Gaines (1966)*. The plate consists of a strip of filter paper of well-defined width, which is partially immersed in the water subphase through the monolayer of interest, as illustrated in *figure 4.4*. The forces acting vertically on the plate are (i) the weight of the plate plus absorbed water, (ii) the upthrust from water displaced from the subphase, and finally (iii) the surface tension of the film, resolved along the contact angle. The total force F is thus

$$F = \rho_p g l w t + 2\gamma(t + w) \cos \theta - \rho_w g d w t \quad (4.2)$$

where ρ_p and ρ_w are the densities of the paper and water respectively, l , w and t are the plate dimensions, d is the immersion depth of the plate, θ is the contact angle between plate and film, and γ is the surface tension of the film-covered surface.

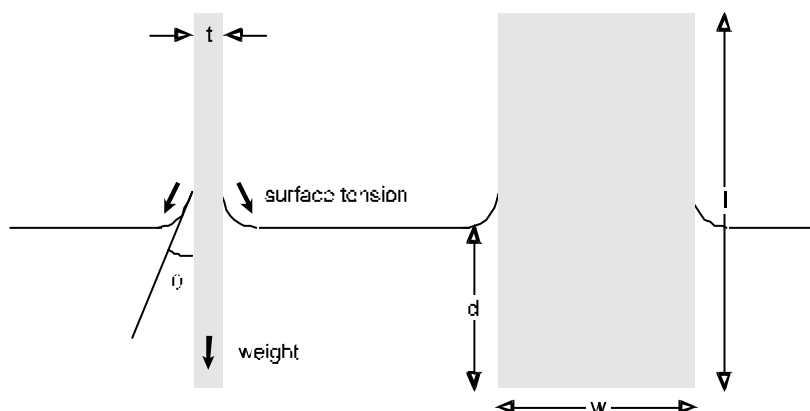


Figure 4.4 The Wilhelmy plate and the forces acting upon it.

The surface tension of the film was monitored by measuring the downward force acting on the plate, which was maintained at a fixed immersion depth. A comparison of the force measured for the film-covered surface and that obtained for a pure water subphase then gave a direct measure of the film surface pressure. Because of the small forces involved, the plate was suspended from a sensitive electrobalance, which was calibrated using a set of known masses. A negative feedback control loop within the balance was used to keep the immersion depth constant. The contact angle is effectively zero for fully wetted filter paper, and so *equation 4.1* and *4.2* may be used to obtain an expression for the surface pressure.

$$\Pi = -\Delta\gamma = -\frac{\Delta F}{2(t + w)} = -\frac{\Delta F}{2w}. \quad (4.3)$$

In this expression, $\Delta\gamma$ is the change in surface tension resulting from the presence of the monolayer, whilst ΔF is the accompanying change in the force acting on the plate. The last expression results from the assumption that the thickness of the Wilhelmy plate is negligible in comparison with the width.

4.3 Film deposition.

The initial aim of spacing dye molecules a given distance from a mirror interface can now be accomplished by the sequential deposition of Langmuir monolayers onto a solid substrate to form an LB multilayer structure. By varying the number of deposited layers, it is possible to produce a transparent film ranging in thickness from a single monolayer ($\sim 2.6\text{nm}$) to half a micrometre, with a resolution of a monolayer. This is achieved using the Langmuir-Blodgett film transfer technique.

4.3.1 The Langmuir-Blodgett technique

This film deposition technique, first developed by Langmuir and Blodgett [*Langmuir (1920), Blodgett (1935)*], involves the vertical passage of a substrate

through a floating monolayer. Because the structure of the deposited LB film is determined by the molecular organisation in this Langmuir film, it is important to ensure that deposition occurs from an ordered state. To achieve this, the monolayer must be compressed into one of the higher-pressure condensed phases before deposition commences. For 22-tricosenoic acid, suitable surface pressures are in the range 25 to 35mNm^{-1} for a temperature of 293K , and deposition occurs from the liquid-condensed L_2' phase.

When a hydrophobic substrate is passed vertically through such a film, a monolayer of molecules will be deposited onto the substrate in the manner depicted in *figure 4.5a*. The substrate surface will then be terminated by the hydrophilic headgroups of this monolayer, and when the substrate is withdrawn from the subphase, a second monolayer of molecules will be deposited on top of the first. This process, shown in *figure 4.5b*, orients the second layer in the opposite sense, leaving the substrate with a hydrophobic surface once again. Repetition of this immersion/emersion process thus allows the deposition of a multilayer stack through the sequential transfer of bilayers. During all of these steps, the surface pressure of the floating monolayer must be kept constant to ensure uniform deposition. Note that if the Langmuir film is in an expanded phase, the film will not deposit onto a substrate; there is a minimum surface pressure below which transfer is not possible.

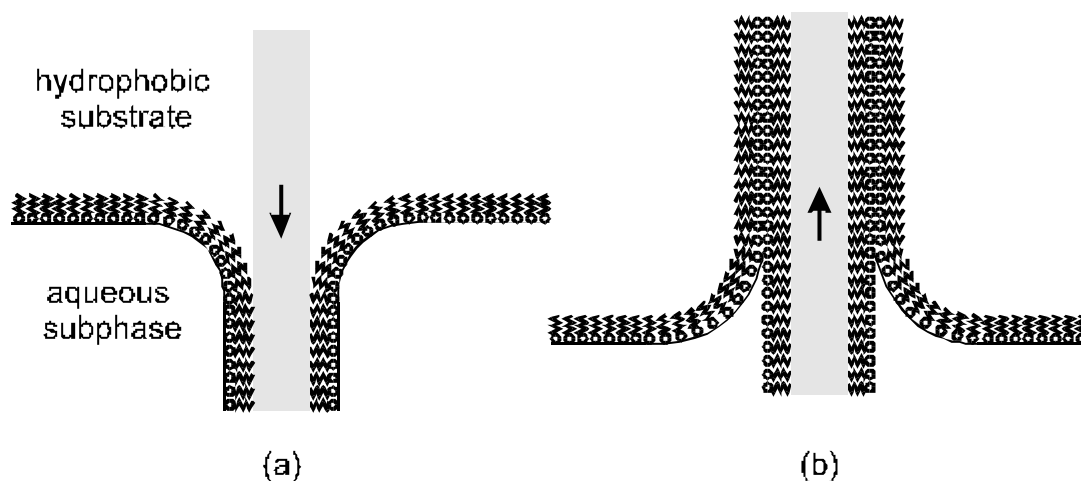


Figure 4.5 Langmuir-Blodgett film transfer on the (a) downstroke, (b) upstroke.

This type of deposition, whereby a layer is transferred to the substrate with every traversal of the air/monolayer interface, is known as *y-type*

deposition. For “simple” LB molecules such as the carboxylic acids, this is the most common situation, but is not the only possible result. Amphiphilic molecules with more complex structures (and stronger dipole moments) may only transfer on the downstroke, leading to *x-type* deposition, or only on the upstroke, leading to *z-type* deposition. This results in the formation of non-centrosymmetric structures, which are essential for the observation of second harmonic signals [Roberts (1990)]. Examples of the structures produced by all three types of deposition are given in *figure 4.6*.

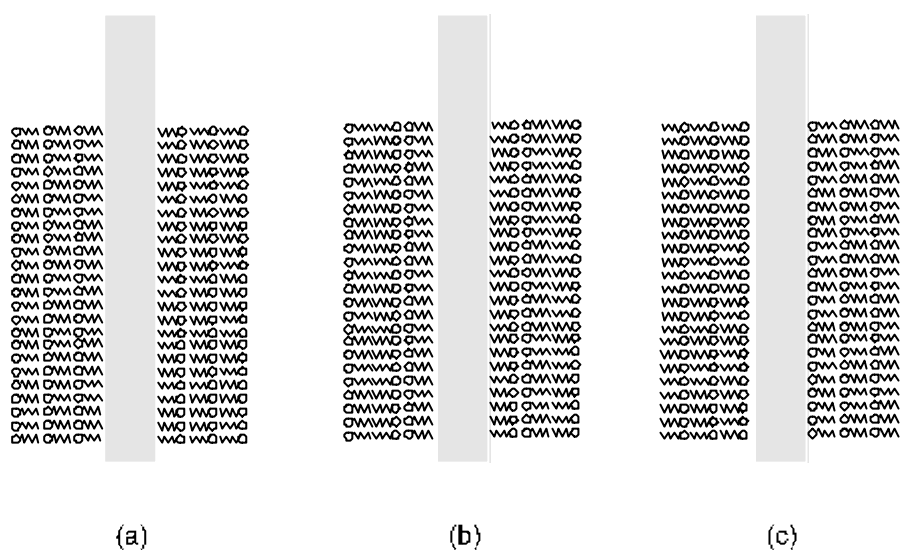


Figure 4.6 The structure of (a) *x-type*, (b) *y-type* and (c) *z-type* Langmuir-Blodgett multilayer films.

4.3.2 Transfer ratios

The deposition of monolayers from a subphase onto a substrate can be characterised by the transfer ratios measured during fabrication. The transfer ratio is given by the decrease in area of the Langmuir film at constant surface pressure divided by the surface area of the substrate (deposition occurs on both sides of the substrate!). If the substrate is covered perfectly by a monolayer in a given deposition, a transfer ratio of unity is expected, assuming of course that the molecules are ordered in the same manner on the substrate as in the film. Conversely, if no film is deposited the transfer ratio should be zero.

Nothing can be inferred about the quality of the deposited film from the transfer ratios, save that if they deviate substantially from the expected values of zero or one, it is likely that the resulting film will be inhomogeneous. Small discrepancies from these ideal values are permissible due to the possibility of deposition on the edges of the substrates; this was not accounted for in the calculation of the surface area of the sample. Since the edges of the silica slides used as substrates are inevitably frosted, it would be difficult to judge the amount of material deposited on the edges, even if the area was known. Typically, it was found that transfer ratios varied in the range from 0.95 to 1.05; samples with ratios outside this range were treated as suspect and were discarded. Note that a 1,1,1 sequence of transfer ratios indicates a y-type deposition, 1,0,1 indicates x-type deposition and ratios of 0,1,0 are the result of z-type deposition. (Here it is assumed that the deposition commences with the downstroke of a hydrophobic substrate.) Once a film has been deposited, it is possible that some molecular rearrangement may occur; this will depend on the interactions between the polar headgroups and the non-polar tails. Films that displayed x- or z-type transfer ratios on deposition may in fact subsequently rearrange into the more stable y-type structure.

4.3.3 The Horizontal transfer technique

While the conventional Langmuir-Blodgett technique as outlined above works extremely well for a wide variety of amphiphiles, occasionally problems are encountered in the deposition of more exotic materials. The limiting factor is the degree to which the floating monolayer must be compressed in order to achieve successful deposition; expanded films are not transferred to substrates *via* vertical transfer, the substrate simply slides through the monolayer. For conventional LB materials, high collapse pressures are easily achieved, and compression is not a problem. For other materials, notably proteins and phospholipids, highly condensed phases simply do not occur, the molecules either form aggregates, or dissolve into the subphase on compression. To transfer films of these materials to a solid support requires the use of an adaptation of the Langmuir-Blodgett technique, first used by *Langmuir and*

Schaefer (1938). The film is compressed as before, this time to a much lower surface pressure at which the film is still stable. The substrate is then brought down to the monolayer in a horizontal fashion thus making contact with the hydrophobic tails of the molecules. Upon withdrawal, a monolayer is carried away with the substrate. This is illustrated in *figure 4.7*.

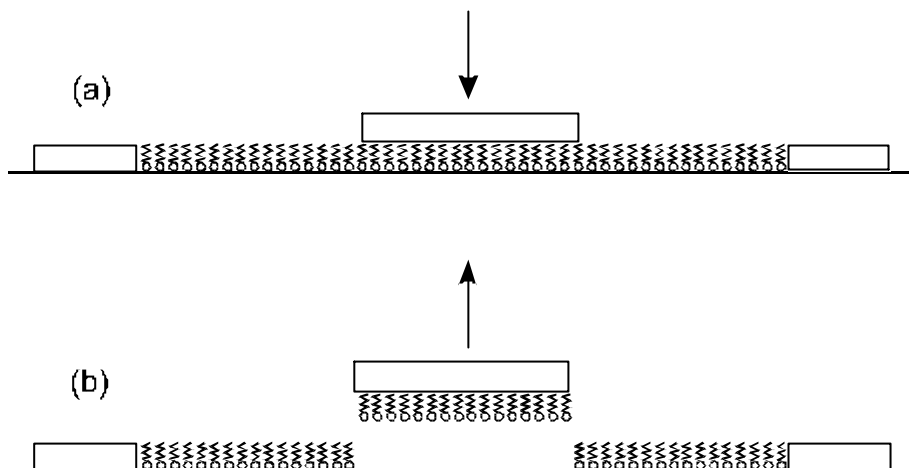


Figure 4.7 The horizontal film transfer technique.

The fluorescent dye material used in this work was unsuited to conventional LB deposition because of its low collapse pressure, and the horizontal technique detailed above had to be used to deposit monolayers onto suitable LB multilayer structures.

4.4 LB deposition apparatus

The deposition of LB films requires relatively little equipment; in the simplest analysis, all that is required is a trough to contain the subphase, thus confining the monolayer film, and a supply of pure water to fill this trough. In actual practise there are important requirements to be satisfied relating to the qualities of these components, and certain refinements can be made to simplify the film fabrication process.

4.4.1 The Langmuir-Blodgett trough

The ideal trough for film deposition contains a small volume of water, yet has a large exposed surface to maximise the area of the floating monolayer. This is achieved by the use of a shallow trough ($\sim 1\text{cm}$ deep), with a well to allow the full immersion of a substrate, as the cross-section in *figure 4.8* illustrates.

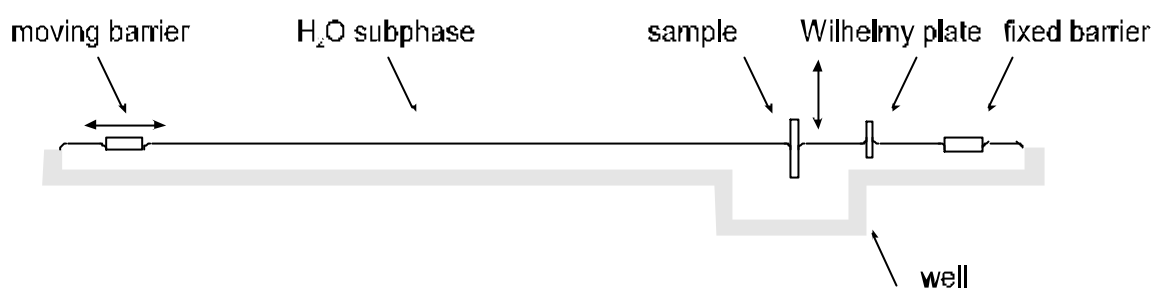


Figure 4.8 The Langmuir-Blodgett trough in cross-section.

The trough is rectangular in plan, and has a surface area of 720cm^2 . The most important requirement is that the water surface is easily accessible to allow ready manipulation of the film and removal of particulate contamination. This is achieved by filling the trough until the meniscus of the water surface is 2 to 3mm proud of the rim. The water surface can then be easily swept clean by barriers, and films can be compressed with no risk of leakage around the edge of the barrier. If there is to be no spillage of the subphase with consequent disruption of the monolayer, the trough must be made from a hydrophobic material. Glass and polymer-coated steel are the traditional solutions, but current thinking tends towards the use of a monolithic block of PTFE. The advantage here is that PTFE is chemically inert and very easy to clean, a prime consideration. The film is then confined by two PTFE barriers extending across the width of the trough, one fixed beyond the well, the other movable; the film can then be compressed by moving this barrier across the trough. The barriers themselves are controlled by a BBC microcomputer, as is the dipping mechanism, allowing fully automated film deposition. The film pressure is

monitored using a Wilhelmy plate immersed in the subphase adjacent to the substrate.

4.4.2 The ultra-pure water system

The most stringent condition to be observed in LB deposition is that the water used to form the subphase must be of the highest possible quality. The trough typically holds $\sim 1 \times 10^{-3} m^3$ of water with a surface area of $0.1 m^2$; the amount of LB material introduced to the surface is $< 1 mg$. Impurities at the part-per-million level in the subphase water will thus pose a serious problem if they collect at the surface, since they will be of a similar concentration to the intended monolayer material. The subphase water was purified using a composite Elgastat UHQ-PS ultra-pure water system, supplied by Elga Ltd. This system employs a multiple stage treatment, incorporating filtration to remove particulates and organic contaminants, and deionisation to remove dissolved inorganic matter.

Initially, water from the local mains supply was pre-filtered to remove large particulate contamination, thus protecting the following filtration stages from damage. A reverse osmosis (RO) unit was then used to remove the bulk ($\sim 95\%$) of the dissolved impurities. This main purification stage produced filtered water at the rate of a few litres per hour, and so the output from the RO unit was continually fed into an 80l reservoir where it was stored until required. On demand, water was taken from this reservoir and pumped through the next set of filters, which produced water with a resistivity of $> 18 M\Omega cm$ and total organic carbon (TOC) content of < 20 parts per billion. The first filter was simply a $0.2 \mu m$ particle filter to protect the subsequent stages. From here, water was passed through an activated carbon filter to remove the trace amounts of organic contamination left after the RO treatment. Remaining dissolved carbon dioxide and other inorganic material was then removed in a two-stage deioniser. The first step, known as a “scrubber”, consists of a bed of mixed acidic and basic resins which scavenge dissolved ions from the feed. The second “polishing” step uses higher quality nuclear-grade resins to reduce metallic contamination to the sub part-per-billion level (as claimed by Elga). Any silica

gel debris introduced by the preceding deionisation stages was then removed by a 0.05 μm pore diameter particle filter. A final UV irradiation stage ($\lambda=254\text{nm}$) served the dual purpose of photo-oxidising any remaining large organic molecules and sterilising the water.

Whilst in operation, the water was recirculated through the final four stages continuously *via* a small holding tank to ensure optimal purity. Before water dispensation, the system was operated for a few minutes to ensure full circulation through these filters and the first half-litre of water produced was discarded. The water quality was judged by monitoring the resistivity of the output water; if this resistivity fell below 18 MWcm , the filter cartridges were replaced. This was necessary roughly every three months.

4.5 Experimental procedure

The deposition of Langmuir-Blodgett films is a lengthy process, which requires the utmost attention to cleanliness in both sample preparation and in the deposition process itself, for even small amounts of particulate contamination can seriously affect the optical quality of the resulting sample. This is especially true of the multilayer samples fabricated in this work since defects in the initial layers act as nucleation centres for larger defects in subsequently deposited layers. The fabrication of good-quality samples is the most critical stage in the experimental programme of work being described. In view of this, the key precaution taken to assure sample quality was that both substrate preparation and film deposition were carried out under clean-room conditions.

4.5.1 The clean room

Cleanliness is essential for successful LB deposition since the greatest single cause of failure in the LB deposition process is the contamination of the subphase by airborne particulate matter. The required dust-free atmosphere is most easily attained by fabricating samples in a clean room environment.

In order to minimise contamination by dust particles, a number of precautions were adhered to whilst within the clean room. Disposable, hooded clean suits and overboots were worn at all times, and replaced whenever wear was noted. Latex surgical gloves were used to avoid contamination of surfaces by grease and sweat from fingers, and were secured to the suit with wrist-tape. The use of solvents necessitated the employment of activated carbon filter masks and these helped to reduce the exposed areas of the worker to a minimum. Outdoor footwear was not worn, and any dust picked up on the soles of the overboots was removed by walking across a series of adhesive tack-mats. Before entering the clean room proper, any remaining dust was removed by a final cleaning with a jet of filtered air. In order to reduce contamination levels further, transfer of material in and out of the clean room was kept to a minimum. If anything needed to be brought in, it was thoroughly cleaned using filtered air. Any material that could shed dust was not permitted within the clean room; acetate foil was used to write on instead of paper, and lint-free cleanwipes (DuPont Micropure 100) were used in preference to tissue.

The clean room itself was split into three sections; each connected by a swing door in series. The outermost section was reserved as a changing area, thus ensuring that the clean room apparel remained dust-free within a clean environment. Any dust raised by the changing process was also confined to this region, well away from the more sensitive areas. Beyond this area was a small antechamber which contained a fume-hood and an ultrasonic bath. This region was used for sample preparation, and chemical synthesis. The innermost room, known as the "inner sanctum" was the cleanest, and contained the trough and ultra-pure water system. The trough itself was mounted on a marble slab supported by a concrete plinth in a bid to reduce vibration, which is known to adversely affect the deposition process. This problem was lessened by the location of the clean room in the basement of the Physics building.

The clean room was operated under positive pressure by the use of a laminar airflow hood situated within the inner sanctum. The filtered air stream emanating from the hood passed from this innermost room through the antechamber into the changing area, and from there into the outside world. The ingress of dust into the clean room was thus impeded by the opposing airflow.

Stagnant regions of air were avoided by the restriction of the airflow to a single path from the laminar flow hood to the external door.

The design of the cleanroom was such that the number of niches and recesses where dust could accumulate was kept to a minimum, and all worksurfaces were covered in glass to allow easy containment and cleaning of solvent spillages. Cleanliness of surfaces was maintained by the regular use of tacky-rollers, followed by removal of the adhesive residue using a solvent-damped clean-wipe. Tear-off adhesive mats were not only restricted to the changing area, the floors of the antechamber and inner sanctum were also covered to trap any rogue dust able to penetrate in spite of the precautions taken. The integrity of the clean room was checked periodically by turning off the room lights and shining a torch around in order to spot any airborne dust. If this was found to be significant a complete clean was initiated to return the room to an unsullied state. Occasional flooding of the clean room with ultra-pure water was found to be an excellent dust removal measure.

4.5.2 Substrate preparation

The prime requisites of substrates intended for LB deposition are that they must be extremely clean, and preferably smooth on the molecular level. Semiconductor wafers, therefore, make excellent substrates, and silicon has been used extensively [Brady (1996)]. For samples intended to be characterised by optical methods, however, it is advisable to use transparent substrates. Flame-polished glass can be obtained with excellent flatness, but suffers from the disadvantage that sodium ion impurities fluoresce strongly under UV illumination. This problem is avoided by the use of silica substrates, which are transparent for light of wavelengths greater than $\sim 160\text{nm}$. For this work, silica microscope slides of dimension $75 \times 25 \times 1\text{ mm}$ and $\lambda/10$ flatness were obtained from Heraeus Ltd. and cut into 25mm squares. To ensure that they were fully degreased, the substrates were then subjected to a rigorous cleaning process. During this process, latex gloves were worn, and handling of the samples was kept to a minimum. The substrates were initially immersed in concentrated nitric acid (70%) for 10 minutes to remove adsorbed contamination, then rinsed in deionised water. The samples were then

transferred to an ultrasonic bath and agitated for 30 minutes at 50°C in a 1% [v/v] solution of Neutracon in deionised water. After rinsing with deionised water and drying, the ultrasonic treatment was repeated using Analar, and finally Aristar grade chloroform (Merck) for two further 30 minute periods. The substrates were then drag-cleaned using lens tissue drenched in solvent. Initially chloroform was used, followed by propan-2-ol. Propan-2-ol is less volatile than chloroform, and the interference fringes produced by the slowly receding solvent front make it easy to spot very small dust particles left on the surface.

The samples were then stored in a dust-free airtight container until they were ready to be used. Before deposition, one final preparation stage was necessary to ensure successful sample fabrication. The silica surface itself is partially hydrophilic due to the presence of dangling –H and –OH groups. To render the surface hydrophobic, and thus ensure good LB deposition, the substrates were silanized by exposure to 1,1,1,3,3,3-hexamethyldisilazane (HMDS) vapour. This has the effect of replacing the dangling –OH groups with non-polar –CH₃ groups, thus ensuring the hydrophobic nature of the surface. Typically, samples placed in a sealed glass jar with a few drops of HMDS were rendered completely hydrophobic after an overnight exposure.

Mirror substrates were fabricated by the thermal evaporation of an optically thick layer of silver onto silica substrates, under high vacuum. The substrates were cleaned and prepared following the above procedure, including the HMDS treatment since LB material has to be deposited on the reverse of the substrate too. Before the deposition commenced, silver grain (99.99%, Koch Chemicals) was heated under a vacuum of $\sim 10^{-4}$ Pa to drive off any surface contamination. During this process, the substrate was protected by a movable shutter. When the silver had stopped outgassing, the deposition could begin. Typically, a 200nm thick film of silver was deposited at the rate of 1nm s^{-1} . The film thickness was monitored using a quartz crystal oscillator, but the actual thickness was not critical as long as it was more than about 100nm thick.

The substrates were left in the chamber to cool under vacuum, and were stored there until needed for LB deposition. Silver itself is hydrophobic when fresh, but on exposure to the atmosphere, a hydrophilic sulfide layer forms. For

this reason, LB deposition was commenced no longer than 30 minutes after the samples were removed from the vacuum chamber.

4.5.3 Solution preparation

The method of introducing LB material onto the subphase is to dissolve it in a volatile, water immiscible solvent and then deposit it drop-wise onto the water surface from a syringe. The solvent then evaporates, leaving behind a monolayer of the LB material on the water surface. The typical volume of solution spread on the subphase is about 100 *nl*, and syringes manufactured for gas-phase chromatography are eminently suitable for LB work. For the deposition of transparent spacer layer structures, 22-tricosenoic acid (99.99%, Fluorochem Ltd.) was used dissolved in Aristar grade chloroform. This LB material was chosen because it is optically transparent and because its optical characteristics and monolayer thickness have all been well characterised [*Barnes and Sambles (1986)*]. The fluorescent dye was treated in a similar manner, but required more care in handling. The LB deposition of this material will be discussed in more detail in a later section.

In common with every other process in LB deposition, extreme care must be taken in the preparation of the solution, since even small amounts of surface-active contamination can adversely affect the formation of stable monolayers. In order to achieve the requisite level of cleanliness, all glassware coming into contact with the solution was cleaned using the same process as that used to clean substrates, with the omission of the final drag-cleaning step. Initially, a 5 *ml* volumetric flask and weighing bottle were cleaned, and dried in a heat cabinet. A microbalance was then used to weigh out approximately 5 *mg* of the solute in a weighing bottle. The weighing bottle was set on the scale pan, and left to settle for ten minutes. At the end of period, the scale reading was noted without disturbing the apparatus, and a small amount of solute placed in the bottle. The balance was left to settle at the new reading for another ten minute period before a second reading was taken, the difference between the two readings being the mass of solute added. The accuracy achieved was typically ± 10 *ng*, although the scales could be read to 1 *ng*. Vibration and

draughts made the attainment of such a precision doubtful, even though the scales were housed in a clean room. The solute was transferred from the weighing bottle by dissolving it in a small quantity of Aristar grade chloroform and pipetting it into the volumetric flask. The weighing bottle was then repeatedly washed with chloroform and drained into the flask to ensure that all of the solute had been transferred. The solution was then made up to the 5ml mark, and quickly sealed to stop the evaporation of solvent (this would significantly alter the concentration of the solution, rendering isotherms inaccurate). The resulting solutions had concentrations in the range $3\text{--}5\text{mM}$. Dissolution of the solute was aided, if necessary, by agitation of the solution in an ultrasonic bath for two or three minutes.

4.5.4 Film deposition

The trough was kept full of ultra-pure water at all times, mainly to stop the accretion of dust on the surfaces, but also to help leach contaminants out of the PTFE. Before use, the trough was emptied using a hose connected to a water pump, and the PTFE surfaces wiped clean using cleanwipes drenched in Aristar grade chloroform. During this process, the wipes were held in PTFE tipped forceps in order to reduce the exposure of the user to the solvent, and to avoid the contamination of the trough with chemicals released from the latex gloves. The trough was then refilled with ultra-pure water, and the surface swept clean four or five times using a PTFE barrier dragged across the surface. After each sweep, the water pump was used to clean the swept area while at its minimum extent, and the barrier was wiped clean. The trough was then emptied, and the entire process repeated. This process may seem excessive, but the chances of successful deposition were greatly increased by the repetition. A good check of the surface cleanliness was to reduce the surface area to a minimum, whilst monitoring the surface pressure, an uncontaminated surface exhibiting no pressure change.

After cleaning, the movable barrier was swept to enclose half the area of the trough, and the LB material spread onto the subphase from solution, drop by drop. The syringe was held a few mm from the water surface during this

process, and extreme care taken not to let the solution fall through the surface onto the bottom of the trough. The drops were applied at random points, and never near the edges of the trough to avoid crystallisation of the material. When the surface pressure reached $\sim 10\text{mNm}^{-1}$, the barrier was moved back to allow the film to expand over the full surface of the trough. If the solution was freshly made, an isotherm measurement was taken as a precaution to ensure that the material was uncontaminated. To do this, the volume of solution spread on the subphase was noted, thus allowing the amount of material present to be calculated. The surface pressure was then measured as the monolayer was slowly compressed at a constant rate of $0.5\text{cm}^2\text{s}^{-1}$, corresponding to a barrier speed of 0.25mms^{-1} . During this process, the temperature was monitored, but was not controlled since the temperature was found to vary by less than $0.5\text{ }^\circ\text{C}$ during the 20 minutes needed to complete the measurement. This temperature change was found insufficient to significantly alter the 22-tricosenoic acid isotherm.

Assuming a satisfactory isotherm was achieved, LB deposition could commence. A clean, hydrophobic substrate was given a final inspection, and any remaining dust blown off with filtered air. The substrate was then held in a PTFE clip and immersed to a depth of $\sim 1\text{mm}$ into an expanded freshly spread film of 22-tricosenoic acid. The water meniscus at the substrate was then checked to ensure that it was convex, indicating that the substrate was not wetted by the subphase. If the substrate was wetted, it was discarded and replaced by another. The film was then compressed at a rate of $1\text{cm}^2\text{s}^{-1}$ until the surface pressure reached 30mNm^{-1} . At this point, the substrate was immersed through the subphase until the desired depth was achieved. 22-tricosenoic acid has excellent deposition qualities, and hence the transfer could be carried out at the rapid rate of 1mms^{-1} . The substrate was then held in the subphase, and the film area adjusted until the surface pressure returned to 30mNm^{-1} . The substrate was then withdrawn from the subphase at the slightly lower speed of 0.6mms^{-1} . The substrate was carefully observed during this process to ensure that the meniscus was parallel to the subphase and moved downwards in a uniform fashion. Since the surface of the sample was hydrophilic, the meniscus was concave, and water could become occluded in the film. It was essential that the subphase was allowed to recede from the sample at this stage to allow the

trapped water to drain away fully. After the deposition of this layer, the sample was left stationary whilst the film surface pressure was equilibrated. This bilayer deposition process was then repeated until the desired number of layers had been transferred. The deposition of the first bilayer was found to be critical, and if this was achieved without problems, the deposition of subsequent layers could be carried out unattended. LB films up to 240 layers could be deposited in this fashion, but fresh Langmuir films of material had to be spread every 40 layers due to the almost complete transfer of the floating film. Occasionally, the meniscus was found to “pin” on the substrate, and this inevitably resulted in the complete disruption of film transfer. If this occurred, the dip had to be abandoned and a completely fresh start made with a new substrate. In spite of the elaborate precautions taken, pinning occurred in a heart-breakingly arbitrary manner.

4.5.5 Choice of dipping parameters

22-tricosenoic acid is an extremely well behaved LB material and can be deposited under a wide range of conditions, which is partly why it was chosen for this study. Not all materials are so forgiving, and the conditions required to achieve good deposition for a particular material need to be determined experimentally using trial and error. The optimum dipping parameters for the fluorescent europium complex, described in the following section were painstakingly determined by R.M. Amos, a co-worker in the group [Amos (1997)].

Factors that need to be considered include the choice of solvent used, and the concentration of material in that solution. The solvent used must not chemically react with the material, and must be sufficiently volatile to rapidly evaporate from the subphase. If the concentration used is too high, the molecules may form dimers, which disrupts the formation of monolayers on the water surface and complicates the analysis of the fluorescence from the system. Conversely, if the concentration is low, large volumes of solvent have to be spread on the subphase. This leads to solvent purity problems, since measurable amounts of contamination can be introduced to the film, even with

Aristar grade solvents. The use of large quantities of solvents is also unpleasant for the LB worker, and potentially hazardous, even when filter masks are worn.

The formation and deposition of films can also be influenced by the pH of the subphase. It is sometimes possible to deposit recalcitrant materials simply by buffering the subphase. If the subphase is buffered with metal salts, floating fatty acid monolayers may be converted to their corresponding salts, leading to the formation of more rigid monolayers. This is especially true when salts containing divalent metals ions such as Cd^{2+} and Ba^{2+} are used, since these ions bind neighbouring monovalent carboxylate ions together in the monolayer. The resulting deposited films are found to have vertically oriented aliphatic chains, unlike films of the free acids, which have tilted chains [*Petty (1996)*].

Once a film is formed, the deposition is dependent on the isotherm of the material; deposition is usually easiest while the film is in the liquid-condensed phase and hence is not too rigid. The optimum surface pressure for deposition with thus vary from material to material, and also on the subphase temperature; rigid monolayers can often be deposited more smoothly at slightly elevated temperatures.

The dynamic treatment of the film on the subphase can also be important; rapid compression can cause non-equilibrium pressures within the film, leading to premature collapse and defect formation. For other materials, which are more soluble in water, long compression times lead to appreciable loss of material to the subphase. This can be observed by compressing the film to a given constant surface pressure and monitoring the film area as a function of time. Good LB materials form a stable film of reasonably constant area, whilst poorer materials rapidly collapse and dissolve into the subphase. More monolayers that are viscous need time to relax after compression, and it is a good idea to include pauses before and after substrate immersion to allow this. This also allows the meniscus to drain from the substrate, resulting in more complete deposition.

The speed of deposition is also highly critical, the more slowly this is done, the higher quality the resulting film. The upstroke is more critical than the downstroke in this respect, because of the need for water to drain from substrate. Exotic molecules tend to aggregate on the subphase, are less mobile and thus require slower deposition anyway. It is possible to deposit films as

slowly as 0.05mms^{-1} with the current arrangement, though with usual dip lengths of 20mm the dip time is prohibitively long for the deposition of much more than the initial bilayer.

Significant problems were encountered when slow layer transfer was required for satisfactory LB deposition onto deep grating structures. Exposed silver surfaces were found to tarnish sufficiently during the course of the deposition that subsequent deposition was impossible due to the partial wetting that resulted. Such samples had to be discarded, since complete data sets could not then be acquired. This was extremely galling, since weeks of preparatory fabrication and characterisation work were thus wasted. This will be discussed in detail in chapter 7.

Some photosensitive materials have to be deposited in the dark, as if there were not problems enough. The use of these materials is not recommended.

4.6 Fluorescent LB monolayers

Now that a method of spacing dye molecules nanometres away from a metal mirror has been outlined, half of the sample fabrication task has been completed. It only remains to specify a suitable fluorescent dye material to deposit on top of such a structure. The properties required of this dyestuff will now be discussed in order of importance to discover what guided the choice of the material eventually selected.

4.6.1 Required dye properties

The pre-eminent consideration was that the dye should have a high quantum efficiency, that is, an excited dye molecule should preferentially decay by a radiative process, rather than a non-radiative process. The reason for this is that while the total SpE rate of the molecule depends on both the radiative and non-radiative decay rates, the inhibition and enhancement effects

considered in this thesis affect *only* the radiative rate. The largest possible change in the SpE rate for a given geometry will thus occur for a dye with small non-radiative loss, and hence high quantum efficiency.

An equally important characteristic was that the fluorescent emission from the dye should be as monochromatic as possible. The reasons for this were two-fold. In the first place, non-monochromaticity implies that the excited state of the dye molecule can radiatively decay *via* a number of different routes. If the probability of decay by each pathway is comparable, then the emission from *all* of these pathways must be altered in order to achieve a noticeable change in the spontaneous emission rate. If only one is inhibited for example, the total change in emission rate will only be a fraction of that achievable if all were to be controlled. A monochromatic emitter will allow thus allow the greatest control to be exerted over the decay process, and in the simplest fashion. A corollary of this is that even if an effect is observed with a polychromatic emitter, it will be the net result of the individual effects on each of the possible radiative decay channels. Since these will all be affected in different ways, the analysis and interpretation of the results will be considerably more complex than if a single wavelength were involved.

This situation is most easily visualised by considering a dye molecule in front of a mirror. Neglecting near-field effects, such as coupling to SPPs, the mirror can be replaced by an image dipole, the fields of which interfere with the real dipole field to either inhibit or enhance the dipole emission. If the dye emits light with different wavelengths, different image dipoles need to be considered. The phase difference of each image dipole, and hence the interference, will depend on which wavelength is considered. The total SpE rate change will thus be a weighted average of the rate change for each of the individual image dipoles.

It is also desirable that the dye molecules do not interact with one another in order to further simplify the system. If, for example, energy could be transferred from one molecule to another non-radiatively, the SpE rate would be significantly increased, especially for molecules in close proximity, which is certainly true for monolayer films [*Dexter (1953)*]. Excitation energy could also migrate through the monolayer until trapped at lower energy sites, where it would become localised. The behaviour of these sites would differ from other

molecules, leading to the existence of alternate decay mechanisms. These processes all complicate the decay dynamics of the system, and would possibly obscure any inhibition/enhancement effects due to the presence of mirror interfaces. Non-radiative energy transfer (Förster transfer) between dye monolayers is a significant field of study in its own right, and has been extensively researched by Kuhn and co-workers [*Möbius (1990)*]. In practise, the possibility of interaction can be minimised by choosing emitters which have a small absorption cross-section at the emission wavelength. This raises questions about the possible ways to excite such an emitter. One answer is to use a three level scheme, consisting of the two energy levels of the optical transition, together with a higher energy level which non-radiatively relaxes to the upper level of the transition. Pumping the upper level, which is chosen to have a large absorption, then populates the upper level of the desired transition by internal relaxation.

The requirements given above are totally general and would be desirable for any proposed experiment involving SpE rate alteration. In addition to these, there are a number of further restrictions which are purely relevant to this study.

The SpE rate of an emitter is most easily and unambiguously determined by measuring the lifetime of the excited state of the emission (the spectral width of the emission will also give an indication of the rate). Most fluorescent emission from dye molecules is the result of electric dipole transitions, and the resulting lifetimes are very short, typically of the order of a few nanoseconds. This is certainly the case for most organic materials used as laser dyes. It is not trivial to measure such lifetimes experimentally and sophisticated signal recovery techniques, such as time-correlated single photon counting, are required. This was not possible with current equipment, but lifetimes in the millisecond range *were* long enough to be measured.

A final consideration in view of the proposed sample fabrication technique was that the dye must be capable of LB deposition, and thus suitable for incorporation as a monolayer within an LB film structure. This is vital to achieve the required resolution in terms of dipole position with respect to a mirror interface.

4.6.2 Choice of fluorophore

Because of the need for an excited state lifetime in the millisecond range, the choice of emitter was effectively restricted to the trivalent metal ions of the lanthanide group, which have metastable excited states with lifetimes of a few hundred microseconds. These extraordinarily long lifetimes are the result of the *weakly allowed* nature of the electric dipole transitions that these ions exhibit. These *f-f* electronic transitions are, strictly speaking, parity forbidden, but mixing of the $4f^n$ electronic states with higher-lying $4f^{n-1}5d$ states of opposite parity means that the relevant matrix elements are non-zero [Imbusch and Kopelman (1981)]. There is an additional advantage besides the long lifetimes, which is that the trivalent lanthanide ions all have extremely sharp line spectra, which is unusual for solid materials at room temperature. The origin of this phenomenon is that the optical transitions involve the $4f$ electrons, which occupy inner orbits and are inevitably well shielded from external influences by electrons in the $5s$ and $5p$ orbitals. The spectra of these ions are thus largely independent of the host material, and they find wide application as phosphors (the red emission from cathode ray tubes is due to Eu^{3+} luminescence), and in optical fibre amplifiers.

Of all of the lanthanides, only europium and terbium have simple energy level schemes with transitions in the visible (most of the lanthanides have transitions in the infrared, notably erbium and neodymium). Terbium ions (Tb^{3+}) have four main transitions in the visible, at $\lambda=490, 545, 570$ and 620nm , all originating from the 5D_4 level, and of similar intensity. This is unacceptable for the reasons given in section 4.5.1 and so Tb^{3+} is unsuitable for use. Europium ions (Eu^{3+}) on the other hand have only two significant transitions in the visible, at $\lambda=590$ and 614nm . Both transitions result from the de-excitation of the 5D_0 level, but the $\lambda=614\text{nm}$ electric dipole transition ($^5D_0-^7F_2$) accounts for 90% of the emission, with the $\lambda=590\text{nm}$ magnetic dipole transition ($^5D_0-^7F_1$) counting for only 8%. The remaining 2% is composed of transitions to other levels in the ground state manifold.

The emission from Eu^{3+} is thus highly monochromatic and the ion is an ideal choice for the emitter, especially since the $\lambda=614\text{nm}$ transition has a

linewidth of $\sim 2\text{nm}$, and is almost completely of electric dipole nature. It only remains to find a way to incorporate the ion into an LB film structure. This was achieved by the chelation of the ion with β -diketonate organic ligands to form the europium complex depicted in *figure 4.9*. The resulting molecule was large enough not to be soluble in water, especially with the addition of the long chain aliphatic counterion, which was included to ensure LB deposition. The ligands were chosen specifically to act as optical “antennae” for the Eu^{3+} ion. The absorption cross-section of the ion at $\lambda=614\text{nm}$ is tiny, which ensures that the ions do not interact, but makes the ion hard to pump directly. The four dibenzoylmethane (or 1,3-diphenyl-1,3-propanedione) ligands, on the other hand, possess highly conjugated π -bridges which readily absorb UV light, exciting the molecules to the singlet state at about 21000cm^{-1} . Since these ligands are in close proximity to the Eu^{3+} ions (they are separated by about 2nm) this excitation energy is rapidly and efficiently transferred to the 5D_0 level of the Eu^{3+} , thus populating the relevant excited state for the 614nm transition. This non-radiative transfer occurs from the triplet state of the ligand within a few nanoseconds of the initial ligand excitation. This time is short in comparison with the lifetime of the Eu^{3+} , and to all intents and purposes, the transfer can be assumed to be virtually instantaneous.

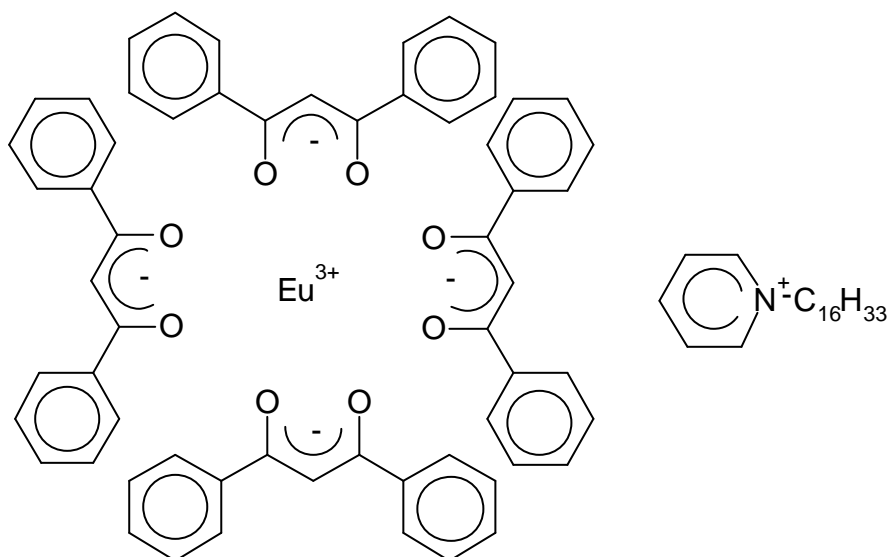


Figure 4.9 The europium complex, N-hexadecyl pyridinium tetrakis (1,3-diphenyl-1,3-propanedionato) europium (III).

The ligand cage also provides a symmetric “cage” for the central ion; previous workers encountered problems with the use of unsymmetrical ligands such as 1-methyl-3-phenylpropan-1,3-dione. The resulting complex was found to exhibit non-exponential fluorescence decays; this was attributed to the different isomers of the complex providing non-identical sites for the Eu^{3+} ion. This led to the development and initial synthesis of the present molecule by R.M. Amos [Amos (1997)]. A very similar complex was used by Drexhage, the sole difference being that the aliphatic chain of the counterion was two CH_2 groups longer than the one used here [Drexhage (1974)].

4.6.3 Synthesis of the Eu^{3+} complex

Initially, attempts were made to obtain the complex from commercial suppliers. This was not possible, and the material had to be synthesised in-house. The initial batches were made by a co-worker, R Amos, but the material was found to degrade significantly over a period of a few months if not stored in a light and oxygen free atmosphere. This necessitated the synthesis of a new batch by the present author.

The synthesis followed the general method of *Melby et al. (1964)*, adapted to include a long chain pyridine group, and proceeded in the following manner. Unless otherwise noted, all chemicals were obtained from the Aldrich Chemical Co., with the highest available purity.

Initially, 2mmol (0.73g) of europium (III) chloride hexahydrate (99.99%) was dissolved in 10ml of deionised water to form a clear aqueous solution. 8mmol (1.79g) of dibenzoylmethane (98%) and 2mmol (0.72g) of N-hexadecyl pyridinium chloride monohydrate (98%) were then added to 70ml of absolute ethanol (99.7%) and gently heated on an electrical hot-plate until all of the solute had dissolved. At this point, the solution was removed from the heat and 8ml of 1M sodium hydroxide (99%) was added drop-wise whilst stirring slowly. As this occurred, the solution became yellow in hue due to the reduction of the dibenzoylmethane by the alkali. When this was complete, the europium chloride solution was slowly added drop-wise to the ethanol solution. An off-white precipitate formed immediately, and the solution was agitated to ensure full

mixing of the reactants. The precipitate, being the europium complex, was then recovered by vacuum filtration using a Büchner filter flask and was washed with ethanol followed by deionised water. The resulting yellowish-white powder was dried out by vacuum desiccation and weighed (2.5g) ready for purification.

This was carried out using a re-crystallisation technique. The complex was dissolved in the minimum volume (~5ml) of hot acetone (Aristar grade, Merck), in which it is soluble. Butan-2-one (HPLC grade, Aldrich) was then added drop-wise until precipitation of the complex was indicated by the presence of cloudiness in the solution. Acetone was then added drop-wise to remove this cloudiness, leaving the complex on the point of precipitation. The solution was then left undisturbed in a freezer at -20°C overnight for the complex to slowly crystallise out. The complex was again recovered by vacuum filtration. The re-crystallisation process was repeated twice more, producing 2g of purified complex in total.

A precaution taken during synthesis was that the europium chloride used was of the highest available purity, which may seem anomalous, given the lower purity of the other starting compounds. The reason for this was that the most common impurities in lanthanide salts are other lanthanide ions. These would inevitably be complexed along with the europium, leading to the formation of alternative lanthanide complexes. This is problematic since they would be almost chemically identical to, and thus difficult to separate from the desired europium complex. Since many lanthanides have energy levels resonant with the europium 5D_0 level (Nd^{3+} $^4I_{9/2}-^2G_{7/2}$, for example), it is conceivable that the fluorescence could be quenched by these impurities, leading to complications in analysing emission data. This problem was minimised by the use of extremely pure europium to start with.

The complex was then assayed by elemental analysis, which was carried out by the University Chemistry department. The results, given in *table 4.1*, verified that the purified complex conformed to the expected molecular formula with respect to the carbon, hydrogen and nitrogen content. The melting point of the complex was then measured (256°C), and found to be extremely well defined ($\pm 1.0^{\circ}\text{C}$), which is indicative of a reasonably pure compound.

	C	H	N
% expected	72.09	6.12	1.04
% found	71.31	5.99	0.98

Table 4.1 Results of the elemental analysis carried out on the europium complex.

The purity of the compound was important to establish since the long chain pyridine counterion can easily be replaced by any other cations present during the synthesis. The mostly likely to be included is the Na⁺ ion introduced by the addition of the sodium hydroxide. It has been shown [Amos (1997)] that the sodium substituted complex forms readily under the conditions described above, but has a fluorescence emission lifetime roughly half that of the intended compound. This is obviously not acceptable, but the problem cannot be resolved by the elimination of the sodium hydroxide, since a strong base is required to reduce the ligand. All strong bases necessarily dissociate in solution to form cations, and so purification is the only solution. The sodium-substituted compound was found to be highly soluble in an acetone/butan-2-one mixture, unlike the long-chain pyridine derivative, and so this impurity was removed very effectively by the re-crystallisation process.

The purified complex was subsequently stored in a light-tight box under vacuum to prevent photobleaching or the ingress of moisture.

4.6.4 Properties of the Eu³⁺ complex

It was discovered by co-workers that the europium complex exhibited poor LB-film forming qualities in comparison with the fatty acids mentioned previously. The following discussion is a summary of the work of Amos (1997), who painstakingly investigated the conditions required to achieve successful deposition of the complex. Rigid adherence to the techniques so developed ensured a high degree of success in all subsequent depositions.

If a film of the complex were spread on a water subphase and left in an expanded state, the film area would remain constant for a few hours. If the film

was compressed however, the films were found to be non-stable, and collapsed steadily with time, which was observed as a gradual decrease in the film area. The fact that the uncompressed film was stable indicated that the molecules did not readily dissolve in water, suggesting that the decrease in film area under compression was not due to loss of material to the subphase. A more likely explanation is that molecular aggregation occurs, which is increased by compression of the film. This would explain the modest collapse pressure of 30mNm^{-1} . Deposition from such a compressed film would give rise to extremely inhomogeneous LB films, and the resulting dye layer would not be monomolecular. The resulting distribution of dissimilar dipole sites would lead to non-exponential decay characteristics, and a significant proportion of the emission would be from microcrystallites of the complex. Stable expanded monolayers could be formed at surface pressures ranging from 5 to 10mNm^{-1} , but these films could not be deposited onto a substrate using the standard LB technique because the low surface pressure meant that no material was transferred. The horizontal transfer method described in *section 4.3.3* was implemented instead, and was found to be an extremely effective monolayer deposition technique [Amos (1997)].

The most reproducible results were obtained by the use of a fresh solution of the complex for each batch of LB samples deposited. The emission lifetime of control samples prepared using a day old solution were found to disagree substantially from those of samples prepared while the solution was still fresh. This discrepancy was attributed to the bleaching of the complex whilst in solution.

The formation of defect-free films was found to be critically dependent on the choice of solvent used to spread the film. The best results were obtained from solutions made from a 4:1 mixture of benzene and acetone, which was reported by Drexhage (1974). Typically, 1mg of the complex was dissolved in 4ml of benzene and 1ml of acetone. The solution inevitably had to be ultrasonically agitated for 2 minutes to ensure the complete dissolution of the complex. Monolayers were formed by the deposition of roughly 200nl of solution onto the subphase drop by drop. This was carried out slowly to ensure the complete evaporation of the solvent. The film was then compressed to a surface

pressure of 5mNm^{-1} at a rate of $2\text{cm}^2\text{s}^{-1}$. Whilst maintaining a constant surface pressure, a substrate was then slowly lowered horizontally through the subphase, picking up a monolayer of the expanded film. After the substrate was lifted away from the subphase, the surface pressure fell below 5mNm^{-1} , indicating the loss of material from the floating film. The substrate was then dried in a desiccator before measurements were made. Further samples could then be deposited by expanding the monolayer, adding more material if required, and recompressing the film. Control or “witness” samples were fabricated in this fashion to ensure deposition under similar conditions to the actual samples themselves. Attempts were made to “dip” two samples at the same time, thus ensuring identical conditions (and saving time), but simultaneous sample immersion was difficult to achieve. The floating monolayer was invariably perturbed by the immersion of the first sample, and the resulting deposition onto the second sample was incomplete. With each sample having up to 16 different spacer layer regions, it was important to ensure uniform coverage every time, and so the “dual-dip” technique was abandoned.

Under UV illumination, the fluorescence of a monolayer film of the complex was very strong, the red Eu^{3+} emission being visible even in a partially darkened room. The fluorescence appeared to be of excellent spatial uniformity by eye, indicating even deposition of the complex across the sample. This was confirmed by observation of the sample fluorescence using a microscope; there was no evidence of crystallite formation at x600 magnification and the fluorescence still appeared uniform. Films deposited at higher surface pressures ($\sim 30\text{mNm}^{-1}$) and viewed under similar conditions *did* display evidence of film collapse, as expected. Instead of uniform fluorescence, the emission was highly striated, and many “pinpricks” of bright fluorescence were visible along the striae, indicating that the formation of crystallites had commenced. This film collapse phenomenon has been observed by other workers using a similar europium complex, but they were unable to produce uniform films [Zhang *et al.* (1997)].

Figure 4.10 shows the normalised fluorescence emission spectrum obtained from a monolayer of the Eu^{3+} complex deposited onto a silica slide, pre-coated with 20 layers of 22-tricosenoic acid. Sample excitation was by pulses of UV light from a nitrogen laser ($\lambda=337\text{nm}$, pulse duration 5ns). The

main emission lines of the Eu^{3+} ion at 614nm and 590nm are clearly visible in this spectrum, and the effective monochromaticity of the fluorescence is obvious. Some structure is visible in the peaks, resulting from the crystal-field (Stark) splitting of the relevant ground state. In most cases, however, the instrumental resolution was insufficient to resolve the fine detail.

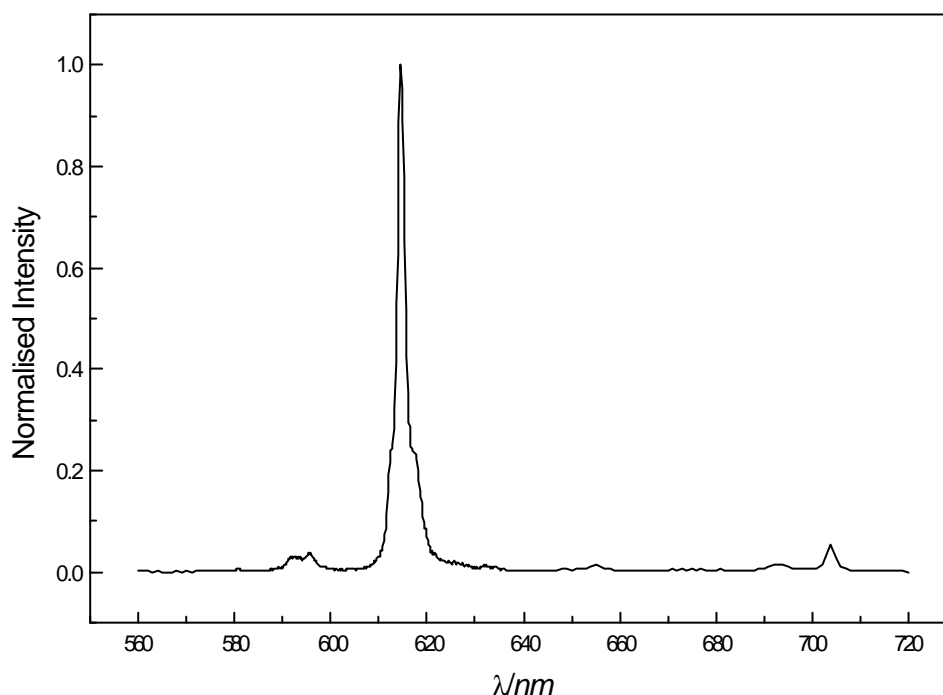


Figure 4.10 The fluorescence emission spectrum of a monolayer of N-hexadecyl pyridinium tetrakis (1,3-diphenyl-1,3-propandionato) europium (III) under UV excitation at 337nm .

Note that the initial deposition of fatty acid layers onto a silica slide was found to help the subsequent formation of a uniform monolayer of the Eu^{3+} complex. (Deposition onto a bare (HMDS treated) slide was occasionally found to result in patchy coverage.) The sample structure mentioned above, that of a silica slide coated with 20 layers of 22-tricosenoic acid followed by a Eu^{3+} complex monolayer, was subsequently adopted as the control geometry. Such control samples were made alongside every regular sample to ensure that reliable europium deposition had occurred.

The time dependence of the 614nm emission from such a sample is presented in *figure 4.11* on a logarithmic scale. This measurement was made by monitoring the time evolution of the fluorescence decay after excitation by a

5ns pulse of UV light; the data presented here was acquired over 200 averaging cycles. The time dependence of this emission is given by a single exponential function with a lifetime of $\tau=0.94ms$, indicating that all of Eu^{3+} ions have an identical excited state lifetime, and thus are situated in identical environments. The lifetime was obtained by fitting the data in *figure 4.11* to a single exponential function using a nonlinear least-squares fitting routine.

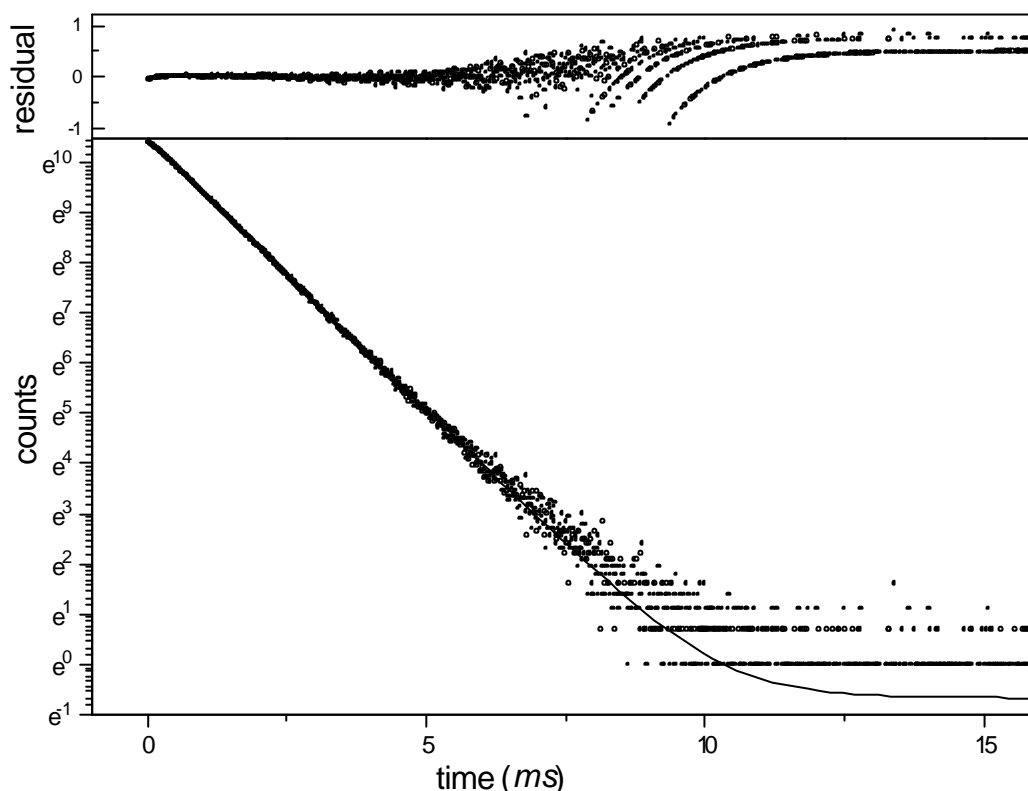


Figure 4.11 The time dependence of the 614nm emission from a monolayer of the europium complex deposited on a control sample. The percentage deviation of the theory from the experimental data (the residual) is plotted above the fluorescent decay with the same time axis.

If the time dependence was found to deviate from a single exponential function, the conclusion drawn must be that non-equivalent Eu^{3+} sites exist within the film; either the film was non-uniform, or the complex was chemically impure to start with. This is extremely important for the experiments described in chapter 6, as discussed below.

One of the aims of this thesis is to show that the fluorescence emission from a dye monolayer above a grating surface is significantly affected by the corrugation of the interface. Dye molecules spaced a set distance away from a planar surface are all located in identical environments, and in the absence of other effects, they should all exhibit the same excited state lifetime. Conversely, dye molecules spaced a set distance away from a grating surface are *not* all in the same environment; the local environment of a molecule above a peak is considerably different from that of a molecule located in a trough. Consequently, one expects that the time dependence of the fluorescence decay measured for a monolayer of dye molecules above a grating should be non-exponential. If the fluorescence decay is non-exponential for a planar surface anyway, for the reasons given above, then it is hard to attribute any subsequent non-exponential behaviour found using a grating sample purely to the corrugation.

The need for a fluorescent monolayer with a single-exponential fluorescence decay when deposited as a planar structure explains the considerable effort taken to first purify, and subsequently prepare uniform monolayer films of the Eu^{3+} complex.

4.7 Summary

In this chapter, the aim of fabricating structures containing fluorescent emitters spaced less than an optical wavelength away from a metal mirror has been discussed. The Langmuir-Blodgett deposition technique has been introduced, and suggested as an ideal fabrication method to achieve this challenging task, which is probably the most difficult aspect of the experimental work contained in this thesis. The method of fabricating LB multilayer structures has been outlined, together with the precautions needed to achieve samples of good optical quality. The qualities required of a fluorescent dye monolayer were also discussed, and a suitable candidate dye was proposed. Details of the synthesis and purification of this material have been given, together with fluorescence data from monolayer films indicating its eminent suitability for the experiments carried out in the following chapters.

Chapter 5

Surface-plasmon energy gaps and photoabsorption

5.1 Introduction

Currently there is much interest in the study of materials which are periodic on the scale of the wavelength of light. These materials exhibit energy gaps for the propagation of electromagnetic modes, in direct analogy with band gaps for electron waves in semiconductor crystals [Yablonovitch (1987), John (1987)]. The absence of available optical modes in these photonic band gaps (PBGs) leads to the inhibition of spontaneous emission for excited species within the crystal whose emission frequency lies within the gap [Yablonovitch (1987)]. Similarly, species which emit at the band edge may exhibit enhanced emission in a photonic material owing to the increased density of modes at the band edge [Tocci *et al.* (1996)]. Most work to date has concentrated on three-dimensional photonic materials which have an energy gap for modes propagating in all directions, but experimental progress has been limited by the difficulty of fabricating structures with sub-micron periodicity suitable for the optical regime. The essential physics, however, remains the same for a periodically modulated surface; instead of inhibiting bulk waves, the propagation of *surface waves* is affected. One such system consists of a metallic grating surface which can support surface-plasmon polaritons (SPPs). For an appropriate surface profile, Bragg scattering of SPP modes from the surface corrugations may open up a band gap in the dispersion curve of the SPP mode. This phenomenon was originally observed by Ritchie *et al.* (1968) and was examined in more detail by Barnes *et al.* (1996).

Recently it has been shown that a band gap prohibiting the propagation of SPPs can affect the emission properties of dye molecules placed on a silver grating [Kitson *et al.* (1995)]. In this chapter, this idea is extended to show how the dye absorption characteristics may be affected in a similar manner. Photons incident on a metallic grating can resonantly excite SPPs. These non-radiative modes are strongly localised at the metal/dielectric interface and have a field that is enhanced by an order of magnitude with respect to the incident radiation [Ræther (1988)]. Dye molecules placed close to the surface experience this enhanced field and consequently absorb more energy from the incident beam (For a weakly absorbing dye layer, the amount of energy absorbed depends linearly on the local field intensity [Drexhage (1974)]). Since the fluorescence intensity is proportional to the amount of energy absorbed, this increased absorption results in correspondingly enhanced emission from the dye molecules when an SPP is excited [Knobloch *et al.* (1993), Kitson *et al.* (1996a)]. The excitation of an SPP resonance effectively increases the coupling efficiency of the pump beam to the dye layer. This phenomenon has been used to enhance many other photochemical processes, for example Raman scattering [Girlando *et al.* (1980)] and photofragmentation [Goncher *et al.* (1984)].

If an energy gap is introduced into the propagation of the SPPs then the absorption spectrum of the system is also substantially modified. Incident photons having frequencies within the band gap are unable to couple to SPPs. There is, therefore, no field enhancement and the absorption and consequent emission are reduced. To optically observe such a gap, the grating profile must contain two harmonic components; the first allows photons to couple to SPPs, while the second component creates the gap by Bragg scattering the SPPs. Suitable choice of the grating pitch ensures that the SPP gap lies within the absorption band of the dye.

In the experiment a metallic grating was spin coated with dye molecules (Sulforhodamine 640) which were pumped using a dye laser tunable through the sulforhodamine absorption band (560-590nm). This allowed the effect of the band gap on the absorption process to be observed by monitoring the dye emission as a function of pump wavelength. By comparing the absorption spectrum of the dye molecules above two metallic grating substrates, one possessing a band gap in the dye absorption band, the other not, it has been

established that the gap has a strong effect on the absorption of energy by the molecules. The results of numerical modelling of the system are also shown, demonstrating how the effect of this photonic band gap may be optimised by adjustment of the grating profile.

5.2 Sample preparation and characterisation

The gratings used in this study were produced by standard holographic techniques and transferred into the silica substrate by fast atom etching in a high vacuum. An optically thick layer of silver ($\sim 100\text{nm}$) was then deposited onto the grating substrate by thermal evaporation. A thin layer of the dye Sulforhodamine 640 was subsequently spin-deposited onto the grating surface from a 10^{-3}M methanol solution at 3500 rpm . Two grating samples were fabricated in this way. The first was chosen to have a pitch of $\sim 550\text{nm}$, and thus possessed an SPP energy gap coincident with the sulforhodamine absorption band (the dye overlayer shifts the gap centre to longer wavelengths). The second grating sample was fabricated with a pitch of 800nm , ensuring that the resulting SPP band gap was well removed from the spectral region of interest. This grating was used as the control sample.

5.2.1 Reflectivity measurements

Characterisation of the grating profiles was achieved by the excitation of SPP modes at the silver-dye interface. These resonances were recorded by measuring the angle-dependent specular reflectivity at 488nm . TM polarised light incident in the plane normal to the grating grooves can resonantly excite SPPs when the angle of the incident beam satisfies the coupling condition of *equation 5.1*.

$$k_0 \sin \theta \pm mG = \pm k_{\text{spp}} \quad (5.1)$$

where k_{spp} is the SPP propagation vector, G is the grating vector ($G = 2\pi/\text{grating pitch}$) and k_0 is the wavevector of the incident beam. This condition simply

matches the momentum of the incident light beam in the plane of the grating with the mode momentum. When the mode is resonantly excited energy is taken from the beam, resulting in a dip in the reflectivity.

Figure 5.1 illustrates the experimental configuration used. The sample was illuminated with laser light modulated by mechanical chopping at around 1 kHz. The polarisation of this incident light could be set to within 0.1° by a Glan-Thompson polariser. To account for variations in the source intensity, a proportion of the incident beam was reflected from a beam-splitter onto a reference detector. The sample itself was fixed to a translation stage mounted on a computer-controlled rotating table. The location of the sample could be adjusted whilst on the table to allow accurate positioning over the centre of rotation. The sample azimuth was also adjustable to within 0.1° to ensure that the grating was in the classical mount (see chapter 3). The signal detector was a 50mm^2 area silicon photodiode mounted on the rotary table in such a manner that it moved at twice the angular velocity of the sample, thus tracking the zeroth order reflection. The detector function of this photodiode was effectively a “top-hat”, so a small amount of beam wander across the face of the detector during a scan had negligible effect. The system was aligned by directing the reflected beam back down the lathe bed through the two apertures, allowing the zero angle to be set to within 0.03° .

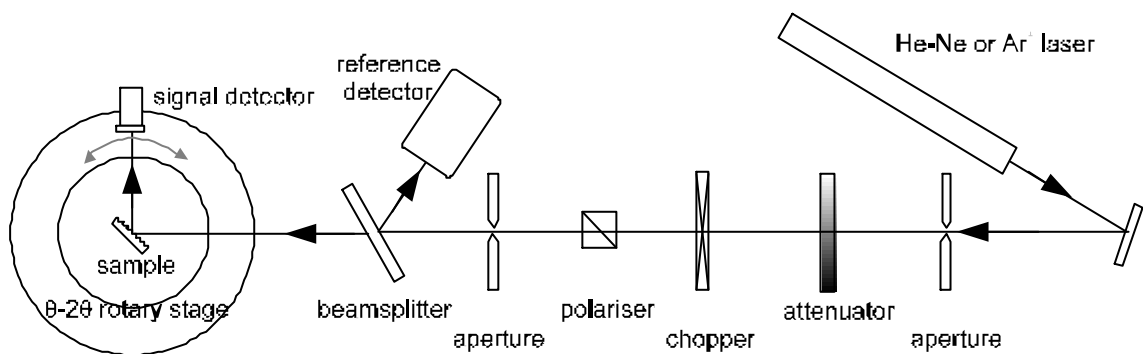


Figure 5.1 The experimental set-up used to measure the angle-dependent reflectivity.

The output from the signal and reference detectors was then fed to two phase-sensitive detectors (PSDs) and the component of the signal modulated

with the chopper frequency recovered. In this way, noise from external sources was filtered out. The PSDs were interfaced with the computer controlling the table, allowing automated data collection. Initially, an unnormalised reflectivity trace was obtained by scanning the angle, and dividing the signal output by the reference output. The angular scan rate was set so that the step time was five times longer than the time constant of the PSDs, which was typically 100ms. This ensured that small variations in the angle-dependent reflectivity were not obscured by the time response of the detection system. The absolute reflectivity was obtained by removing the sample and measuring the intensity of the laser beam directly. Dividing the signal by the reference from this scan gave a normalisation constant, which was then used to correct the unnormalised reflectivity data. The signal to noise ratio for the final data was typically 2000:1 or better.

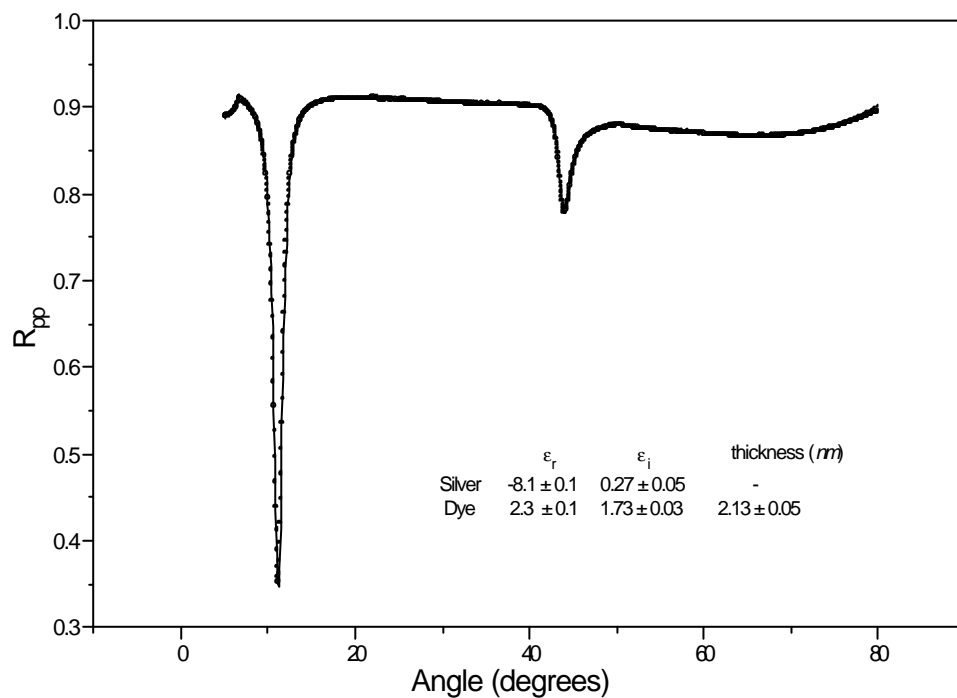


Figure 5.2 Angle-dependent reflectivity of the dye-coated SPP energy gap grating at 488nm for TM polarised incident light. The circles are experimental data and the line is a theoretical fit.

Figure 5.2 shows the angle-dependent reflectivity of the dye-coated and silvered SPP energy gap grating at 488nm. Two resonances can be seen, at

11.05° and 43.95°, which correspond to first-order ($m=-1$) and second-order ($m=+2$) coupling to the SPP mode respectively. By fitting theoretical models of the reflectivity generated by the Chandezon method to the experimental data obtained for the bare silver grating, the silver dielectric constant and grating profile were obtained, which were then held fixed. The dye-coated grating reflectivity data was then fitted using these values by varying the sulforhodamine layer thickness and dielectric constant.

Since the coupling to SPP modes is highly sensitive to the harmonic content of the grating profile, the profile is best represented as a sum of harmonic components [*Wood et al. (1995)*].

$$a(x) = a_0 \sin Gx + a_1 \sin(2Gx + \phi_1) + \dots \quad (5.2)$$

The G component couples incident photons to the non-radiative SPP modes, while the $2G$ component creates the SPP energy gap by Bragg scattering as discussed previously. Fitting the reflectivity data for this grating gave the following parameters, pitch = $550.5 \pm 0.1 \text{ nm}$, $a_0 = 11.7 \pm 0.5 \text{ nm}$, $a_1 = 2.1 \pm 0.1 \text{ nm}$ and $\phi_1 = -\pi/2$. The extra harmonic components in the profile arise from the nonlinear response of the photoresist during exposure, only the first two or three components are generally significant. The phase ϕ_1 is limited to be either $\pm\pi/2$, since the gratings are not blazed and therefore must have a symmetrical profile.

5.3 Experimental

The fluorescence intensity from the sample at a fixed wavelength was recorded as a function of both wavelength and angle of incidence of the pump beam, effectively measuring the angle-resolved excitation spectrum of the system. The experimental set-up used to accomplish this is illustrated schematically in *figure 5.3*. The sample was mounted on a translation stage held above, but not fixed to, a computer-controlled rotary table. The fluorescence was excited by a pump beam incident on the sample via an optical fibre mounted on the rotary table. In this way, the angle of incidence of the pump beam on the sample could be varied without changing the orientation of the sample with respect to the collection optics. This is important since the

dominant decay route for excited dye molecules above a metallic surface is to couple to SPP modes at the interface.

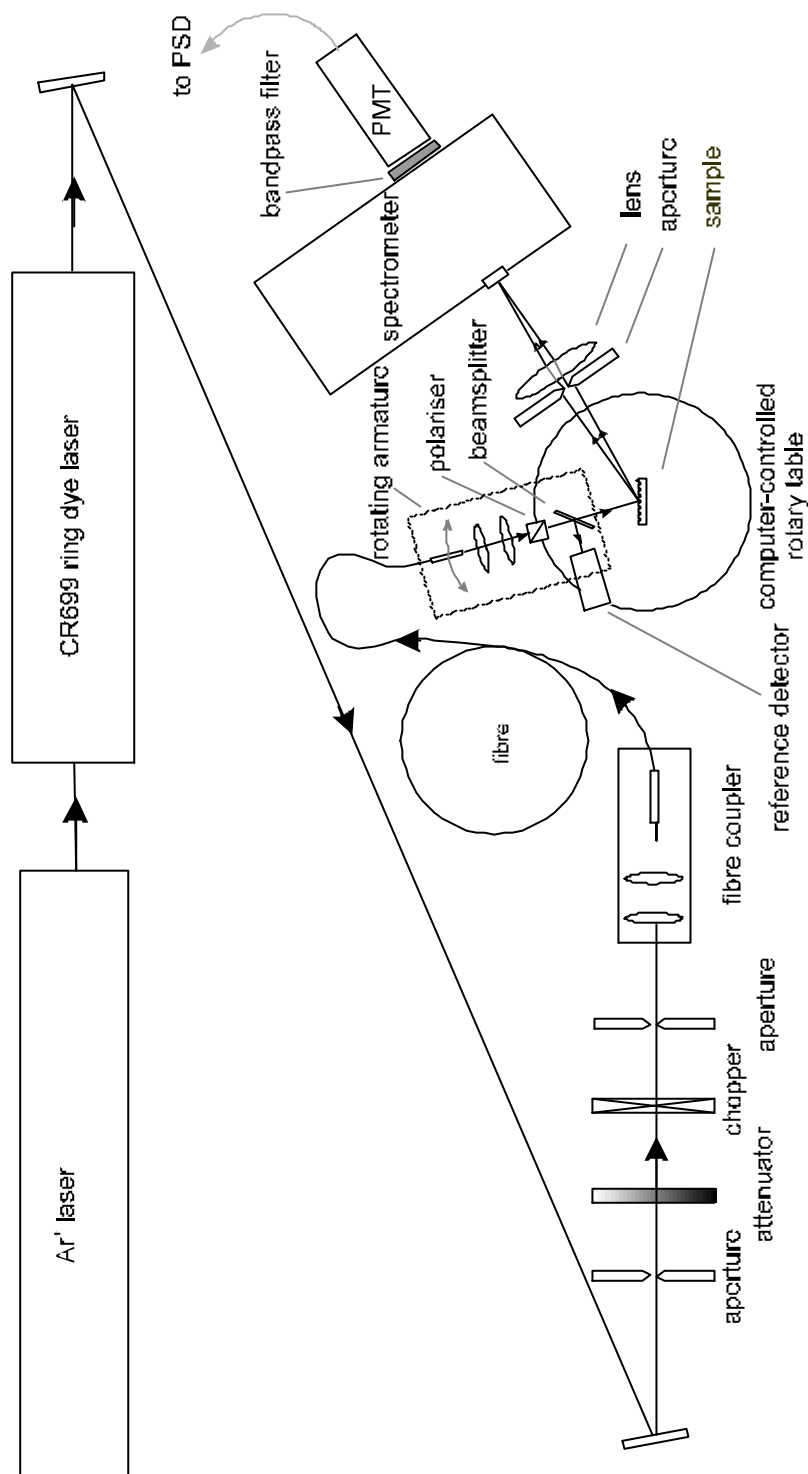


Figure 5.3 The experimental arrangement used to measure the angle-dependent excitation spectrum of the sample.

If the surface is corrugated then these SPP modes can undergo Bragg scattering and couple to photons propagating in directions which satisfy *equation 5.1*, thus conserving in-plane momentum [Kitson *et al.* (1996b)]. The resulting emission from the sample is strongly dependent on angle, hence the importance of maintaining the same orientation between the sample and collection optics.

Fluorescence from the sample was collected using a lens (aperture-limited to a 2° collection angle) and focused onto the entrance slits of a spectrometer set to pass light with a wavelength of 650nm (resolution of $\pm 5\text{nm}$). This emission wavelength was chosen since it is well removed from the dye absorption band and thus collection of stray pump light was minimised. After wavelength selection, the light was detected by a photomultiplier tube at the exit slits of the spectrometer and the signal recovered by phase sensitive techniques. The laser source used was an argon-ion pumped dye laser, tunable from 560nm to 590nm . The beam was mechanically chopped at 800Hz and then coupled into a multimode fibre using a microscope objective lens. The output end of the fibre was mounted on an armature attached to the rotary table. Light from the fibre was collimated by another microscope objective lens and apertured to give a 1mm diameter beam. The polarisation was then set by a Glan-Thompson polariser also mounted on the armature. A beamsplitter was used to take a reference signal so that variation in the laser power could be accounted for. The pump beam was then made incident on the sample over the centre of rotation of the table, thus ensuring that the same point on the sample was excited for all angles of incidence. The angle-resolved excitation spectrum of the sample was then measured by recording the fluorescence emission intensity as a function of both the angle of incidence and wavelength of TM polarised incident light.

5.4 Results

5.4.1 Experimental data

Figure 5.4 shows the angle-resolved excitation spectrum measured for TM polarised light incident in the classical mount on the sample with the gap. If

a cross-section is taken through the plot at a constant wavelength of $\lambda=582\text{nm}$, two peaks occur on either side of the normal to the sample. These correspond to the incident light coupling into SPP modes *via* first order scattering from the grating ($m=\pm 1$ in *equation 5.1*). The dye molecules above the grating experience the enhanced evanescent field associated with the SPP, and hence absorb more energy from the beam giving rise to the increase in emission. As the wavelength of the incident light is decreased (and wavevector consequently increased), the angle at which light couples to the SPP mode decreases since the in-plane momentum must be conserved (*see equation 5.1*).

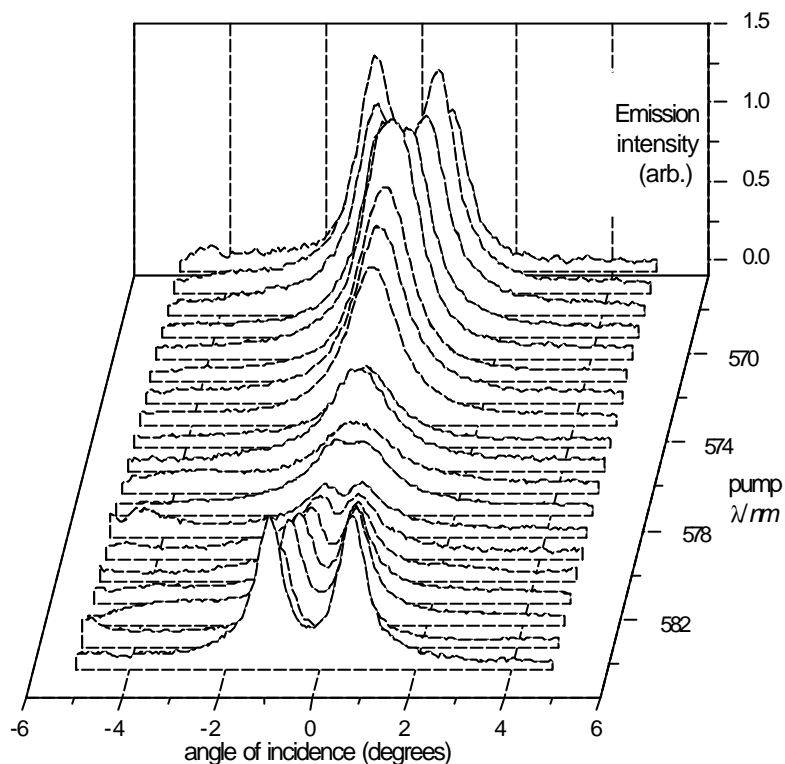


Figure 5.4 Photoluminescence from the dye layer on the SPP energy gap grating as a function of the angle of incidence and wavelength of TM polarised incident light. The luminescence peaks correspond to the excitation of SPP modes by the incident light beam and it can be seen that the emission is considerably enhanced when this condition is met. The peaks effectively trace out the dispersion curve of the SPP modes.

As a result the two peaks move together, crossing at zero degrees when $\lambda=577nm$. At this point, the incident light can couple into counter-propagating SPP modes at the interface. These modes have a wavevector of G and can Bragg scatter from the $2G$ component of the grating profile to set up a standing wave. Two such standing waves are possible, corresponding to different field profiles at the interface, which lead to the formation of a forbidden energy gap as observed by *Ritchie et al. (1968)*. It can be seen that the emission intensity from the dye layer falls abruptly in this wavelength region as the two modes coincide and only recovers as the modes separate again. It is evident that the absorption of the dye layer (given by the area under each curve) is reduced in the energy gap region where there are no SPP modes available to provide the field enhancement.

5.5 Analysis

To see the effect of the SPP energy gap on the absorption spectrum of the sample more clearly, the total emitted power can be plotted as a function of the excitation wavelength. This is achieved by integrating the emission intensity over all incidence angles for a given pump wavelength. This integral will be proportional to the amount of energy the dye absorbs at that wavelength – essentially the absorption coefficient of the system. *Figure 5.5* shows such a spectrum (calculated from the data in *figure 5.4*). To account for the intrinsic dye absorption spectrum, the results have been normalised by dividing by the absorption spectrum obtained from the control sample without a gap in the dye absorption spectrum. In the region of the SPP energy gap, the emission of the dye layer is reduced by a factor of two, corresponding to a reduction in the amount of energy absorbed from the incident beam. This hole “burnt” in the dye absorption spectrum by the gap is centred at $577nm$, and has a width of $10nm$. Note that the absorption does not fall to zero, even at the centre of the gap. On the low wavelength side of the gap there is an increase in the dye absorption, but this is not found on the high wavelength side. To explain these features we consider the nature of the dispersion of the SPP modes involved and the coupling between these modes and incident light.

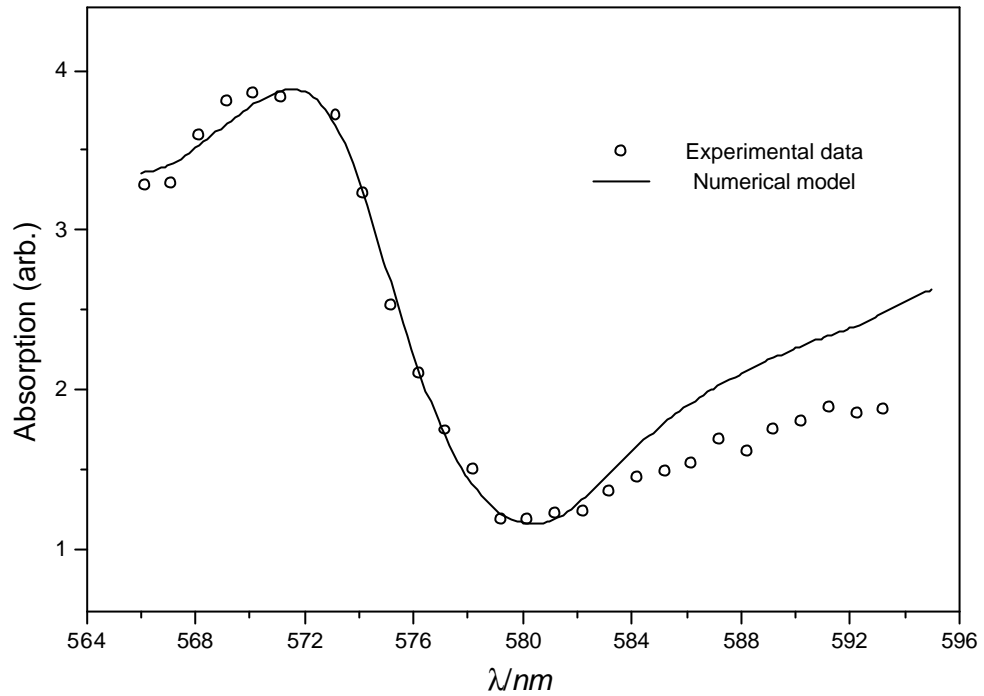


Figure 5.5 Normalised absorption spectrum for the SPP energy gap sample, obtained by integrating the area under each curve in *Figure 5.4* over the full incident angle range. The spectrum was normalised by dividing through by the spectrum obtained from a sample without a gap. The circles are experimental data and the line is the result of numerically modelling the local optical field intensity within the dye layer using fitted parameters for the optical constants and surface profile of the grating structure (see *section 5.5.1*).

In *figure 5.6*, the theoretically generated reflectivity of the sample is plotted as a function of the angle and wavelength of incident light. The model was generated using the Chandezon method and the grating parameters and dye layer thickness determined from the fit in *figure 5.2*. The optical constants of the silver and the dye layer were determined experimentally as a function of wavelength by fitting reflectivity data taken from the control sample. The reflectivity plot in *figure 5.6* is qualitatively very similar to the angle-resolved excitation spectrum of the sample given in *figure 5.4*. The peak emission from the dye layer and the SPP mode positions coincide, and the reflectivity plot shows the existence of an SPP gap, which is replicated in the emission data. The width of the SPP resonance is comparable with the gap width, so even at

the gap centre incident photons can non-resonantly couple to SPPs. This weak coupling means that dye molecules within the gap still experience an enhanced field, resulting in a non-zero absorption within the SPP gap.

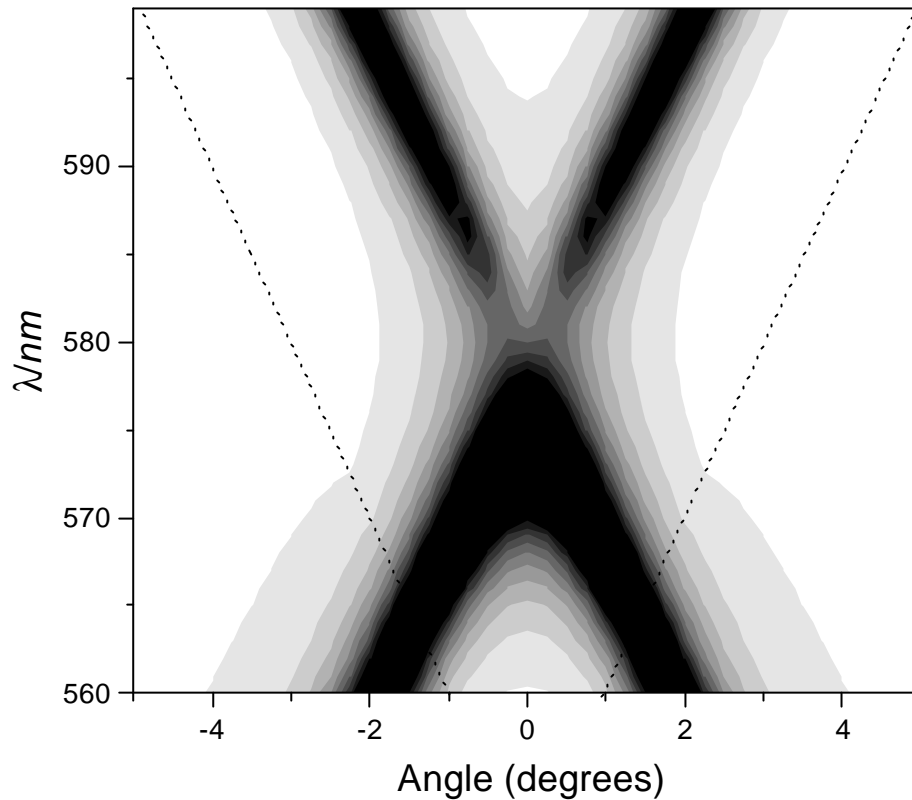


Figure 5.6 Theoretical plot of the reflectivity of the energy gap grating sample as a function of the angle of incidence and wavelength of an incident beam of TM polarised light. The dark regions correspond to low reflectivity and the light regions, high reflectivity. The dotted lines represent the light lines of the first diffracted orders.

From *figure 5.6* it is evident that the coupling strength of incident light to the SPP branches on either side of the gap is different. Incident light is coupled strongly to the lower wavelength branch and weakly to the high wavelength branch. This is a result of the symmetry of the surface and depends on the relative phase between the fundamental and first harmonic components of the profile, a phenomenon also seen by *Weber and Mills (1986)*. This coupling strength difference is important since the SPP branches above and below a gap are flattened at the band edge. This means that the number of available SPP

modes per unit energy interval is large and so the resultant SPP-dye interaction is proportionally greater when incident light is coupled in at these band edges. Thus for the low wavelength band edge, where coupling is permitted, an increase in the absorption of the system is seen, corresponding to the increased coupling which results from the greater number of SPP modes. Conversely, on the high wavelength side of the gap, the absorption is smaller since although the SPP mode density is large, the incident light is not coupled to these modes.

The dependence of the enhanced SPP-dye molecule coupling on the nature of the SPP dispersion curve can be seen very clearly by plotting the mode dispersion on the same axes as the measured absorption spectrum. *Figure 5.7* shows the absorption spectrum of the energy gap sample together with the dispersion curve obtained from the scattered emission peak positions. The dip in the absorption spectrum coincides well with the gap in the SPP dispersion, whilst the low wavelength absorption peak tallies well with the flattened lower wavelength band edge. On the high wavelength side of the gap, the lack of coupling to the band edge SPPs means that the absorption of the system is small.

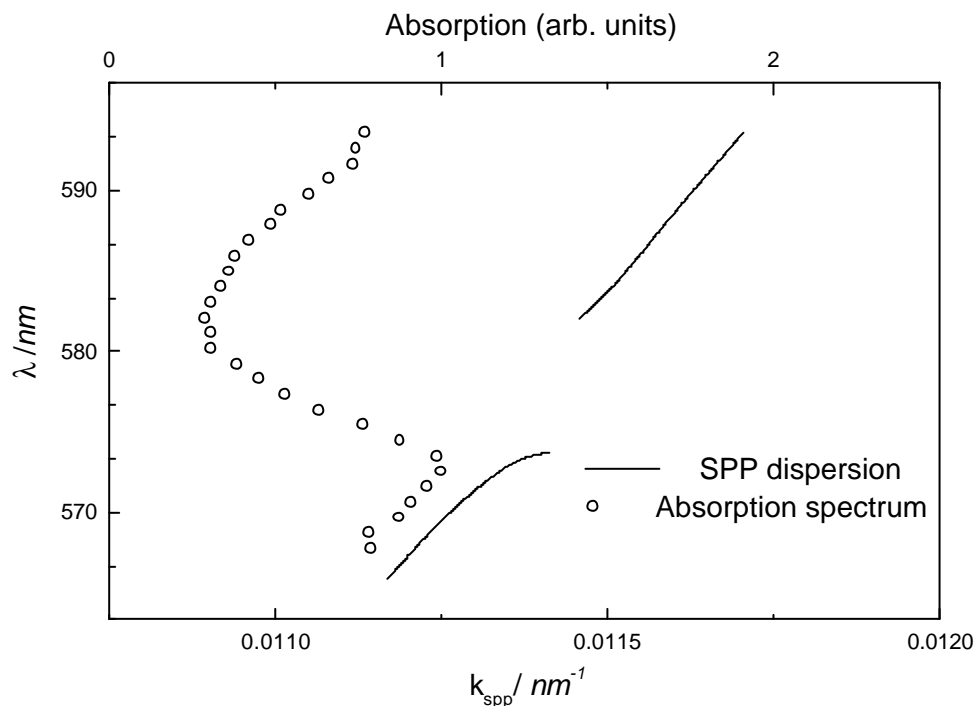


Figure 5.7 The absorption spectrum and SPP dispersion of the energy gap sample plotted on the same axes. The influence of the gap can be clearly seen.

The corresponding data for the control sample is given in *figure 5.8*. As expected, the dispersion curve is continuous, and has no gap feature. Correspondingly, the absorption spectrum is flat, except for a slight rise at long wavelengths. This is due to the intrinsic absorption spectrum of the sulforhodamine dye itself (The spectral region considered here lies on the shoulder of a stronger absorption peak, which has a maximum at about 610nm.)

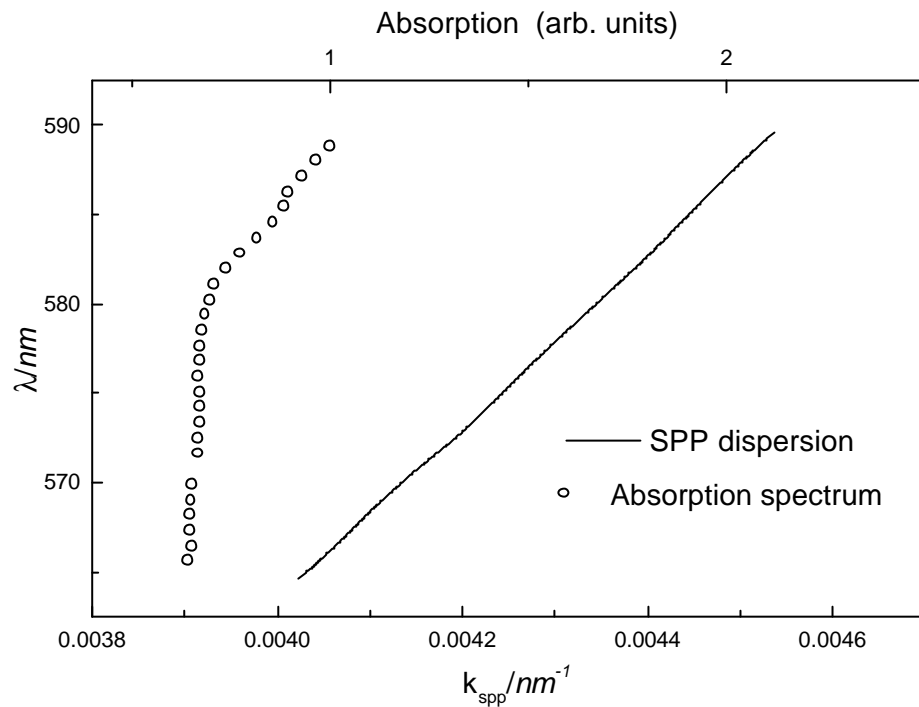


Figure 5.8 The absorption spectrum and SPP dispersion of the control sample plotted on the same axes. The dispersion curve is continuous, and there is correspondingly no gap in the absorption spectrum.

5.5.1 Theoretical modelling

The line in *figure 5.5* is the result of numerical modelling of the response of the system based on the Chandezon method using the grating parameters, dye layer thickness and dielectric constants obtained previously. The agreement between the two curves is fairly good, with the theory replicating all the features found in the experimental data. Including the dispersion of the dye layer in the calculation may help reduce the discrepancy found for the longer wavelength data.

It is possible to model the effect of the SPP energy gap on the (enhanced) absorption of this system because both the enhancement and the gap can be described in terms of the local electric field intensity above the grating surface. The absorption and consequent emission from the dye layer is linearly related to the local electric field intensity within the layer, and will be given by the following relation,

$$I_{fl}(\lambda_{in}, \theta_{in}) = \alpha(\lambda_{in}) |\mathbf{E}_{loc}(\lambda_{in}, \theta_{in})|^2 \beta(\lambda_{fl}, \theta_{out}) \quad (5.3)$$

where I_{fl} is the emission intensity for a given angle and wavelength of incident light, α is the intrinsic absorption spectrum of the dye, $|\mathbf{E}_{loc}|^2$ is the local electric field intensity, and β is a factor which includes both the emission spectrum of the dye and also the angular radiation pattern of the emitted fluorescence; the latter being influenced by the grating profile. If the spectrum obtained for the sample with a gap is normalised as discussed above, then the following result is obtained (where I''_{fl} , \mathbf{E}''_{loc} refer to the gap sample, I'_{fl} , \mathbf{E}'_{loc} the control sample)

$$\frac{I''_{fl}}{I'_{fl}} = \frac{|\mathbf{E}''_{loc}|^2}{|\mathbf{E}'_{loc}|^2}. \quad (5.4)$$

This expression allows a direct comparison between the experimental results and theory since knowledge of the factors α and β is no longer required. (*equation 5.4* includes the assumption that the factor β is the same for both grating samples, but since the emission intensity was recorded for a fixed emission wavelength and angle range, even if β does vary, it will only introduce a scaling factor into the expression.) The quantity on the left can be obtained experimentally, whilst the right hand side is simply a ratio of field intensities which can be calculated.

The fields within a corrugated multilayer system can be modelled using the Chandezon method, which was discussed in chapter 3. There is an additional complication in that the electric field intensity within the dye layer varies across the grating groove as well as with distance away from the metal. In order to account for this variation, the field intensity was calculated for each point lying on a ten-by-ten grid which extended length-wise across a groove and

vertically up through the dye layer. These values were then averaged to give the mean electric field intensity within the dye layer for a given angle of incidence of light. The angle dependence of this mean field intensity then correlates with the measured emission from the system, as shown by *Kitson et al. (1996a)*. If both sides of *equation 5.4* are integrated over the incident angle range, the normalised absorption spectrum is obtained and the form of the experimentally determined absorption gap can be compared to a theoretical model, as shown in *figure 5.5*.

Whilst the agreement between theory and experiment in this figure is fairly good, the discrepancy at longer wavelengths is quite considerable. A possible explanation is that the dye absorption spectrum affects the emission of the system in a two-fold manner. The term $\alpha(\lambda)$ in *equation 5.3* accounts for the intrinsic absorption of the dye, but any change in dielectric constants of the dye layer with wavelength will affect the dispersion of the SPP modes also. The increase in dye absorption with wavelength (see *figure 5.8*) will broaden the SPP modes, leading to a smaller measured enhancement. This effect is *not* taken into account in the model unless the dispersion is included in the calculation of the local field intensities. If this were done, the present overestimation of the enhanced absorption would be decreased, bringing the model into line with the experimental results.

The development of this model means that it is now possible to systematically investigate how the response of the system depends on the surface profile, allowing the optimisation of the gap size and depth.

5.5.2 Gap optimisation

To optimise the absorption gap introduced into the response of the system, consideration must be paid to the mechanism which generates the gap. The absorption of the system must first be enhanced, and the features of the grating profile which affect this enhancement have been discussed in detail by *Kitson et al. (1996a)*. The greatest enhanced absorption was obtained for thin dye layers with thickness $d \sim 2nm$, deposited on gratings with a fundamental harmonic amplitude, a_0 of $\sim 20nm$. In brief, the dye layer must be as thin as

possible to minimise the damping of the SPP modes by the highly absorbing dye and there is an optimum fundamental grating amplitude which maximises the coupling between incident light and the SPP modes. In the subsequent modelling the optimum parameters, $a_0=20nm$ and $d=2nm$ were used. Consideration must also be given to those parameters which directly affect the gap. Since the gap arises because of the Bragg reflection of the SPP modes from the 2G component of the grating profile, the amplitude a_1 of this component will play a key part in determining the width and depth of the gap. The relative phase ϕ_1 of this component with respect to the fundamental is also important, determining the coupling between incident light and the SPP modes on either side of the gap. Since the dye layer thickness affects the damping of the SPP modes, it too plays a part in determining the form of the gap, increasing layer thickness both broadening and shallowing the feature. The modelling presented here is restricted to variation of these three most significant parameters, (a_1 , ϕ_1 and d).

Figure 5.9 shows the normalised absorption spectra obtained by varying the amplitude of the 2G component of a $550nm$ pitch grating, whilst keeping the fundamental amplitude fixed at $20nm$ with a dye overlayer of thickness $2nm$. For this case the phase between the fundamental and the 2G component is zero. It can be seen that as the amplitude of the second harmonic increases, the gap feature increases both in depth and in width. The absorption at the high- and low- wavelength sides of the gap also increases due to the increased flattening of the SPP bands as discussed previously. The asymmetry in the band edge absorption is due to coupling between the SPP modes and the first order diffracted beams. The dotted lines in *figure 5.6* show the light lines for the first order diffracted beams, points on these lines correspond to diffracted photons grazing across the surface of the grating. Points lying below the line (lower wavelengths) correspond to diffracted beams propagating at less than grazing angles, whilst those above correspond to evanescent beams which do not propagate. Those parts of the SPP dispersion curve which lie beneath the light lines can couple to the diffracted beams and this provides a strong radiative damping mechanism.

When the dispersion curve crosses these light lines, the diffracted beams become evanescent and the SPP modes can no longer couple to them, thus removing the damping mechanism. The result is that for shorter wavelengths (below about 565nm) there is an additional decay channel for the SPP modes, which reduces the field enhancement, and therefore the absorption of energy by the dye molecules. This explains the sharp fall in absorption on the low wavelength side of the gap. Note that even when the second harmonic is zero there is still a slight decrease in the absorption which is a result of scattering twice from the fundamental harmonic component of the grating. Since this is a second order process however, the resultant feature is smaller than those which result from the second harmonic itself. Simply increasing the fundamental amplitude a_0 does not increase the gap depth, since the increased scattering means that the SPP modes on either side of the gap become overcoupled and hence broadened. This results in the overlap of the wings of the high and low energy SPP branches in the gap region, which allows slightly enhanced coupling to the dye molecules, even in the gap itself.

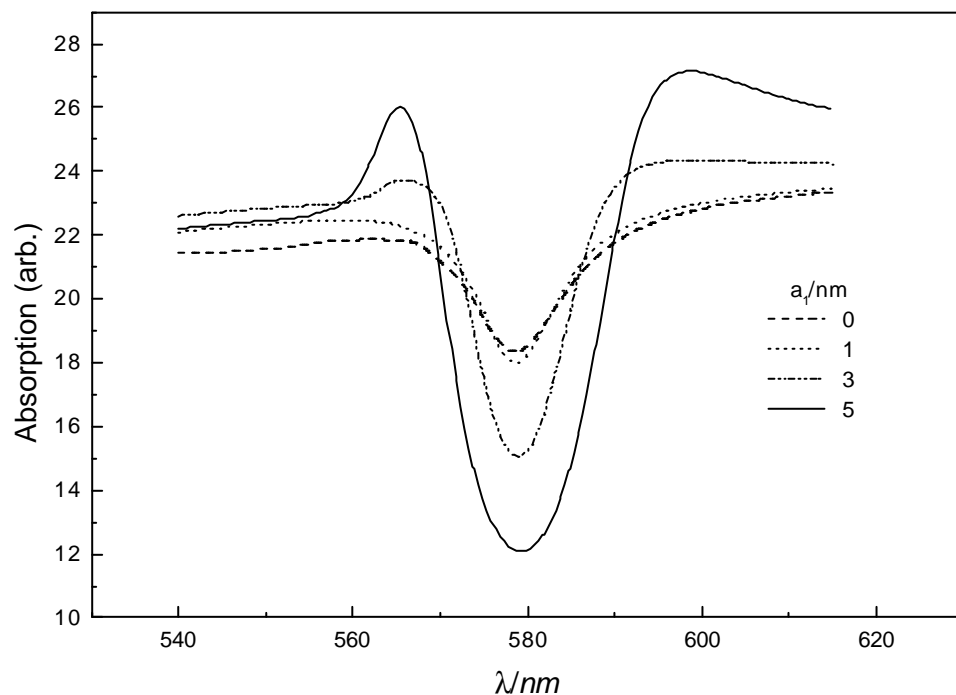


Figure 5.9 Numerical modelling to show the effect of increasing the amplitude of the second harmonic component of the grating profile on the normalised absorption spectrum of a dye coated grating ($\lambda_g=550\text{nm}$, $a_0=20\text{nm}$, $\phi_1=0$, $d=2\text{nm}$).

By varying the phase of the second harmonic with respect to the fundamental it is possible to alter the coupling between incident light and the SPP branches on either side of the gap. *Figure 5.10* shows the modelled normalised absorption spectra for a 550nm pitch grating with fundamental harmonic component of 20nm and a second harmonic of 5nm for phases of 0° and $\pm\pi/2$. These were chosen since they correspond to optimum coupling to the SPP branches on either side of the gap. When the harmonics are in phase, light can couple to the flattened SPP branches on both sides of the gap. If the phase is changed to $-\pi/2$ then we can only couple to the low wavelength SPP branch, whilst if we have a phase of $+\pi/2$ we can only couple to the high wavelength SPP branch. By comparison with *figure 5.5*, it is clear that the experimental sample has a phase difference of $-\pi/2$, which agrees with the fitted parameters for the sample.

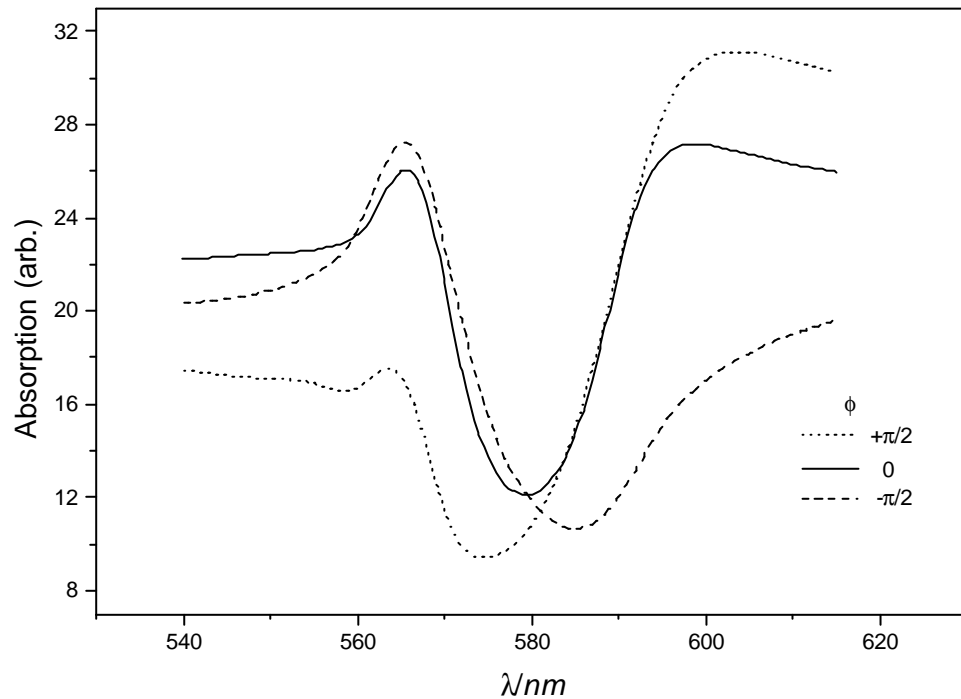


Figure 5.10 Numerical modelling to show the effect of varying the phase of the second harmonic of the grating profile with respect to the fundamental on the normalised absorption spectrum of a dye-coated grating ($\lambda_g=550\text{nm}$, $a_0=20\text{nm}$, $a_1=5\text{nm}$, $d=2\text{nm}$).

The reason for the difference in coupling strength for the two situations arises from the differing roles of the two components of the grating profile. Bragg scattering of SPP modes by the second harmonic component of the grating profile creates the energy gap. The surface charge distributions for the SPP branches on either side of the gap observed at normal incidence are thus standing waves with maxima at the peaks or troughs of this component. The coupling to these modes, however, is governed by the fundamental component of the profile. For incident light to couple to these modes, there must be a component of the optical electric field normal to the fundamental harmonic in the surface profile at the appropriate points to excite surface charge. By varying the position of these two components relative to one another, charge can be thus be selectively excited at either the peaks or the troughs of the second harmonic component, allowing coupling to either the high or low wavelength SPP branch respectively.

The final parameter which can be controlled is the thickness of the dye layer. This is important since the most absorbing part of the system is the dye layer, and it strongly damps the SPP modes resulting in both a reduction in the field enhancement, and a broadening and shallowing of the gap feature. *Figure 5.11* shows how the normalised absorption spectrum of the dye layer on a 550nm pitch grating varies as a function of the thickness of the dye layer. As before, the grating has a fundamental amplitude of 20nm and an in-phase second harmonic amplitude of 5nm . As the dye layer thickness is increased and the field enhancement diminished, it is found that the absorption of the system in general decreases. The absorption gap feature both broadens and shallows as the increased damping increases the width of the SPP modes. Since the evanescent field of the SPP mode is confined within the dye layer more completely as the layer thickness increases, the mode is more sensitive to the refractive index of that layer.

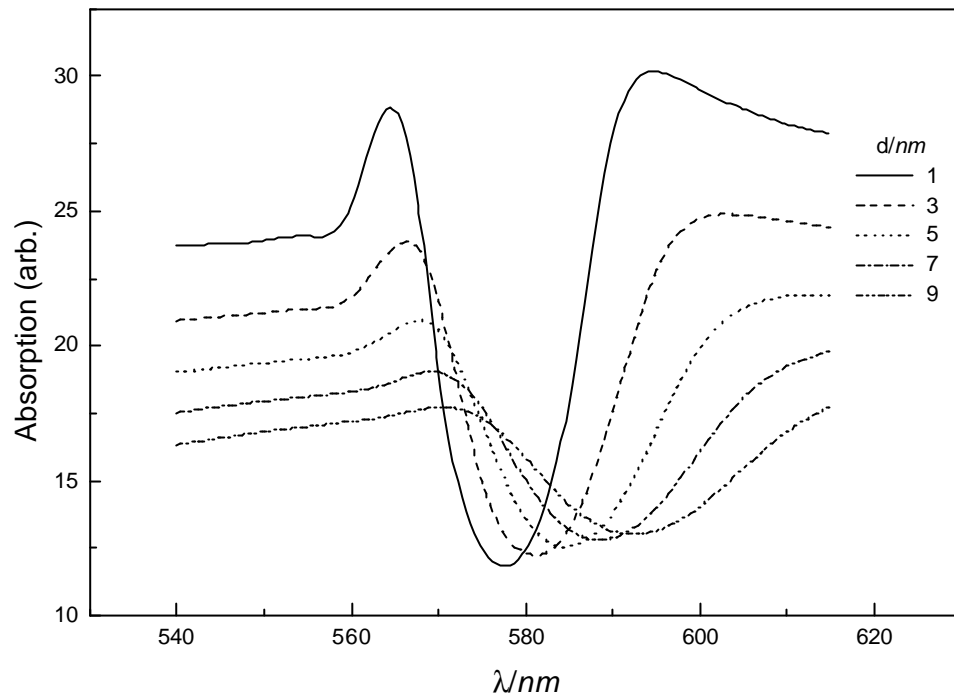


Figure 5.11 Numerical modelling to show the effect of varying the dye layer thickness on the normalised absorption spectrum of a dye-coated grating. ($\lambda_g=550nm$, $a_0=20nm$, $a_1=5nm$, $\phi_1=0$)

As a consequence, the centre of the gap moves to higher wavelengths (the index of the layer is greater than that of air). It is obvious that to obtain a sharp gap feature the dye layer must be as thin as is possible. The actual thickness used will obviously be a compromise between the gap width needed, and the increase in signal possible by the deposition of a thicker layer of dye material.

5.6 Summary

In this chapter, it has been shown how an SPP energy gap affects the absorption of dye molecules close to a metal grating. The absorption properties of a dye layer placed in close proximity to a metallic surface are strongly enhanced by the coupling between the incident light and the SPP modes of the interface. Introduction of an energy gap into the propagation of these modes removes the enhancement, thereby reducing the absorption of the system.

Experimentally, a factor of two decrease in the absorption of such a system has been measured for wavelengths corresponding to the SPP energy gap region. Conversely, a slight increase in the absorption was measured for excitation at the SPP band edge, where the SPP mode density is greater. By numerically modelling the system using an application of the Chandezon method, good agreement has been found between experiment and theory. This allowed the investigation of the effect of varying the profile of the grating on the SPP energy gap, thus demonstrating how control of the available SPP mode density can be used to influence the absorption spectrum of the system. Suitable choice of the grating profile allows both the depth and width of the gap to be altered, and the coupling to the band edge SPP branches can also be determined. The enhanced absorption of the dye molecules, mediated by the SPP-dye molecule coupling, can thus be either removed, or improved further.

In the following chapter, the emission characteristics of dye molecules above planar mirrors will be considered, as a prelude to the investigation of emission above gratings.

Chapter 6

Fluorescence above a planar mirror

6.1 Introduction

The spontaneous emission (SpE) rate of an emitter is not a fixed quantity, but instead depends on the local electromagnetic mode density, a point first noted by *Purcell (1946)*. The electromagnetic mode density can be most easily affected by modifying the boundary conditions for the electromagnetic field in the vicinity of the emitter. The electromagnetic modes to which the emitter can couple are thus altered, causing a change in the emission rate of the species. The simplest possible boundary condition that can be imposed on an electromagnetic field is that of a plane mirror, and it was this geometry that was adopted in the first experimental demonstration of decay rate modification. This was achieved by *Drexhage (1974)*, who studied the time-dependent emission of fluorescent dye molecules located within a wavelength of a planar metallic mirror.

To study the effect of *corrugating* the mirror interface on the emission process, which is the aim of the work reported in this thesis, it was first necessary to establish the validity of the proposed experimental technique. In order to do this, the original experiments carried out by Drexhage and co-workers were repeated to provide a comparison for the eventual corrugated interface data. The results indeed confirm that the fluorescent Eu^{3+} monolayers used conform to the ideal required for the experiments, as detailed in chapter 4.

Two different types of measurement were made for the planar geometry considered in this chapter. Initially, measurements were made of the lifetime of the excited state of the Eu^{3+} ions as a function of their separation from a mirror surface, thus determining the decay rate as a function of distance from the mirror. This data was then modelled using the theory developed by *Chance Prock and Silbey (1978)*, and good agreement found. The radiation pattern of

the Eu^{3+} ions was then measured, giving an indication of the spatial distribution of the emission (again, as a function of the molecule-mirror separation). This data was also successfully modelled, this time using a simple interference treatment. This last set of experiments was important since the principal decay mechanism of excited ions near a mirror is the excitation of surface modes, such as the surface-plasmon polariton. For planar systems, these modes are non-radiative, and the radiation pattern is solely determined by the interference between the direct emission and that reflected from the mirror. Corrugating the interface to form a grating allows the surface modes to scatter and re-radiate, leading to the perturbation of the planar radiation pattern by sharp emission peaks.

6.2 Sample design and fabrication

The samples used in this chapter were fabricated from silica slides coated with an optically thick layer of silver. A “staircase” spacer structure of fatty acid molecules was then deposited on top of this mirror using the Langmuir-Blodgett technique. The final step in the process was the deposition of a monolayer of Eu^{3+} ions on top of the spacer layers using the horizontal transfer technique.

Initially, the silica slides ($\lambda/10$ flatness) were cut into squares of side 25mm and cleaned using the procedure detailed in chapter 4. Briefly, this entailed immersion in a bath of concentrated nitric acid for 10 minutes to oxidise contamination followed by rinsing in deionised water. After this initial step, the substrates were ultrasonically agitated for 30 minutes in a detergent solution, rinsed in deionised water, then ultrasonically treated once more, this time using chloroform. The final step of the cleaning process was drag cleaning using lens tissue soaked in solvent to remove particulate debris. This was first done using chloroform, then propan-2-ol. Any remaining dust was removed using a jet of filtered inert gas. These clean substrates were then rendered hydrophobic by treatment with HMDS; the substrates were placed in a gondola to ensure that both faces of the slide were exposed to vapour. This gondola was then placed in a screw-top glass jar with a few drops of HMDS, sealed, and left overnight.

Mirrors were then deposited onto the substrates by thermal evaporation of silver under vacuum, again as detailed in chapter 4. Four substrates were coated in a single evaporation, the maximum number that could be fitted into the chamber at one time. Typically, a silver film 200nm thick was sufficient to form an optically thick mirror. Because silver readily reacts with atmospheric sulfur to form a hydrophilic sulfide layer [Kovacs (1978)], the samples were only removed from the vacuum chamber immediately before LB deposition was due to begin.

The LB deposition process commenced with the preparation of the clean room. The trough was emptied, thoroughly cleaned with wipes soaked in chloroform (Aristar grade) and refilled with fresh ultra-pure water. The samples were transferred from the vacuum chamber to a vacuum desiccator and brought into the clean room. The surface of the subphase was swept several times with a moving barrier to remove any contamination acquired during retrieval of the samples from the evaporator. The spacer layer material, 22-tricosenoic acid, was then spread onto the water subphase from solution to form a floating monolayer. One of the samples was held in a PTFE clip and attached to the dipping arm. This arm was then lowered into the subphase until the water surface was just broached. The floating monolayer was then compressed at $1\text{cm}^2\text{s}^{-1}$ until the surface pressure reached 30mNm^{-1} , the deposition pressure. LB transfer could then begin. This was carried out with an immersion rate of 0.8mms^{-1} and an emersion rate of 0.6mms^{-1} to ensure good transfer onto the silver (for HMDS treated silica, speeds of 1mms^{-1} were commonly used).

It was found that up to sixteen different spacer layer regions could be deposited onto each 25mm square sample; any more and the resulting sample areas were too small to use. Four such multi-region samples were required to cover the desired range of molecule-mirror separations (up to $\sim 600\text{nm}$) with sufficient resolution. To obtain consistency between these samples it was necessary to use silver mirrors which had been deposited during the same evaporation; this ensured that the silver parameters were as identical as possible.

The spacer layers for the first sample were deposited in a two-stage process. Initially, 48 layers of 22-tricosenoic acid were deposited in three steps, giving four rectangular regions of spacer layer thickness 0, 16, 32 and 48 layers

each. The monolayer on the subphase was then removed using a water pump, the trough topped up, the water surface swept and a fresh film spread and compressed. The sample was then rotated by 90° , and 12 layers deposited on top of the original structure in three steps of 4 layers each. This is illustrated as a plan view in *figure 6.1*. The resulting structure had sixteen regions, with film thicknesses ranging from zero to 60 layers, in steps of 4 layers. The remaining samples were treated in an identical fashion, except that they had 60, 120 and 180 layers complete coverage respectively before the step structure was deposited on top. In this way, a series of samples covering the molecule-metal separation range from 0 to 240 layers in 4 layer steps were fabricated. Because the thickness of a 22-tricosenoic acid layer is $\sim 2.6\text{nm}$ [Barnes and Sambles (1986)], this corresponds to metal-molecule separations ranging up to 624nm ($\sim \lambda$) in 10.4nm steps. The samples were then stored in a desiccator until deposition of the Eu^{3+} layers could be carried out.

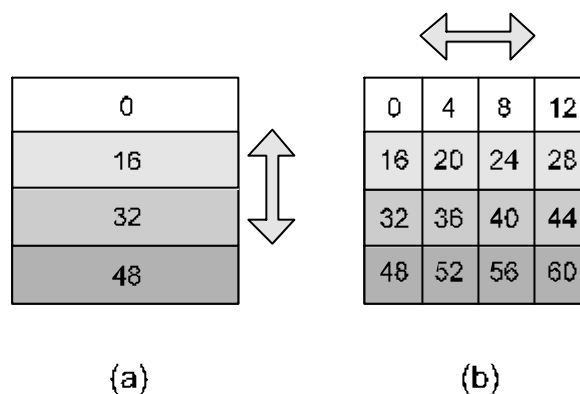


Figure 6.1 A plan view of the 0 to 60 spacer layer sample, showing the two step fabrication process. (a) Deposition of 48 layers in 16 layer steps, followed by a 90° rotation and (b) deposition of 12 layers in 4 layer steps.

At this point, a fresh solution of the Eu^{3+} complex was made up by dissolving 1mg of the complex in 5ml of a 4:1 mixture of benzene and acetone. The floating monolayer of 22-tricosenoic acid was then removed from the subphase using a water pump, and the trough emptied. After cleaning with chloroform, the trough was refilled with ultra-pure water, the surface swept with a barrier and a monolayer of the Eu^{3+} spread from $\sim 200\text{ml}$ of solution. This film was then compressed at a rate of $2\text{cm}^2\text{s}^{-1}$ until the surface pressure reached

$5mNm^{-1}$. The surface pressure was then held constant while the sample was lowered through the layer horizontally. The film was then expanded and the sample retrieved. Several fluorescent films could be deposited from one floating monolayer by replenishing the film whilst in the expanded state and recompressing. The samples thus produced were then stored in a vacuum desiccator until fluorescence measurements could be made.

After deposition of the Eu^{3+} monolayers onto the mirror substrates, a control sample, consisting of a HMDS treated silica slide coated with 20 layers of 22-tricosenoic acid was also coated to check the quality of the Eu^{3+} solution and its subsequent deposition. The fluorescence lifetimes measured for these control samples were typically in the range 0.93 to 0.94ms, this was taken to indicate that a satisfactory Eu^{3+} monolayer had been deposited. (The measured lifetime for a monolayer was found to fall from 0.93ms to around 0.86ms if the complex had photobleached whilst in storage; it was important to check that this had not occurred.)

The set of four samples thus allowed the measurement of the fluorescence properties of a monolayer of the Eu^{3+} complex separated by a known distance up to a wavelength away from a silver mirror. The remainder of this chapter details the experiments carried out on these samples.

6.3 Excited state lifetime measurements

In order to minimise photobleaching by fluorescent room lights, or degradation caused by exposure to the atmosphere, fluorescence measurements were made soon after the Eu^{3+} monolayer had been deposited onto the samples. No more than an hour elapsed between removal of the samples from the clean room and the completion of the lifetime measurements.

6.3.1 Experimental technique

The fluorescence from the Eu^{3+} monolayers was measured using a time-resolved photon-counting technique. The experimental set-up used is illustrated in *figure 6.2*. The excitation source was a pulsed nitrogen laser which emitted

5 ns pulses of UV light with a wavelength of $\lambda=337\text{nm}$. The output from this laser was found to include plasma fluorescence in the red part of the spectrum as well as the main UV component. Because of this, the laser emission was filtered using a band-stop He-Ne mirror, which strongly reflected light from 550 to 630 nm. This helped to reduce the background signal which could possibly have affected the measurement of the Eu^{3+} emission at $\lambda=614\text{nm}$.

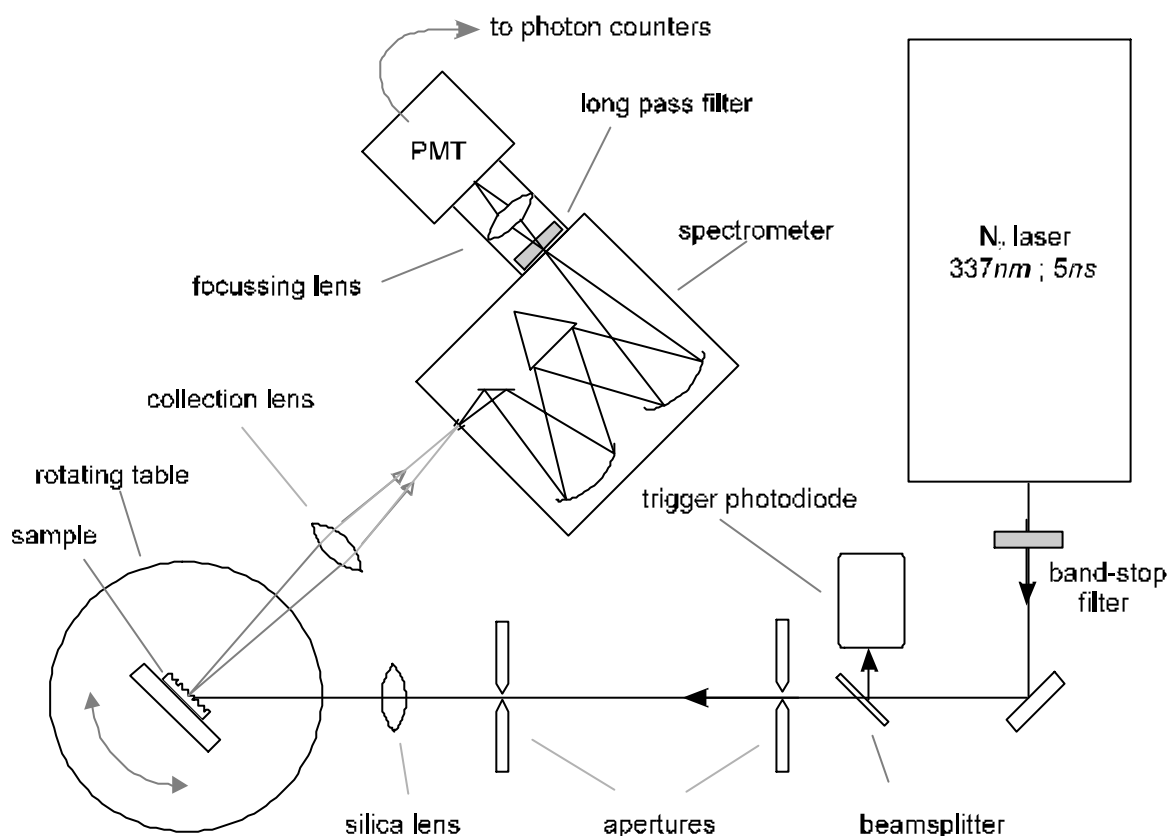


Figure 6.2 The experimental configuration used to measure excited state lifetimes.

The beam was then incident upon on a beamsplitter, and the reflected light directed onto a trigger detector (a fast rise-time photodiode) in order to provide a timing pulse for the photon-counting electronics. Since the beam divergence was very large, a pair of 1 mm diameter apertures spaced $\sim 1\text{m}$ apart were used to limit the spatial extent of the beam. This was possible since the intensity of the laser light was far greater than required to excite the sample, and so considerable loss could be tolerated. In order to excite only a single

spacer layer region (each 6mm by 6mm), the beam was then loosely focused to a 2mm^2 spot on the sample using a 40mm focal length silica lens. The angle of incidence was about $\sim 45^\circ$, but the actual value itself was not critical.

The fluorescence emission about the sample normal was collected by another lens and focused onto the entry slits of a spectrometer set to pass light of wavelength 614nm . The monochromatic light emerging from the exit slits of the spectrometer was then focused onto a photomultiplier tube (Hamamatsu R955) contained within a peltier-cooled housing. As a precaution, a long-pass interference filter ($\lambda > 550\text{nm}$) was placed in front of the window of this housing to protect the photomultiplier tube (PMT) from any stray pump light. The PMT was used in a photon counting configuration *i.e.* each pulse in the output voltage corresponded to the arrival of a photon at the photocathode. The dark count rate of the PMT, mostly caused by the thermal liberation of electrons at the cathode, was significantly reduced by cooling the PMT. The dark count rate of this detector was typically about 100 counts per second at room temperature, but was only ~ 2 counts per second at the operating temperature of -30°C .

It was necessary to amplify the output signal pulses from the PMT because of the severe RF interference caused whenever the laser fired. This was achieved by using two stages (x25) of a fast pre-amplifier (Stanford SR445) connected to the detector by a short run (40cm) of coaxial cable. The pulses were discriminated using either a multichannel scaler photon counter (Stanford SR430) in the case of lifetime measurements, or a dual channel gated photon counter (Stanford SR400) in the case of spectral or radiation pattern measurements. The overall time resolution of the kit was $\sim 10\text{ns}$.

The multichannel photon counter was configured with 2048 bins, each 10.24ms wide. Upon receiving a trigger pulse from the photodiode, the internal time base was set running, and the first time bin opened. After counting the pulses arriving in this first 10.24ms , the next bin was opened and the process repeated, until sampling had taken place for all 2048 bins. The histogram obtained in this manner was sequentially sampled over multiple timing cycles (laser pulses) and summed to improve the signal-to-noise level. In this way, the decay of the fluorescence emission could be measured over several decades in intensity, allowing the lifetime to be determined with an accuracy of $\pm 1\%$. Both

counters were capable of interrogation by a computer, which could also be used to control the spectrometer during the acquisition of spectra.

6.3.2 Results

The fluorescence decay data acquired from the samples using the above technique was analysed by computer using a non-linear least squares fitting routine. It was found that if the intensity of the UV beam used to excite the Eu^{3+} monolayer was low, the time-dependence of the decay for any spacer layer thickness was given by a single exponential function. This was important, indicating that all the Eu^{3+} ions experienced identical optical (and chemical) environments, and thus had identical excited state lifetimes. The time evolution of the fluorescence from Eu^{3+} ions spaced at two different distances from a silver mirror is given in *figure 6.3*. It can be seen that the quality of the data is excellent, the decay remaining single exponential at least eight lifetimes into the decay.

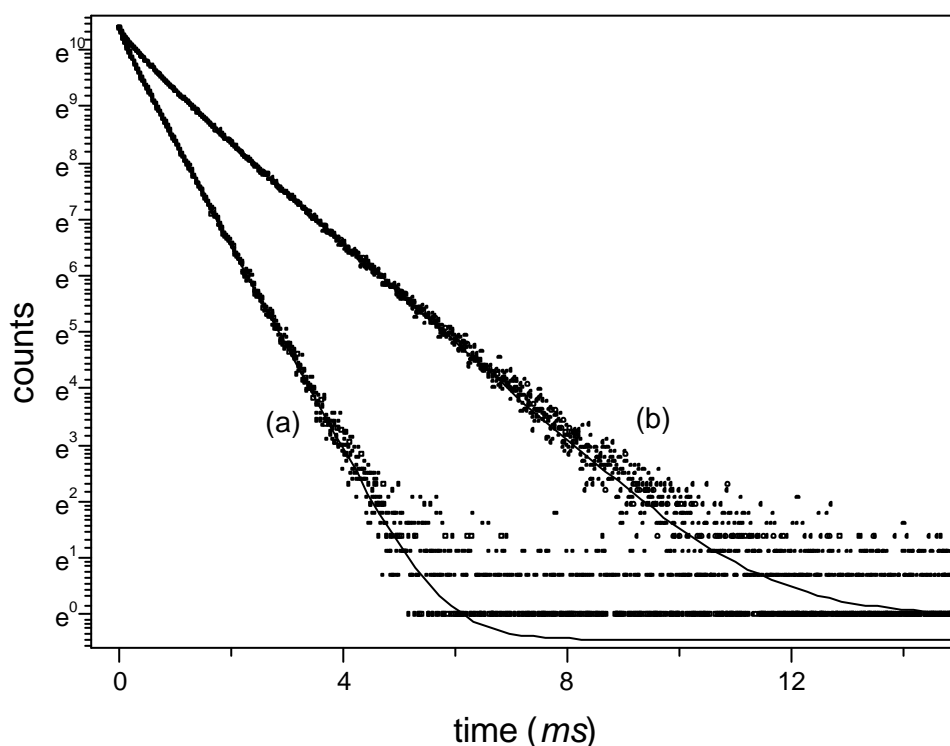


Figure 6.3 Fluorescence decay curves for Eu^{3+} ions located (a) 83nm and (b) 218nm distant from a silver mirror, together with the single exponential fits.

The main inference to be drawn from the single exponential behaviour is that the 22-tricosenoic acid spacer layers are of excellent homogeneity and locate the Eu^{3+} ions a uniform distance away from the metal mirror. If there were a distribution of ion-metal separation distances, the resulting time dependence of the fluorescence would be multi-exponential due to the variation in excited state lifetimes of the different ion sites. The Eu^{3+} complex must also form a good monolayer, or even sub-monolayer, since the formation of crystallites or other gross defects would also lead to lifetime variations. The single-exponential functional form fitted to the data is given in *equation 6.1*.

$$I(t) = I_0 \exp(-t/\tau_1) + I_d \quad (6.1)$$

$I(t)$ is the intensity of the fluorescence at time t after the laser pulse, I_0 is the initial intensity of the fluorescence, I_d is the offset due to dark counts and τ is the lifetime of the Eu^{3+} ions.

The nature of the fluorescence decay observed for monolayer films was found to be dependent on the intensity of the UV light used to excite the Eu^{3+} ions. If the intensity was low, then the time dependence was a good single exponential, as shown in *figure 6.3*. If the intensity was increased by focusing the beam to a smaller sized spot on the sample, it was found that the decay became non-exponential. The non-exponential decay could be modelled using two exponential lifetime components, and it was found that the longer lifetime of the two was equal to the single lifetime value obtained for low-power excitation. The fact that the shorter lifetime component is only observed under high-power excitation suggests two possible explanations. The phenomenon was previously attributed to a transient temperature rise within the LB film due to the intensity of the laser pulse: the lifetime of Eu^{3+} ions is known to be temperature dependent [Amos (1997)]. An alternative explanation is that energy transfer is occurring between neighbouring excited Eu^{3+} ions, giving rise to a co-operative emission process [Wright (1976)]. When this occurs, two ions de-excite simultaneously with the emission of a photon of twice the energy of the original excited state. This alternative decay mechanism for the Eu^{3+} excited state gives rise to non-exponential time dependencies for the fluorescence decay of emitters, and could explain the deviation found at high pump intensities. This is possible

because the probability that two neighbouring ions are excited at the same time will increase with the intensity of the pump beam; in other words, increasing the pump intensity makes the co-operative emission process more likely. The observation of short wavelength emission from Eu^{3+} ions would be a definite signature of co-operative emission, and although this was not seen for a monolayer sample, it was observed for bulk samples, but only under higher power excitation. To decide which process is actually occurring will require further investigation, and it is likely that both phenomena are responsible, at least in part. Since the problem could be completely avoided by the use of low power excitation, however, this was left as a future experiment.

Fluorescence decay measurements were made on all of the different spacer layer regions of the four planar samples, together with the control samples, and the data fitted to the single exponential model given in *equation 6.1*. The resulting excited state lifetimes of the Eu^{3+} ions are presented in *figure 6.4* as a function of the ion-metal separation; this is given in terms of the number of spacer layers.

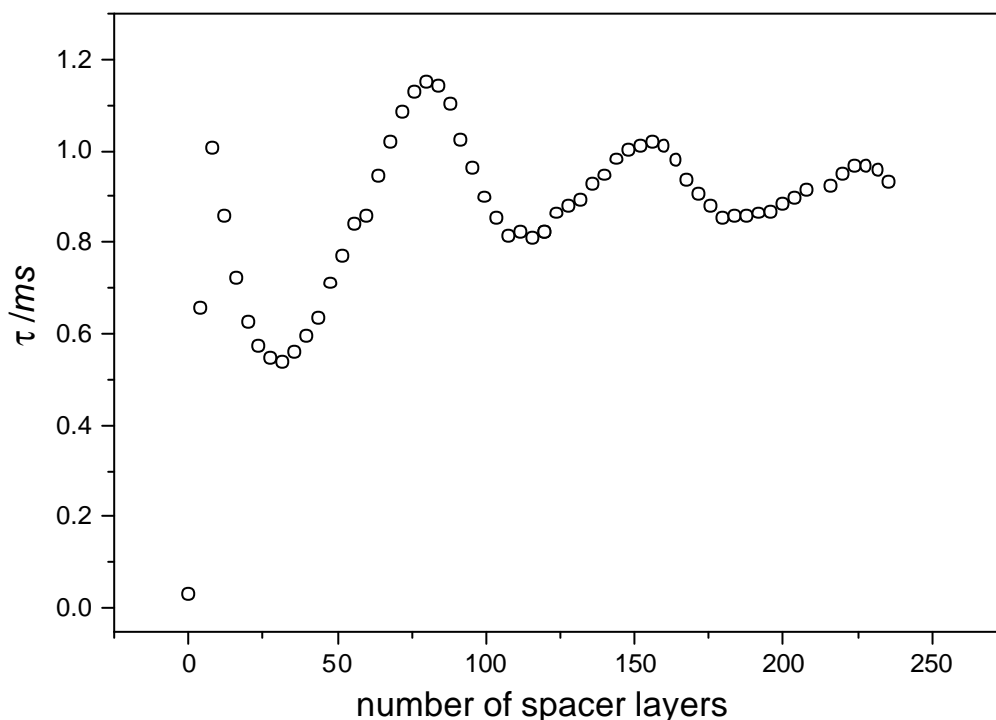


Figure 6.4 The experimentally measured excited state lifetime of the Eu^{3+} complex in front of a silver mirror as a function of the ion-metal separation. Note that the thickness of a single spacer layer is equal to 2.6 nm.

It is obvious that the mirror has a large effect on the excited state lifetime of the Eu^{3+} ions, and Drexhage's original experiment provided conclusive proof that spontaneous emission rates depend intimately on the local optical environment. The data presented in *figure 6.4* is very similar to the results of Drexhage and the more recent experiments of Amos [Drexhage (1974), Amos (1997)], and this allows the possibility of extending this study to investigate non-planar interfaces.

There are two regimes of interest in *figure 6.4*, illustrating the different physical processes governing the behaviour of excited molecules above metallic interfaces.

For separations greater than about 10 spacer layers, the lifetime is seen to oscillate as a function of ion-metal separation. As the ion-metal separation increases, the amplitude of these oscillations decreases. This behaviour results from the interference between the emission direct from the dipole and that reflected from the mirror. If the dipole is considered a simple oscillator, the reflected field at the dipole site acts as a driving term. If this reflected field is in phase with the oscillator, then the radiation rate is increased, whereas if it is out of phase, the radiation rate will be decreased. As the separation distance increases, the strength of the reflected field at the dipole site decreases since the field arises from a dipole, and thus falls off as $1/r^2$. The lifetime oscillations will therefore decrease in amplitude with increasing ion-mirror separation.

The validity of these simple ideas can be confirmed by consideration of the experimental results. Ignoring the initial rise and fall, the lifetime maxima occur at ion-mirror separations of roughly 80 and 160 spacer layers, whilst the minima occur at roughly 120 and 160 layers. Given that the thickness of a single spacer layer is 2.6nm and the layer refractive index ~ 1.6 , the corresponding round-trip optical paths are $\sim \lambda$ and $\sim 2\lambda$ for the maxima, and $\sim 3\lambda/2$ and $\sim 5\lambda/2$ for the minima ($\lambda=614\text{nm}$). Since the phase change of light on reflection from a good metal is π , it can be seen that the lifetime maxima and minima occur for phase differences of odd and even multiples of π respectively. As the lifetime is inversely related to the decay rate, it follows that the decay rate is at a maximum when the reflected field is in phase with the dipole, and *vice-versa*, as expected. The preceding argument is somewhat simplistic, and

does not consider complications such as orientation of the dipole moment with respect to the mirror, but is sufficient to explain the basic features of the phenomenon.

For ion-mirror separations of less than 10 spacer layers, a completely different kind of behaviour is seen; the lifetime of the excited state decreases rapidly as the ion approaches the mirror. The reason for this quenching is that energy can be transferred non-radiatively to the metal mirror in this regime— the ions de-excite *via* the generation of surface-plasmon polaritons at the metal-dielectric interface. As mentioned in chapter 3, this process is the dominant decay mechanism for dipoles in close proximity to a metal surface, and the availability of this extra strong decay channel means that the spontaneous emission rate of the dipoles increases. In actual fact, coupling to the SPP modes of the metal surface is an appreciable loss mechanism for the dipoles well before the lifetime falls monotonically to zero at around the 10 spacer layer distance. Further information about the details of the decay process can be gained from consideration of theoretical models of the behaviour of dipoles in front of a mirror.

Originally, Drexhage modelled his results using a simple power-flux model which considered the interference between the direct and reflected fields of the dipole. By integrating the power passing through a hemisphere centred upon, and in the far field of the dipole, Drexhage was able to correctly calculate the lifetime of the dipole for large dipole-mirror separations. The quenching of dipoles in close proximity to the metal was, however, unable to be accounted for in this model. The reason for this failure was that the transfer of energy to the metal was *not* included in the calculation. The exact nature of the quenching was unknown at this time, but subsequent work revealed the importance of the SPP mode in this process [*Pockrand et al. (1981)*]. It is interesting to note that extending Drexhage's model to include complex angles *would* reveal the SPP contribution to the decay rate. This is because excitation of the bound surface modes such as the SPP occurs *via* the evanescent components of the dipole field, which can be represented in terms of a complex angle.

A comprehensive theoretical treatment of the decay kinetics of dipoles in front of reflecting interfaces, which included the excitation of non-radiative modes such as the SPP implicitly, was developed by *Chance, Prock and Silbey*

(1978). This theory will be used to model the experimental results given in *figure 6.4*, and so the main features of the theory are presented in the following section.

6.4 Theoretical analysis

The problem of determining the radiation field of an oscillating dipole in front of a planar interface was originally treated by *Sommerfeld (1949)*, who was interested in long distance propagation of radio waves over the earth's surface. Interest was revived in this topic by the experiments of Drexhage. These experiments showed that the emission of light by fluorescent molecules was not determined solely by the nature of the emitter, but also depended on the local optical environment. Specifically, the emission rate was shown *not* to be an immutable property of the emitter, as was previously thought.

The emission of light by a fluorescent species is an intrinsically quantum mechanical process, involving a transition between different states resulting in the subsequent emission of a photon. Despite this, it is not necessary to use a quantum mechanical model to explain the effect of an interface on a nearby emitter. It is possible to treat the emitting species as a radiating dipole aerial and describe the interaction of the radiated electric field with the metal using Maxwell's equations. This purely classical model is found to give excellent agreement with experiment, in spite of the photon nature of light. The equivalent quantity to the lifetime of the excited state in this model is the radiation resistance of the dipole aerial.

Many different formulations of the classical solution to the dipole half-space problem have been published, see for example *Sipe (1981)* and *Novotny (1997)*, but all reduce to calculation of the reflected electric field at the dipole site. These classical models, which use a macroscopic permittivity, break down for very small emitter-metal separations ($d < 2nm$) since non-local effects become important. In this regime, the spatial dispersion of the metal has to be described by a wavevector-dependent permittivity. Quantum-mechanical processes such as wavefunction hybridisation also need to be taken into account [*Ford and Weber (1985)*]. In this last process, the excited state wavefunction of the emitting species can overlap with the wavefunctions of the

metal atoms, allowing electron transfer to the metal. Since the separation distances considered in this work lie the range $2nm < d < 600nm$, a classical treatment using macroscopic permittivities is more than sufficient to explain the data.

6.4.1 Dipole emission above a planar mirror

In this section, the formulation of the classical model developed by *Chance, Prock and Silbey (1978)* will be presented. The emitter itself is regarded as a point dipole simple harmonic oscillator (i.e. its dimensions are much smaller than the radiation wavelength) which consists of a bound charge. The fields associated with this oscillating dipole are taken to be those of a simple electric dipole, and they interact with the metal according to Maxwell's equations. The optical response of the media surrounding the dipole are given by their complex permittivities, and so Fresnel reflection coefficients can be used to describe the effects of the interfaces.

The equation of motion of the dipole moment μ can be written in the form

$$\ddot{\mu} + \omega_0^2 \mu = \frac{e^2}{m} E_r - b_0 \dot{\mu} \quad (6.2)$$

where ω_0 is the unperturbed oscillation frequency of the dipole, m is the effective mass of the dipole, E_r is the reflected field at the dipole site and b_0 is the damping (decay) rate of the dipole in the absence of the mirror. Note that the first term on the right-hand side of *equation 6.2* represents the force acting on the dipole due to the reflected field, and is thus a driving term. The second term represents the decay of the dipole by both radiative and non-radiative emission and is a damping term. The problem is thus that of a forced, damped simple harmonic oscillator, acting under the reflected radiation field of the dipole moment associated with the oscillator. Since the reflected field and the dipole moment have the same oscillation frequency, trial solutions can be written in the form

$$\mu(t) = \mu_0 \exp(-bt/2) \exp - i(\omega_0 + \Delta\omega)t \quad (6.3)$$

$$E_r(t) = E_0 \exp(-bt/2) \exp - i(\omega_0 + \Delta\omega)t.$$

In these expressions, b is the modified decay rate caused by the presence of the mirror, and $\Delta\omega$ is the corresponding shift in the oscillation frequency of the dipole.

Substituting *equations 6.3* into *equation 6.2*, and realising that b^2 is small in comparison with ω_0^2 , the following expressions are obtained upon separation into real and imaginary components

$$\Delta\omega = \frac{b^2}{8\omega_0} - \frac{b_0 b}{4\omega_0} - \frac{e^2}{2\mu_0 m \omega_0} \text{Re}(E_0) \quad (6.4)$$

$$b = b_0 + \frac{e^2}{\mu_0 m (\omega_0 - \Delta\omega)} \text{Im}(E_0)$$

It can be seen that the mirror affects both the decay rate of the dipole and the frequency of oscillation, although the frequency shift $\Delta\omega$ is too small to easily observe (it is of the order $\sim\text{MHz}$ for optical transitions). Inspection of the second relation of *equation 6.4* shows that the problem of calculating the dipole decay rate effectively reduces to the calculation of the reflected field at the dipole site.

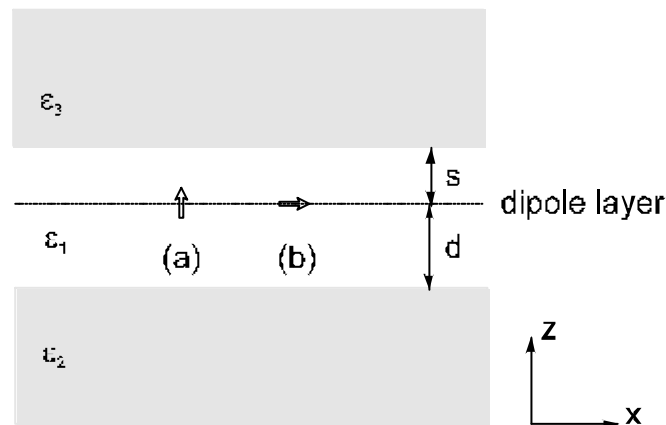


Figure 6.5 The geometry used in the dipole decay rate calculation, (a) perpendicular dipole, (b) parallel dipole.

The geometry of interest is illustrated in *figure 6.5*, and consists of a dipole located within a planar layer of finite thickness which is bounded by two semi-infinite media. This corresponds to the experimental situation since the Eu^{3+} ions are actually contained *within* the LB layer, which is bounded on one side by air ($\epsilon_3=1$), and on the other by the effectively infinite silver film.

The reflected field at the dipole site will depend on the orientation of the source dipole, and so the dipole orientation has to be taken into account in the decay rate calculation. Any arbitrarily oriented dipole can be resolved into three orthogonal component dipoles, one of which will be perpendicular to the mirror interface, with the other two lying in the plane of the interface. For the planar interface problem, these two dipoles are indistinguishable and so only two cases have to be calculated explicitly, the perpendicular dipole and the parallel dipole, see *figure 6.5*.

The reflected field is evaluated by expressing the source dipole field for a given orientation as a Fourier sum of plane waves, with each component distinguished by its momentum in the plane of the interface.

$$\mathbf{E}(\mathbf{r}) = \int_0^{\infty} \mathbf{E}_k \exp i\mathbf{k}\cdot\mathbf{r} dk \quad (6.5)$$

Substituting this expansion into Maxwell's equations and applying the relevant boundary conditions at the interfaces allows the reflected field to be obtained as the sum of the reflected fields due to each plane wave component. The total reflected field is thus obtained as a summation over the in-plane wavevector. The details of this calculation are given by *Chance, Prock and Silbey (1978)* and only the results quoted here. *Equation 6.4* can be written in the form

$$b_{\perp,\parallel} = b_0(1 - qz_{\perp,\parallel}) \quad (6.7)$$

where b_{\perp} is the decay rate for the perpendicular dipole, b_{\parallel} is the decay rate for the parallel dipole and q is the quantum efficiency of the emission (radiative decay rate/total decay rate). z_{\perp} and z_{\parallel} are given by the expressions in *equations 6.8* and *6.9* below, which are quoted here without proof.

$$z_{\perp} = 1 - \frac{3}{2} \operatorname{Im} \int_0^{\infty} \frac{(1 - r_{12}^p e^{-2\beta_{12}})(1 - r_{13}^p e^{-2\beta_{13}})}{(1 - r_{12}^p r_{13}^p e^{-2(\beta_{12} + \beta_{13})})} \frac{u^3}{l_1} du \quad (6.8)$$

$$z_{\parallel} = 1 - \frac{3}{4} \operatorname{Im} \int_0^{\infty} \left\{ \frac{(1 - r_{12}^s e^{-2\beta_{12}})(1 - r_{13}^s e^{-2\beta_{13}})}{(1 - r_{12}^s r_{13}^s e^{-2(\beta_{12} + \beta_{13})})} + (1 - u^2) \frac{(1 - r_{12}^p e^{-2\beta_{12}})(1 - r_{13}^p e^{-2\beta_{13}})}{(1 - r_{12}^p r_{13}^p e^{-2(\beta_{12} + \beta_{13})})} \right\} \frac{u}{l_1} du \quad (6.9)$$

In these equations, $r_{13}^{p,s}$ and $r_{12}^{p,s}$ are the Fresnel reflection coefficients for TM and TE polarised light reflecting from the interfaces above and below the dipole respectively. β_{13} and β_{12} give the retardation of the fields due to the phase changes incurred in the trip from the dipole site to the relevant interface and back again. The variable u is the component of the wavevector in the plane of the interface normalised with respect to the wavevector of the far field dipole emission, and $l_1 = -i(1 - u^2)^{1/2}$.

The integrals in *equations 6.8* and *6.9* are evaluated using a computer by numerically integrating over all positive values of u , the normalised in-plane wavevector. This allows the dipole decay rate to be calculated as a function of the dipole position above the mirror interface. Note that integrands effectively give the dipole power loss as a function of in-plane momentum in the expansion of the dipole field. Since the modes of the system, such as the SPP, occur at well-defined in-plane wavevectors, inspection of the integrands allows the various mechanisms contributing to the dipole decay to be separated and examined individually.

6.4.2 Assumptions of the model

Now that the theoretical model has been introduced, the assumptions made in applying this model to the experimental system under consideration will be discussed.

The first assumption made is that the Eu^{3+} emission at 614nm arises from an electric dipole transition. This is known to be a good approximation since the radiation pattern measurements which are presented in *section 6.5*;

agree well with the expected emission from an electric dipole source. The spatial distribution of the emission at 590nm , however, is completely different from that at 614nm , and is seen to arise from a magnetic dipole transition.

The model also assumes that the dipole oscillates at a single frequency, *i.e.* that the emission is monochromatic. While the Eu^{3+} ion was an excellent choice of fluorophore to satisfy this condition, it deviates slightly from being a truly monochromatic emitter. The excited state of the Eu^{3+} ion which gives rise to the 614nm emission (5D_0) can decay to seven different lower levels (7F_n , $n=0-6$). Each of these transitions can depopulate the excited state, and so all should be considered when calculating the observed decay rate, not just the 614nm transition. As discussed in chapter 4, only two of the transitions are significant; those giving rise to the 614nm and 590nm emission. The 614nm emission is by far the most important, accounting for some 90% of the emitted power, with the 590nm contributing 8%. It will be seen that good agreement can be obtained by only considering the 614nm emission; to include the 590nm transition would require altering the theory to allow magnetic dipole sources also. The natural linewidth of the 614nm emission itself is about 2nm , and so a rigorous calculation would require the use of a suitably weighted distribution of different wavelength sources, centred on 614nm . This was considered an unnecessary refinement in the present study.

For the purposes of the calculation, it is assumed that the LB spacer structure used to position the Eu^{3+} monolayer above the metal is isotropic and loss-less. This is an approximation since it is known that 22-tricosenoic acid is biaxial, with a small but finite absorption [Barnes and Sambles (1986)]. The isotropic assumption is acceptable because the dielectric anisotropy is small ($\Delta\epsilon=(\epsilon_{\parallel}-\epsilon_{\perp})\sim 0.21$), and the calculation effectively averages over all propagation directions within the film. In the case of the radiation pattern data, the non-isotropic nature of the LB spacer layer is more important, and leads to discrepancies from the simple isotropic model used, especially for thicker layers.

The optical properties of the Eu^{3+} complex are assumed to be identical to those of 22-tricosenoic acid, but since the Eu^{3+} is only a monolayer thick, any perturbation introduced by the refractive index difference is expected to be

minimal. The Eu^{3+} ion is also assumed to lie within the centre of the complex for the purposes of calculating the ion-metal and ion-LB/air interface separation, and a molecule of the complex is taken to be roughly 2.6 nm across. This is justifiable by comparison with the known size of similar molecules. The size of the complex also helps to ensure that the Eu^{3+} ions are non-interacting, notwithstanding the small absorption cross-section of the 5D_0 level, since neighbouring ions are separated by at least 2.6 nm . The transfer of energy between ions, which would lead to changes in the decay kinetics, occurs by a non-radiative dipole-dipole interaction, which has a $1/r^6$ distance dependence. This means that transfer is only likely to occur for molecules in very close proximity. The fact that the emitters are located within a monolayer helps, as the acceptor ions lie within a plane, and do not completely surround the donor ion.

The final assumption made is that the emitters are isotropically orientated with respect to the mirror interface. Many organic molecules have optical transitions associated with bonding electrons, and therefore their dipole moments are fixed with respect to the molecular axes. This is not true for the Eu^{3+} complex since the dipole moment is associated with the Eu^{3+} ion, which is free to rotate within the ligand cage. Since the lifetime of the excited state is so long ($\sim 0.9\text{ ms}$), however, the ion is free to sample all possible orientations of the dipole moment before decay occurs. This is the basis for the assumption of an isotropic distribution of dipole moments. The isotropic decay rate is calculated by appropriate averaging of the perpendicular (\perp) and parallel (\parallel) dipole decay rates,

$$b_{\text{iso}} = \frac{1}{3} b_{\perp} + \frac{2}{3} b_{\parallel}. \quad (6.10)$$

6.4.3 Modelling the lifetime data

The model developed in the preceding sections will now be used to model the experimental results presented in *figure 6.4*, which were obtained from the Eu^{3+} /LB spacer/silver mirror system. Various parameters are required by the model to calculate the dipole decay rate, and the values used to achieve

the best fit are discussed. It will be seen that good agreement is found between theory and experiment.

The decay rate calculation gives the modified decay rate of the dipoles in terms of the free-space dipole decay rate. In order to apply the model to the experimental results, some kind of normalisation needed to be carried out to provide the appropriate scaling. This was achieved by dividing the experimentally measured distance-dependent lifetimes by the measured lifetime of the control sample, giving a set of normalised experimental lifetimes. The model was then used to calculate the modified lifetime $[1/(\text{decay rate})]$ in the presence of the interface system, which was then divided by the calculated lifetime for the control geometry. In this way, the experimental lifetimes could be compared to the theoretical prediction with the correct scaling.

The input parameters required by the model are as follows,

λ_0	the Eu^{3+} emission wavelength
q	the quantum efficiency of the $\text{Eu}^{3+} {}^5D_0$ level
\hat{d}_{LB}	the thickness of a 22-tricosenoic acid monolayer
$\hat{\epsilon}_{\text{LB}} = \epsilon'_{\text{LB}} + i\epsilon''_{\text{LB}}$	the complex permittivity of the 22-tricosenoic acid
$\hat{\epsilon}_{\text{Ag}} = \epsilon'_{\text{Ag}} + i\epsilon''_{\text{Ag}}$	the complex permittivity of the silver.

The emission wavelength was simply obtained from the measured emission spectrum of the Eu^{3+} complex, and the value used was that of the peak of the main 614nm emission, $\lambda_0=614.7\text{nm}$. The silver parameters were obtained experimentally by characterising a witness sample deposited in the same evaporation as the silver mirrors used in the lifetime measurements. The diffraction grating used as the substrate had a well-known surface profile and so fitting the angle-dependent reflectivity to a theoretical model yielded the permittivity of the silver. This was carried out using the method outlined in *section 5.2.1*, except that a He-Ne laser operating at 612nm was used as the light source. In this way, the dispersion of the silver parameters with wavelength was kept to a minimum. The monolayer thickness and optical permittivity of the 22-tricosenoic acid spacer layers were obtained from *Barnes and Sambles (1986)*.

The only free parameter left in the model was thus the quantum efficiency of the emitter. Modelling of the lifetime showed that the only parameter which significantly affected the amplitude of the lifetime oscillations (see *figure 6.4*) was the quantum efficiency of the emitter. This is not too surprising, since the amplitude of the lifetime oscillation is an indication of the degree of the modification caused by the mirror. In the regime, where these oscillations are observed (large ion-mirror separation), the mirror can only affect the radiative decay rate of the dipole. The effect of the mirror is thus primarily determined by the proportion of the dipole emission which occurs radiatively, a quantity given by the quantum efficiency of the emitter. If the quantum efficiency were zero, the mirror would have no effect on the dipole, since the decay would be totally non-radiative, whereas the maximum modification occurs for a quantum efficiency of one. The reflection coefficients of the mirror will also affect the oscillation in lifetime with ion-mirror separation, since better mirrors will result in stronger reflected fields at the dipole site. The amplitude of the oscillation is, however, much less sensitive to the quality of the mirror than it is to the quantum efficiency of the emitter. The parameter that controls the reflectivity, the real part of the silver permittivity, is well known in any case and can be fixed when fitting the data.

In view of this, lifetimes were calculated as a function of the ion-mirror separation distance for a series of different values of the quantum efficiency ranging from 0.5 to 1, and normalised appropriately. All of the other parameters were kept fixed. The ratio of the values of the lifetime at the second maxima and minima was chosen as a measure of the amplitude of the lifetime oscillations in these curves, and was plotted as a function of the quantum efficiency. The quantum efficiency corresponding to the experimentally measured lifetime ratio was then interpolated from this calibration curve, and used as the value of the Eu^{3+} ion quantum efficiency in the modelling. The value found, $q=0.73$, is in good agreement with previous studies, which gave $q=0.7$ [Drexhage (1974)].

Table 6.1 gives the parameters used in the model to obtain the best fit to the experimental data of *figure 6.4*, assuming an isotropic distribution of dipoles. The experimental data and the resulting theoretical model are presented in *figure 6.6*, and the agreement between the two is seen to be extremely good.

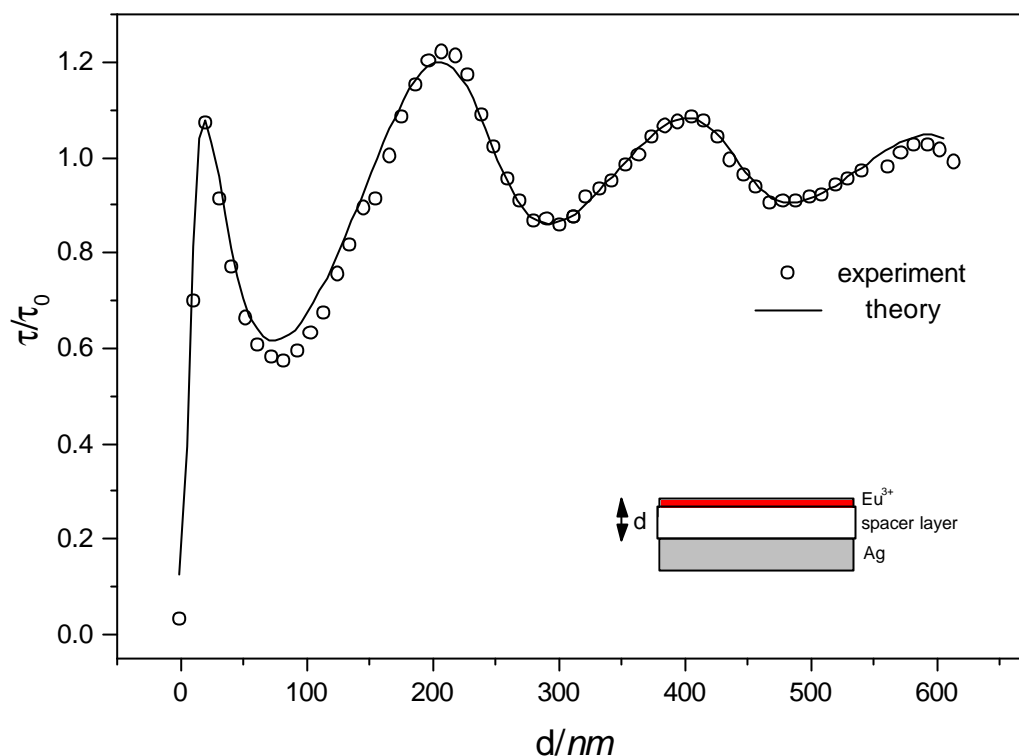


Figure 6.6 The distance dependence of the 5D_0 lifetime of Eu^{3+} ions located in front of a silver mirror. The open circles are experimental data, whilst the line is the theoretical model described in the preceding section, and is calculated using the parameters in *Table 6.1*. Both sets of data are normalised as described in the text. The inset shows the sample geometry.

Eu^{3+} emission wavelength, λ_0	614.7 nm
Quantum efficiency, q	0.73
Silver complex permittivity, $\hat{\epsilon}_{\text{Ag}}$	-14+0.7i
22-tricosenoic acid complex permittivity, $\hat{\epsilon}_{\text{LB}}$	2.49+0.0i
22-tricosenoic acid monolayer thickness, \hat{d}	2.68 nm
Control sample Eu^{3+} lifetime, τ_0	0.94 ms
Calculated decay rate modification for control sample	0.78

Table 6.1 The parameters used to model the experimentally measured distance dependence of the Eu^{3+} lifetime.

The last two rows in *table 6.1* give the control sample parameters which were used to normalise the distance-dependent lifetime data, thus allowing a direct comparison to be made between theory and experiment.

Note that to obtain a satisfactory fit, the optical thickness of the LB spacer layer had to be slightly increased from that obtained using the values of permittivity and monolayer thickness given in *Barnes and Sambles (1986)*. This was to ensure that the lifetime oscillations of the experimental data and theoretical model were in phase, and was achieved by increasing the thickness of a single monolayer from 2.6nm to 2.68nm , a change of 3%. This was deemed acceptable since the thickness of a monolayer depends on the tilt angle of the molecules within the film. Since the tilt angle is determined by the deposition conditions, including surface pressure and temperature, it is possible that slight variations in monolayer thickness can occur. The required change in optical path could also have been achieved by increasing the real part of the permittivity of the LB film, but the values quoted were considered less liable to change than the monolayer thickness.

It is interesting to note that in fitting this distance-dependent lifetime data, a value was obtained for the quantum efficiency of the emitter, a difficult quantity to estimate reliably by other methods.

6.4.4 Discussion

As mentioned earlier, inspection of the integrands of *equation 6.8* and *6.9* allows the power lost by the dipole to the various modes of the system to be examined. By plotting the contribution to the decay rate as a function of in-plane wavevector u , the importance of the various decay channels can be estimated for different sample geometries. This is possible because the dispersion characteristics of the modes which the dipole can couple are known, and thus occur at well-defined wavevectors (see chapter 3). Features in the integrand can thus be assigned to the excitation of different modes by the dipole.

In *figures 6.7* and *6.8*, the contribution to the decay rate of the dipole given by the integrands is plotted as a function of u and the dipole-mirror separation d , for parallel and perpendicularly-oriented dipoles respectively. The

integrands used are those calculated for the theoretical lifetime dependence given in *figure 6.6*, and thus correspond to the experimental sample geometry. Note that the integrated area underneath the plot for a given distance gives the total contribution of the mirror to the decay rate of a dipole in that location. The figures are plotted as grey-scale maps, with high power loss depicted in darker tones.

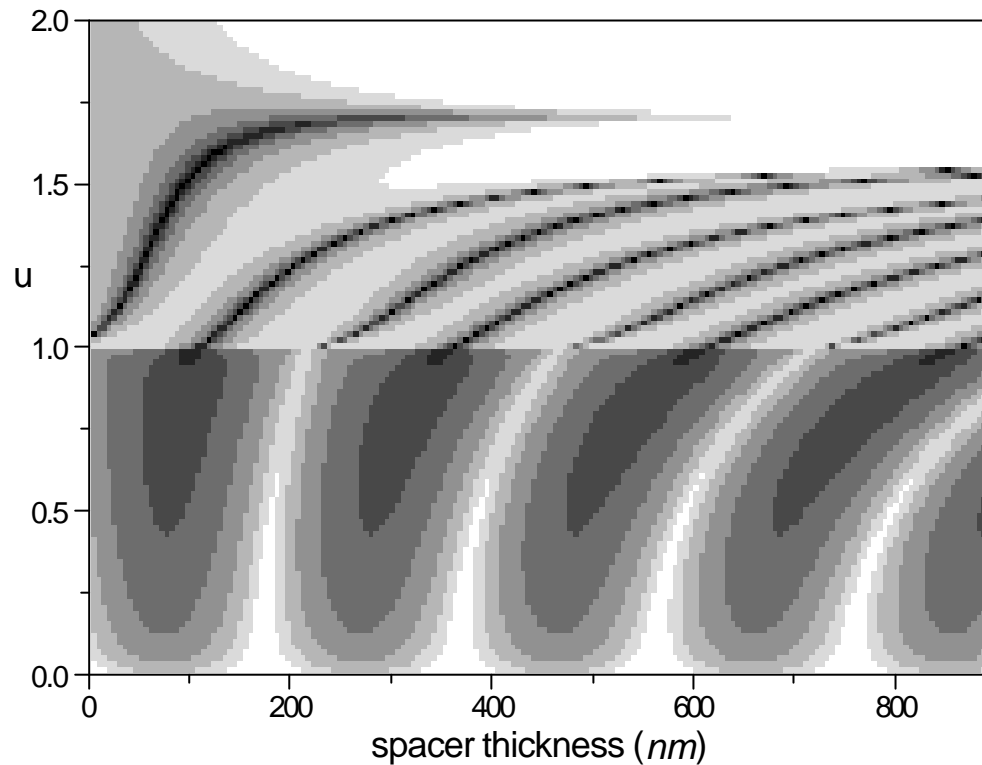


Figure 6.7 The contribution to the decay rate of a parallel oriented dipole above a silver mirror as a function of the normalised wavevector u and the dipole-mirror separation distance. The contribution is plotted on a logarithmic scale, with high power loss indicated by darker tones.

There are several features of interest in these plots. Firstly, note that contributions with $u < 1$ correspond to radiative emission into the half-space above the layer system. The direction of propagation of this emission can be found from the relationship $u = \sin \theta$, where θ is the angle between the propagation direction and the layer normal. This distribution could therefore be

used to calculate the radiation pattern of the system, but the situation is actually a little more complicated than at first sight since the contribution plotted is the result of integrating the emitted power over *all* azimuthal angles.

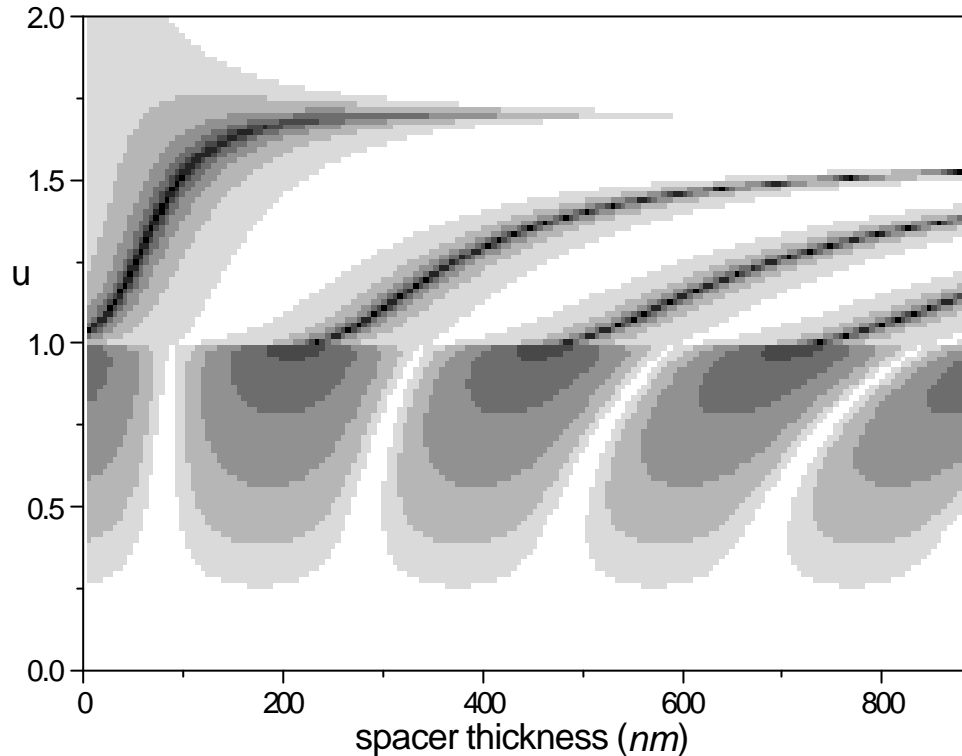


Figure 6.8 The contribution to the decay rate of a perpendicularly oriented dipole above a silver mirror as a function of the normalised wavevector u and the dipole-mirror separation distance. The contribution is plotted on a logarithmic scale, with high power loss indicated by darker tones.

For the perpendicularly oriented dipole, the contributions for $u < 1$ do give the correct radiation pattern, since this dipole has cylindrical symmetry about the layer normal, and the emission is thus independent of azimuth. To be exact, however, the contribution from the integrand has to be scaled by dividing by the area of the annulus into which light is emitted for a given polar angle θ . This cannot be done for the parallel dipole since in this case the emission is dependent on the azimuth; the polarisation of the emission varies from purely TM-polarised for the plane parallel to the dipole moment and layer normal, to purely TE-polarised in the plane orthogonal to the dipole moment. This means

that the $u < 1$ contribution for the parallel dipole is the average of the radiation pattern over all azimuthal angles. This point will be returned to in *section 6.5*, where an alternative model will be described that resolves this problem.

Contributions with $u > 1$ correspond to emission *beyond* the critical angle for the LB layer/air interface, and this emission cannot therefore escape from the sample. In this regime, the emission is characterised by coupling to the bound modes of the system, i.e. the surface-plasmon polariton (SPP) mode at the silver/LB interface and the guided modes of the LB spacer layer. Since the energy coupled to these non-radiative modes cannot radiate from the sample, it is effectively lost as useful emission in device applications. In the following chapter, a method of recouping this loss is demonstrated, leading to large enhancements in the emission from the system at certain angles.

As the dipoles are spaced further from the mirror, the thickness of the spacer layer must obviously increase. This statement may sound trite, but the presence of this increasing thickness overlayer not only locates the dipole further from the mirror, but also changes the nature of the available surface modes which the dipole can couple to. The dispersion of the various modes with overlayer thickness is immediately apparent by inspection of *figures 6.7* and *6.8*. The mode which exists with no LB overlayer present is the SPP mode, which originally occurs at $u = 1.03$, just beyond the light line. As the LB overlayer thickness increases, the SPP wavevector also increases because of the higher refractive index of the LB, as discussed in chapter 3. When the field of the SPP mode is completely contained within the LB layer, the wavevector attains a constant value of $u \sim 1.7$, in good agreement with *equation 3.13* on substitution of the values $\epsilon'_1 = \epsilon'_{Ag} = -14$ and $\epsilon'_2 = \epsilon'_{LB} = 2.49$.

As mentioned in chapter 3, the structure can also support waveguide modes within the LB spacer layer in addition to the SPP mode. Initially these modes are leaky, and comprise the radiative emission of the system. As the thickness of the film (guiding layer) increases, a point is reached when these modes become fully guided, and are thus bound to the LB layer. These *guided* modes exist beyond the $u = 1$ light line, *i.e.* they correspond to emission at angles greater than the critical angle for the LB/air interface, and have a maximum wavevector equivalent to a photon propagating tangential to the

interfaces within the LB layer. The leaky-to-guided transitions for each mode are denoted by the thickness cut-offs given in *equations 3.42* and *3.47*.

Upon increase of the LB film thickness, the first waveguide mode introduced is the TE_0 mode, which becomes fully guided when $d=100nm$. This compares with the value of $\sim 126nm$ predicted by the simple theory in chapter 3, using the parameters $\lambda_0=614nm$ and $\epsilon_r=2.49$. The agreement is not exact, but *equation 3.42* was derived using the assumption that the metallic substrate was perfect, and thus totally excluded the electric fields of the modes. The theory presented in *figures 6.7* and *6.8* was calculated using parameters describing a real metal, and so some penetration of the fields into the metal is expected. This will have the effect of allowing the mode to exist for a slightly thinner guiding layer, in agreement with the modelling, and indeed experiment (see chapter 7).

The next mode to be introduced upon increase in film thickness is the TM_1 mode, which appears when $d=250nm$. The corresponding cut-off calculated using *equation 3.47*, is $251nm$, in much better agreement with the exact theory. Further increase in film thickness leads to the introduction of TE and TM modes in rotation, again as given by *equations 3.42* and *3.47*.

The perpendicularly oriented dipole can only excite TM modes since its radiated field is TM-polarised for all azimuthal and polar angles, whereas the parallel dipole can excite both TE and TM modes since the polarisation of the radiated field depends on the azimuth. This point was mentioned earlier in connection with the possibility of modelling radiation patterns. A consequence of this effect is that the perpendicular dipole loses more energy to the SPP mode than the parallel dipole since it can excite SPPs for all azimuthal propagation angles. If the silver film is optically thin, then the dipole can excite SPPs on both sides of the film, leading to increased quenching of the dipole. This has been experimentally observed by both *Adams et al. (1980)*, and *Amos and Barnes (1997)* in the latter case using the same LB technique as described here.

The quality of the agreement between the experimental and theoretically obtained lifetime dependencies, as shown in *figure 6.6*, allows predictions to be made about the relative importance of the different decay mechanisms, including the radiative emission and the excitation of SPPs and guided modes within the LB spacer layer. By selectively integrating the area under each of

these features in the decay rate contribution versus wavevector plot, the power lost to each mode can be studied as a function of the dipole position, and sample structure. This powerful technique has been used to study the emission of Eu^{3+} ions contained within planar microcavity structures by co-workers. By comparison of experimentally obtained decay rate data with the theoretical model, the power loss of the dipole to the bound modes of the system was highlighted [*Worthing et al. (1998)*].

6.5 Radiation pattern measurements

After completing the lifetime measurements on these samples, the spatial distribution of the emission was measured, in order to act as a control for the grating experiments described in the next chapter. Measurements were made of the angular distribution of both the main Eu^{3+} emission at 614nm and the subsidiary 590nm emission, and substantial differences were found between the resulting radiation patterns. This data was acquired using a slight adaptation of the photon-counting experimental configuration already described in *section 6.3.1* and the modification is detailed below.

6.5.1 Experimental technique

In order to measure the radiation pattern of the various samples, a system was required that would enable the measurement of the angle-dependent emission intensity, ideally as a function of both emission wavelength and polarisation. The most important consideration was that the angle of incidence of the pump beam on the sample should be kept fixed during the measurements. This was because variation in the pumping conditions can cause large changes in the fluorescence emission intensity, especially for grating samples, as was noted in chapter 5. The experimental set-up which was used to achieve this is illustrated in *figure 6.9*.

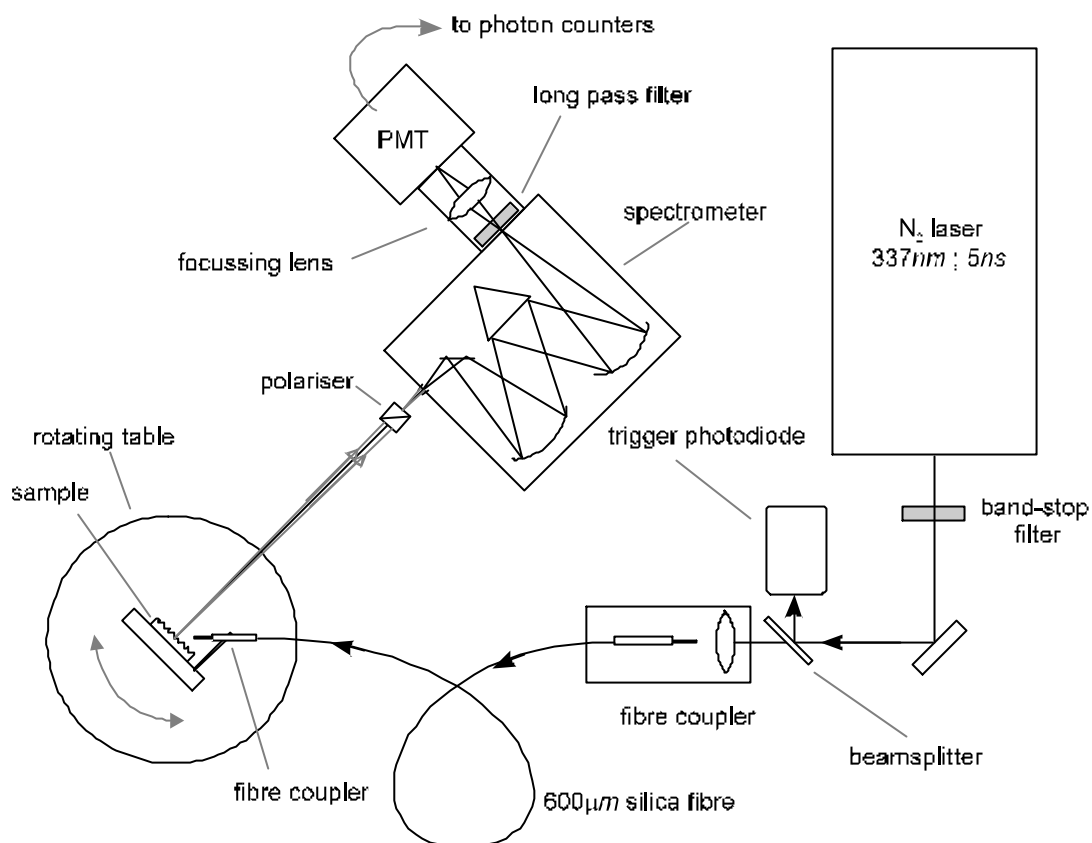


Figure 6.9 The experimental configuration used to make the radiation pattern measurements.

The sample was mounted on a translation stage attached to a computer-controlled rotating table to allow the emission angle to be scanned. Centring of the sample on the table rotation axis was achieved using the translation stage, and the sample azimuth could then be set with an accuracy of 0.1° . The fluorescence was excited by UV light made incident on the sample from an optical fibre mounted on the sample holder. In this way, the angle of incidence of the pump beam was held fixed with respect to the sample while the emission data was being acquired. The source of the UV light was the nitrogen laser that was used in the lifetime measurements. As before, the pump beam was filtered using a He-Ne mirror and a trigger signal obtained from a fast photodiode detector. The light was then coupled into the $600\mu\text{m}$ core diameter silica fibre using a 25mm focal length silica lens. Silica optics were used in preference to glass throughout to both reduce UV absorption losses, and avoid the ensuing fluorescent emission from impurities.

The fluorescent emission from the sample was not collected using a lens but was simply made incident on the slits of a spectrometer in order to increase the angular resolution of the experimental results. This was an important consideration due to the expected angular width of the emission from the grating samples considered in chapter 7. The rotation stage was positioned 200mm away from the spectrometer, and the slit width was set to 2mm , so the angular resolution achieved was $\pm 0.3^\circ$, a suitable compromise in terms of achieving a reasonable signal intensity (and wavelength resolution). The polarisation of the emission was selected using a Glan-Thompson polariser placed immediately before the spectrometer. The spectrometer was set to pass light of wavelength $\lambda_0=614\text{nm}$ so that the Eu^{3+} electric dipole emission could be measured; this could be changed to $\lambda_0=590\text{nm}$ in order to measure the magnetic dipole emission. In both cases the wavelength resolution achieved was $\pm 5\text{nm}$, again, this was a compromise between achieving an acceptable wavelength resolution whilst maintaining a reasonable signal intensity. This spectrally selected emission was then detected using the cooled PMT arrangement described previously.

The system was aligned by removing the PMT assembly and directing a He-Ne laser beam normally onto the rear slits of the spectrometer. The position of the rotating table and sample mount were then adjusted until the laser beam issuing from the entry slits passed over the centre of rotation of the sample. UV pump light from the cleaved end of the optical fibre was then directed at the point on the sample illuminated by the He-Ne laser, exciting fluorescence in a 1mm^2 spot. This procedure ensured that fluorescence emission was collected from a fixed point on the sample surface as the emission angle was scanned. So that this lengthy procedure did not have to be carried out for every sample (and for every single region on a sample!), a second laser beam was directed through the system in counterpropagation to the first. This beam passed over the now correctly positioned centre of rotation of the sample and onto the entrance slits of the spectrometer, thus defining the optical axis of the system. Subsequent samples could then be aligned by reference to this beam alone, allowing the detector to be left in a fixed position. The zero angle could be set with an accuracy of $\pm 0.2^\circ$ by directing the specular reflection of this beam from

the sample back down the system. In a similar way, the azimuth of grating samples could be set to $\phi=0^\circ$ by directing the ± 1 diffracted orders back down the system.

Radiation patterns were then measured by monitoring the intensity of the fluorescence emission as a function of the emission angle for both p- and s-polarisations. The signal from the PMT was discriminated using the gated photon counter, which was configured to average the fluorescence signal over 100 laser pulses for each emission angle in order to increase the signal to noise ratio.

6.5.2 Results

Using this technique, the radiation pattern of the fluorescence emission from planar mirror structures was measured for dipole-mirror separations ranging from 20 spacer layers to 200 spacer layers, in steps of 20 layers of 22-tricosenoic acid. The samples used to achieve this were those previously used to obtain the distance dependence of the Eu^{3+} excited state lifetime, which was described in *section 6.3*. Radiation patterns were measured corresponding to p- and s-polarised emission, for both the 614nm and 590nm Eu^{3+} ion transitions.

Ideally, it would have been desirable to obtain radiation patterns which were directly comparable in terms of intensity from one ion/mirror separation to another, but this was not possible for a number of reasons. Due to the deposition process, it could not be guaranteed that each sample region had the same coverage of the Eu^{3+} complex. The corresponding emission intensity could then vary from region to region purely because of variation in the number of Eu^{3+} ions in the illuminated area of the sample. More importantly, the intensity of the UV illumination was not constant from measurement to measurement because of changes in the orientation of the fibre coupler used to illuminate the sample. Neither of these issues were a problem for the lifetime measurements since only the time dependence, and not the intensity of the fluorescence, was important.

Another problem was that the samples were found to bleach to an unacceptable extent over the course of a series of scans. Again, this was not a problem for the lifetime measurements since typically only 200 averages were

required to obtain a complete time-dependence, and the sample did not bleach appreciably in this time. Because of the signal averaging necessary, a similar exposure to the atmosphere *and* UV pump beam occurred for every single angle of the angle-dependent data sets. Since measurements were usually made every 0.5° , for a total of 360 points, it is thus not surprising that the intensity of the fluorescence was found to decrease over the course of a series of measurements. Bleaching was not a problem for the initial angle scans made on a given sample, but the fluorescence intensity was found to be significantly reduced for the measurements made on regions examined later, due to the cumulative exposure. In these cases, a fresh monolayer of Eu^{3+} complex was deposited on the top of the sample, and measurements recommenced. The perturbation caused by the extra monolayer of dye was found to make little difference to the measured radiation patterns. This was confirmed by comparison of the measurements made on a sample before and after deposition of the second monolayer of the Eu^{3+} complex; within the limits of resolution the second radiation pattern was a simple scaling of the original.

6.5.3 Electric dipole radiation patterns

In view of these problems, the peak emission intensity for each radiation pattern was simply normalised to one, allowing the general evolution of the radiation pattern with ion-mirror separation to be determined. The experimentally measured radiation patterns for the 614nm Eu^{3+} ion electric dipole emission are presented in *Figure 6.10* for a progression of ion/mirror separations, ranging from 20 spacer layers to 200 spacer layers in 20 spacer layer steps. The actual ion/mirror separation thus ranges from 52nm to 520nm in 52nm steps. In each radiation pattern, an emission angle of zero degrees corresponds to normal emission from the sample, and $\pm 90^\circ$ to grazing emission. The solid lines are the relevant theoretical dependencies obtained using a simple model, which takes into account the interference between the direct emission from the dipole and the reflected field from the mirror; this will be described in *section 6.5.5*. The parameters used in the model to obtain the theoretical curves in *figure 6.10* are given in *table 6.2*.

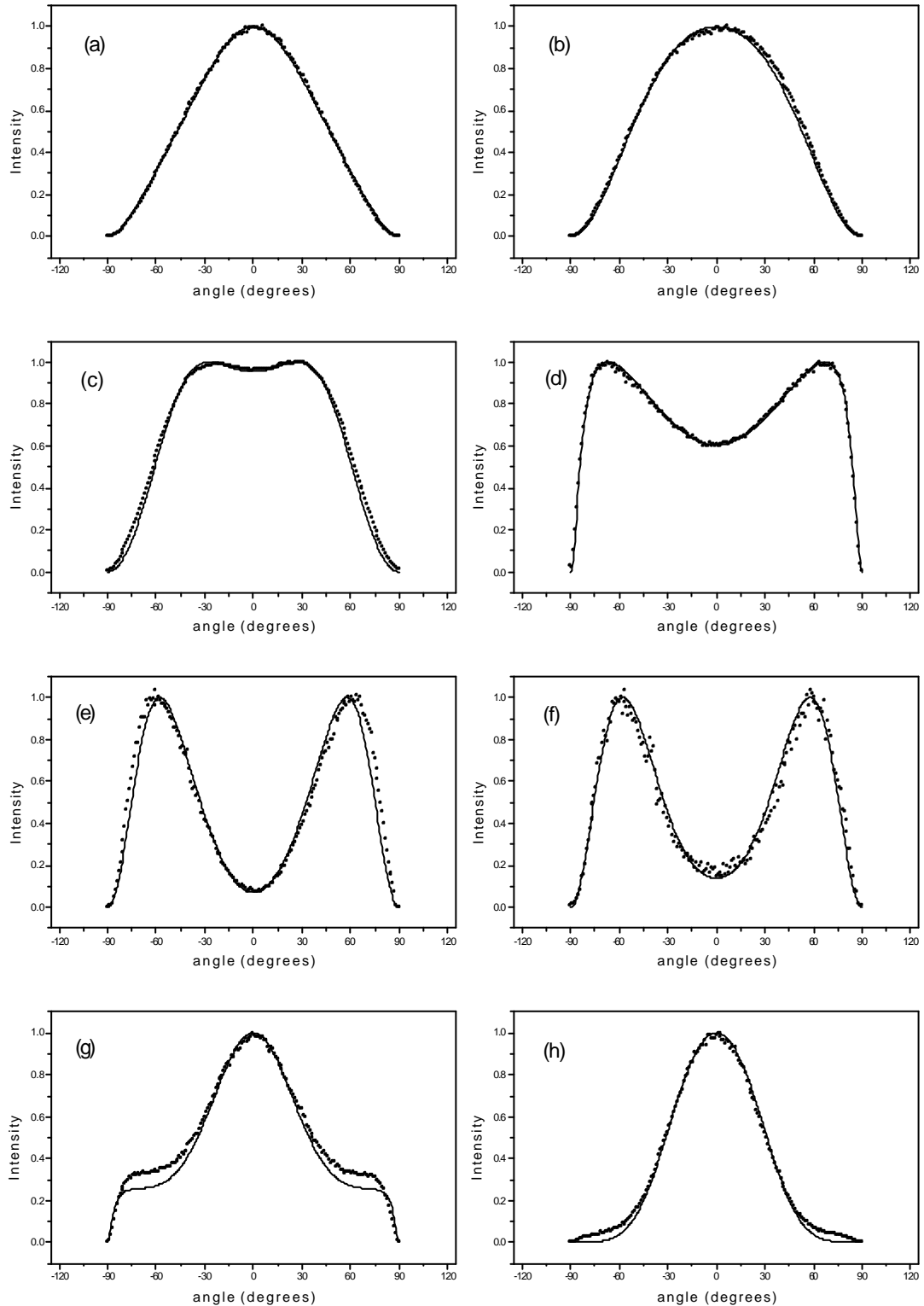


Figure 6.10 Radiation patterns of the 614nm Eu^{3+} electric dipole emission (normalised) for various ion/mirror separation distances. The plots in the left column are for p-polarised emission, on the right, s-polarised emission. (a, b) 52nm (c, d) 104nm (e, f) 156nm and (g, h) 208nm. The open circles are experimental data and the solid lines theoretical models.

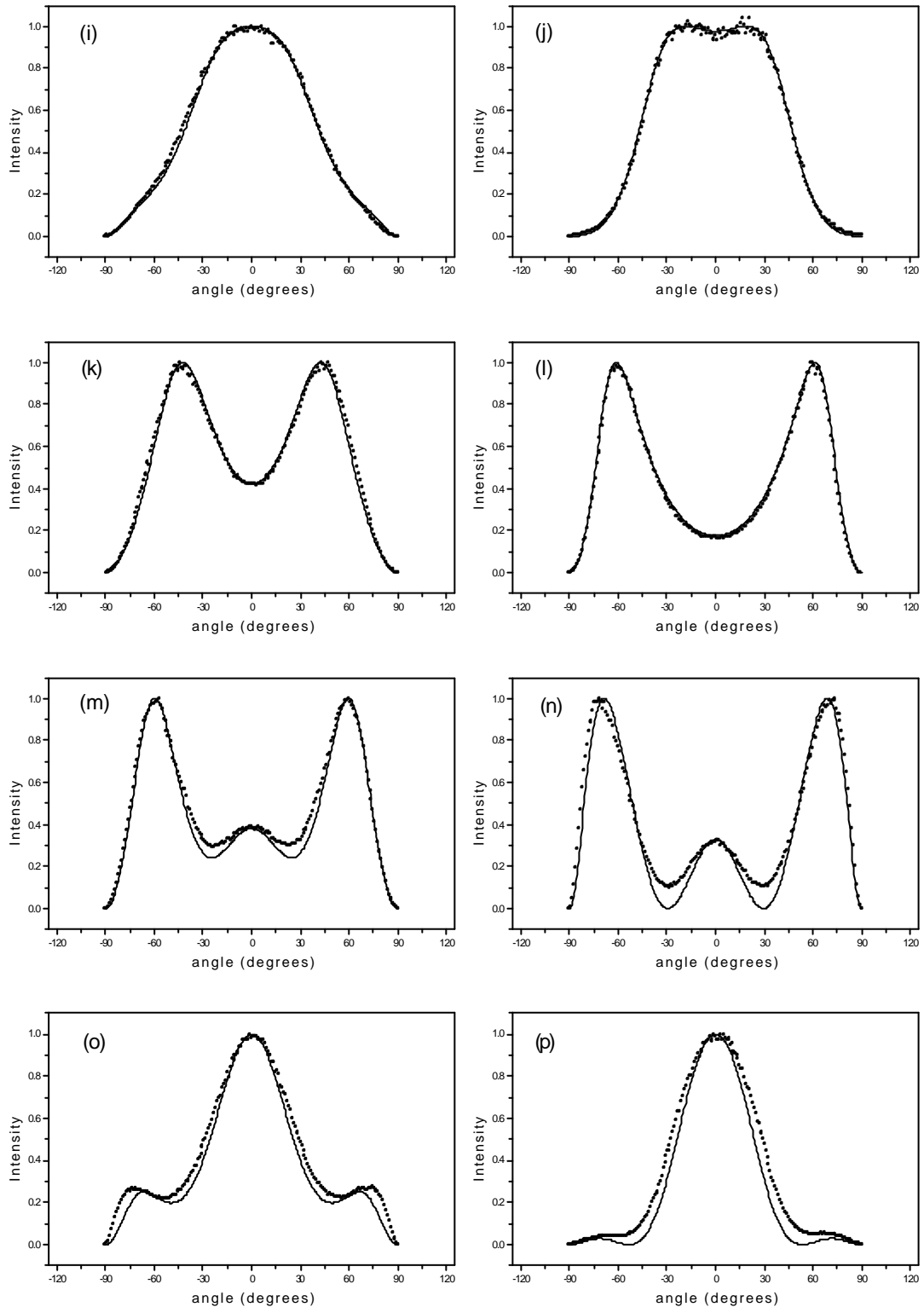


Figure 6.10 (continued) Radiation patterns of the 614nm Eu^{3+} electric dipole emission (normalised) for various ion/mirror separation distances. The plots in the left column are for p-polarised emission, on the right s-polarised emission. (i, j) 260nm (k, l) 312nm (m, n) 364nm and (o, p) 416nm . The open circles are experimental data and the solid lines theoretical models.

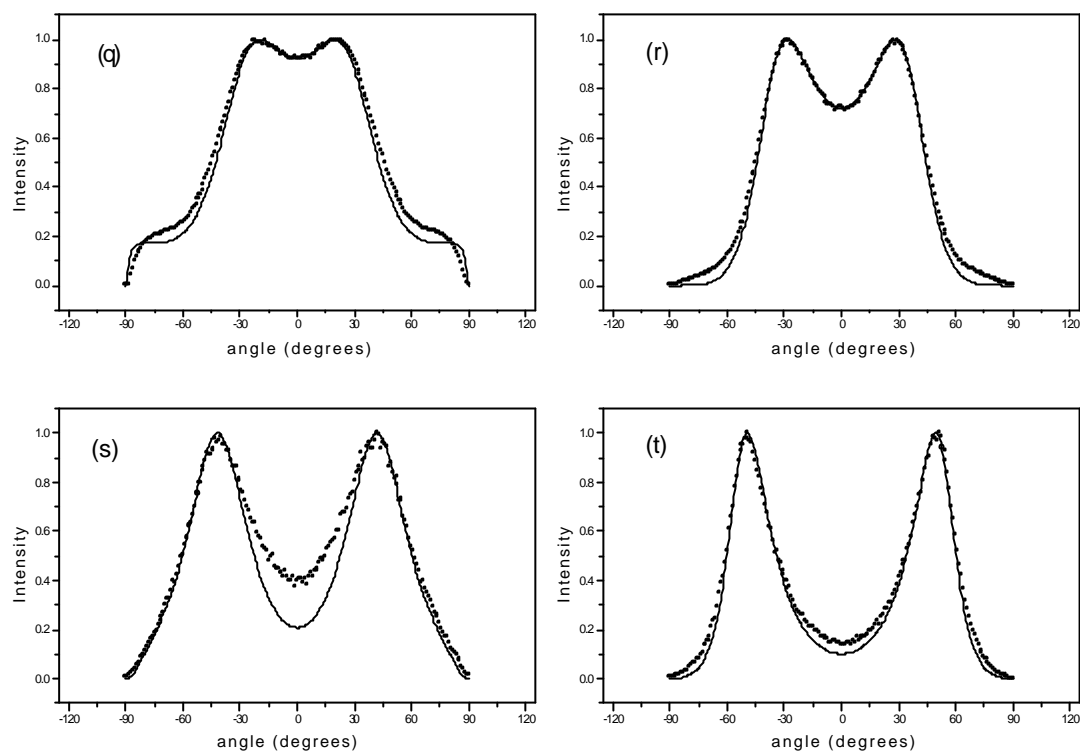


Figure 6.10 (continued) Radiation patterns of the 614nm Eu^{3+} electric dipole emission (normalised). The plots in the left column are for p-polarised emission, on the right s-polarised emission. (q, r) 468nm (s, t) 520nm. The open circles are experimental data and the solid lines theoretical models.

Eu^{3+} emission wavelength, λ_0	614.7 nm
Silver complex permittivity, $\hat{\epsilon}_{\text{Ag}}$	-14+0.7i
22-tricosenoic acid complex permittivity, $\hat{\epsilon}_{\text{LB}}$	2.49+0.0i
22-tricosenoic acid monolayer thickness, \hat{d}	2.68nm

Table 6.2 The parameters used to obtain the theoretically modelled radiation pattern dependencies of figure 6.10.

Measurements similar to these have been made before [Drexhage and Fleck (1968), Drexhage (1974)], except that in these studies, reflection effects at the LB layer/air interface were avoided by placing the substrates in index-matching fluid. This had the effect of eliminating wave-guiding behaviour in the

LB layer, leading to the measurement of substantially different radiation patterns from those observed here.

It is possible to identify a general trend in the radiation patterns of *figure 6.10* with increase in the ion/mirror separation (and thus film thickness). Apart from a slight phase difference, the behaviour of the p-polarised (TM) and s-polarised (TE) emission are qualitatively similar; the s-polarised radiation patterns will be taken as representative of both, and discussed in more detail.

For small separations, the emission is concentrated into a lobe normal to the substrate, see *figure 6.10b*. As the ion/mirror separation increases, this emission lobe splits into two separate peaks either side of the normal. These lobes split further apart as the ion/mirror separation increases, until the main emission is almost grazing the interface [*figure 6.10d*]. This point corresponds to the LB film thickness ($d \sim 100\text{nm}$) which is sufficient to support the first bound waveguide mode (TE_0), see *section 6.4.4*. Further increase in the film thickness leads to decrease in the intensity, and eventual disappearance of the high angle lobes, and the appearance of another emission peak in the sample normal direction [*figure 6.10h*]. The cycle then repeats, with the central peak splitting and moving out to high angles [*figure 6.10l*], and a new central emission maximum appearing [*figure 6.10n*]. Comparison with the theoretical modelling of *section 6.4.4* shows that every time an emission lobe passes off beyond the substrate horizon in the radiation pattern, a new guided mode is spawned.

This behaviour can be understood by realising that the lobes observed in the radiation pattern are simply emission from the leaky waveguide modes of the LB spacer layer, which are excited by the Eu^{3+} monolayer. As the film thickness d increases, the normal wavevector of a mode (that normal to the plane of the substrate) decreases, since it is proportional to $1/d$ (*equation 3.40*). To conserve total momentum, the tangential wavevector of the mode must thus increase, and conservation of tangential momentum across the LB layer/air interface means that the corresponding radiation from the mode occurs at a higher angle. Eventually, the point is reached when the mode propagating in the LB layer has the maximum tangential momentum than can be supported in the air, and so grazing emission occurs from the sample. This point is the cut-off marking the transition from leaky waveguide modes to fully guided waveguide modes; the disappearance of the leaky modes thus leads to the creation of fully

bound waveguide modes. The phenomenon was discussed fully in *section 3.3*, and corresponds to a normalised wavevector of $u=1$ in *figures 6.8* and *6.9*. Beyond this thickness, the emission from these leaky modes decreases as the energy is coupled to the newly spawned waveguide mode instead. Further leaky modes can then be supported which, as they are initially standing waves, radiate normally from the sample.

6.5.4 Magnetic dipole emission

Measurements were subsequently made of the Eu^{3+} magnetic dipole emission at 590nm for ion/mirror separations ranging from 20 to 180 spacer layers, again in 20 spacer layer steps. These measurements were made on the same samples as were used to obtain the electric dipole emission data, and in the same manner.

The evolution of the magnetic dipole radiation pattern with increasing ion/mirror separation was found to display very similar trends to the electric dipole emission. Because of this, only a sample of the magnetic dipole emission data is presented in this chapter to illustrate the radically different angle dependence compared to the electric dipole emission. The full set of experimental magnetic dipole emission data, for a progression of ion/mirror separations is given, together with theoretical modelling, in *Appendix A*.

Figure 6.11 shows the measured electric and magnetic dipole radiation patterns for an ion/mirror separation of 60 spacer layers (equivalent to a distance of 156nm). The different nature of the magnetic dipole emission is obvious, peak emission occurring in the normal direction, as compared with the electric dipole emission, which has the peak emission at about 60° .

Note that the difference in wavelength between the two transitions is *not* sufficient to explain the differences between the measured radiation patterns; the 590nm emission can only be modelled in a satisfactory way by assuming a magnetic dipole source. The wavelength difference might be expected to have an effect, since for the same ion/mirror separation the phase retardation of the 590nm emission will be slightly greater than the 614nm emission. The wavelength difference only corresponds to a 5% change in path length,

however, and modelling shows that this change does not give rise to a large enough shift in the radiation pattern.

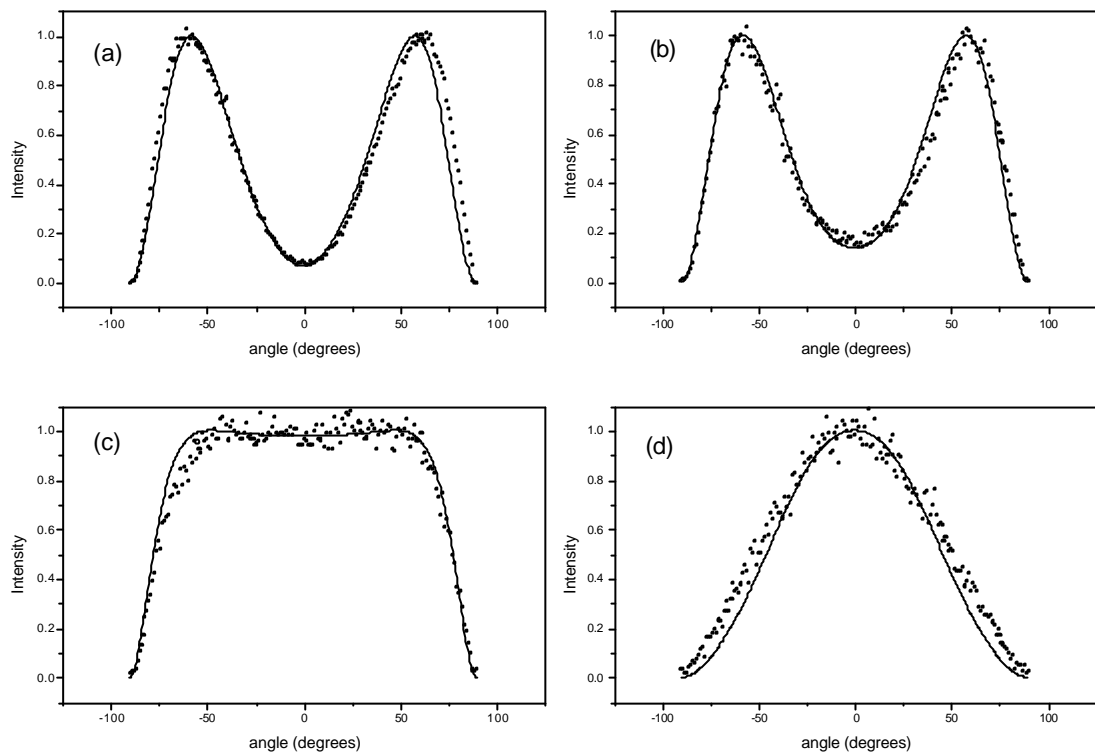


Figure 6.11 A comparison of the normalised radiation patterns measured for the electric (a, b) and magnetic dipole (c, d) Eu^{3+} emission, corresponding to an ion/mirror separation of 60 spacer layers (156nm). The plots in the left column are for p-polarised emission, whilst the right column is s-polarised emission. The hollow circles are experimental data, whilst the line is the theoretical dependence. The parameters used in the model are given in *Appendix A*.

The magnetic dipole data exhibits proportionally greater noise than the electric dipole data, which is a direct result of the reduced intensity of the 590nm emission compared to the 614nm emission (see *figure 4.10*).

As can be seen from both *figures 6.10* and *6.11*, the experimental data is well modelled by the simple interference theory, with discrepancies between the two occurring mainly for the higher emission angles. This theory will now be described.

6.5.5 Modelling radiation patterns

It has already been mentioned that the CPS model used to describe the lifetime data can also be used to model radiation patterns, but only the emission arising from perpendicularly oriented dipoles. There is a further problem, in that although the radiation from these dipoles is totally p-polarised, the emission from an isotropic dipole distribution will also include p-polarised contributions from those parallel dipoles with dipole moments lying in the plane of emission. This theory, therefore, cannot be used to model the measured emission patterns without substantial modification.

In view of this, a simple interference model was used instead, which was developed from a formulation given by *Greenler (1977)*. This model assumes that the emitting molecules are dipole emitters confined to a thin layer adsorbed directly onto a metal surface, and hence there is no geometrical phase change to consider. The radiation pattern is determined by considering the interference between the direct and reflected emission from the dipoles. Including the retardation resulting from spacing the emitters from the metal allows this model to be applied to the experimental data, and gives expressions in agreement with those of *Drexhage (1974)* for an appropriate choice of phase changes upon reflection.

To calculate the radiation pattern for an isotropic distribution of emitters, three different orthogonal dipole orientations have to be considered, which are depicted in *figure 6.12*. The first orientation (a) has the dipole moment lying perpendicular to the interface. In the other two, the dipole moment is parallel to the interface; in case (b) the dipole moment lies within the plane of emission, whilst in case (c), it is perpendicular to the plane of emission. Considering radiation into the plane of emission only, cases (a) and (b) give p-polarised light, whereas case (c) gives s-polarised light.

Initially, only the single interface problem will be considered, that of a monolayer of dipoles located a given distance above a planar mirror. The extension of this model to include the LB film/air interface will be discussed later.

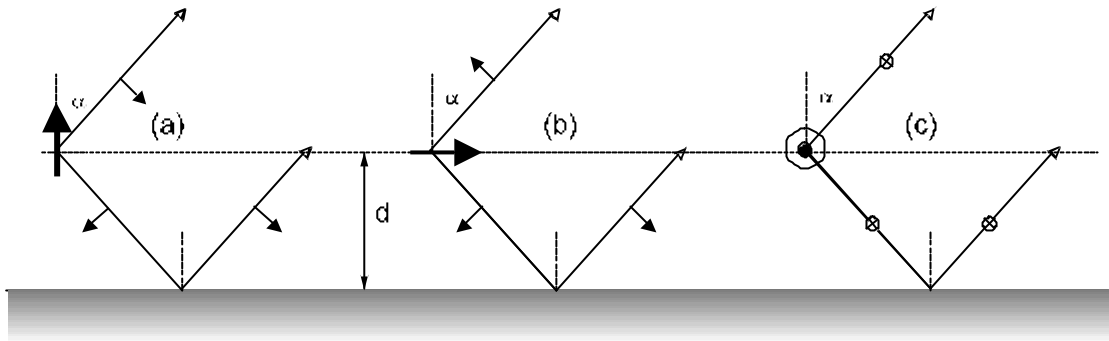


Figure 6.12 The three different dipole orientations: (a) dipole perpendicular to interface, (b) dipole parallel to interface, in plane of emission, (c) dipole parallel to interface, normal to plane of emission. The smaller solid arrowheads indicate the direction of the electric fields at a given moment in time, assuming an electric dipole source, and zero phase change on reflection from the metal.

The emission intensity in any given direction is given by the expression

$$I(\alpha) = I_1 + I_2 + 2\sqrt{I_1 I_2} \cos \Delta \quad (6.11)$$

where I_1 and I_2 are the intensities of the direct and reflected waves respectively, and Δ is the phase difference between these waves in the far field. This phase difference, defined in *equation 6.12*, is made up of two components, corresponding to the geometric phase φ (due to retardation), and the phase shift on reflection from the interface δ , which will be polarisation dependent.

$$\Delta = \varphi - \delta; \quad \varphi = \frac{4\pi nd}{\lambda} \cos \alpha \quad (6.12)$$

Here, n is the refractive index of the medium the dipole is located in, and d is the dipole/mirror separation distance. The intensities I_1 , I_2 , and the phase change δ differ for the three dipole orientations, and the appropriate values are given in *table 6.3*. Note that the emission intensity for an electric dipole varies as $\sin^2 \alpha$, where α is the angle between the propagation direction and the dipole axis. It is assumed that the dipole has a maximum emission intensity of unity. ρ_p and ρ_s are the amplitude reflection coefficients for p- and s-polarised light reflecting from the metal/dielectric interface respectively, and the accompanying

phase changes are δ_p and δ_s . The values for these Fresnel coefficients can be calculated from the permittivities of the different media, and appropriate formulae are given by *Born and Wolf (1970)*. The extra phase change of π for case (b) arises purely from the geometrical arrangement. Inspection of figure 6.12 shows that if there is no phase change on reflection from the mirror, the direct and reflected waves from the dipole should cancel. This is ensured by the addition of the π phase change.

dipole orientation	l_1	l_2	δ
(a)	$\sin^2 \alpha$	$\rho_p^2 \sin^2 \alpha$	δ_p
(b)	$\cos^2 \alpha$	$\rho_p^2 \cos^2 \alpha$	$\delta_p + \pi$
(c)	1	ρ_s^2	δ_s

Table 6.3 The values taken by l_1 , l_2 and δ for the three different electric dipole orientations. The dipole emission is taken to have a maximum intensity of unity.

The radiation patterns for the three different dipole orientations can then be obtained by substituting the values from *table 6.3* into *equation 6.11*, and give the following relative angular intensity distributions

$$\text{Case (a)} \quad I(\alpha) = \sin^2 \alpha \left[1 + \rho_p^2 + 2\rho_p \cos(\varphi - \delta_p) \right] \quad (6.13)$$

$$\text{Case (b)} \quad I(\alpha) = \cos^2 \alpha \left[1 + \rho_p^2 - 2\rho_p \cos(\varphi - \delta_p) \right] \quad (6.14)$$

$$\text{Case (c)} \quad I(\alpha) = \left[1 + \rho_s^2 + 2\rho_s \cos(\varphi - \delta_s) \right]. \quad (6.15)$$

The radiation patterns for p- and s-polarised emission for an isotropic distribution of dipoles can be obtained directly from *equations 6.13-6.15*, and are given by

$$I_p(\alpha) = 1 + \rho_p^2 - 2\rho_p \cos 2\alpha \cos(\varphi - \delta_p) \quad (6.16)$$

$$I_s(\alpha) = 1 + \rho_s^2 + 2\rho_s \cos(\varphi - \delta_s) \quad (6.17)$$

The experimental situation is complicated by the presence of the LB film/air interface above the layer of dipoles. This alters the radiation pattern by refracting the emitted waves, and altering their intensity by multiple beam interference within the LB film. This complicates the derivation of the radiation patterns quite considerably. As a result, only the final results will be quoted here; their derivation follows from summation of the partial waves propagating within the LB layer [Koppelman (1969)]. The relevant geometry is given in figure 6.13.

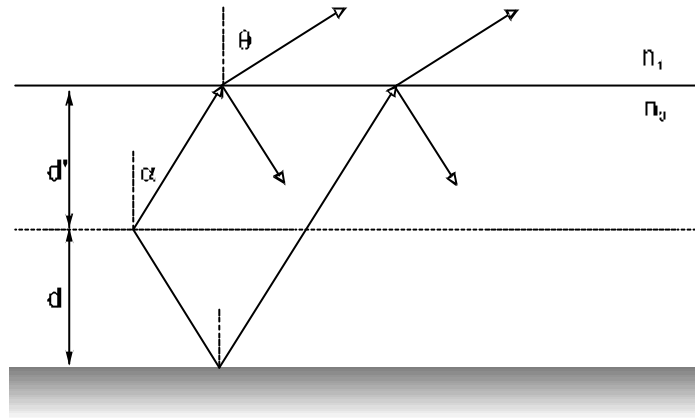


Figure 6.13 The double-interface geometry for calculation of radiation patterns.

The radiation patterns for s- and p-polarised emission from dipoles embedded within a double interface system, assuming isotropic media, are given by $I_s(\theta)$ and $I_p(\theta)$ respectively,

$$I_p(\theta) = \frac{I_p(\alpha) t_{10}^{s2}}{1 + \rho_p^2 r_{01}^{p2} - 2\rho_p r_{01}^p \cos(\varphi' - \delta_p)} \quad (4.17)$$

$$I_s(\theta) = \frac{I_s(\alpha) t_{10}^{s2}}{1 + \rho_s^2 r_{01}^{s2} - 2\rho_s r_{01}^s \cos(\varphi' - \delta_s)} \quad (4.18)$$

where

$$\varphi' = \frac{4\pi n_0(d + d')}{\lambda} \cos \alpha \quad (4.19)$$

and

$$n_1 \sin \theta = n_0 \sin \alpha. \quad (4.20)$$

$r_{01}^{p,s}$ and $t_{10}^{p,s}$ are the Fresnel reflection and transmission coefficients for the LB film/air interface, which are dependent on α , n_0 and n_1 . Suitable expressions are given in *Born and Wolf (1970)*.

The expressions given in *equations 4.18* and *4.19* were those used to produce the theoretical dependencies given in *figures 6.10* and *6.11*. The agreement between theory and experiment is quite good, especially since the theory assumes that the LB spacer layer is optically isotropic. This assumption is untrue, as mentioned previously, since 22-tricosenoic acid multilayers are known to be birefringent. This was not important in modelling the distance dependence of the Eu^{3+} fluorescence lifetime, since the lifetime is related to the *total* power loss from the dipole. Because the emission from the dipole samples the entire local environment; the anisotropy is effectively “averaged out”. The radiation pattern measurements are more sensitive to this anisotropy since the emission in a particular plane will be dependent primarily on the refractive index that the electric vector samples, which will itself depend on the molecular orientation.

The 22-tricosenoic acid molecules are expected to be tilted slightly from the vertical within the LB spacer layer due to the nature of the deposition process; the tilt, on average, pointing in the direction that the samples were dipped. In this work, radiation patterns were measured with the emission plane orthogonal to the dipping direction. Because of this molecular orientation and sampling direction, the s-polarised radiation patterns should agree with the isotropic theory better than the p-polarised emission. (Both polarisations were fitted with the same parameters.) This is because the s-polarised emission samples the refractive index associated with the short axis of the molecules for *all* emission angles. (Because of the molecular tilt, it is also slightly sensitive to the long-axis refractive index, but the proportion remains the same for all emission angles.) Depending on the emission angle, the p-polarised radiation samples *both* the long- and short-axis refractive indices; for normal emission, the short axis index is appropriate, whereas for grazing emission, a mixture of both indices is sampled. As a result, discrepancies should be expected for high angle emission in the p-polarised radiation patterns.

6.6 Spectral measurements

In addition to the lifetime and radiation pattern measurements, the emission spectra of the samples were also examined. Because of the different angle dependence of the electric and magnetic dipole emissions at 614nm and 590nm respectively, it is expected that the emission spectrum of a monolayer of the Eu^{3+} complex in front of a mirror should show dramatic variation with ion/mirror separation. This was observed for three dipole/mirror separations by *Drexhage (1974)*. *Figure 6.14* shows the unpolarised emission spectra measured for the Eu^{3+} /mirror system for a variety of separation distances. These spectra were measured for normal emission; the emission spectrum will also vary with angle.

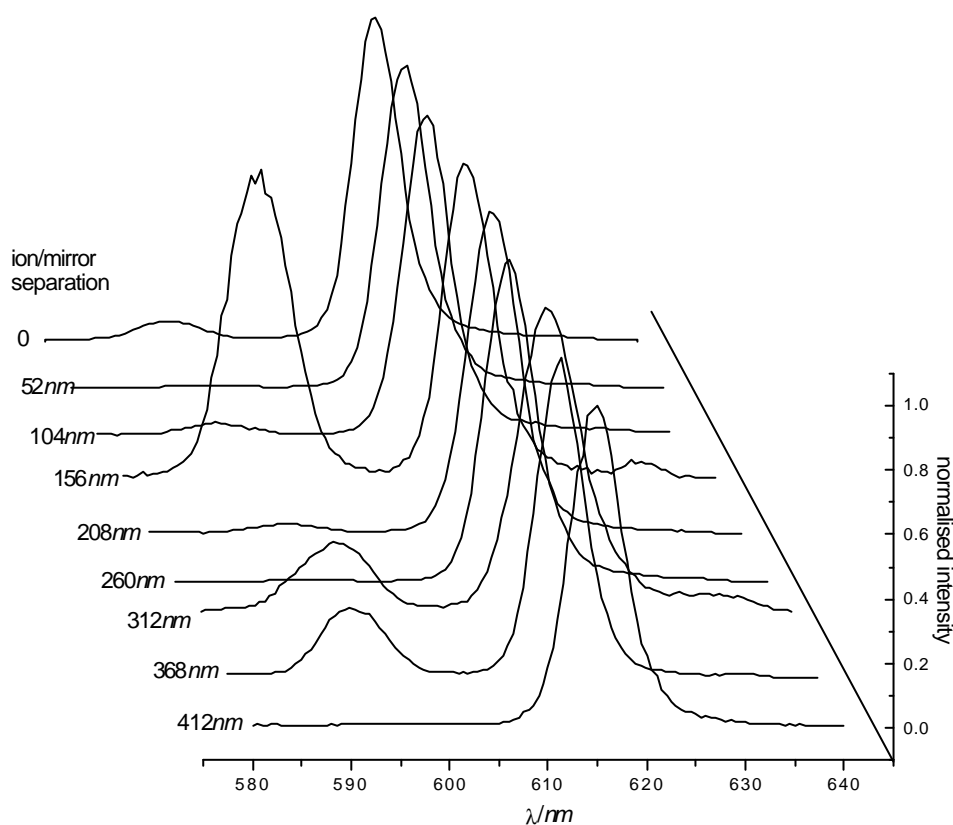


Figure 6.14 Emission spectra for the Eu^{3+} /mirror system for a variety of ion/mirror separations.

Note that the spectra in *figure 6.14* have been normalised so that the emission peak at 614nm has unit intensity in each case. It can be seen that the

590nm emission exhibits a drastically different distance dependence than the 614nm emission, again, evidence that the two emissions have a completely different nature. If both emissions resulted from electric dipole transitions, the 590nm peak would not be expected to cycle in intensity with distance.

The two emission bands are almost equal in intensity for an ion-mirror separation of 156nm. This is found to be reasonable by inspection of *figure 6.11*, which gives the relevant radiation patterns for this ion-mirror separation. The peak emission for the 614nm transition is seen to occur at high angles, whilst the peak emission at 590nm is normal to the sample, giving rise to their nearly similar normal emission intensity.

Figure 6.15 shows the emission spectra measured for an ion-mirror separation of 412nm at a high emission angle, and for emission normal to the sample ($\theta=0^\circ$). In this case, although the $\theta=0^\circ$ spectrum is normalised to give a peak intensity of unity, the $\theta=70^\circ$ spectra has the same scaling, and so the two are directly comparable.

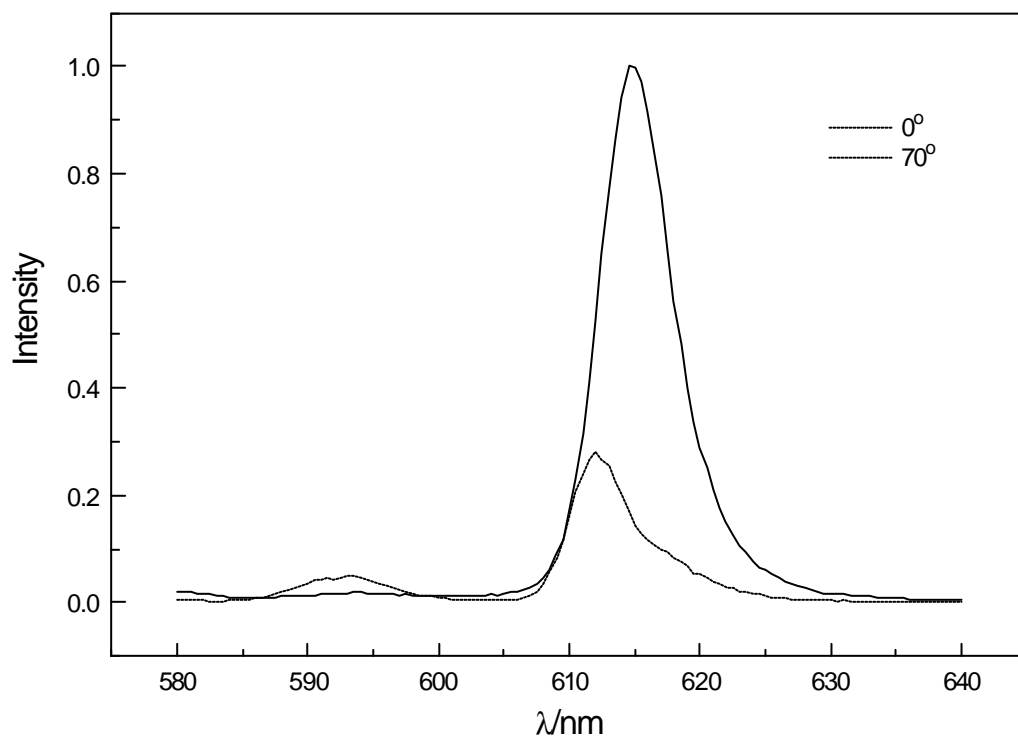


Figure 6.15 The emission spectra measured for an ion/mirror separation of 412nm at emission angles of 0° and 70° .

There are two features of interest in *figure 6.15*. Firstly, the relative intensity of the 590nm and 614nm emission bands is seen to depend on the emission angle, which as mentioned, is to be expected from their different radiation patterns. Secondly, it can be seen that the main 614nm emission in the $\theta=70^\circ$ spectrum is blue-shifted with respect to the $\theta=0^\circ$ spectrum, that is to say, the emission is stronger from the low-wavelength side of the emission peak. This can also be explained from the form of the radiation pattern since the emission from the low-wavelength shoulder of the 614nm transition will peak at a slightly higher angle than that from the long-wavelength shoulder. (Increasing the emission wavelength has the same effect as decreasing the ion-mirror separation.) The emission spectrum measured at higher angle will thus have an asymmetric 614nm peak, exhibiting greater emission on the shorter wavelength side of the peak.

6.7 Summary

In this chapter, the fluorescence emission from a monolayer of Eu^{3+} ions located above a planar mirror has been thoroughly investigated. Initially the distance dependence of the Eu^{3+} excited state lifetime was experimentally determined, and good agreement found with a classical model originally developed by *Chance, Prock and Silbey (1978)*. The nature of the power loss from the Eu^{3+} ions was also briefly discussed, and the surface modes excited by the dye monolayer identified.

The radiation pattern of the emission was also determined by measuring the angle-dependence of the fluorescence. Good agreement was found with a simple model which considered the interference between the direct emission from a dipole source and the reflected emission from the metal mirror. These measurements also demonstrated the different nature of the 614nm and 590nm emission from the Eu^{3+} ions. The emission at 614nm was seen to arise from an electric dipole transition, whilst the 590nm emission was attributed to a magnetic dipole transition. This will be confirmed in *Appendix A*, where the 590nm radiation patterns will be seen to be well modelled by assuming a

magnetic dipole source. The different nature of these two main emission bands also affects the emission spectra of the Eu^{3+} ion/mirror system. The relative intensity of the two bands has been shown to cycle with ion/mirror separation, giving further evidence of the non-electric dipole nature of the 590nm emission.

The experimental results from this chapter have demonstrated the eminent suitability of the LB technique for investigation of the fluorescence emission from dye monolayers above a mirror interface. The choice of the Eu^{3+} complex was shown to be an apposite one, particularly with respect to the quality of the monolayers formed. The emission lifetime was found to be highly single-exponential, emphasising the identical optical environment of the Eu^{3+} ions within the monolayer (all having the same distance from the mirror interface); a prerequisite for the study of fluorescence above corrugated interfaces.

This subject will be studied in the following chapter, where the fluorescence of dye monolayers deposited onto metallic diffraction gratings will be examined using similar techniques to those described here.

Chapter 7

Fluorescence above corrugated surfaces

7.1 Introduction

In the previous chapter, the fluorescence of dye monolayers above planar mirror interfaces was studied in some detail, and the nature of the factors affecting the decay process discussed for different molecule/mirror separations. It was found that the dominant decay process for dye molecules close to the mirror was the excitation of surface-plasmon polaritons at the metal interface. The coupling to the SPP mode decreases with increasing molecule/mirror separation and for large separations, it is the interference between the direct and reflected dipole fields determines the spontaneous emission rate. It is, therefore, the intensity and phase of the reflected field at the dipole site that is of importance.

In chapter 5, it was seen that the availability of the SPP modes, and hence the interaction between SPPs and dye molecules was significantly affected by corrugation of the surface profile. This was demonstrated by the observation of enhanced photoabsorption by dye molecules when SPPs were excited, and the removal of this excitation channel when SPP propagation was prohibited by a grating-induced energy gap. The possibility that incident light may be diffracted from the corrugation also means that the reflected field from a grating will be considerably different from that of a planar structure, and so the interference condition will also be perturbed.

It is expected therefore, that the fluorescent emission from dye molecules above a grating will be significantly affected by the surface corrugation, since the grating will affect both the propagation of SPPs, *and* the reflected field at the dipole site. The situation is complicated by the different effect the corrugation has on the various decay mechanisms. The overall perturbation introduced by

the grating is thus hard to predict because the total emission rate will be determined by the interplay between these various decay routes.

7.1.1 Grating induced perturbations

The preceding discussion indicates that there are two separate issues to consider in deciding what effect a metallic grating has on the spontaneous emission rate of nearby dye molecules. When the molecules are very close to the interface, and can couple strongly to the SPP mode, it is the perturbation of the SPP modes by the corrugation that will determine the spontaneous emission rate modification caused by the grating. The major modification created by a grating is the introduction of an SPP energy gap, which is caused by the Bragg scattering of SPP modes from the corrugation. If the energy of the molecular optical transition lies within the gap region, then there will be no available SPP modes for the molecules to couple to, and so decay by the excitation of SPP modes is not possible. The dominant decay route for the molecules is thus removed and so the emission should be inhibited. Conversely, if the emission coincides in energy with the SPP band edges then the emission rate may be considerably enhanced because of the increased density of SPP modes per unit energy interval at the band edge.

When the molecules are sufficiently distant from the interface that they can no longer couple to the SPP modes of the interface, the effect of the corrugation is determined by the modification of the reflected field at the dipole site. The diffractive nature of the grating surface is now of paramount importance because the ability of the grating to scatter the dipole field will lead to a change in intensity (and phase) of the fields at the dipole site. The interference condition will thus be altered, and hence the spontaneous emission rate of the molecules changed. In a simple way, this effect can be explained by consideration of the redistribution of the emitted power amongst the diffracted orders. The reflected field at the dipole site will no longer consist of simply the contribution from the specular reflection, but will be the sum of all the available diffracted orders.

The relative strength of these different effects will obviously be determined by the exact profile of the grating surface. The existence of an SPP energy gap for a given wavelength, for example, depends on the parameters describing the profile. The position of gap centre will be determined by the pitch of the grating, whilst the gap width is related to the depth of the corrugation. In *section 6.4.4* it was also seen that a dielectric overlayer increases the wavevector of SPP modes, and this causes the position of the gap centre to decrease in wavelength with increase in the LB spacer layer thickness.

The exact profile is also important when the molecule/grating separation is large, since the scattering of the dipole fields will also depend strongly on the grating parameters. For an incident component of the dipole field to be diffracted by the grating, the wave must sample a sufficient number of grating periods to experience the periodic modulation of the surface. If the pitch of the grating is longer than the wavelength of the emission then this condition is not satisfied, and minimal scattering of the dipole field is expected. In this case therefore, the interface effectively behaves as a planar surface.

If the pitch is much shorter than the emission wavelength, however, the near field of the dipole experiences many grating periods, and thus scattering of the field components may occur. In this case, all of the scattered orders will contribute to the field at the dipole site. The overall effect will thus depend on whether these different contributions add together in phase or not. The resulting interference condition will be much altered from the planar case, and so it is expected that if the grating pitch is shorter than the emission wavelength significant changes should be observable in the lifetime oscillations (see *figure 6.6*). Since the scattering strength increases with the grating depth, it is expected that this diffractive effect will become more important as the grating amplitude increases.

It is possible that the dipole emission will be significantly perturbed by the grating scattering of individual field components. This may possibly lead to the enhancement of the spontaneous emission rate by the coupling of previously non-dissipative components of the dipole field to modes such as the SPP, or to direct emission. The exact result of the scattering on the power loss as a function of in plane momentum will realistically only be discovered by the development and application of a theory similar to that outlined in *section 6.4*.

The situation is further complicated by the reduced translational symmetry of the corrugated surface compared to a planar surface. The local field above the peaks of the grating will be completely different to that in the troughs, leading to the inequivalence of dipole sites laterally displaced across a grating period. The dye monolayer thus experiences a continuously changing optical environment as a grating groove is traversed, even though it is positioned at the same height above the interface. The result will be that the time dependence of the fluorescence decay of a dye monolayer above a grating interface will be non-exponential, unlike that for a planar interface. The degree of non-exponentiality will be determined by the difference in the local field at the extremal dipole sites, and so will be related to the amplitude of the grating profile.

In the preceding discussion, it has been seen how corrugation of the surface may affect the spontaneous emission rate of the dipole due to the alteration of the planar boundary conditions. This is not the only effect that may be observed, since breaking the translational symmetry of the surface also allows the scattering and re-radiation of the surface modes excited by the decay of the molecules. In the planar case these modes are non-radiative, and are bound to the structure. Corrugation of the structure allows these modes to scatter from the periodicity and hence lose in-plane momentum, allowing strong re-radiation to take place.

7.1.2 Previous studies

Whilst there has been much study of the fluorescent emission from corrugated structures, most work has focussed on the details of the surface mode re-radiation, and relatively little attention paid to the possible change in the spontaneous emission rate. The first experimental study was by *Knoll et al. (1981)*, who examined the grating scattered fluorescent emission arising from the SPP modes excited by a dye monolayer. The origin of this emission was determined by measuring the angle and wavelength dependence of the emission peaks, effectively mapping out the SPP dispersion curve. This work confirmed that the bulk of the emission from a dye layer near a metal was to the

SPP mode for spacer layer thicknesses of $\sim 10\text{nm}$. In a similar study, *Adams et al. (1982)* deposited much thicker spacer layer films (up to $2\mu\text{m}$) onto silver gratings and reported the observation of scattered waveguide modes as well as SPP re-radiation. This was a direct result of the ability of the thicker spacer layer used in that study to support guided modes. The existence of these grating scattered peaks was predicted by *Aravind et al. (1981)* using a perturbation approach that assumed small amplitude corrugations.

Recent studies at Exeter have been motivated by the possibility of controlling the emission of dye molecules by modification of the propagation of these surface modes. Initial experiments examined the emission from dye molecules directly adsorbed onto shallow metallic gratings, and inhibition of the SPP re-radiated emission was observed in the region of an SPP energy gap [*Kitson et al. (1995)*]. Unfortunately, the temporal dependence of the fluorescence could not be measured in this study, and so the effect of inhibiting the SPP decay channel on the overall emission rate of the dye molecules was uncertain. It is possible that the spontaneous emission rate of the molecules was unaltered and that the emission was simply shifted to an alternative decay channel, such as direct radiation. This highlights the importance of measuring the excited state lifetime of the emitting species, since only this gives the spontaneous emission rate unequivocally.

Such time-dependent studies have been carried out recently by *Amos (1997)*, who made the first measurements of the spontaneous emission rate of Eu^{3+} ions above metallic grating structures. In these experiments, significant changes in the excited state lifetime were only seen for the deepest gratings studied, which had a pitch of 400nm and amplitude of 60nm . The largest effects seen were for larger molecule/grating separations, and were attributed to the reduction in reflectivity of the corrugated surface in comparison to a planar surface. Despite the lifetime modification seen, the fluorescent decays were single exponential for all molecule/grating separations measured, and so the expected inequivalence of different dipole sites above the grating could not be confirmed.

So far, very little theoretical work has been done on the fluorescence emission of dye molecules above corrugated surfaces, especially in comparison

with the large body of work carried out for the planar case. Most of the relevant studies have concentrated on the limiting case of small amplitude corrugation in an attempt to model the effect of surface roughness on emission rates. As discussed in chapter 2, Leung and co-workers have predicted large decay rate changes for small surface corrugations, which have not yet been observed experimentally [Leung *et al.* (1988), Blacke and Leung (1997)]. Comparison of experimental results with these papers is difficult, however, since the authors perform calculations as of function of the dipole oscillation frequency, which is not a parameter easily varied experimentally.

In this chapter, the results of an experimental study of the fluorescent emission from dye monolayers above grating interfaces is presented, which builds on the planar interface work carried out in chapter 6. Initially a shallow grating structure of long pitch was studied, and both the spontaneous emission rate and radiation pattern were measured as a function of molecule/mirror separation. Subsequently, a series of gratings of shorter pitch were studied, and the effect of varying the amplitude of the grating profile investigated. Again, measurements were made of both the spontaneous emission rate and the radiation pattern.

7.2 Grating fabrication

The fabrication and characterisation of the corrugated samples used in this chapter was much more difficult than the equivalent procedure for the planar samples used in chapter 6. In order to carry out a systematic study of the effect of the grating profile on the fluorescence from dye monolayers, a wide range of gratings of different pitch and amplitude were required. Because of this, the diffraction grating substrates used in this work were all fabricated in-house, using a holographic technique. Substrates were coated with a light-sensitive photoresist film, which was subsequently exposed to the interference pattern created by the recombination of two expanded beams of coherent laser light on the substrate surface. Exposure to light renders the photoresist more soluble in developer, and so development removes the exposed regions of resist to leave behind a sinusoidal surface profile.

The resulting profile is very sensitive to the nature of the development process, leading to slight variation in the profile from sample to sample. This meant that every grating sample had to be characterised before deposition of the multilayer spacer/dye monolayer structure. Deposition of LB material onto these corrugated structures was also found to be considerably more difficult than deposition onto planar surfaces, and the technique used had to be suitably adapted. Because of these technical difficulties, the fabrication of the grating samples and the LB deposition technique used will be described in some detail before the experimental results are presented.

7.2.1 Substrate preparation

The grating structures studied in this chapter were fabricated on silica substrates identical to those used in the planar work described in chapter 6. The choice of substrate was mainly governed by the suitability for LB deposition, and this point will be discussed further in *section 7.2.5*.

Initially, the silica slides were immersed in concentrated nitric acid for 10 minutes to remove gross contamination, and then rinsed in deionised water. The slides were then degreased by ultrasonically agitating them at 50°C in a bath of acetone for 30 minutes. After drying, the rear faces of the slides were then painted with black lacquer (Ebonite) to minimise back reflections during exposure in the interferometer. The front faces were then drag-cleaned using lens tissue soaked in chloroform, followed by a similar treatment using propan-2-ol. After removing any remaining dust using filtered inert gas, the now clean slides were placed in a light-tight die-cast box and baked in an oven at 120°C for 60 minutes. This process was designed to drive off any moisture, which is known to reduce the adhesion of photoresist to silica. To further improve the photoresist adhesion, the substrates were exposed to HMDS vapour in a similar manner to that described in *section 6.2*. These precautions were taken since it had been previously found that deep grating structures written into photoresist films can cause the photoresist film to become detached from the silica substrates during the deposition of LB material [*Amos (1997)*]. This is believed to be due to the surface tension of the floating monolayer, though the exact

mechanism is unknown. No such problems were encountered during the present study, and so the baking and HMDS treatment seems to have achieved the desired effect.

The photoresist material was then deposited onto the substrates using a spin-coating technique. This was carried out in a clean-room environment to reduce contamination of the samples with airborne dust particles. As with the LB deposition technique, dust can seriously affect the spin-deposition of films, since even small dust particles on the face of the substrate can cause the creation of “boomerang” defects. Usually, this is not a great problem because the defect regions can be avoided when carrying out an optical experiment. For samples intended for LB deposition, however, it is important to obtain as defect-free a surface as possible. This is important because the presence of imperfections on the substrate leads to poor LB film transfer; the disruption caused by the initial defect grows with each new layer of film deposited, and can lead to samples becoming unusable. Variation in the grating fabrication process meant that it was also impossible to guarantee identical grating profiles on successive substrates. In order to ensure that different spacer layer regions could be compared for a given grating profile, it was thus necessary to put as many regions as possible on a single grating substrate. The presence of defects would therefore reduce the useable area substantially.

Because of the sensitivity of the photoresist material to short wavelength light, the deposition had to be carried out under safe lighting conditions to avoid pre-exposure of the samples. This was achieved by placing yellow filters over the fluorescent room lights. The substrates were then centred on the vacuum chuck of the spinner and drag-cleaned a final time. Photoresist (Shipley S1805) was then deposited drop-wise onto the substrate using a syringe until the surface was completely coated. The substrate was then spun at 3000 *rpm* for 40 seconds in order to form a thin uniform film. Because the formation of defect-free films was critically dependent on the absence of particulate contamination, all of the glassware used to handle photoresist was cleaned and rinsed in acetone before any photoresist was introduced. The photoresist was itself filtered immediately prior to deposition using a 0.2 μm pore diameter filter attached to the end of the syringe in order to remove any coagulated material.

The thickness of the deposited films could be varied by altering the spin speed [Vukusic *et al.* (1992b)]; the values quoted above gave rise to films of thickness $\sim 0.5\text{nm}$, as determined by an interferometric method. The substrates so coated were replaced in the light-tight box and then baked again in the oven at 90°C for 30 minutes. This had the effect of driving off solvent occluded within the photoresist film, leaving behind the desired polymer base. After cooling, the photoresist-coated substrates were ready to be exposed in the interferometer.

7.2.2 Exposure and development

Many designs of interferometer are suitable for grating fabrication [Hutley (1982)]; the one used in this study is illustrated in *figure 7.1*. It was chosen for its compactness, ease of use and had the advantage of not needing to be operated in a dust-free environment.

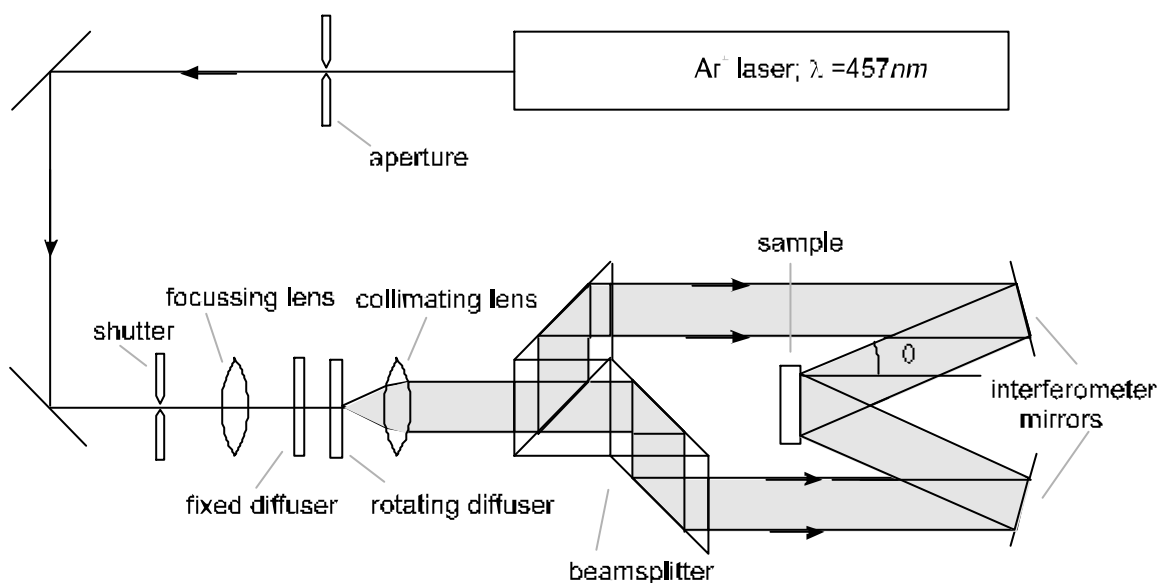


Figure 7.1 The interferometer used for grating fabrication.

The light used to expose the samples was provided by an argon ion laser operating on the $\lambda = 457.9\text{nm}$ line. The $\lambda = 488\text{nm}$ line could also be used, but since the photoresist absorption maximum lies in the UV region, it is more sensitive to light of shorter wavelength, and correspondingly shorter exposures

could be used. This helped to minimise the effects of thermal drift during the exposure.

The light is first focussed onto a rotating diffuser using a short focal length lens. A stationary diffuser is then placed just before the rotating diffuser ($\sim 10\text{mm}$) and its position adjusted until the resulting speckle pattern reduces the transverse spatial coherence of the beam to roughly the size of a dust particle. A second lens is then placed a focal length away from the rotating diffuser to produce an expanded and collimated beam.

The diffusers have a very important rôle to play in the successful operation of the system, and are instrumental in allowing the interferometer to be used outside an ultra-clean environment. In the absence of the diffusers, the light diffracted from any dust particle within the system would be coherent with the rest of the wavefront, leading to the formation of interference rings on the grating substrate. This obviously severely limits the quality of the gratings produced, since the interference rings are considerably larger in dimension than the dust particles that create them. The use of diffusers creates a random speckle pattern instead of a spatially coherent beam, the size of the speckle and thus the transverse spatial coherence being determined by the spacing between the ground-glass diffusers. When this now spatially incoherent light is recombined at the substrate, only light originating from the same initial speckle region before the beamsplitter can interfere coherently. This effectively removes the interference problem, since any scattered light from dust particles is completely incoherent with the rest of the wavefront and can only interfere with the region of speckle which followed the opposite path through the interferometer.

The beamsplitter itself is composed of five 45° prisms made from BK7 glass, the hypotenuse of the first prism being coated with a suitable thickness of aluminium to split the beam into two beams of equal intensity. The prisms are matched together using a liquid crystal material which is isotropic at room temperature (PCH32, Merck); the material being selected for its non-volatility. Note that since five prisms are used, not seven, the two optical paths through the beamsplitter are not equal. This is not a problem since the coherence length of the laser ($\sim 200\text{mm}$) is much greater than the resulting path difference.

The two expanded beams emerging from the beamsplitter are then reflected from two interferometer mirrors to overlap on the substrate, thus creating an interference pattern. The pitch of the grating is determined by the periodicity of this interference pattern, and is thus related to the angle of incidence of the beams on the substrate. The grating pitch λ_g is given by the formula

$$\lambda_g = \frac{\lambda_0}{2 \sin \theta} \quad (7.1)$$

where λ_0 is the wavelength of the radiation writing the grating, and θ is the angle made by either beam with the substrate normal. Using the shortest wavelength light source available, this technique allowed gratings to be written with pitches ranging from $\sim 230\text{nm}$ to about $3.5\mu\text{m}$. This pitch can be shortened if necessary by matching the substrate to a prism, allowing the grating pitch to be reduced by a factor equal to the refractive index of the prism.

The interferometer is aligned by removing the diffusers and replacing the substrate with a mirror. The two interferometer mirrors are then positioned so that the beams overlap on the substrate mirror. A fiducial reference marker is placed in the expanded beam before the beamsplitter, and coarse alignment achieved by overlapping the resulting two images on the mirror substrate. The marker is then removed, and replaced by a short focal length lens. This destroys the collimation of the incident beam, replacing the plane wavefronts with spherical wavefronts. If the system is not aligned perfectly, then interference fringes appear in the back-reflected beam emerging from the side of the interferometer. The beams can then be aligned to within a wavelength by adjusting the interferometer mirrors to eliminate these fringes whilst simultaneously maintaining the passage of the back reflections from the interferometer through the initial aperture. The substrate is held within a kinematic mount, so the alignment mirror can be removed and replaced with a photoresist-coated blank without destroying the alignment of the system. This arrangement allows alignment to be maintained from exposure to exposure, and so many samples can be exposed without needing to realign the system. The sample holder itself is mounted on a screw thread so that the incidence angle of the beams, and hence the grating pitch, can be varied easily and precisely.

After successful alignment, the photoresist-coated samples can then be exposed in the interferometer; the “fringe” lens must be removed and the diffusers replaced in the system. The eventual grating profile is dependent on both the exposure time and the subsequent development time; the gratings used in this study were typically exposed for between 2 to 10 minutes, depending on the depth of grating required. The laser itself was operated with a power output of $\sim 300\text{mW}$, which resulted in an irradiance of $\sim 6\text{mWcm}^{-2}$ at the sample. The effect of the exposure is to record the interference pattern as a solubility profile in the photoresist film. This can be converted into a surface relief profile by dissolving away the exposed resist using a suitable developer. The exposed samples were thus immediately removed from the interferometer, and placed in a beaker. About 50ml of developing solution (50% [v/v] Shipley Microposit developer in deionised water) was then poured onto the substrate, completely immersing it. After a period of 60 seconds, the substrate was removed from the solution and quickly rinsed with deionised water to halt the development process. The use of dilute developer slowed the dissolution of the exposed resist, thus allowing greater control over the development process. After drying the substrate with filtered inert gas, the quality of the grating could be checked. This was carried out by illuminating the substrate with a filament lamp and observing the uniformity (or not) of the diffraction across the width of the grating region. The gratings produced in this manner were not chemically, or mechanically robust, and further treatment was required to produce usable samples.

7.2.3 Post-treatment

Immediately after development, the gratings were placed under a mercury spectral lamp for 2 minutes to completely expose the remaining photoresist. The gratings could then be made more robust by exposing them to short wavelength UV light ($\lambda=254\text{nm}$) from a second mercury lamp for 25 minutes. This had the effect of cross-linking the photoresist, increasing the mechanical strength of the grating. The hardness of the gratings could be increased further by baking them in an oven at 180°C for 4 hours. Even after

this process, the gratings were not totally resistant to chemical attack, and were adversely affected by both organic solvents and acids. This made the removal of LB films and metal coatings difficult and subsequent cleaning impossible.

Accordingly, such photoresist gratings could be used only once, and thus characterisation of the surface profile had to be carried out *prior* to the deposition of LB multilayer structures. This would normally take place *after* the intended experiment, so that time and effort were not wasted on the characterisation of samples that were rendered unusable by poor LB deposition in subsequent stages of the fabrication process.

7.2.4 Fast atom etching

More permanent structures could be made by transferring the grating profile into the silica substrate, which is chemically inert, and extremely mechanically robust. This was achieved by fast-atom etching the gratings using a beam of argon atoms. The photoresist grating substrates were placed in a vacuum chamber which was evacuated to a pressure of $10^{-3}Pa$ and then purged with oxygen-free argon until the pressure reached $\sim 6Pa$. This process was designed to flush any oxygen from the chamber, since oxygen atoms preferentially etch photoresist, leading to severe flattening of the etched grating profile. A continuous flow of argon was then fed to an ion gun within the chamber *via* a needle valve, maintaining a constant chamber pressure of $6Pa$. A plasma was then struck by ionising the argon atoms using an electron gun, and the argon ions accelerated through a potential of $1.5kV$ at a current of $20mA$. The ion beam was then neutralised, and made incident upon the samples.

The samples themselves were mounted using heat-sinking compound onto a copper stage positioned about $200mm$ below the ion gun. These precautions were taken to in an effort to minimise the heating of the photoresist film during the etching process. Excessive levels of heat could melt the thin photoresist film, either shallowing or destroying the grating profile before it could be transferred to the silica. The stage was slowly rotated during the etching process, sweeping the samples through the ion beam. This ensured that the

etching was uniform across the sample, and allowed the samples time to cool between beam exposures. Samples intended for etching were deposited from photoresist diluted 1:1 with thinners (Hoechst AZ1350) and spun at the increased speed of 4000 rpm to produce thinner photoresist films. Even so, the time taken to etch through to the silica completely was typically between 6 and 8 hours.

Unfortunately, it was found that the resulting grating profiles were substantially shallowed by the etching process, and consequently, deep photoresist grating structures could not be transferred into silica substrates. In the studies carried out here therefore, the use of etched gratings was limited to the shallower profiles, and deep grating studies had to be carried out using photoresist-based structures.

7.2.5 LB deposition

As mentioned previously, the deposition of LB material onto corrugated surfaces was found to be an extremely vexatious process. Whereas the deposition of LB spacer layers onto planar surfaces was a relatively facile procedure, and good film quality was easy to achieve, this was not so with corrugated substrates used. This was especially true of the more extreme cases of gratings with short pitch and/or large amplitude.

The presence of the grating corrugation was found to induce the formation of significantly more defects in the transferred film than was found for planar substrates. Not surprisingly, the problem was more significant for the deeper gratings attempted. The number and size of these defects was also found to increase with the number of layers deposited, since irregularities in the underlying layers acted as nucleation centres for defects in subsequently deposited layers. Inevitably, once this process had started to occur, the sample was rendered unusable since the transfer process was completely disrupted.

The principal mechanism which complicated deposition was the “pinning” of the film at defect sites on the substrate during transfer. While transfer is taking place, it is essential that the meniscus drains away from the substrate uniformly as the sample is withdrawn from the subphase. This indicates that the

monolayer has been transferred to the substrate smoothly, and with minimal problems. Occasionally it was observed that the meniscus did not drain away from the substrate smoothly, but would instead become trapped at a certain point on the substrate surface. As the substrate was withdrawn further, the meniscus would be pinned to this point, and film transfer could not occur in the region of the substrate immediately below the defect. If this occurred then the sample inevitably became wetted on the next downstroke since in the defect region the hydrophilic ends of the 22-tricosenoic acid molecules would be outermost. In these cases, regrettably, the sample had to be discarded.

The poor deposition on the grating substrates is most likely caused by the macroscopic curvature of the surface, as reported in previous work [Amos (1997)], and similar precautions were taken to ensure good deposition in this study. It was found to make a good deal of difference whether the grating sample was immersed through the subphase with the grooves running vertically, or horizontally. In the horizontal case, the LB transfer was found to be extremely poor, which is possibly a result of the constantly changing angle of contact between film and water as the substrate is immersed in the subphase. This problem is avoided by immersing the sample with the grooves running vertically, since in this case the contact angle is constant. Unfortunately, it was not always possible to follow this procedure when depositing multi-region samples, since it was necessary to rotate the sample by 90° half way through the deposition process to achieve the required structure. In these cases, the first deposition was always carried out with the grooves running vertically, since good transfer in the first layer helped to ensure the trouble-free transfer of subsequent layers.

The other, more significant precaution taken whilst dipping grating substrates was the use of extremely slow transfer speeds. Whilst 22-tricosenoic acid was routinely deposited onto planar substrates at speeds of $\sim 1\text{ mms}^{-1}$, the rate had to be substantially reduced for grating structures. For shallow gratings, transfer speeds of $\sim 0.4\text{ mms}^{-1}$ were employed, which decreased to 0.05 mms^{-1} for the deepest gratings studied (pitch $\sim 415\text{ nm}$, amplitudes of $\sim 120\text{ nm}$). The use of such slow deposition rates was found to significantly improve the quality of the deposited films. This was aided by the ability to halt the process at the first sign of a problem, allowing the meniscus sufficient time to drain back to the

subphase surface. The incorporation of long pauses (~20s) between up- and downstrokes also helped to ensure that the meniscus had enough time to relax between deposition of layers.

After the deposition of the first couple of bilayers, the defect-free nature of which was critical for continued success, the deposition speed of subsequent layers could be increased to $\sim 0.4 \text{ mm s}^{-1}$. (Once coated by an initial layer of fatty acid, the subsequent deposition was found to proceed more smoothly). If the initially deposited layer was to only cover part of the substrate, a situation common during the fabrication of multi-region structures, slow transfer speeds could not be used for the whole deposition process. This was because significant degradation of the exposed silver surface occurred during the time taken to transfer the film at slow speeds. Subsequent deposition onto the exposed silver was extremely poor because of the now hydrophilic nature of the silver, and considerable wetting was encountered.

The nature of the substrate used was also found to influence the deposition process. Square silica slide substrates were chosen in preference to the standard 25mm diameter, 6mm thick silica disks initially used because they are much thinner ($\sim 1 \text{ mm}$), and consequently did not perturb the floating monolayer so much during LB deposition. The thick frosted sides of the disk substrates were found to wet considerably, distorting the subphase meniscus whilst deposition was in progress. This led to serious disruption of the floating monolayer, causing defects to form within the film, and hence adversely affected the LB deposition process. The non-uniform sample width of the disk substrates was also found to be a problem, since the transfer of material onto the substrate did not occur at a constant rate during immersion. This caused further disruption of the monolayer and defect formation on the periphery of the dipping region. The presence of a corrugated surface made good quality LB deposition a difficult proposition, and the success of the operation was critically dependent on the maintenance of a defect-free floating monolayer during deposition. The extra disruption caused by the disk substrates was thus to be avoided at all costs. The use of thin square substrates allowed the deposition of LB material onto deeper grating structures than was previously possible [Amos (1997)].

The square slides also had a larger surface area, and so more spacer layer regions could be deposited on a single sample, avoiding problems with sample-to-sample repeatability. The only problem encountered using these substrates was during spin-deposition of the photoresist film, where the film thickness was found to be non-uniform in the corners of the substrate. This was not serious, however, since these regions were easily avoided.

7.3 Long pitch grating measurements

The experimental study of fluorescence above corrugated surfaces commenced with investigation of the effect of making a small perturbation to the planar interface already considered. To this end, the first corrugated structure studied was a shallow grating of long pitch (*i.e.* the pitch was greater than the emission wavelength, and much greater than the grating depth). The etched grating used, of pitch 800.1 nm , was fabricated using the technique outlined in the preceding section.

7.3.1 Characterisation

After cleaning using standard techniques, an optically thick layer ($>200\text{ nm}$) of silver was deposited onto the grating by thermal evaporation. The sample was then immediately characterised by the excitation of SPP modes at the silver/air interface. This was achieved by measuring the angle-dependent reflectivity of the sample for incident TM-polarised light, as detailed in *section 5.2.1*. Using light of wavelength 632.8 nm , both -1 and $+2$ SPR features could be observed. Fitting the experimentally determined reflectivity to a theoretical model allowed both the grating profile and the permittivity of the silver to be determined. The experimental reflectivity data and the theoretical model are presented in *figure 7.2*, and the resulting fitted grating parameters given in *table 7.1*.

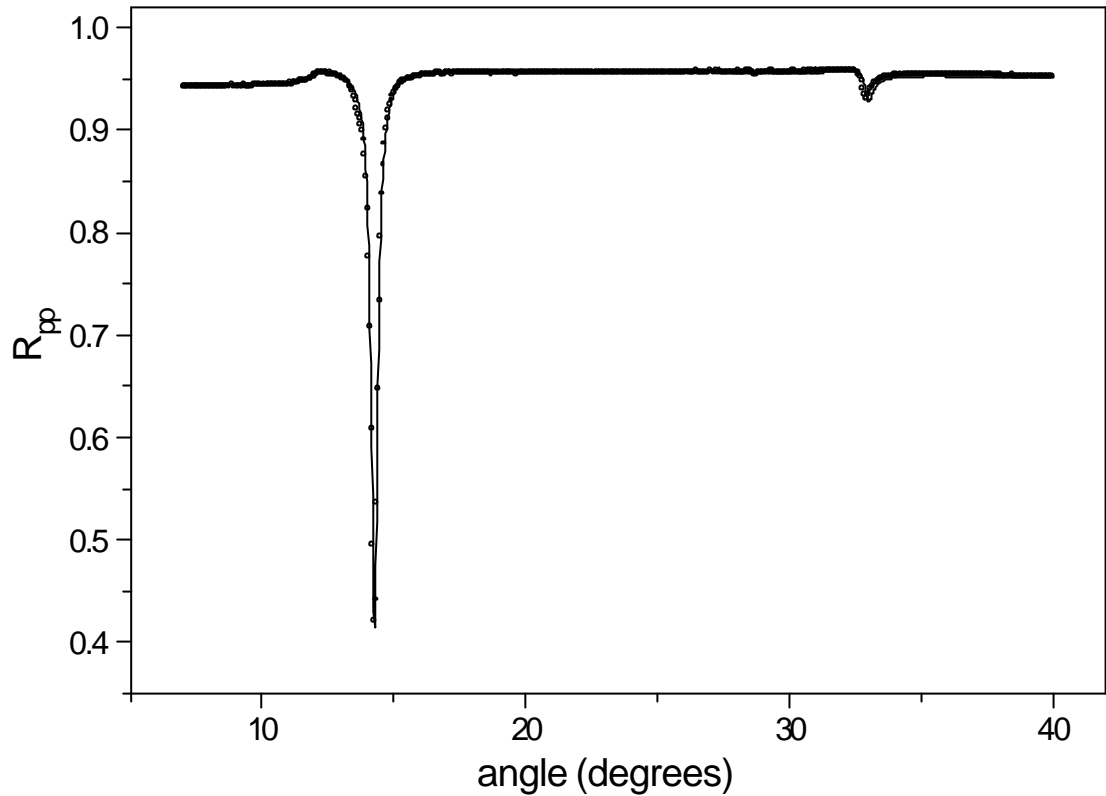


Figure 7.2 Angle-dependent reflectivity of the 800.1 nm pitch grating for TM polarised incident light of wavelength 632.8 nm . The circles are experimental data and the line is a theoretical fit.

Grating pitch, λ_g / nm	800.1 ± 0.1
a_0 / nm	10.0 ± 0.1
a_1 / nm	-0.9 ± 0.1
a_2 / nm	0.3 ± 0.1
$\hat{\epsilon}'_{\text{Ag}}$	-14.30 ± 0.05
$\hat{\epsilon}''_{\text{Ag}}$	0.79 ± 0.01

Table 7.1 Parameters used to obtain the fit in *figure 7.2*. The grating parameters relate to the components of the grating profile in the expansion $a(x) = a_0 \sin Gx + a_1 \sin(2Gx + \pi/2) + a_2 \sin 3Gx$, where $G=2\pi/\lambda_g$.

Once characterisation had taken place, the grating was stored in a vacuum chamber until the LB spacer layer structure could be deposited, in order to avoid degradation of the silver. The spacer layer structure was built up using a similar approach to that used for the planar samples. Initially, 216 layers of 22-tricosenoic acid were deposited onto the grating in seven steps, forming seven regions each a multiple of 36 layers thick. The grating grooves were oriented vertically during this first deposition to aid smooth deposition. The grating was then rotated through 90° and the process repeated by the further deposition of 30 layers, this time in six layer steps. The depositions were carried out at 0.6mms^{-1} , with the surface pressure kept constant at 30mNm^{-1} . The resulting structure had 38 regions each 4mm by 4mm , covering the range from 12 to 246 spacer layers in steps of six spacer layers. In this way, the entire range of ion/mirror separations of interest could be examined using a single sample. A monolayer of the Eu^{3+} complex was then deposited on top of the structure using the horizontal transfer technique with a surface pressure of 5mNm^{-1} . A monolayer of the complex was also deposited onto a pre-prepared witness sample consisting of 20 layers of 22-tricosenoic acid on a planar silica substrate.

7.3.2. Lifetime measurements

Measurements were then made of the time dependence of the fluorescence emission from the Eu^{3+} monolayer for each different spacer layer region of the grating sample. This data was then fitted to an exponential decay function to give the excited state lifetime of the Eu^{3+} complex as a function of the ion/grating separation distance. This data is presented in *figure 7.3*, together with the planar results from *figure 6.4* as a comparison.

It can be seen that the distance dependence of the lifetime of the Eu^{3+} ions situated above the grating is substantially the same as that found for the planar sample, for both large *and* small ion/mirror separations. The perturbation introduced by the corrugation appears to have had little effect on the spontaneous emission rate of the Eu^{3+} ions, which is perhaps to be expected, given the small depth to pitch ratio of the grating ($d/\lambda_g \sim 0.025$).

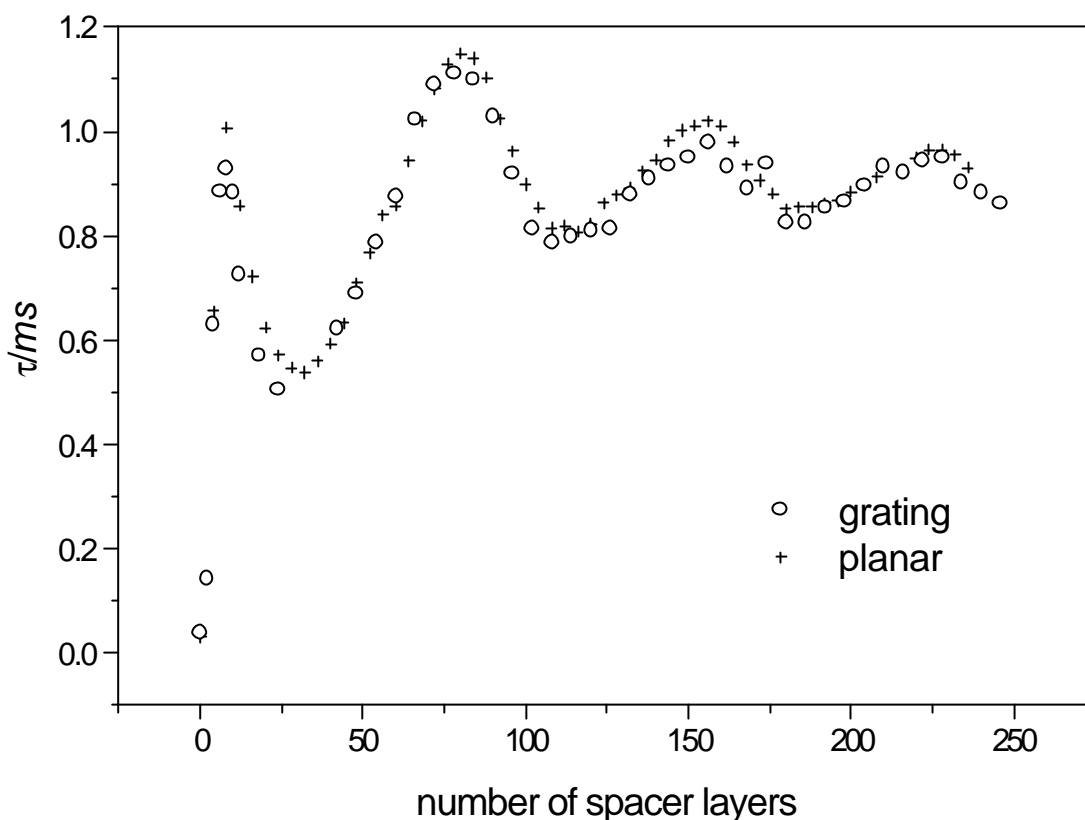


Figure 7.3 The experimentally measured lifetime of the Eu^{3+} complex above a silver grating of pitch 800.1 nm as a function of the ion/metal separation. The hollow circles are the grating data, whilst the crosses are a planar comparison taken from *figure 6.4*. Note that the thickness of a single spacer layer is equal to 2.6 nm .

Figure 7.3 shows that the amplitude of the lifetime oscillations is undiminished for the grating sample, suggesting that in this distance regime, the reflected field at the dipole site is comparable to that of the planar sample. It is conjectured that the near field of the dipole does not sample enough of the grating surface to scatter from the periodicity, and so only the specularly reflected fields are significant at the dipole site. The surface is thus effectively non-diffractive for the dipole emission, and the scattered orders do not influence the emission. This is reasonable, since the extent of the dipole near field, comparable with the emission wavelength, is similar to that of the grating pitch.

The dependence of the lifetime for small ion/mirror separations is also very similar to the planar case, which implies that the coupling to, and the nature of the SPP modes is unperturbed by the grating corrugation.

It was found that the time dependence of the emission was given by a single exponential function for all spacer layer thicknesses considered, indicating that the Eu^{3+} ions within a given film had the same decay rate, and hence experienced identical local environments. For this grating therefore, the difference in environment between the regions above a grating peak and those above a grating trough was minimal. Examples of the time-dependence of the fluorescence emission for spacer layer thicknesses corresponding to the initial lifetime minima, and the second lifetime maxima, together with single exponential fits, are given in *figure 7.4*. These ion/mirror separations were chosen because they exhibit the most extreme difference in lifetime.

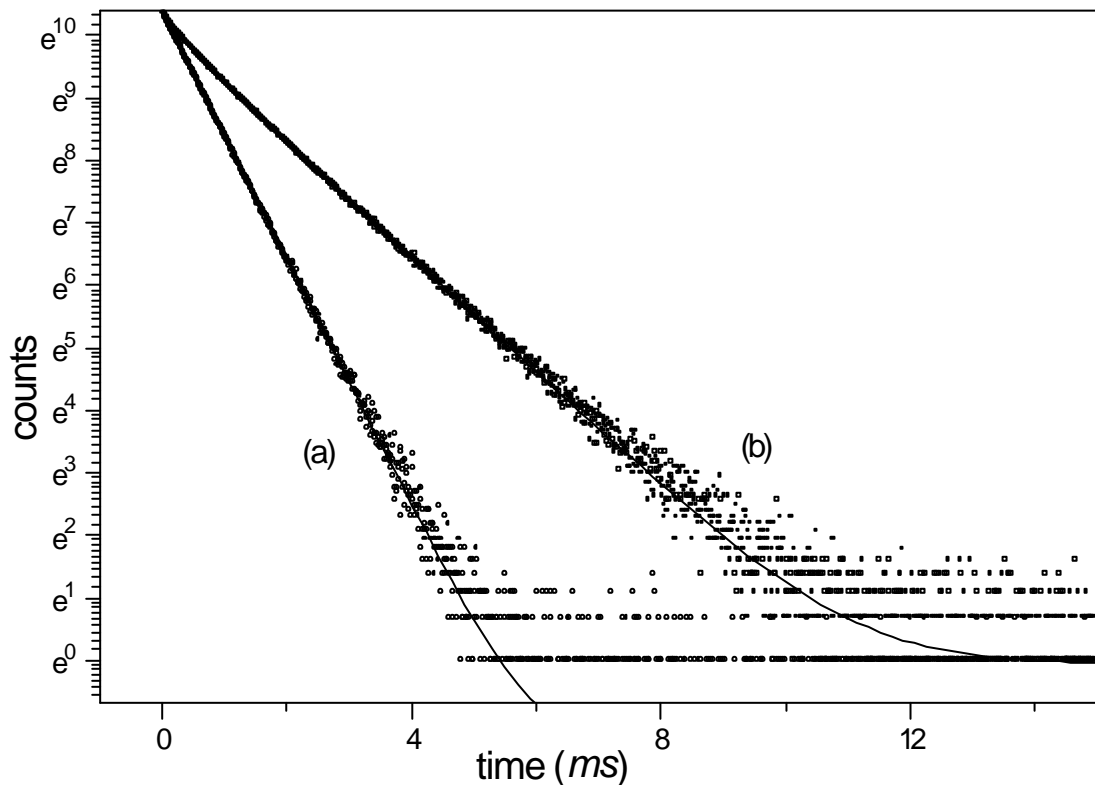


Figure 7.4 Fluorescence decay curves for Eu^{3+} ions located (a) 24 spacer layers and (b) 72 spacer layers distant from the 800.1 nm pitch silver grating, together with the single exponential fits.

7.3.3 Radiation pattern measurements

Using the method developed in the previous chapter, radiation patterns were measured for each different spacer layer region of the 800.1 nm pitch grating sample, for both p- and s-polarised $\lambda=614.7\text{ nm}$ emission. In the measurements made in this section, the sample azimuth was fixed at $\phi=0^\circ$, *i.e.* the radiation patterns were measured with the plane of emission perpendicular to the grating grooves. Whilst the presence of the grating corrugation caused little discernible change in the spontaneous emission rate of the Eu^{3+} ions from the planar interface dependence, considerable difference was found in the radiation patterns measured.

As well as the directly radiated emission, the angle-dependence of which was measured in chapter 6, the dye monolayer can also lose energy by excitation of surface modes such as the SPP and the waveguide modes supported by the structure. This was illustrated in *figures 6.7 and 6.8*, where the power loss of a monolayer of dipoles above a planar mirror was plotted as a function of the tangential wavevector and dipole/mirror separation. For the planar surface, these modes are non-radiative, and so the energy associated with them is effectively bound to the substrate.

Corrugation of the surface relaxes the condition that the wavevector must be conserved tangential to the interface, and allows these modes to become scattered by integer multiples of the grating vector. It was postulated in the previous section that the corrugation did *not* cause scattering of the dipole near field, since the extent of the near field was smaller than the pitch of the grating. This argument does not apply for the surface modes subsequently excited by the dipoles however, since these modes have propagation lengths of the order of 30 nm , or greater in the case of waveguide modes [Ræther (1988)]. After excitation by the dipole therefore, these modes propagate across the surface traversing many grating periods, and can thus scatter from the periodicity to couple to radiation modes according to the relation

$$k_M \pm mG = \pm k_0 \sin \theta. \quad (7.2)$$

Here, k_m is the wavevector of the relevant mode, $G=2\pi/\lambda_g$ is the grating vector and θ is the angle of emission of the scattered radiation, measured from the substrate normal. *Equation 7.2* is effectively the modified conservation of momentum relation for the corrugated surface.

The existence of this scattering mechanism results in the appearance of sharp emission peaks in the radiation patterns of corrugated samples. These peaks are absent from the planar radiation patterns and each peak can be identified with the scattering and re-radiation of a given surface mode. Examples of the measured radiation patterns from the 800.1 nm pitch grating sample are given in *figure 7.5* for spacer layer thicknesses of 60 and 180 layers respectively.

It can be seen from *figure 7.5* that the radiation patterns for the grating sample consist of two contributions. Superimposed on top of the planar emission patterns, recognisable from chapter 6, are a series of narrow emission peaks which correspond to $-G$ scattered surface mode emission. The data in *figure 7.5* has been normalised so that the peak of the background planar emission has an intensity of unity, in order to allow a comparison with the corresponding planar radiation patterns. In each plot, the dashed line is the theoretical angle dependence calculated for a planar sample of the same thickness, and there is reasonable agreement between the planar theory and the grating data. This corroborates the idea that the dipole fields have not been significantly scattered by the grating; there are no “extra” interference maxima or minima to be seen, for example.

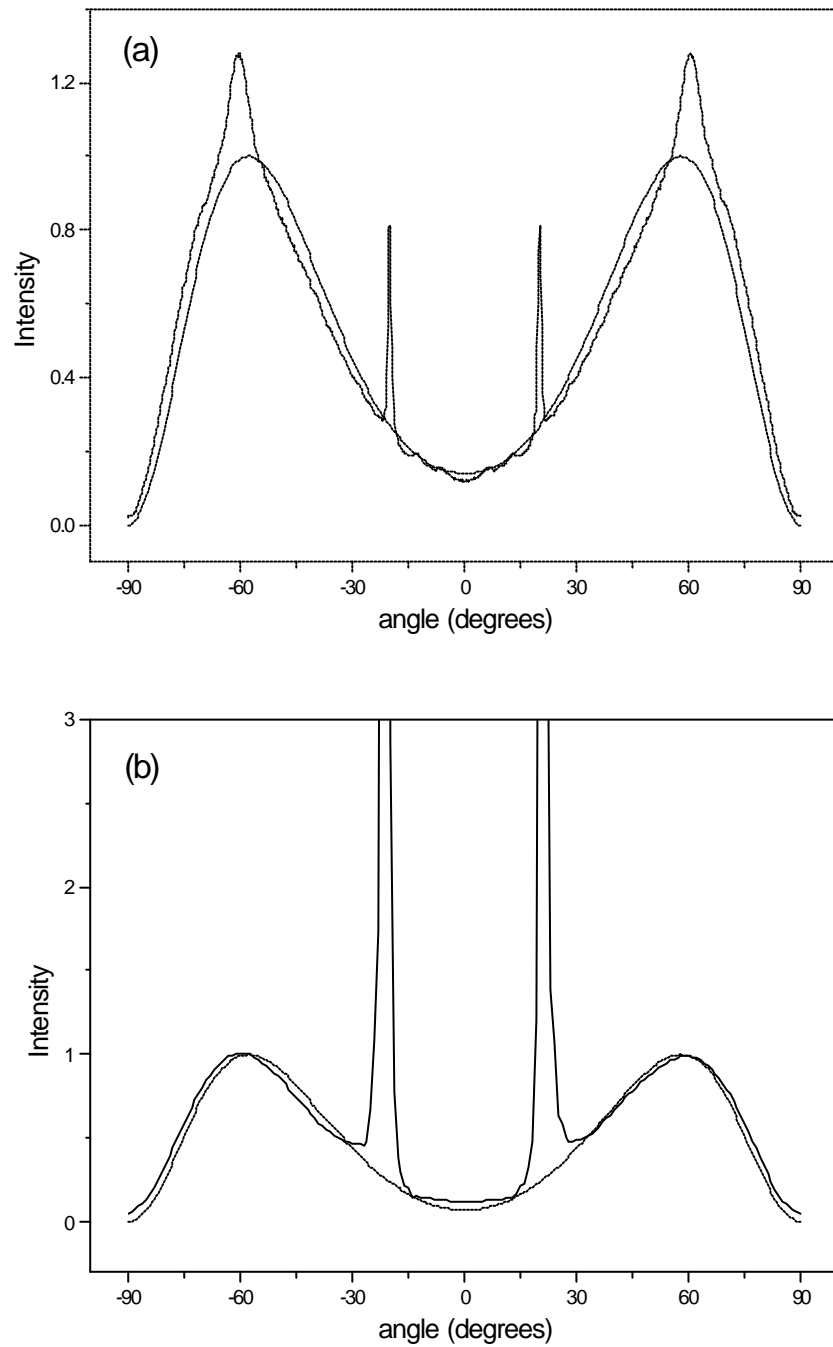


Figure 7.5 Radiation patterns of the 60 spacer layer region of the 800.1 nm pitch grating sample, for (a) p-polarised emission and (b) s-polarised emission. The continuous lines are the experimental data, whilst the dashed line is the theoretical dependence for the corresponding thickness planar sample. The azimuthal angle is zero in each case.

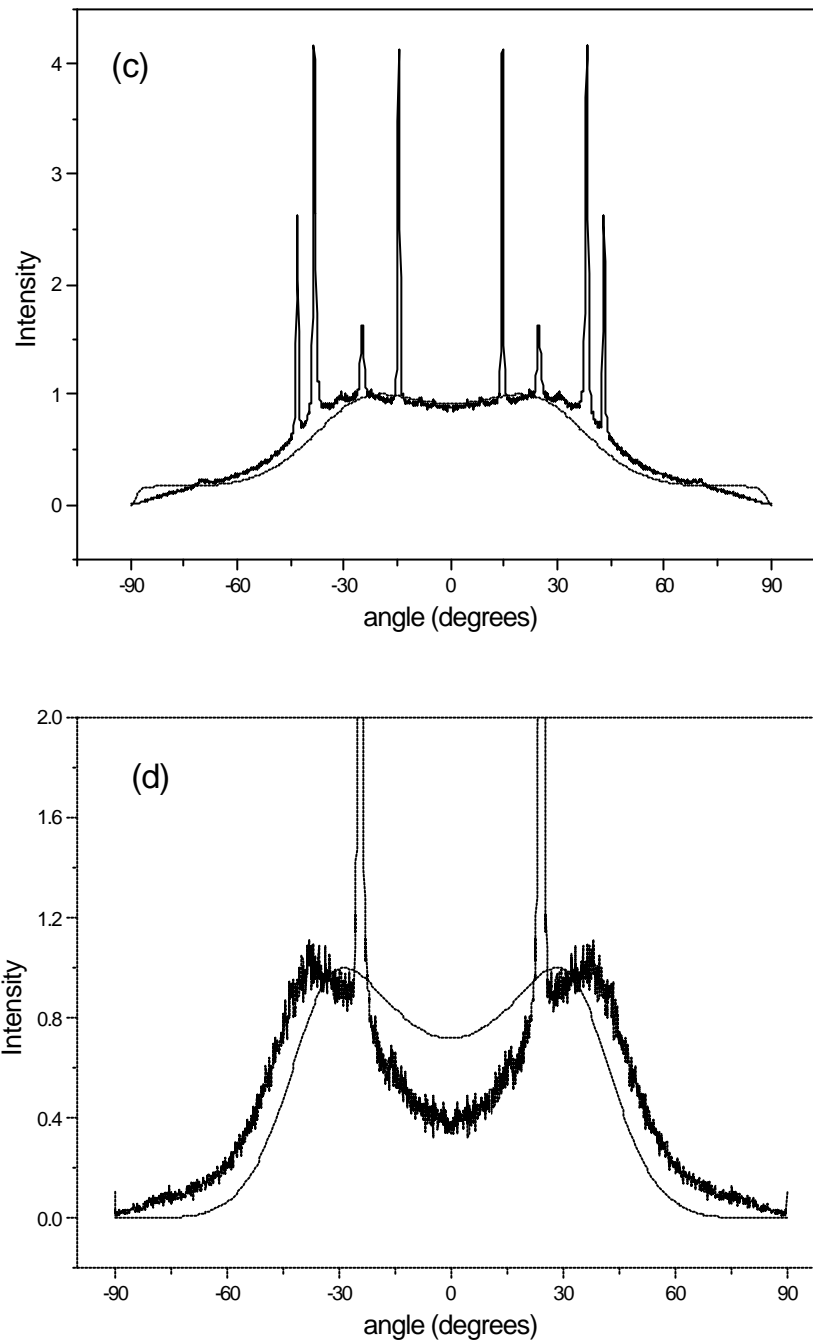


Figure 7.5 (continued) Radiation patterns of the 180 spacer layer region of the 800.1 nm pitch grating sample, for (c) p-polarised emission and (d) s-polarised emission. The continuous lines are the experimental data, whilst the dashed line is the theoretical dependence for the corresponding thickness planar sample. The azimuthal angle is zero in each case.

Examination of *figure 6.8* shows that the 60 layer (156nm) thick region of the sample is capable of supporting both the SPP mode and the first TE waveguide mode for 614.7nm emission. Both of these modes undergo $-G$ scattering from the grating to give the emission peaks in the radiation patterns of *figure 7.5a* and *b*. The TE_0 waveguide mode emission is visible in the s-polarised radiation pattern as a sharp peak at $\sim 21^\circ$, whilst the SPP emission is visible in the p-polarised radiation pattern as a broader peak at $\sim 60^\circ$, superposed on the peak of the planar emission. The p-polarised radiation pattern also has a much smaller emission peak at $\sim 20^\circ$, coincident in angle with the TE_0 emission peak in the s-polarised radiation pattern. The 60 layer film is not thick enough to support the first TM waveguide mode, and so the peak must be associated with the scattered TE_0 mode emission.

This anomalous behaviour is a result of the anisotropy of the LB spacer layer; the waveguide modes are not purely TE- or TM-polarised as they would be for an isotropic guide, but have a mixed polarisation state instead. This leads to polarisation mixing and thus the scattered emission from the TE_0 mode has a TM-polarised component, which is observed as a peak in the p-polarised radiation pattern.

Again, examination of *figure 6.7* shows that the 180 spacer layer region of the sample can support the SPP mode as well as four different waveguide modes (the TE_0 , TM_1 , TE_1 and the TM_2). These modes are all observed as scattered emission peaks in the p-polarised radiation pattern, but only the TE_1 emission is visible in the s-polarised data. The intensity of any scattered peak in the radiation pattern is dependent on a whole host of parameters, and so it is not surprising that certain features are not visible in the radiation pattern for a given sample thickness.

The most important consideration is the distribution of the modal fields through the guide structure, since this will determine the strength of coupling between the monolayer of dye molecules and the waveguide mode. If, for example, the dye monolayer lies at the node of the field distribution for a given mode, then the dye molecules will be unable to excite that particular waveguide mode. The converse holds true, and maximum coupling is obtained for waveguides whose field antinodes coincide with the dye layer.

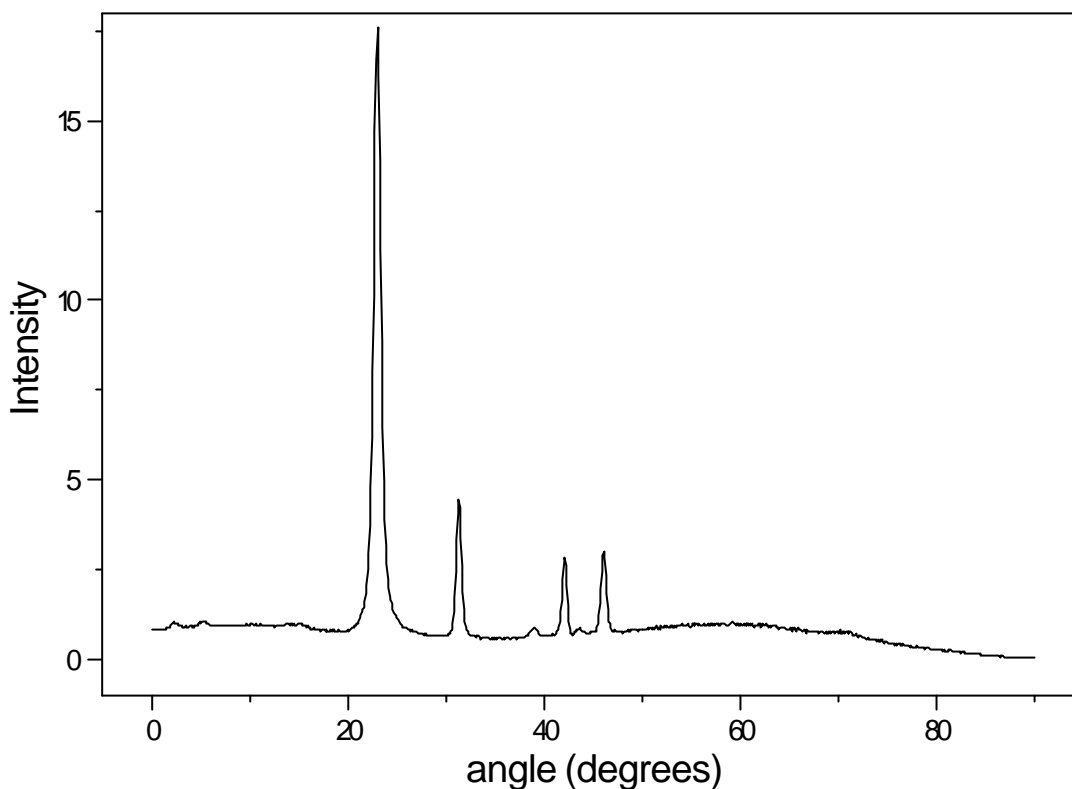


Figure 7.6 The p-polarised radiation pattern for the 222 spacer layer region of the 800.1 nm pitch grating sample. Four main emission peaks are visible, corresponding to (l-r) the TM_2 , TE_1 , TM_1 and TE_0 modes respectively. It can be seen that the highest order mode, the TM_2 , is the most intense.

The result of this argument is that the waveguide modes which are most strongly excited are those which have field maxima near the LB/air interface, since that is where the dye monolayer is located. A corollary of this is that the coupling to a given mode is strongest when it has just become guided, since the field intensity is large near the boundary for that case. As the thickness increases and the mode wavevector increases, the modal fields become more tightly confined within the guide, and so the coupling strength correspondingly decreases [Kaminow *et al.* (1974)]. The molecule/mode coupling for a given thickness of structure should thus be strongest for the highest order waveguide mode excited, since it will be closest to the cut off.

Experimentally, it is observed that the peak corresponding to the highest order mode is indeed the most intense, as *figure 7.6* shows for the p-polarised radiation pattern of the 222 spacer layer region of the grating sample. (For the

scattering provided by this grating, modes are introduced at low angle, and move to higher angles as the thickness of the guide increases.) The intensity of the peaks will also depend on the efficiency of mode scattering by the grating, however, and so the situation is not as clear cut as may be thought.

Consideration of the intensity of the emission peaks shows that it is possible to obtain significant increase in the intensity of the fluorescence signal by suitable choice of the observation angle. The most notable example here is that of the s-polarised emission from the 60 spacer layer region. The peak intensity of the TE_0 scattered emission is ~35 times greater than the peak emission of the planar background emission. This has obvious use in sensing applications, as suggested by *Sullivan et al. (1994)*.

7.3.4 Distance dependence of radiation patterns

By measuring the p- and s-polarised radiation patterns for the various regions of the grating sample, it is possible to map out the dependence of the dispersion of the various modes on the guide layer thickness. This is achieved by plotting the sine of the emission angle (in effect the normalised mode wavevector) for each mode as a function of the sample thickness. The true wavevector can be obtained by multiplying the sine by the free space wavevector and adding a grating vector. The distance dependence of the modal dispersion so determined is given in *figure 7.7* for both the p- and s-polarised emission respectively.

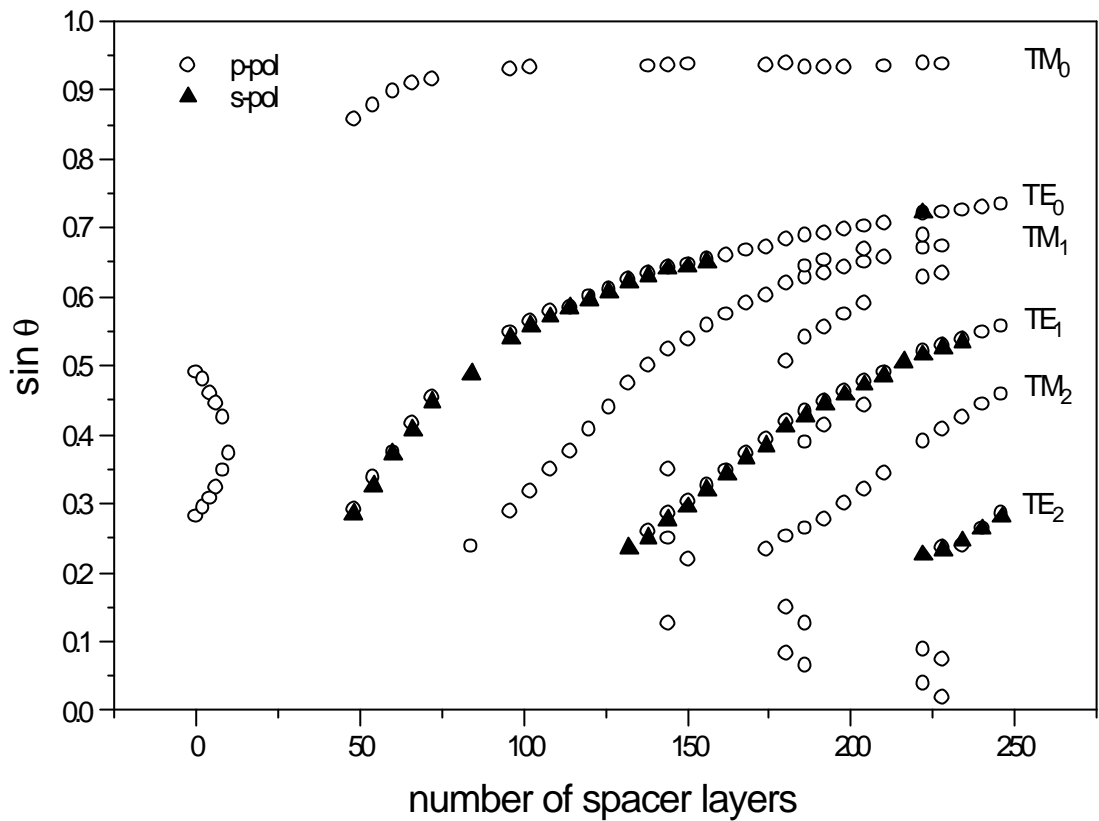


Figure 7.7 The dependence of the mode dispersion on the spacer layer thickness for the 800.1 nm pitch grating sample, as measured from both the p- and s-polarised fluorescence emission peaks. The relevant mode designations are made assuming an isotropic guide layer, although it can be seen that the modes are of mixed polarisation. Note that one spacer layer is 2.6 nm thick.

The dispersion of the modes given in *figure 7.7* compares well with the mode structure presented in *figure 6.7*, which was calculated for a planar isotropic structure. This is not really surprising given the shallowness of the grating; the dispersion of the modes will not be perturbed substantially by the presence of the corrugation. The main point to note is that the peaks have been scattered by $-G$ from the grating, which in this case, shifts the modes down in normalised tangential wavevector by 0.768 (k_g/k_0), bringing them into the $u < 1$ radiative region. The modes actually occur for normalised wavevectors with $u > 1$, and thus become radiative upon scattering.

The main branches of the dispersion curve have been assigned the relevant mode designations, assuming the guide layer is isotropic. This

assumption is seen to be untrue, as was suggested in chapter 6, since the emission from every TE mode is observed to have a small p-polarised component in addition to the main s-polarised emission. This s to p conversion suggests that the modes are actually of mixed polarisation state, indicating that the molecules within the LB film must be tilted out of the emission plane.

Interestingly, the corresponding p to s conversion is not seen; the TM modes do not give any measurable s-polarised emission. This is odd since the molecular orientation *does* allow this conversion process to take place. A possible explanation lies in the increased loss of the TM modes relative to the TE modes. This arises from the increased penetration of the fields of the TM modes into the metal film, leading to correspondingly higher absorption [*Kaminow et al. (1974)*]. If the TM modes suffer greater absorption, then the field intensity within the guide will be diminished, giving rise to a correspondingly smaller p to s conversion signal. It is observed that the TM modes do indeed have wider emission peaks than the TE modes (TM~0.7 as opposed to TE~0.5), which supports the idea that the TM modes have greater losses.

There are several other features of interest in *figure 7.7*. It can be seen that there are extra mode branches in the p-polarised emission which are not explicable from the above arguments. Inspection of *figure 7.6* shows that these features are of very low intensity; in addition to the four main waveguide emission peaks, six other minor features can be seen for a spacer layer thickness of 222 layers. These peaks arise from two main causes. The extra mode branches lying between the TE₀ and TM₁, TM₁ and TE₁ and the TE₁ and TM₂ branches are thought to arise from the anisotropy of the guide, since polarisation mixing can lead to the mode splitting. The other three anomalous branches, one of which splits off from the TM₀ branch for small d, the other two observable for $\sin\theta < 0.2$, arise from +2G scattering from the grating, and thus correspond to the emission from modes travelling in the opposite direction across the sample. This 2G scattering process is shown in *figure 7.8*, together with the experimental data, showing how the “anomalous” peaks are generated. Since the 2G scattering depends on the amplitude of the second harmonic

component of the grating profile, the scattered peaks are expected to be of low intensity ($a_1 \sim 1 \text{ nm}$), as is the case.

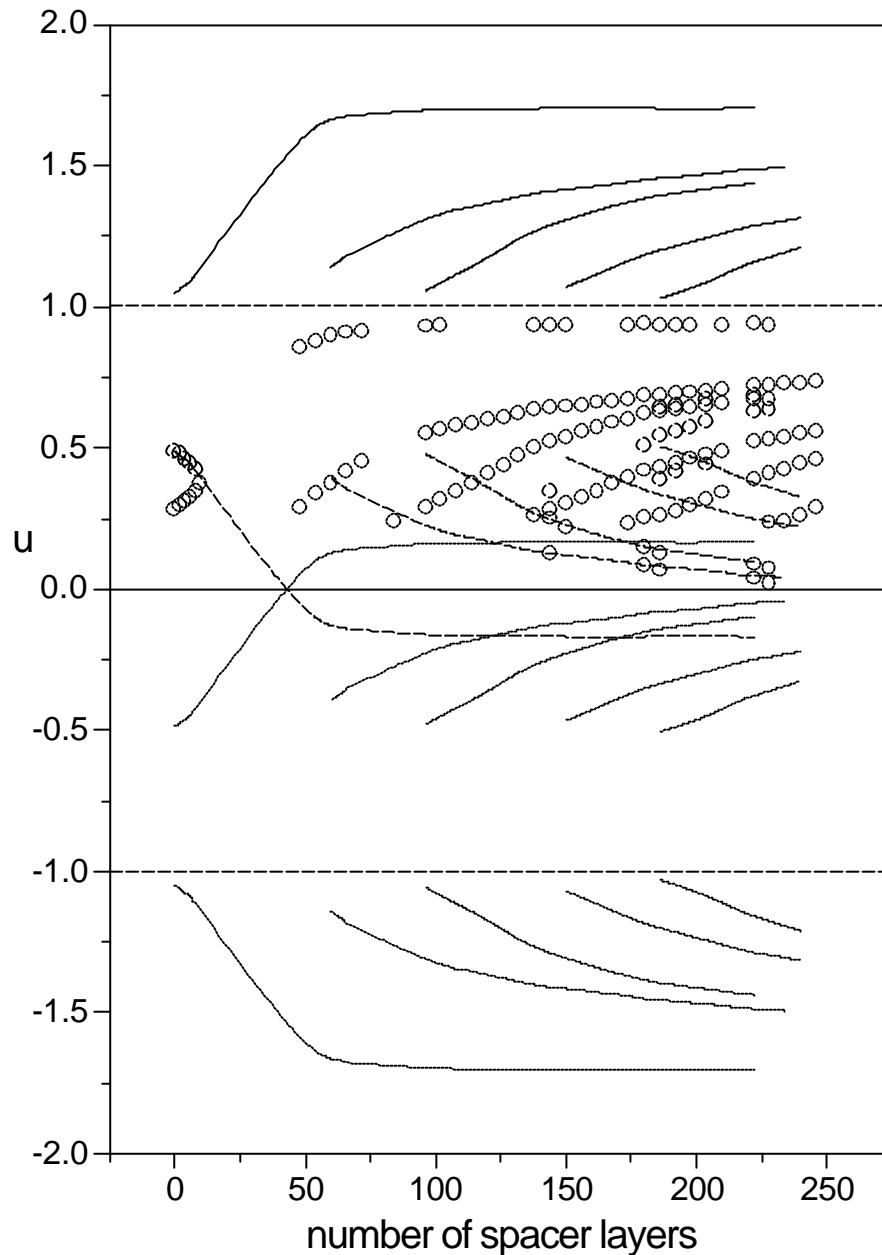


Figure 7.8 The data from *figure 7.7* re-plotted on expanded axes to show the nature of the scattering processes giving rise to the observed emission peaks. The black open circles are the experimental data, the dashed lines $+2G$ scatter and the dotted lines $-2G$ scatter. The continuous lines for $u < -1$ and $u > 1$ give the dispersion of the modes for a planar surface.

The thickness dependent modal dispersion presented in *figure 7.7* compares well with the results obtained by *Adams et al. (1982)* from

fluorescence measurements made on variable thickness nitrogen films adsorbed onto a silver grating.

7.3.5 Azimuthal dependence of radiation patterns

Since the dye monolayer can excite surface modes travelling in all directions across the grating surface, grating scattered emission can be observed for other azimuthal angles than the $\phi=0$ case considered in the previous section. In this case, the coupling condition given in *equation 7.2* must be altered, since the mode propagation direction is no longer coincident with the grating vector. The corresponding vector equation is

$$\mathbf{k}_M \pm m\mathbf{G} = \pm \mathbf{k}_0 \sin \theta \quad (7.3)$$

The resulting k -space map for a grating with $G < k_0$, corresponding to the experimental case, is given in *figure 7.9*.

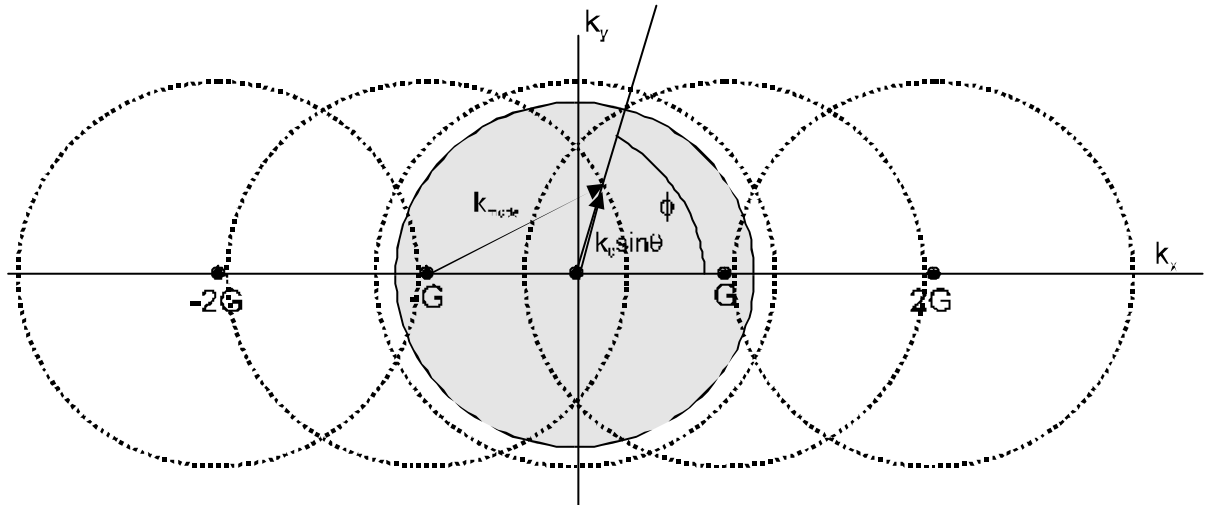


Figure 7.9 The k -space map for a grating with $G < k_0$. The shaded region has a radius of k_0 and corresponds to the wavevector range open to photons propagating in the air above the grating. The dotted circles have a radius of k_{mode} , and represent the wavevector of a given surface mode. Note that only the scattered circles enter the shaded region and can thus couple to photons.

Normally, the circle in k-space corresponding to a given surface mode lies outside the light circle (the shaded region in *figure 7.9*) and so cannot couple to photons. The modes can be scattered by integer multiples of the grating vector into the light circle, allowing these modes to couple to photons, as seen in the previous section. For the case under consideration, both G and $2G$ scatters can couple the mode to photons. The grating grooves lie along the y direction on *figure 7.9*, and so the scattering occurs in the $\pm k_x$ direction. It is obvious that as the azimuthal angle ϕ changes, the length of the vector giving the momentum of the scattered light must change for coupling to be maintained. This means that as the azimuthal emission angle changes, the peak emission occurs at a different polar angle. Application of the cosine rule results in the following relation

$$k_m^2 = k_0^2 \sin^2 \theta + (nG)^2 + 2nGk_0 \sin \theta \cos \phi \quad (7.4)$$

which gives the dependence of the emission angle of the scattered peaks θ on the azimuth.

To test this relation, the p-polarised radiation pattern of the 6 spacer layer region of the 800.1 nm pitch grating was measured for a series of different azimuthal angles. The emission from this region is dominated by the re-radiation from the SPP mode, and so a series of scattered peaks were observed. *Figure 7.10* shows the angle of the peak emission as a function of the azimuth of the emission plane with respect to the grating grooves. The data is plotted in polar form, with the radius equal to $\sin \theta$, effectively giving the in plane wavevector of the emitted light versus ϕ . Note that data was measured for the first quadrant only, and was replicated in the other three to obtain the full k-space map. The open circles represent the SPP emission peaks measured at 614.7 nm , whilst the solid squares are the corresponding SPP emission peaks measured at 592 nm . As expected, the 592 nm SPP modes occur at higher polar angles, since they have a greater wavevector. The similarity to the k-space map of *figure 7.9* should be noted, although no $2G$ scattered emission was observed.

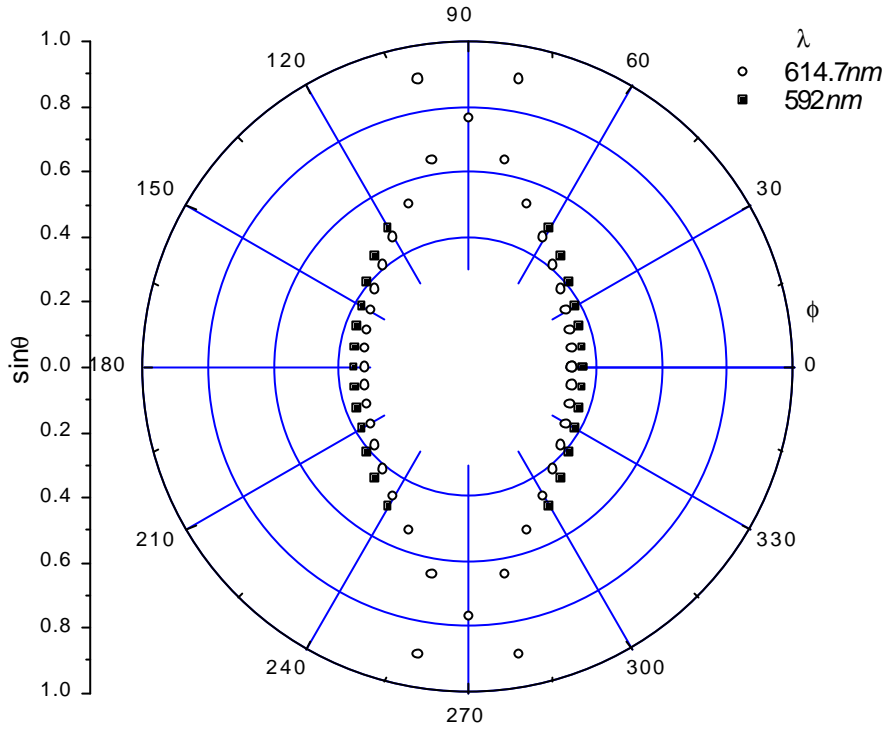


Figure 7.10 The measured azimuthal angle dependence of the peak SPP emission obtained from the 800.1 nm pitch grating sample. Both 614.7 nm and 592 nm SPP emission was observed, the 592 nm peaks occurring at higher emission angles.

The data presented in *figure 7.10* can be re-plotted to test the validity of *equation 7.4*. If the equation holds true, then a plot of $\sin^2\theta$ against $\sin\theta \cos\phi$ should be linear, with an intercept of $(k_m^2 - n^2G^2)/k_0^2$, and a gradient of $-2nG/k_0$. This has been done for the 614 nm emission peaks of *figure 7.10*. The theoretical dependence of *equation 7.4* was calculated using appropriate values of k_m , G and k_0 , and plotted with the experimental data. The mode momentum k_m was obtained from the $\phi=0$ radiation pattern, and found to be $1.09k_0$.

The agreement between experiment and theory is good, with slight discrepancies occurring only for small azimuthal angles, and so it appears that the simple trigonometric relation of *equation 7.4* models the azimuthal dependence of the emission well. The discrepancy for small azimuths is expected, since the grating corrugation will slightly perturb the wavevector of the SPP mode from the planar value assumed in *equation 7.4* [Pockrand

(1974)]. This perturbation will be strongest for SPPs propagating parallel to the grating vector, and will decrease with azimuth, so that the modes propagating along the groove direction effectively experience a planar surface. To be strictly correct therefore, k_m in *equation 7.4* should be a function of azimuth. For the shallow grating used here, the perturbation will be small, and *figure 7.11* shows that this is so. Deeper gratings will exhibit much greater discrepancies for small azimuths, however. The error bars on the experimental data refer to the uncertainty in determining the peak emission angle; note there will also be an error in setting the azimuth, though this is expected to be slight.

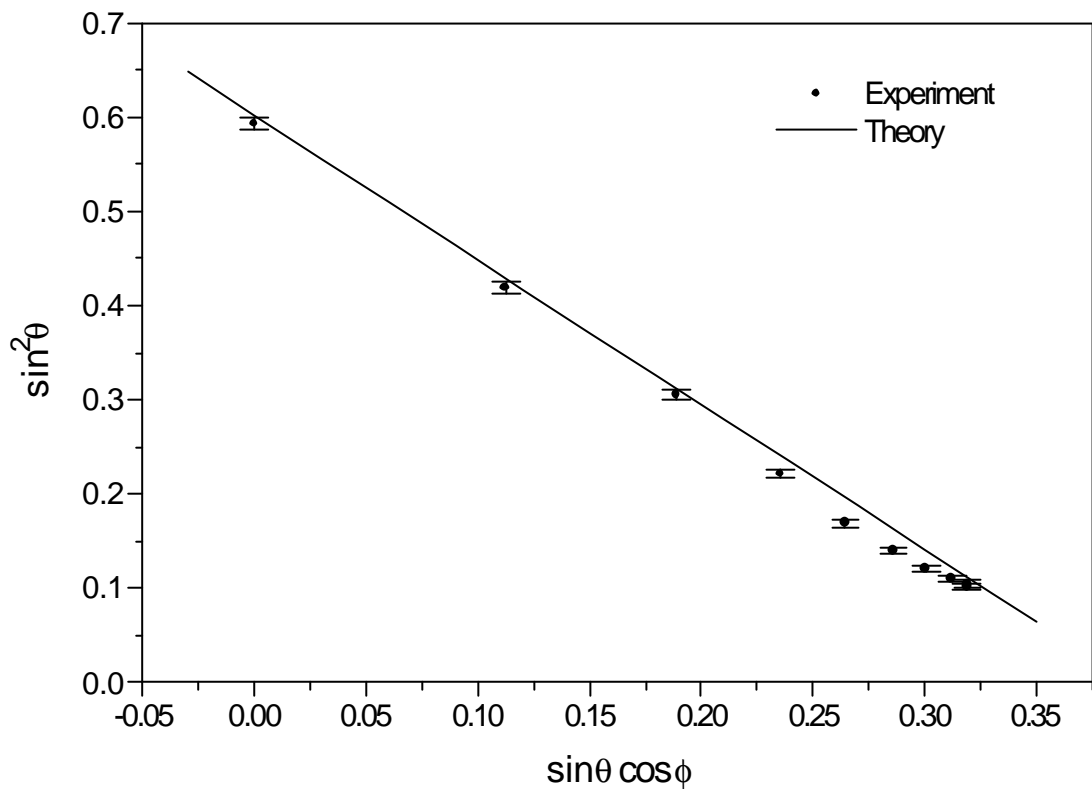


Figure 7.11 The azimuthal emission data of *figure 7.10* re-plotted to determine the validity of the proposed mode scattering mechanism.

7.3.6 Summary for long pitch gratings

The experiments carried out in the preceding sections have shown that the perturbation introduced by a shallow, long pitch grating corrugation has little effect on the spontaneous emission rate of dye molecules situated above it. Little diminution was seen in the amplitude of the lifetime oscillations, indicating that scattering of dipole near field was insignificant. This was expected because of the shallowness of the grating and since the emission wavelength was smaller than the grating pitch. There was also little change in the quenching of the emission for molecules close to the interface, indicating that the coupling to SPPs was similarly unperturbed from the planar case. The fluorescence lifetime was found to be single exponential in form for all spacer layers thicknesses considered. This meant that the dye molecules all experienced identical local environments for a given thickness region, and hence there was no variation in emission rate with lateral displacement of the dye molecules across a grating groove. These results are in broad agreement with the time-resolved measurements made by *Amos (1997)*.

The most significant effect of the corrugation was observable in the radiation patterns of the emission. The angular dependence of the emission was seen to be composed of two contributions, the first resembling the radiation patterns measured for planar samples in chapter 6, and thus corresponding to direct emission from the dye monolayer. This emission was reasonably well modelled by the interference model also introduced in chapter 6, supporting the assertion that the dipole fields are not significantly perturbed by the surface corrugation. The second contribution, consisting of extremely narrow emission peaks, was caused by the scattered emission from surface modes excited by the dye monolayer. These modes have a long propagation length in comparison with the grating pitch, and so can scatter from the corrugation to couple to photons. Both the distance, polarisation and azimuthal dependence of these scattered emission peaks were measured, and compared to theoretical predictions.

Note that the scattering of these modes into photons can have no effect on the spontaneous emission rate of the dye molecules – the scattering of the

modes from the grating occurs *after* the de-excitation of the relevant molecule. Only an alteration of the molecular coupling *to* the modes can affect the spontaneous emission rate, but the coupling perturbation introduced by the grating studied here was not sufficient to affect this. It is thus seen that a large change in the emission intensity from a given system can be achieved without affecting the spontaneous emission rate.

In summary then, the 800nm pitch grating was shown to be a small perturbation from the planar boundary conditions. The fluorescence emission from the dye monolayer was largely unaltered, with the scattering of surface modes into photons the only significant change observed.

7.4 Short pitch grating measurements

The shallow, long pitch grating corrugation did not significantly affect the spontaneous emission rate of the dye molecules; the interface effectively looked planar to the dipole fields. A more severe perturbation of the interface was obviously required in order to see any change in the emission rate from the planar case.

Previous work using the Eu^{3+} complex had shown lifetime changes from the planar case for a silver grating of pitch 400nm and amplitude 30nm [Amos (1997)]. In this study, the emission lifetime was measured for molecule-grating separations from 0 to 80 layers and thus included the largest lifetime maxima. It was seen that the lifetime at this point had decreased from the planar case, and it was speculated that the increased scattering of the dipole fields had caused a large change in the interference conditions. A grating of similar pitch, but of amplitude 60nm exhibited greater changes from the planar lifetime dependence for smaller molecule/grating separations. Measurements were only made for 0 to 80 spacer layers, however, and so the amplitude of the lifetime oscillations could only be tracked for one oscillation. In all cases, however, the time-dependence of the emission was found to be single exponential in form, implying the equivalence of dipole sites across a grating groove.

Since the effect of the corrugation appears to become more important as the pitch decreases, and the amplitude of the profile increases, a series of

experiments were carried out using a batch of shorter pitch gratings. In this case, short implied that the emission wavelength of the dye molecules was larger than the grating pitch. For these structures, scattering of the dipole fields was expected to be significant, and hence changes were expected from the planar interface spontaneous emission rate.

7.4.1 Design and characterisation of samples

In order to allow comparison with previous work, a batch of gratings of pitch $\sim 400\text{nm}$ were fabricated using the holographic technique described previously. By varying the exposure and development times used, photoresist gratings were produced with amplitudes ranging from $\sim 20\text{nm}$ to $\sim 100\text{nm}$. This allowed the effect of increasing the grating amplitude to be investigated. At least two gratings were made for each set of fabrication conditions so that, within the manufacturing tolerances, multiple samples were obtained for a given sample profile. This allowed the measurement of a reasonable number of points on the lifetime versus distance curve.

When exposing the substrates, part of the beam was blanked off so that each sample had a planar region surrounding the grating. Measurements could then be made on both planar and grating regions for each spacer layer thickness, ensuring that any change in lifetime seen was due to the grating corrugation. This was important because it was uncertain whether the photoresist film would provide as smooth a surface as the silica substrates used in all the previous work. Any variation in the grating results could have been attributable to the possibly microscopically rough surface of the photoresist.

After deposition of an optically thick silver film, all of the gratings were then characterised by measuring the angle-dependent reflectivity for TM-polarised light, and fitting to theory, as was done for the long pitch grating in *section 7.3*. Immediately after characterisation, the samples were returned to the vacuum chamber in order to avoid contamination of the silver. Examples of the reflectivity data and fitted theory are given in *figure 7.12* for two of the gratings fabricated, in order to indicate the quality of the fits. The fit parameters obtained for all of the gratings used are given in *table 7.2*.

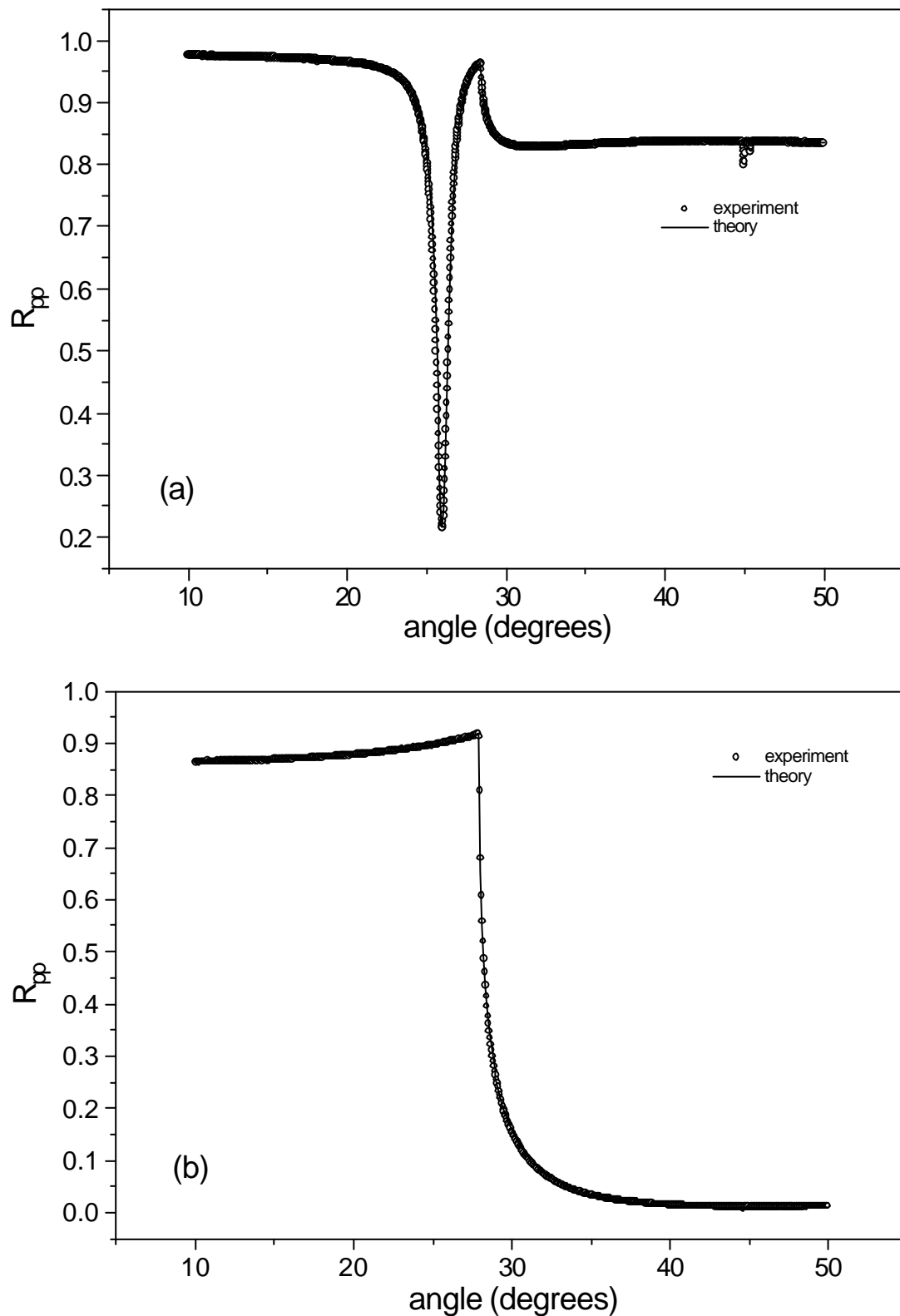


Figure 7.12 Reflectivity of two of the 400nm pitch gratings for TM-polarised incident light ($\lambda=612\text{nm}$). (a) Grating 1 ($a_0 \sim 17\text{nm}$), and (b) Grating 11 ($a_0 \sim 75\text{nm}$). The circles are experimental data and the line is a theoretical fit.

Grating no.	λ_g/nm $\pm 0.1nm$	a_0/nm $\pm 0.1nm$	a_1/nm $\pm 0.1nm$	ϵ'_{Ag} ± 0.02	ϵ''_{Ag} ± 0.01
1	414.4	17.1	-0.1	-14.58	0.74
2	414.7	21.0	-0.2	-15.10	0.71
3	414.3	29.8	-0.3	-14.09	0.69
4	414.5	31.5	-1.5	-14.03	0.69
5	416.6	33.1	-0.5	-14.01	0.68
6	415.9	38.4	4.1	-15.4	0.79
7	416.3	42.0	2.5	-13.11	0.87
8	415.3	67.4	8.4	-12.68	0.83
9	415.8	67.8	5.6	-13.38	0.89
10	416.1	65.7	4.2	-13.65	0.75
11	415.3	74.2	10.6	-13.37	0.80
12	416.7	75.2	9.7	-13.13	0.87
13	416.6	127.6	9.4	-12.59	0.95
14	416.3	132.0	5.5	-11.34	0.83

Table 7.2 The fit parameters obtained from reflectivity measurements for the short pitch gratings used. The parameters used are defined in *table 7.1*.

After characterisation, the grating pairs were then ready for deposition of the LB spacer structures, which was carried out using the precautions outlined in *section 7.2.5*. Since the corrugation was expected to have most effect for small molecule-interface separations, the spacer layer structures deposited covered the spacer region from 0-76 layers. Ten spacer layer regions of different thickness could be deposited onto each sample, with both planar and grating areas covered by each thickness spacer.

The approach taken was to deposit ten regions covering the range 0-72 spacer layers on the first grating sample of a pair, in steps of 8 layers. The second grating of the pair was then completely coated with 4 spacer layers, before repeating the initial deposition process, producing a sample with spacer

layer regions covering the range 4-76 layers. In this way the thickness range from 0-76 spacer layers was covered in steps of 4 layers for each amplitude of grating considered, using only two grating samples. Moreover, the data acquired would be interlaced; that is to say, adjacent points on the measured lifetime dependencies would originate from different samples, thus highlighting any variation in profile between the two samples.

In all, six different depth grating profiles were considered; in increasing order of approximate amplitude, 20nm , 30nm , 40nm , 68nm , 75nm and 130nm . For two of the grating amplitudes, $a_0 \sim 30\text{nm}$ and $a_0 \sim 68\text{nm}$, three samples were made. Consequently, the third sample for each amplitude was coated with 80-156 spacer layers, allowing the evolution of the lifetime oscillations with distance to be thoroughly investigated.

7.4.2 Lifetime measurements

As before, the excited state lifetime of the Eu^{3+} ions was measured for each sample as a function of the spacer layer thickness. Measurements were made for both the grating areas and the planar control regions. The results will be presented and discussed for each of the grating amplitudes, and trends in the behaviour of the lifetime dependence with grating amplitude discussed.

7.4.3 20nm amplitude gratings

The Eu^{3+} excited state lifetimes measured for the $\lambda_g \sim 415\text{nm}$, $a_0 \sim 20\text{nm}$ grating samples (gratings 1 and 2; see *table 7.2*) are given in *figure 7.13*. It can be seen that there is little difference in the distance dependence of the lifetime between the planar and grating regions, indicating that the amplitude of the grating is insufficient to cause significant scattering of the dipole fields. There is some scatter in the grating data for the larger molecule/grating separations, which is caused by the difference in the grating amplitudes of the two samples used (17nm and 21nm respectively).

As with the long pitch grating studied in the previous section, it was found that all fluorescence decays measured were single exponential in form, implying that all dipole sites within a monolayer were equivalent for a given spacer layer thickness.

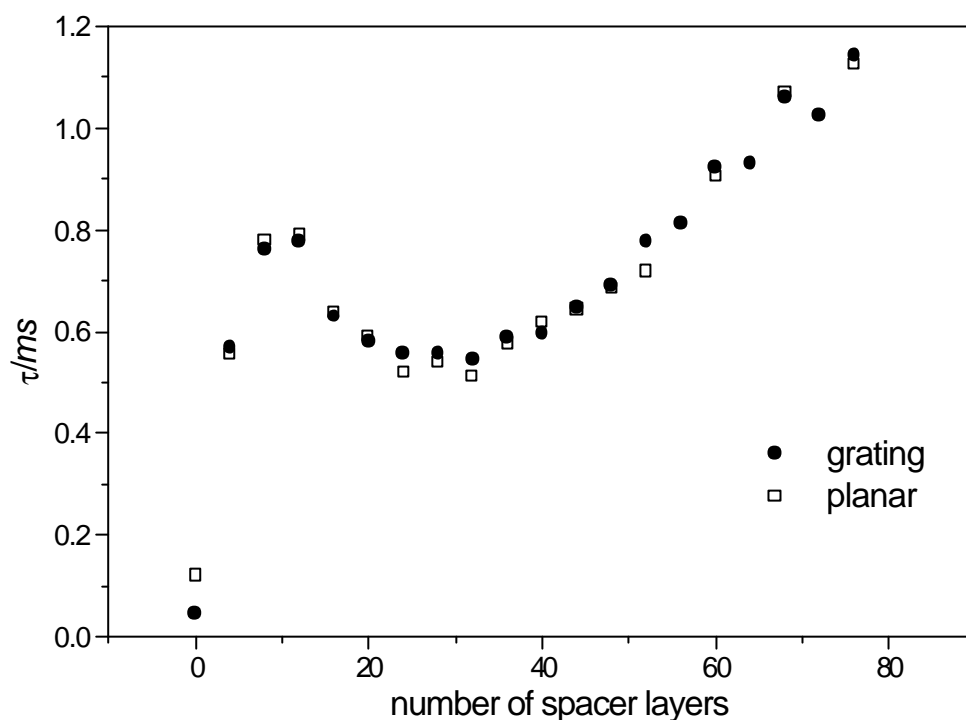


Figure 7.13 The lifetime of the Eu^{3+} ions above a silver grating of amplitude $\sim 20\text{nm}$ as a function of the ion-metal separation. The full circles are the grating data, whilst the hollow squares are the corresponding planar comparison.

7.4.4 30nm amplitude gratings

Figure 7.14 shows the measured excited state lifetime of the Eu^{3+} ions as a function of the ion-metal separation for the $\lambda_g \sim 415\text{nm}$, $a_0 \sim 30\text{nm}$ grating samples (gratings 3,4 and 5). Unlike previous studies, measurements were made for ion-metal separations greater than 80 spacer layers, and a full lifetime oscillation can now be seen. Small changes in the distance dependence from the planar case can be seen; the magnitude of the oscillations is clearly reduced, hinting that the interference condition is changing and that the dipole fields are indeed being scattered by the grating corrugation. The lifetime is also reduced slightly from the planar case for very small ion-metal separations,

suggesting that the coupling to the SPP mode has increased. As with the $a_0 \sim 20\text{nm}$ data however, all fluorescence decays were single exponential in form.

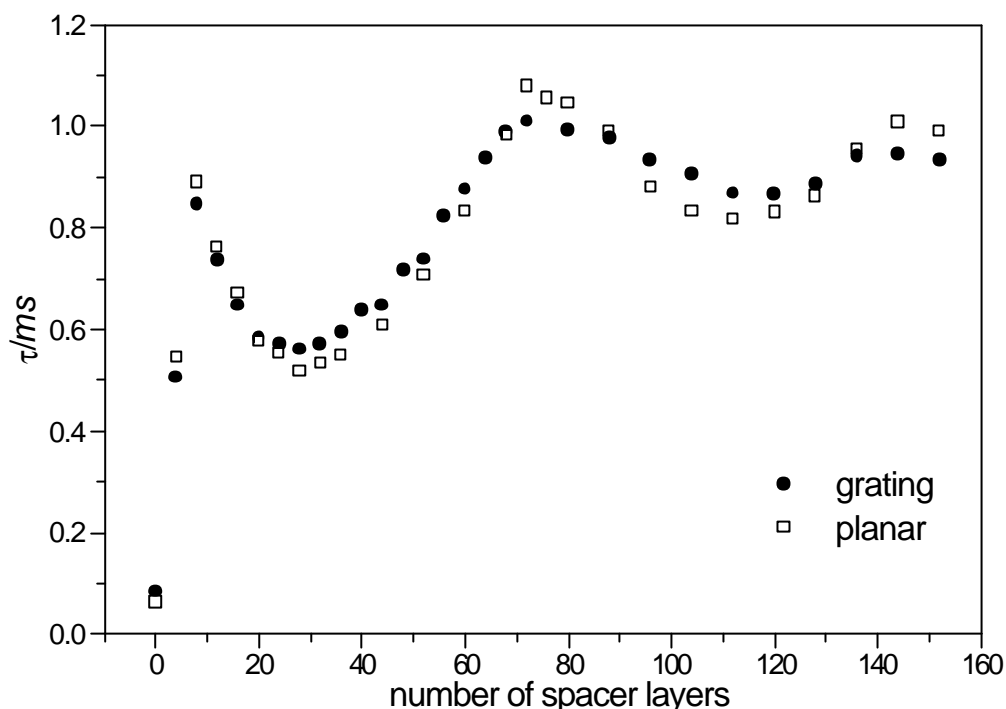


Figure 7.14 The lifetime of the Eu^{3+} ions above a silver grating of amplitude $\sim 30\text{nm}$ as a function of the ion-metal separation. The full circles are the grating data, whilst the hollow squares are the corresponding planar comparison.

7.4.5 40nm amplitude gratings

Figure 7.15 shows the measured excited state lifetime measured from the $\lambda_g \sim 415\text{nm}$, $a_0 \sim 40\text{nm}$ grating samples (gratings 6 and 7). Again, the lifetime dependence of the grating region is very similar to the planar region, but there is a significant increase in the lifetime for the grating sample for spacer layer thicknesses of 20 to 60 layers. This covers the first minima in the lifetime distance dependence and may indicate a potential decrease in the lifetime oscillations for larger molecule/grating separations, though the data does not extend far enough to say for certain. It is, however, obvious that a grating amplitude of $\sim 40\text{nm}$ (corresponding to a depth-to-pitch ratio of 0.1) is large enough to cause changes in the spontaneous emission rate. The fluorescence

decays were again given by a single exponential function, and so no variation in ion lifetime with change in lateral position across the grating grooves could be determined.

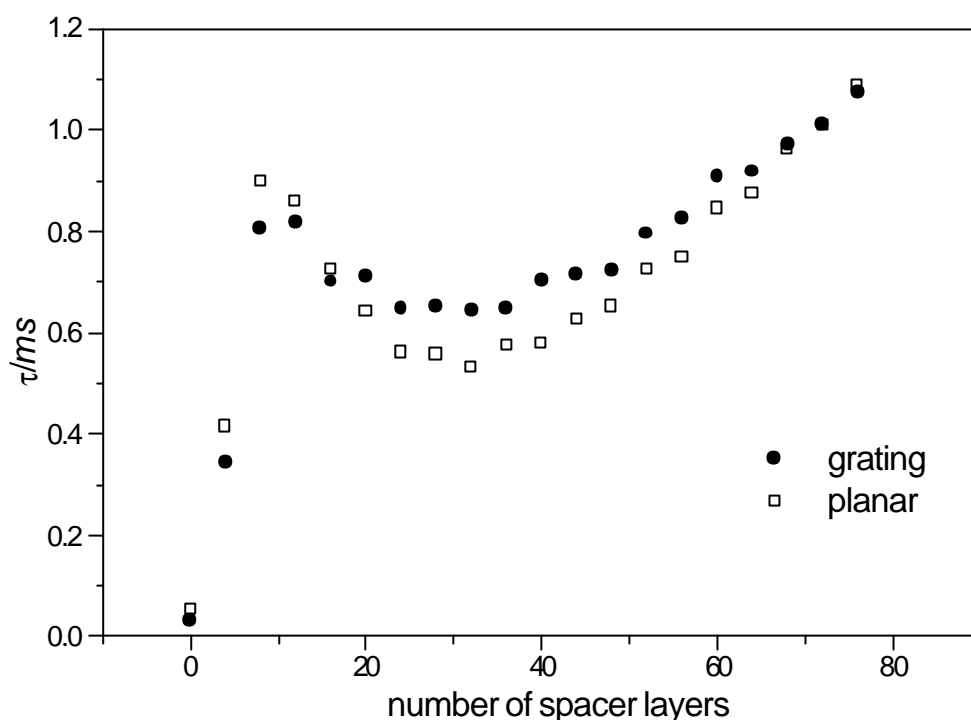


Figure 7.15 The lifetime of the Eu^{3+} ions above a silver grating of amplitude $\sim 40\text{nm}$ as a function of the ion-metal separation. The full circles are the grating data, whilst the hollow squares are the corresponding planar comparison.

7.4.6 68nm amplitude gratings

The lifetime data for the $\lambda_g \sim 415\text{nm}$, $a_0 \sim 68\text{nm}$ grating samples (gratings 8,9 and 10) as a function of ion-metal separation is given in *figure 7.16*. The changes from the planar distance dependence exhibited by the $a_0 \sim 30\text{nm}$ gratings are much more pronounced for this larger amplitude grating structure. In particular, the magnitude of the lifetime oscillations is smaller still, suggesting that increased scattering of the dipole fields by the deeper grating structure is occurring, perturbing the dipole field interference condition. The lifetime quenching for small molecule/grating separations is also much greater, indicating a possible increase in coupling to the SPP mode with grating depth.

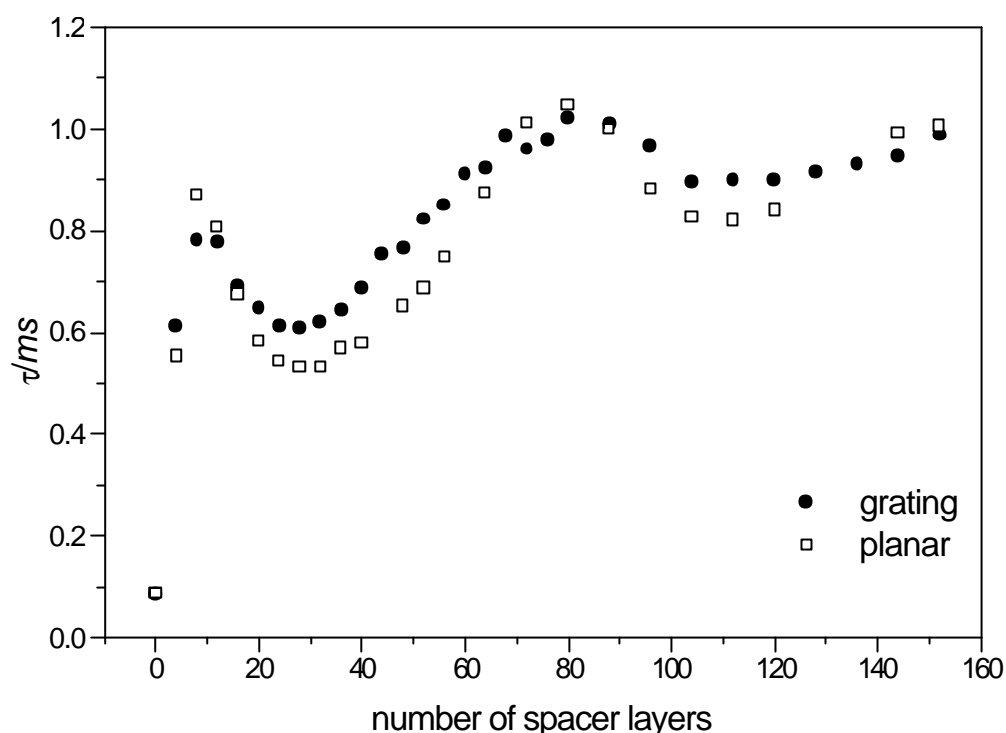


Figure 7.16 The lifetime of the Eu^{3+} ions above a silver grating of amplitude $\sim 68\text{nm}$ as a function of the ion-metal separation. The full circles are the grating data, whilst the hollow squares are the corresponding planar comparison.

Again, all fluorescence decays measured were still single exponential in form, in agreement with *Amos (1997)*, who found a similar result for gratings of similar pitch and amplitude. The $a_0=68\text{nm}$ data can be directly compared with the 30nm amplitude data since both of sets of data were measured for 0-160 spacer layer structures, and not 0-80 layers like the others. The extension of the spacer layer thickness shows explicitly how an increase in the grating amplitude affects the magnitude of the lifetime oscillations for the large ion-metal separation regime. Comparison between the distance dependence for the $a_0\sim 30\text{nm}$ and $a_0\sim 68\text{nm}$ grating samples is best made by plotting the data on the same axes; this is done in *figure 7.17* with the inclusion of the planar distance dependence from chapter 6. The effect of increasing the amplitude of the grating corrugation on the magnitude of the lifetime oscillations can be clearly seen, the amplitude becoming progressively smaller as the grating depth increases.

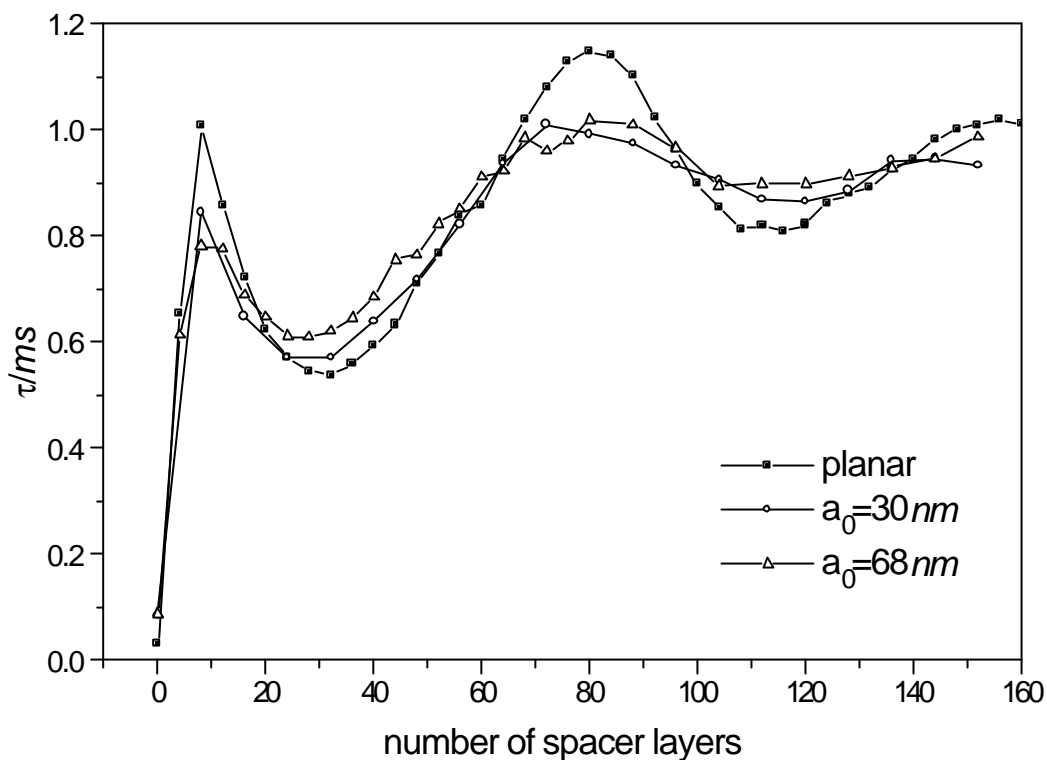


Figure 7.17 The Eu^{3+} ion excited state lifetime distance dependence for a planar interface and two different depth grating structures. Note that the lines are merely guides to the eye.

7.4.7 75nm amplitude gratings

The excited state lifetime distance dependence for gratings of amplitude $a_0 \sim 75\text{nm}$ (gratings 11 and 12) continues the trends observed so far with increasing grating depth, as is shown in *figure 7.18*. The lifetimes in the region of the minima at ~ 30 layers are significantly higher for the grating data, compared with the planar data, suggesting that the damping of the lifetime oscillations with increasing grating amplitude is still occurring. The fluorescence decays were still observed to be single exponential for all regions, thus again, no difference in the emission rate could be detected for dipoles located over the peaks or troughs of the grating profile. Sample fluorescence decay data for both the grating and planar regions for an ion-metal separation of 32 spacer layers are given in *figure 7.19*, together with the single exponential fits. The difference between the grating and planar lifetimes can be clearly seen.

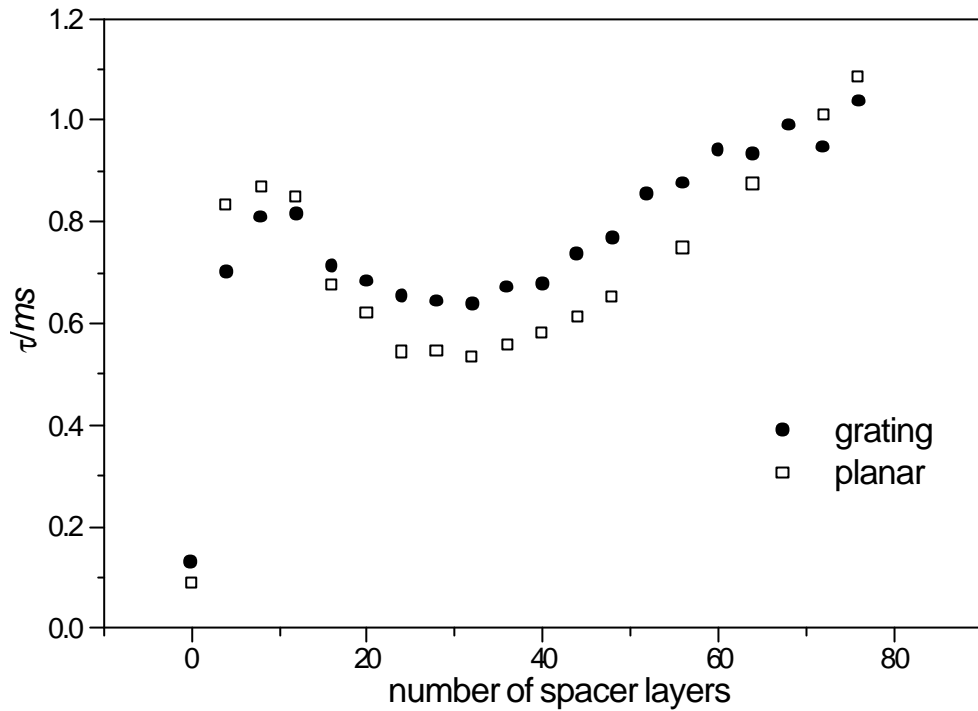


Figure 7.18 The lifetime of the Eu^{3+} ions above a silver grating of amplitude $\sim 75\text{nm}$ as a function of the ion-metal separation. The full circles are the grating data, whilst the hollow squares are the corresponding planar comparison.

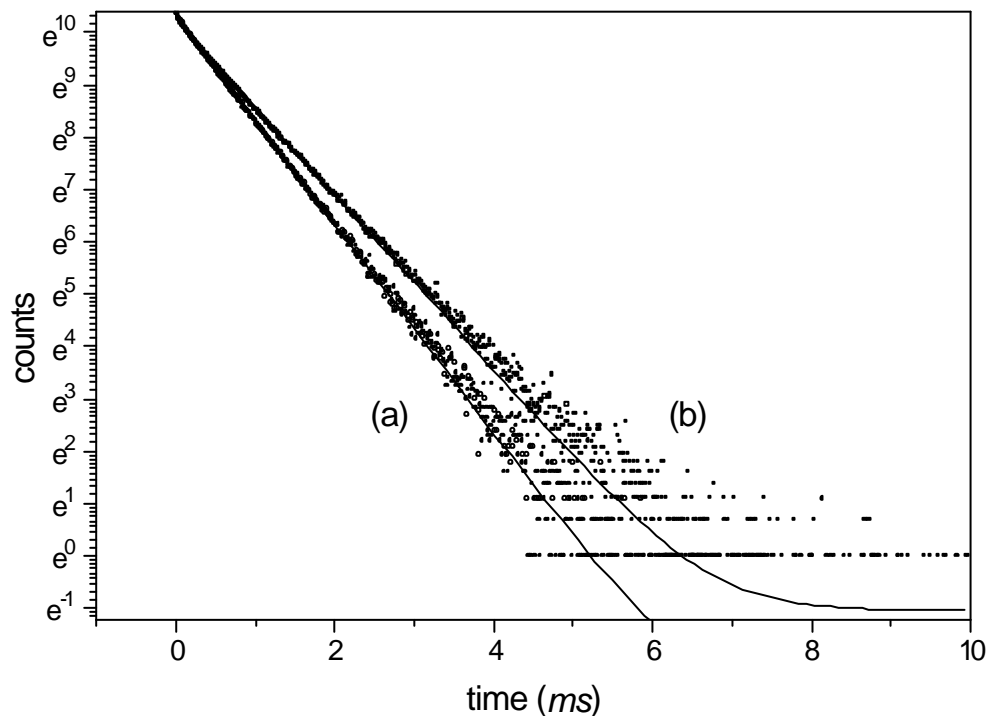


Figure 7.19 Fluorescence decay curves for Eu^{3+} ions located 32 spacer layers above (a) a grating of pitch 415nm and amplitude 75nm , and (b) a planar interface, together with the single exponential fits.

7.4.8 130nm amplitude gratings

The final gratings examined (gratings 13 and 14) were the deepest and gave the most interesting results of all the samples studied. The most significant change from previous samples was that the fluorescence decays measured for the grating region were *not* exponential in form for any of the ion-metal separations considered. While it is conceivable that a highly intense UV pump beam could cause similar non-exponential behaviour, as discussed in chapter 6, extreme care was taken to excite the samples using a very low intensity pump beam to avoid this problem. The pumping conditions used to excite the grating and planar regions were identical, and so any change in the fluorescent decay kinetics caused by the method of excitation should be manifested in the planar data too. The fluorescence decays measured for the planar regions of the sample were all still single exponential, indicating that the grating region non-exponentiality was not caused by over-pumping. Sample-specific effects can be eliminated too, since two different grating samples were used to make these fluorescence decay measurements.

The non-exponential fluorescence decays thus suggest that for this grating profile, the Eu^{3+} ions within a given monolayer *do* experience different local environments, and so have correspondingly different spontaneous emission rates at different points above the grating structure. This is the first time that such non-exponential behaviour has been observed.

A sample fluorescence decay for the 32 spacer layer region of the grating region is presented in *figure 7.20*, and the corresponding planar region data in *figure 7.21*. In both cases, the data has been fitted to a single exponential function, and the deviation (experiment–theory) of each set of data from this function is plotted above the fluorescence decay. The planar data is seen to be well approximated by the single exponential function, with only random deviations from the theory caused by noise occurring. The grating data shows significant deviations from the single exponential function, and it appears that both longer and shorter lifetime components are present in the experimental data, rather than the assumed single exponential lifetime. This is to be expected since the measured fluorescence decay arises from a

continuous distribution of ion positions above the grating surface, and hence a continuous distribution of lifetimes components should be present.

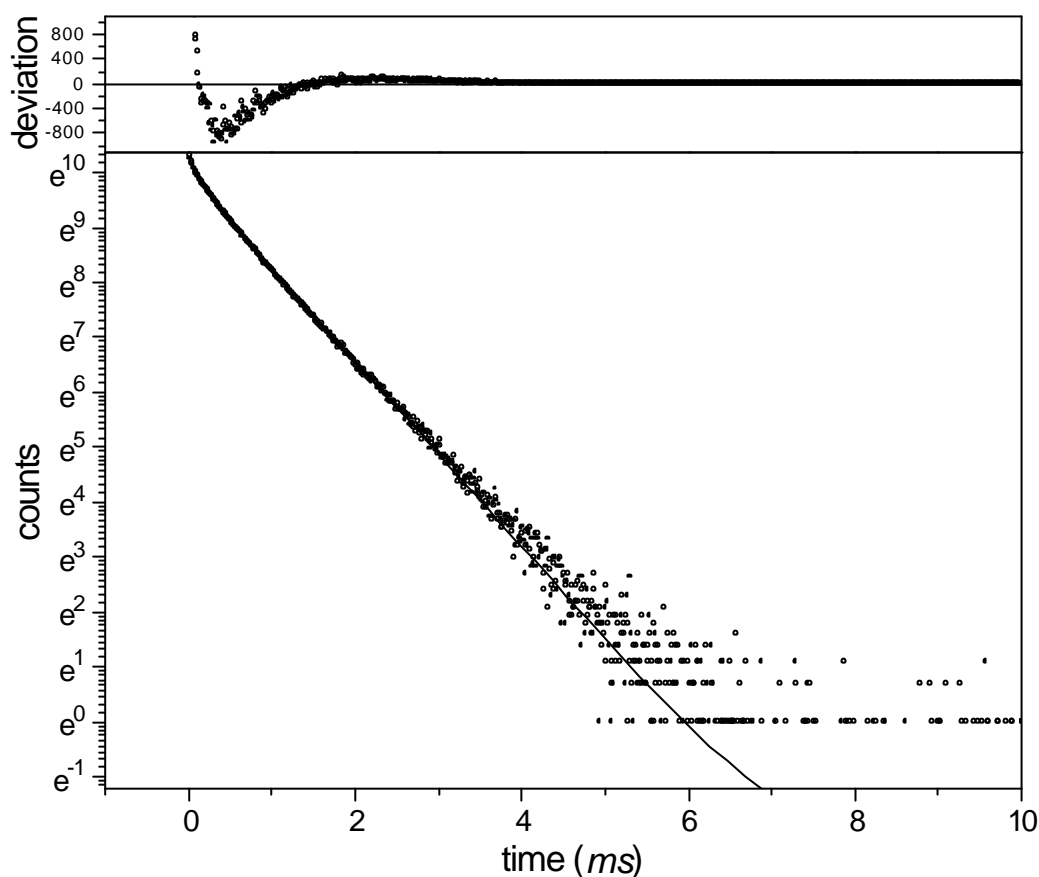


Figure 7.20 The fluorescence decay of Eu^{3+} ions located 32 spacer layers above a grating of pitch 415nm and amplitude 130nm , together with a single exponential fit. The deviation from this fit (experiment-theory) is given above the decay, indicating the non-exponential character of the decay.

It is extremely difficult to correctly analyse non-exponential data to obtain the true lifetime distribution unambiguously, and it was not feasible to attempt this in the present study. As an approximation, the grating fluorescence decay data was fitted to a biexponential function with two lifetime components, in order to obtain the distance dependence of the “lifetime” of the Eu^{3+} ions for the 130nm amplitude gratings. The reasoning behind this was that the grating surface provides two extreme local environments for the dye molecules. The greatest difference in the local optical field, and hence lifetime, at a fixed height

above the grating surface is expected for molecules located above the grating peaks and the grating troughs. The two components of the biexponential fit may then give an indication of the spread of lifetime components in the true distribution. The function fitted to was of the form

$$I(t) = I_1 \exp(-t/\tau_1) + I_2 \exp(-t/\tau_2) + I_d \quad (7.5)$$

where τ_1 and τ_2 are the two lifetimes, and I_1 and I_2 are the amplitudes of these components. I_d is the background light level. Unsurprisingly, the biexponential form fit the experimental data a lot better than the single exponential, purely because of the increase in the number of fitting parameters

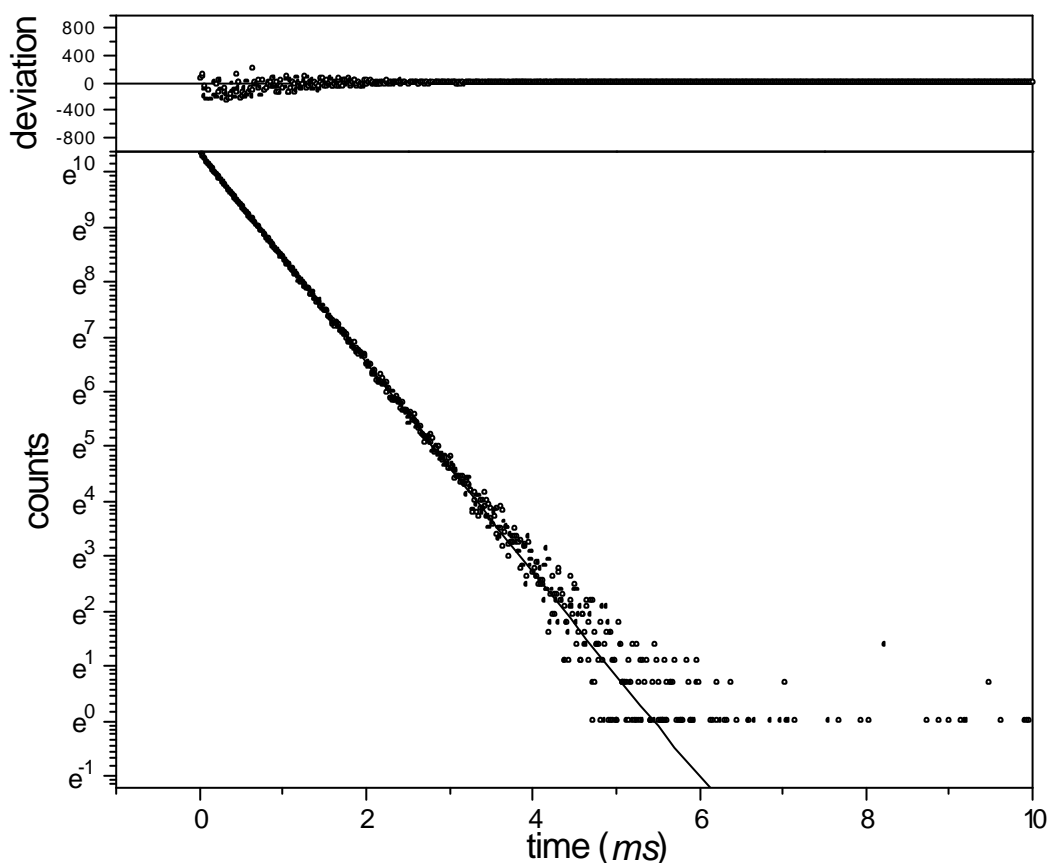


Figure 7.21 The fluorescence decay of Eu^{3+} ions located 32 spacer layers above the planar region of the 130nm amplitude grating sample, together with a single exponential fit. The deviation from this fit (experiment-theory) is given above the decay, indicating the single exponential character of the decay.

The distance dependence of the Eu^{3+} emission “lifetime” obtained from the biexponential fits for these 130nm amplitude gratings is presented in *figure 7.22*, together with the single exponential lifetime data from the corresponding planar region.

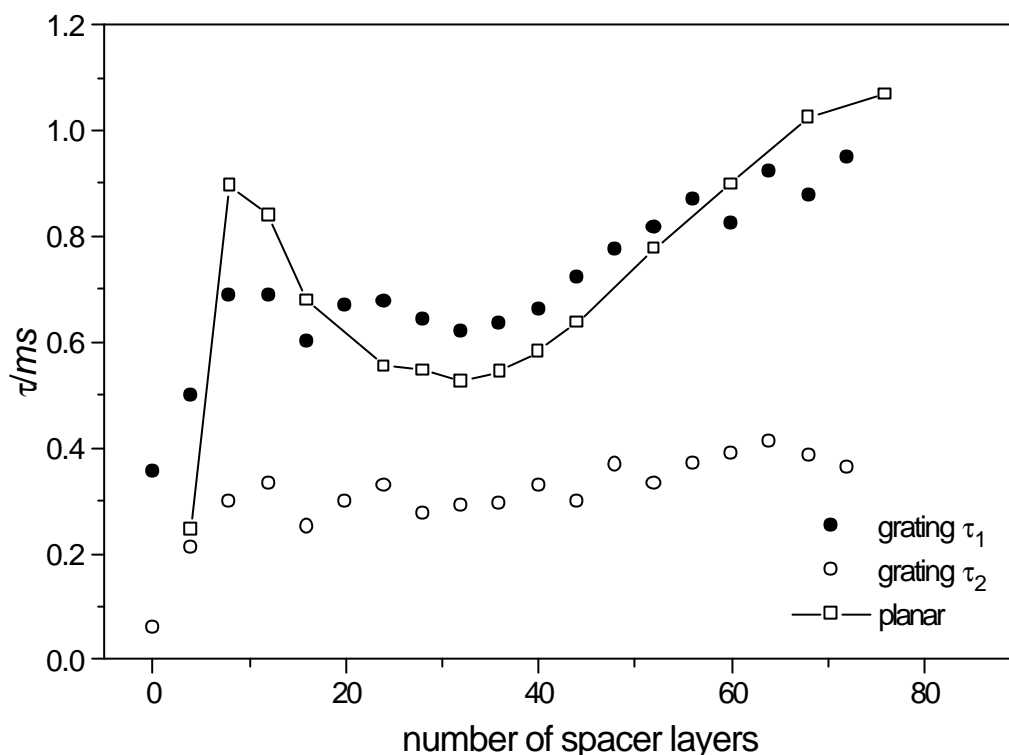


Figure 7.22 The “lifetime” of the Eu^{3+} ions above a silver grating of amplitude $\sim 130\text{nm}$ as a function of the ion-metal separation. The circles (full *and* hollow) are the grating data, whilst the hollow squares are the corresponding planar comparison. τ_1 and τ_2 refer to the long and short lifetime components of the biexponential fit respectively. The line for the planar data is merely a guide to the eye.

Figure 7.22 shows that the distance dependence of the longer lifetime τ_1 component of the biexponential fit resembles the lifetime dependence measured for the previous grating amplitudes, and is thus probably the more significant of the two lifetime components presented. It can be seen that there are considerable differences between the planar lifetime dependence and the grating τ_1 lifetime dependence, continuing the trend observed for shallower grating structures. Most obviously, the oscillations in lifetime for ion-metal

separations of greater than 20 spacer layers are strongly damped, indicating that the interference condition experienced by the dipole has changed. The quenching observed for small ion-mirror separations (up to 12 spacer layers) is also much increased from the planar case, possibly indicating that the coupling to the SPP mode is much greater for the grating structure.

It is more difficult to say anything certain about the shorter lifetime component, except that it is a measure of the deviation of the fluorescence decay from single exponential behaviour. The relative importance of the two lifetime components is shown in figure 7.23, which plots the fraction of the fluorescence decay corresponding to the long lifetime component, $I_1/(I_1+I_2)$, (see equation 7.5) as a function of ion-metal separation.

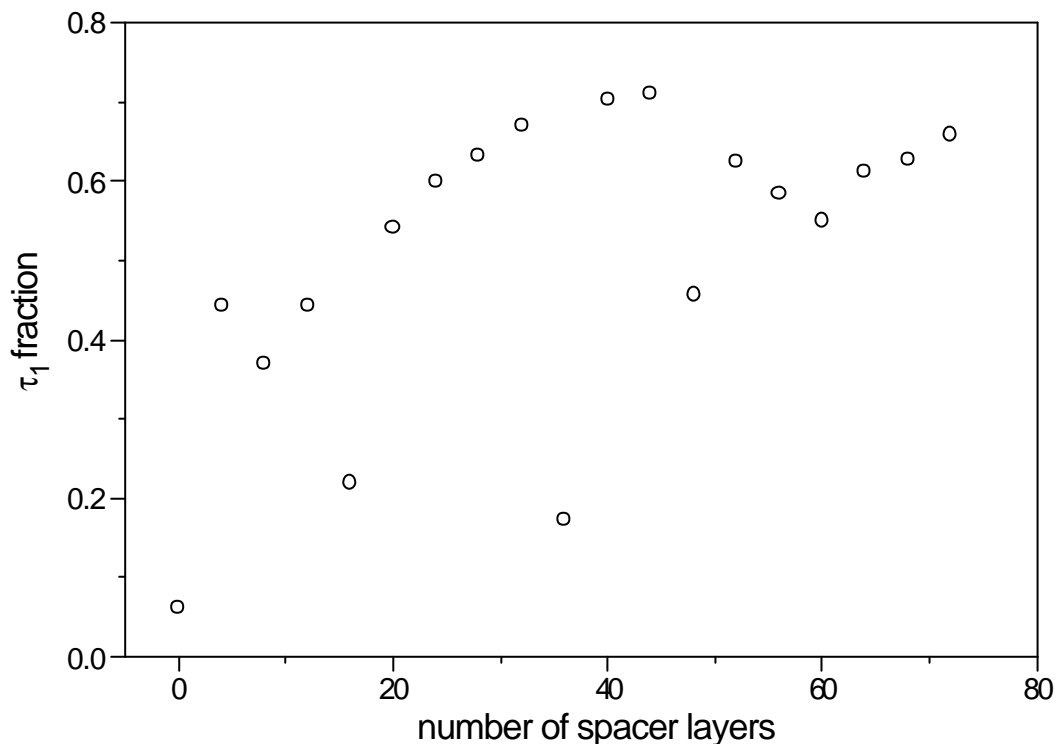


Figure 7.23 The fraction of the fluorescence decay corresponding to the long lifetime component for the 130nm amplitude grating sample.

Figure 7.23 shows that as the ion-metal separation increases, the deviation of the fluorescence decay from a single exponential function becomes smaller for the grating sample. It thus appears that the variation in the local environment of the various dipole sites above the grating surface decreases as

the ion-metal separation increases, which seems reasonable as the influence of the grating profile will diminish with distance.

7.4.9 Radiation pattern measurements

In addition to the lifetime measurements, the radiation patterns of the short pitch grating samples were measured for the Eu^{3+} $\lambda=614\text{nm}$ emission to see if there was any perturbation from the long pitch grating results. In those measurements, it was noted that the radiation pattern consisted of two contributions, one of which resembled the planar sample radiation pattern, while the other was the result of surface mode scattering. The fact that the planar radiation pattern contribution was not greatly altered for the long pitch gratings suggested that little scattering of the dipole fields had taken place. This was in agreement with the conclusions drawn from the corresponding lifetime measurements.

Conversely, the lifetime measurements for the short pitch gratings suggest that significant scattering of the dipole fields is taking place, leading to changes in the spontaneous emission rate from the planar dependence. It was decided to repeat the radiation pattern measurements for the short pitch samples to see if there was any evidence of this scattering. Measurements were made at an azimuthal angle of $\phi=0$ for several of the grating amplitudes, namely the 30nm samples and the 68nm samples.

Figures 7.24a and b show the p- and s-polarised radiation patterns for the 104nm spacer layer region of the 30nm amplitude gratings, whilst *figures 7.24c and d* show the corresponding data for the 68nm amplitude grating. This particular spacer layer thickness was chosen because it corresponds to the second minima in the distance dependence of the lifetime, where both samples exhibited the greatest lifetime difference between the planar and grating regions. It was thus expected that any change in the radiation pattern caused by the scattering of the dipole field would be most obvious for this spacer layer thickness. Note that the emission was only measured over the angle range 0° to 90° and the same data was also plotted for -90 to 0 to aid visualisation.

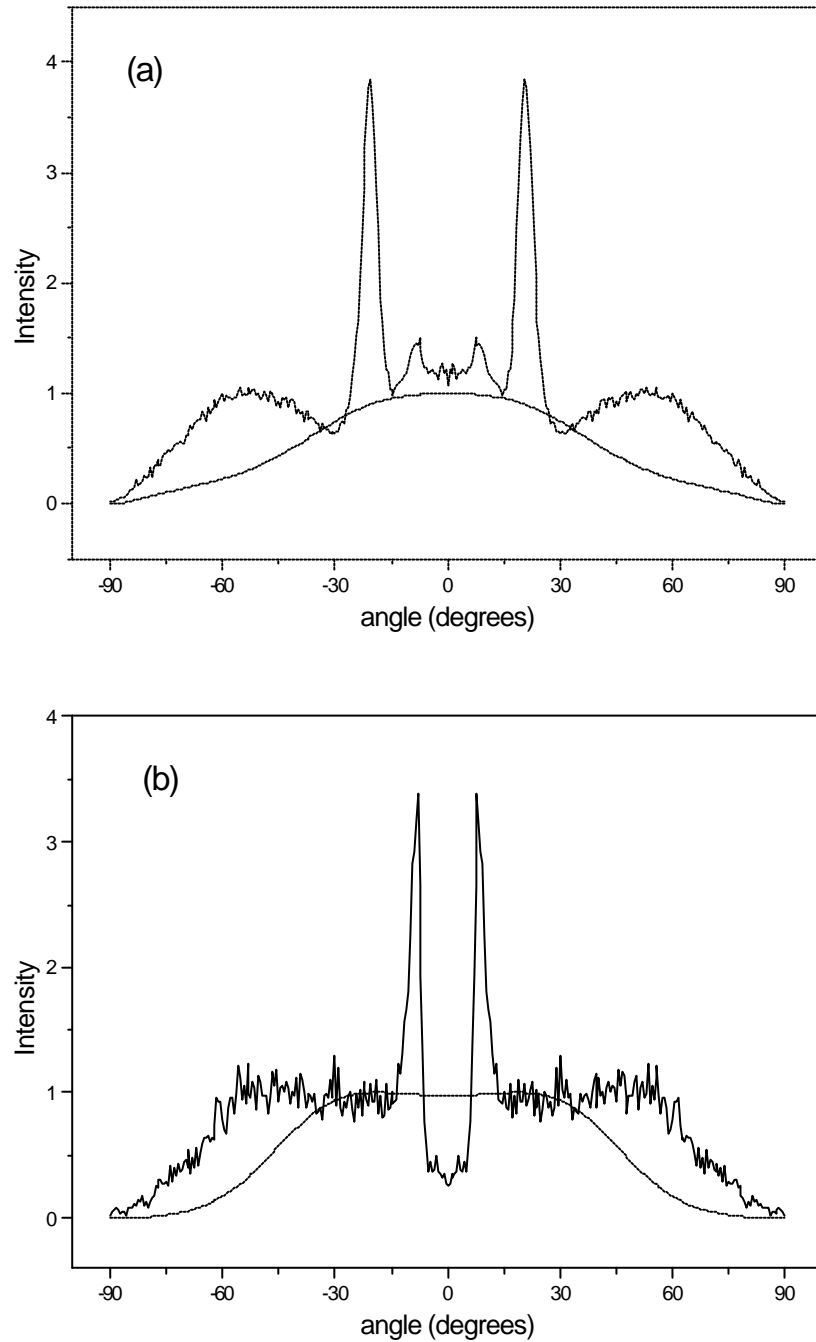


Figure 7.24 Radiation patterns of the 104 spacer layer region of the 30nm amplitude grating sample, for (a) p-polarised emission and (b) s-polarised emission. The continuous lines are the experimental data, whilst the dashed line is the theoretical dependence for the corresponding thickness planar sample. The azimuthal angle is zero in each case.

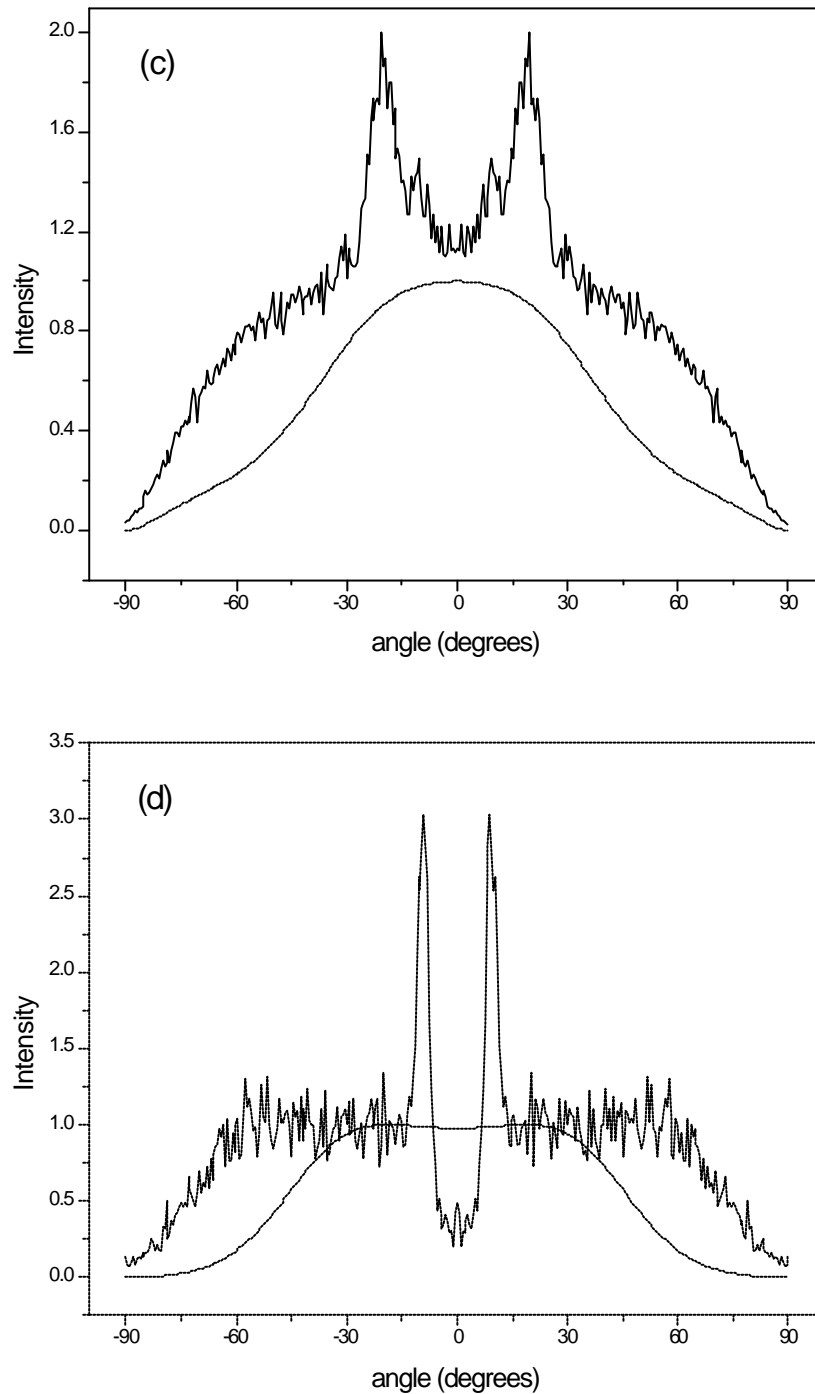


Figure 7.24 (continued) Radiation patterns of the 104 spacer layer region of the 68nm amplitude grating sample, for (c) p-polarised emission and (d) s-polarised emission. The continuous lines are the experimental data, whilst the dashed line is the theoretical dependence for the corresponding thickness planar sample. The azimuthal angle is zero in each case.

Figure 7.24 shows that the radiation patterns of the short pitch grating samples are composed of two contributions, in common with the long pitch grating results. Again, both the narrow emission peaks corresponding to the re-radiation of surface modes and a slowly varying background resulting from the direct radiation from the dye molecules can be clearly seen. To compare the direct emission contribution with that expected from a similar planar sample, the theoretical planar radiation patterns for each spacer thickness have been plotted along with the grating data. The grating data was normalised to give a peak direct emission of unity in each case.

It can be seen that the angular dependence of the direct emission from the dye molecules is significantly different from the results expected for a planar sample of the same thickness, for both short pitch gratings considered. The angle dependence of this direct emission is determined by the interference between the directly emitted dipole fields and those reflected by the interface. For this reason, the observed change in angle dependence for the grating samples suggests that the interference condition for the dipoles *has* been significantly altered by the presence of the corrugation. In this case therefore, it appears that the grating corrugation is sufficient to scatter the dipole fields, corroborating the reasoning used to explain the damping of the oscillations in the distance dependent Eu^{3+} lifetime measured for these samples.

The grating corrugation not only affects the direct emission, but also alters the SPP mode re-radiation, as can be seen in *figure 7.25*. In this figure, the p-polarised radiation patterns for the 4 spacer layer region are presented for the 30, 68, 75 and 130nm amplitude gratings. Again, all of the patterns have been normalised so that the background emission peaks at unity, and the data offset vertically to allow easy comparison.

The main feature observable for each radiation pattern is the SPP re-radiation peak, which becomes progressively more damped as the amplitude of the grating corrugation increases. The intensity of the emission decreases (with respect the direct emission), and at the same time the emission broadens, suggesting that the SPP mode giving rise to the emission is being severely perturbed by the grating corrugation. The angle of peak emission also increases, suggesting that the dispersion of the SPP mode is also affected by the grating.

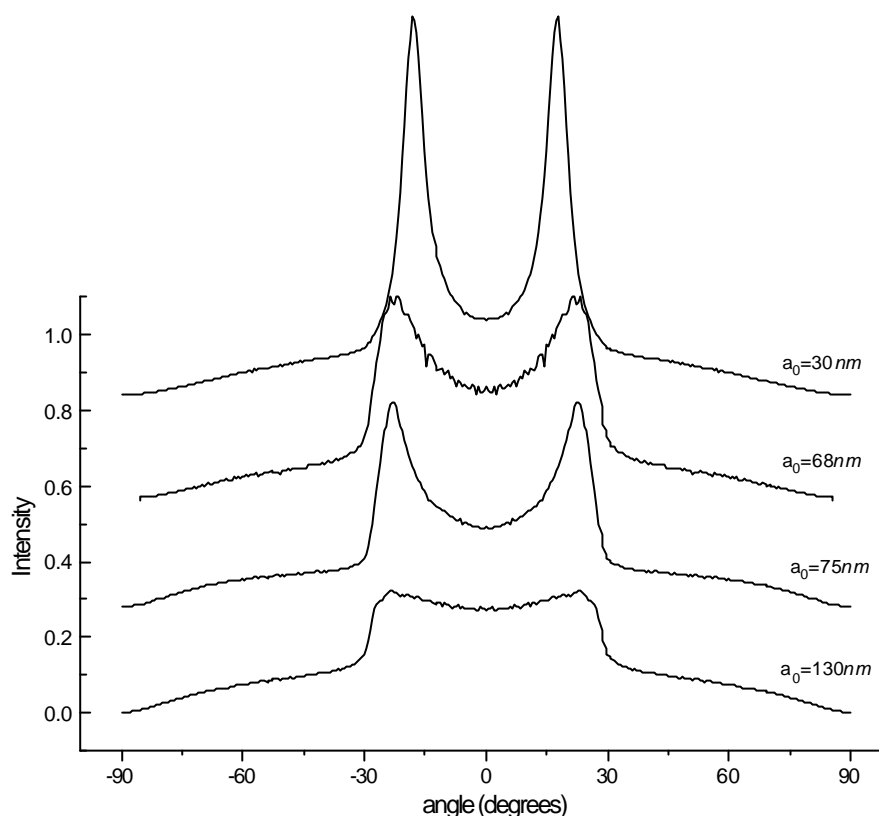


Figure 7.25 The p-polarised radiation patterns for the 4 spacer layer thick regions of the short pitch grating samples. The increase in damping of the SPP emission with grating amplitude can be clearly seen. Results for four different grating amplitudes are given

Since the quenching of the dye for small ion-metal separations is mainly determined by the molecule–SPP coupling, the increase in the SPP damping as the grating amplitude increases has great implications for the excited state lifetime of the molecule. Substantial broadening of the SPP mode caused by the depth of corrugation could lead to increased molecule-SPP coupling, and hence a reduction in the lifetime of the molecules. The exact effect on the lifetime is difficult to assess without a theoretical model, since the molecule excites SPPs propagating at all azimuths on the grating, and the grating only significantly perturbs the SPPs propagating parallel to the Bragg vector. The full extent of the effect of the grating perturbation on the excited state lifetime can thus only

be explained by considering all azimuthal angles, and is beyond the scope of this work.

7.4.10 Discussion of short pitch grating results

The fluorescence decay measurements of the previous section show that the spontaneous emission rate of dye molecules positioned above the shorter pitch gratings was significantly altered by the corrugation, in contrast with the results obtained from long pitch grating samples. For the shallowest gratings examined ($a_0 \sim 20nm$), the lifetime distance dependence was unchanged from that of a planar surface, suggesting that the interface still appeared planar to the dye molecules. As the grating amplitude was increased, the magnitude of the lifetime oscillations for larger ion-metal separations decreased significantly. This reduction was attributed to the increased scattering of the dipole fields, since scattering of the dipole fields will affect the interference condition, thus perturbing the lifetime oscillations. The scattering is expected to be more important for the shorter pitch gratings considered here since the dipole fields are able to sample more of the surface corrugation. The scattering will also be greater because of the increased grating amplitudes studied for these shorter pitch gratings.

Because of this, it could not be determined whether the pitch was the significant factor in determining the degree of scatter for a given wavelength emitter. A suitable figure of merit characterising the grating profile is the depth-to-pitch ratio. Significant changes in the spontaneous emission rate of the dye molecules above the $415nm$ pitch gratings were only observed for amplitudes $30nm$ and greater, corresponding to depth-to-pitch ratios in excess of 0.1. To determine whether the pitch is significant, the distance dependence of the lifetime should be determined for an $800nm$ pitch grating of similar depth-to-pitch ratio, *i.e.* with amplitude $40nm$. If there is no change from the planar lifetime distance dependence for this structure, then the pitch of the grating structure is likely to be important in determining whether the dipole fields can sample the corrugation.

The proposal that the change in spontaneous emission rate was caused by the scattering of the dipole fields for the deeper grating structures studied

was substantiated by the radiation pattern measurements subsequently made. Deviations from the expected planar angle dependence of the direct radiation from the dye monolayer were found for grating samples exhibiting decreased lifetime oscillations. This suggested that the interference conditions for these samples were significantly perturbed from the planar interface case as a result of the scattering of the dipole fields.

That this scattering may be important can be appreciated by consideration of *figure 7.12*, which gives the angle dependent reflectivity for two of the grating structures used. The reflectivity of the shallow grating ($a_0 \sim 17\text{nm}$) only falls below 80% when the SPP mode is excited, which only occurs for a very narrow angle range. The reflectivity of the deeper grating ($a_0 \sim 75\text{nm}$), by way of contrast, is only $\sim 5\%$ for incident angles above the critical edge at 30° . This is due to the strong diffraction that can scatter incident light into to the -1 order for this grating structure. If the dipole fields are able to sample this corrugation, strong scattering can occur, leading to a reduction in the intensity of the specularly reflected field at the dipole site. Since it is the reflected fields that affect the dipole emission rate, any decrease in these fields will cause smaller changes in the emission rate. The influence of the scattered orders also needs to be taken into account, including their phase relative to the specular field.

The quenching of the lifetime for small ion-metal separations was also affected by the grating amplitude, and was increased slightly for some of the deeper gratings considered. This could be due to the perturbation of the SPP modes by the grating corrugation. It is known that as the grating amplitude increases, the wavevector of the SPP mode also increases [*Pockrand (1974)*], and this leads to a greater density of SPP modes per unit wavevector for a given frequency. An increased density of states at the dye emission frequency would allow the molecules to couple more strongly to the SPP mode of the metal grating surface, thus increasing their emission rate.

The change in nature of the SPP modes with increasing grating amplitude was again confirmed by the radiation pattern measurements which showed that the mode was substantially damped for the deeper grating structures.

In attempting to explain the lifetime dependence with distance there is another important consideration to be made, which is related to the dispersion

of the SPP modes at the grating surface. This is the existence of SPP energy gaps for the grating structures used. If the grating has an energy gap for the propagation of SPP modes at the emission frequency of the dye, then the quenching of the dye by excitation of SPP modes will be severely reduced. This will lead to changes in the lifetime dependence for small ion-metal separations, where coupling to the SPP mode is most important.

For a single grating corrugation such as that considered here, the gap does not extend over all azimuthal angles for SPP propagation on the surface, but only extends over a limited angle range [Barnes *et al.* (1997)]. Since the dye molecules can excite SPPs propagating in all azimuthal directions on the metal surface, the effect of the gap is clearly limited by the angle range over which it can restrict the propagation of SPPs. The azimuthal extent of the gap is determined by both the grating pitch/wavelength ratio, and the gap width [Amos (1997)]. Since the gap width increases with grating amplitude (chapter 5), it can be seen that the azimuthal extent of the SPP gap increases with the grating amplitude. This implies that the deeper gratings should be influenced more by the existence of an SPP gap, and should exhibit reduced molecule-SPP coupling.

This contradicts the experimental evidence presented earlier, which is that the quenching of the molecules in the limit of small ion-metal separations, is if anything, increased for the larger amplitude gratings. The existence of the SPP gap however, implies the existence of band edges, which as standing waves have an increased density of states per unit frequency interval. The molecule-SPP coupling will thus be increased for the band edges, in direct competition with the effect of the gap. Which process is dominant in determining the extent of molecular quenching is hard to judge in the absence of a rigorous theoretical model.

The fluorescence decays measured were single exponential for all but the deepest structure considered. This suggests that there is no difference in the excited state lifetime for molecules located above the grating peaks and troughs for these structures. The deepest grating studied, of amplitude $\sim 130\text{nm}$ did exhibit non-exponential fluorescence decays, indicating that there was a difference in the excited state lifetime for molecules situated at different points above the grating surface. As the ion-metal separation increased for this

sample, the deviation from a single exponential decay decreased, indicating the increasing equivalence of the different dipole sites.

It seems likely that all gratings have a distribution of different lifetimes for molecules laterally displaced across a grating groove, but that it is hard to resolve any change from single exponential behaviour if the components are similar in lifetime. The non-exponential behaviour of a fluorescence decay will be discernible only if the extreme lifetime components are sufficiently different in value, which explains why non-exponentiality was seen only for the deepest structure.

7.5 Summary

In this chapter, the planar interface work of chapter 6 has been extended by the study of the fluorescence emission from a monolayer of Eu^{3+} ions above silver grating structures, and the effect of the surface corrugation investigated. This was carried out for both long and short pitch gratings, and for a variety of grating amplitudes. The distance dependence of the spontaneous emission rate of the Eu^{3+} ions was shown to change little from the planar dependence for the shallow grating structures considered, but significant changes were observed for the deeper grating structures (those with depth-to-pitch ratios greater than 0.1). The radiation patterns of the emission from the grating structures were also measured, and consisted of the direct emission from the dye molecules, and the re-radiated emission from surface modes scattered by the corrugation. While the direct emission from the shallow gratings resembled that from a planar mirror, the direct emission from the deeper structures did not, and this was taken to indicate that the dipole fields were scattered by the deeper corrugations.

All fluorescence decays observed were single exponential in form, except those for the deepest grating structure studied. The non-exponential decays measured for this sample are a possible indication of the variation in dipole sites above the grating surface.

Chapter 8

Conclusions and future work

In this thesis, the optical interactions of a dye layer with a nearby metallic interface have been studied for both planar and corrugated surface profiles. The results obtained in these investigations have already been discussed within each of the experimental chapters (5,6 and 7) and it is the purpose of this chapter to summarise the major conclusions of the work.

8.1 Absorption of light

In chapter 5, it was shown that the absorption of light by a thin dye layer located above a metallic surface is strongly enhanced by the coupling between the incident light and the SPP modes of the interface. The absorption of the dye molecules is proportional to the intensity of the local optical field, which is greatly increased when the SPP mode is resonantly excited. If the metal surface is corrugated, TM-polarised light on the surface can excite these modes, leading to an order of magnitude increase in the absorption of the incident light by the dye molecules when the modes are excited.

It was subsequently demonstrated that the use of a suitable grating profile introduces an energy gap for the propagation of the SPP modes over a given spectral range. Accordingly, the enhancement mechanism is removed, leading to a reduction in the absorption of the dye molecules and the appearance of a gap in the absorption spectrum of the system. Conversely, at the edges of the gap region, an increase in the absorption of the system was observed. The SPP modes at the edges of the gap region are standing waves, and thus have an extremely high density of states for a given frequency interval. This increases the interaction between the SPPs and the dye molecules,

leading to the increased absorption observed. A factor of two reduction in the absorption of a layer of dye molecules was experimentally measured for wavelengths corresponding to the SPP energy gap region of the grating structure.

Good agreement was found between the experimental data and theory by numerical modelling the fields associated with the SPP mode within the dye layer. The influence of the different components of the grating profile on the response of the system was then modelled, demonstrating how control of the SPP mode density can be used to change the absorption spectrum of the system. Both the width and depth of the absorption gap can be varied by suitable choice of the profile.

8.2 Emission of light

It is not only the absorption of light by dye molecules that is altered by the presence of a nearby interface; the emission is also affected, leading to changes in both the spontaneous emission rate and the angular distribution of the fluorescence. The influence of a nearby interface on the emission of light by dye monolayers was considered in chapters 6 and 7, for planar and corrugated surfaces respectively.

8.2.1 Planar interfaces

By using the Langmuir-Blodgett technique, monolayers of a Eu^{3+} complex were spaced known distances away from a planar silver mirror, and both the spontaneous emission rate and radiation pattern of the emission were measured as a function of the ion-metal separation. The spontaneous emission rate was shown to be quenched for small ion-metal separations, which was due to the excitation of SPP modes at the interface. Further away, the emission rate was observed to oscillate with distance, as a result of the interference between the direct and reflected fields. Good agreement was found with a classical model treating the Eu^{3+} ions as simple harmonic dipole oscillators, driven by the field reflected from the mirror interface.

The radiation patterns of the Eu^{3+} ion emission was measured for both the main 614nm and the weaker 592nm emission. Substantial differences were observed in the angular dependence of these two emissions implying that they arose from electronic transitions of completely different nature. By fitting the angle dependence of the emission to a simple model which considered the interference between the direct emission from the dipole and the reflected field from the mirror, it was shown that the 614nm emission arose from an electric dipole transition, and the 592nm emission from a magnetic dipole transition, in agreement with studies by previous workers [Drexhage (1974)]. Slight discrepancies between the experimental and theoretical results were attributed to the non-isotropic nature of the spacer layer, which was not accounted for in the model used.

8.2.2 Corrugated interfaces

In chapter 7, the planar interface was replaced by a diffraction grating to allow the effect of corrugating the interface on the emission to be investigated. It was shown that a shallow corrugation of long pitch ($\lambda_g=800\text{nm}$, $a_0\sim 10\text{nm}$) had relatively little effect on the spontaneous emission rate of the dye monolayer, and this was explained by the lack of scattering of the dipole fields. For this structure, the only significant change from the planar results was in the radiation patterns measured. The angular dependence of the emission closely resembled that of a planar mirror, but was perturbed by the appearance of narrow emission peaks. These resulted from the scattering of the surface modes excited by the dye molecules from the corrugation into photons. The dependence of the angle of peak emission of these modes was studied as a function of the grating azimuth, and the thickness of the spacer layer structure, thus confirming the nature of the scattering process. The non-isotropic nature of the spacer layer structure, which was suspected to give rise to discrepancies in the planar radiation patterns measured in chapter 6, was confirmed by the observation of mixed polarisation components in the re-radiated emission from the guided modes.

Significant change in the distance dependence of the spontaneous emission rate of the dye monolayer was observed for the deeper short pitch grating structures ($\lambda_g=415nm$, $a_0>30nm$). In particular, the lifetime oscillations observed for large ion-metal separations were progressively damped as the grating amplitude increased. It was proposed that this was the result of the increased scatter of the dipole fields by the corrugation, leading to a change in the interference conditions at the dipole site. The angular dependence of the emission from these structures was also composed of narrow emission peaks from the surface modes scattered by the grating as well as the slowly varying background component due to the interference of the direct and reflected emission from the dye monolayer. Unlike the shallow gratings, however, this direct emission exhibited significant deviations from that of a planar mirror, indicating that scattering of the dipole fields from the grating could indeed be taking place. This observation supports the proposition made to explain the reduction in magnitude of the lifetime oscillations observed at large ion-metal separations for the deeper grating structures.

The increased scattering of the dipole fields by the deeper short pitch grating structures studied could be due to the increased sampling of the grating corrugation by the dipole fields due to the reduced pitch, as proposed by [Amos(1997)]. Alternatively, it may be the perturbation of the fields caused by the depth of the grating that causes the dipole field interference condition to be altered. Both conditions are likely to be of importance, since no change in the distance dependence of the spontaneous emission rate was observed for the shallowest of the short pitch grating samples studied ($\lambda_g=415nm$, $a_0=20nm$).

To determine whether the pitch is of significance in the scattering process, gratings should be studied which have similar depth-to-pitch ratios but have pitches longer and shorter than the emission wavelength respectively, thus examining gratings with equivalent aspect ratio. A difference in the behaviour of the two gratings would then indicate that the scattering was pitch-dependent.

Possibly the most important observation made was that the fluorescent decays measured from dye monolayers above the deepest grating structures studied were non-exponential, unlike those for shallower profiles. This indicates

the existence of a distribution of different spontaneous emission rates for the sampled fluorescence, likely to be caused by the different dipole sites above the grating surface. The non-exponentiality would be less evident for the shallower structures studied because of the smaller difference in local environment above the peaks and troughs of the grating structure.

8.3 Future work

There are a number of interesting questions which are posed by the observations made in this work, the most important of which is the origin of the perturbation in the lifetime distance dependence observed for the deepest grating structures. The radiation pattern measurements made for an azimuth of $\phi=0^\circ$ show that the planar interference condition has been altered for these structures, indicating that scattering of the dipole field is a likely mechanism, but this is by no means certain. An investigation of the azimuthal dependence of the radiation patterns should help to clarify this point. The direct emission at azimuths of 90° should resemble the planar dependence for these structures, since the surface corrugation will not be sensed, at least for the TM-polarised emission. This would indicate that the deviations of the radiation pattern observed for the $\phi=0^\circ$ case are caused by scattering from the grating, and not a cavity resonance effect for example.

The effect of the dispersion of the SPP mode on the quenching of the emission is also moot, since a variety of different effects come into play as the grating depth increases. Band gaps can be introduced into the propagation of the mode by the corrugation, which leads to a reduction in the non-radiative energy transfer to the metal, and hence reduced quenching. The existence of a gap however, also implies the existence of band edges for the SPP modes, which have an increased density of states, and thus cause increased dye-SPP coupling. These two effects are in competition, and so the overall effect depends sensitively on the exact sample structure. The centre energy for the gap depends on the pitch of the grating, and also on the thickness of the dielectric overlayer, and so the importance of the SPP gap in determining the

quenching will vary from one ion-mirror separation to the next. The dispersion of the SPP modes is not only affected by the existence of the gap, since the mode wavevector is also increased for SPP propagation parallel to the Bragg vector.

For this reason, it is important that a theoretical description of the emission of fluorescence emission above a corrugated structure is developed. An appropriate start point would be the classical theory developed by Chance, Prock and Silbey (1978) for the planar interface, which treats the emitter as a simple harmonic dipole oscillator. Whereas the CPS theory uses the Fresnel reflection coefficients for a planar interface, the new theory would need to include the appropriate reflection coefficients for a corrugated interface. This would entail the use of a suitable co-ordinate transform, as used in the Chandezon method. All three dipole orientations relative to the interface would have to be considered, instead of the two necessary for the CPS model, due to the reduced symmetry of the corrugated surface. The excitation of the SPP mode would be naturally included in this formulation, and so suitable analysis of the power loss as a function of the in-plane momentum, as detailed in chapter 6 for the planar case, would allow the role of the SPP mode to be elucidated.

The grating only affects the propagation of the SPP mode for a spread of azimuthal angles about the direction normal to the grating grooves, and so the effect of any SPP gap is limited for a single corrugation. If the corrugation were to be repeated every 60° , the SPP gap could extend over all azimuthal angles, thus eliminating the effect of enhanced coupling at the band edges. Suitable structures exhibiting full two-dimensional SPP gaps have already been made at Exeter, and it is hoped that time-resolved fluorescence measurements will be made soon. These samples should exhibit no dye molecule/SPP coupling, and so the quenching of the emission for small ion-metal separations should be eliminated.

The difference in spontaneous emission rate for dye molecules located at a fixed height above the peaks and troughs of a grating, possibly observed in chapter 7, could be confirmed by the use of a site-selective excitation technique. The technique that immediately springs to mind is the use of an interference pattern to pump the sample. Suitable choice of the pitch of the interference pattern would allow either the molecules at the peaks, or troughs of the grating profile to be excited, and thus the difference in spontaneous

emission rate could be demonstrated directly. This technique is, however, fraught with technical difficulties, and there is an alternative method which is experimentally much simpler.

As mentioned previously, the SPP modes at the edge of the energy gap are standing modes. The field distributions associated with these band edge modes are thus fixed with respect to the grating profile, and it happens that the field maxima for the upper band edge occur at the grating troughs, while the maxima for the lower energy band edge occur at the grating peaks [*Barnes et al. (1995)*]. Exciting these band edge SPP modes thus allows the preferential excitation of the molecules at either the peaks or troughs of the grating profile.

8.4 Publications

“Surface-plasmon energy gaps and photoabsorption” Andrew P, Kitson SC and Barnes WL (1997) *J. Mod. Opt.* **44**, 395.

References

- Adams A, Rendell RW, West WP, 1980 Phys. Rev. B **21** 5565
Broida HP, Hansma PK and Metiu H
- Adams A, Moreland J and Hansma PK 1981 Surf. Sci. **111** 351
- Adams A, Moreland J, Hansma PK, 1982 Phys. Rev. B **25** 3457
and Schlesinger Z
- Amos RM 1997 Ph.D Thesis, University
of Exeter (Unpublished)
- Amos RM and Barnes WL 1997 Phys. Rev. B **55** 7249
- Aravind EF, Hood E and Metiu H 1981 Surf. Sci. **109** 95
- Barnes WL and Sambles JR 1986 Surf. Sci. **177** 399
- Barnes WL, Priest TW, Kitson SC, 1995 Phys.Rev. B **51** 11164
Sambles JR, Cotter NPK and Nash DJ
- Barnes WL, Preist TW, Kitson SC and 1996 Phys. Rev. B **54** 6227
Sambles JR
- Barnes WL, Kitson SC, Preist TW and 1997 J. Opt. Soc. Am. A **14**
Sambles JR 1654
- Barnes WL 1998 J. Mod. Opt. **45** 661
- Benner RE, Dornhaus R and Chang 1979 Opt. Comm. **30** 145
RK
- Berreman D 1972 J. Opt. Soc. Am. **62** 502
- Berreman D 1973 J. Opt. Soc. Am. **63** 1374
- Blacke WL and Leung PT 1997 Phys. Rev. B **56** 12625

-
- Björk G, Machida S, Yamamoto Y and Igeta K 1991 Phys. Rev. A **44** 669
- Blodgett KB 1935 J. Am. Chem. Soc. **57** 1007
- Born M and Wolf E 1970 *Principles of Optics* 4th ed. (Pergamon press, Oxford)
- Brune M, Schmidt-Kaler F, Maali A, Dreyer J, Hagley E, Raimond JF and Haroche S 1996 Phys. Rev. Lett. **76** 1800
- Bryan-Brown GP, Jory MJ, Elston SJ and Sambles JR 1993 J. Mod. Opt. **40** 959
- Bücher H, Drexhage KH, Fleck M, Kuhn H, Möbius D, Schafer FP, Sondermann J, Sperling W, Tillman P and Wiegand J 1967 Mol. Cryst. **2** 199
- Casimir H and Polder D 1948 Phys. Rev. **73** 360
- Casimir HBG 1948 Proc. Ned. Akad. Wet. **60** 793
- Chance RR, Miller AH, Prock A and Silbey R 1975 J. Chem. Phys. **63** 1589
- Chance RR, Prock A and Silbey R 1975 J. Chem. Phys. **62** 771
- Chance RR, Prock A and Silbey R 1975 J. Chem. Phys. **62** 2245
- Chance RR, Prock A and Silbey R 1976 J. Chem. Phys. **65** 2527
- Chance RR, Prock A and Silbey R 1978 Adv. Chem. Phys. **37** 1
- Chandezon J, Dupuis MT, Cornet G and Maystre D 1982 J. Opt. Soc. Am. **72** 839
- Crossen G, Drabe KE and Wiersma DA 1993 J. Chem. Phys. **98** 5276

-
- Cotter NPK, Priest TW, and Sambles JR 1995 J. Opt. Soc. Am. A **12** 1097
- Daffesthofer M, Port H, and Wolf HC 1995 Chem. Phys. **200** 225
- De Martini F and Jacobovitz GR 1988 Phys. Rev. Lett. **60** 1711
- De Martini F, Innocenti G, Jacobovitz GR and Mataloni P 1987 Phys. Rev. Lett. **59** 2955
- De Martini F, Marrocco M, Mataloni P, Crescentini L and Loudon R. 1991 Phys. Rev. A **43** 2480
- DeVoe RG and Brewer RG 1996 Phys. Rev. Lett. **76** 2049
- Dexter DL 1953 J. Chem. Phys. **21** 836
- Dodabalapur A 1997 Sol. St. Comm. **102** 259
- Doermann FW and Halpern O 1939 Phys. Rev. **55** 486
- Drexhage KH 1970 Sci. Am. **222** 108
- Drexhage KH 1974 Prog. Opt. **12** 165 ed. E Wolf (North-Holland, Amsterdam)
- Drexhage KH, Fleck M, Kuhn H, Schäfer FP and Sperling W 1966 Ber. Bunsenges. Phys. Chem. **70** 1179
- Drexhage KH, Fleck M and Kuhn H 1967 Ber. Bunsenges. Phys. Chem. **71** 915
- Drexhage KH and Fleck M 1968 Ber. Bunsenges. Phys. Chem. **72** 330
- Dutra SM and Knight PL 1996 Phys. Rev. A **53** 3587
- Elston SJ, Bryan-Brown GP, Preist TW and Sambles JR 1991a Phys. Rev. B **44** 3483
- Elston SJ, Bryan-Brown GP and Sambles JR 1991b Phys. Rev. B **44** 6393
- Fano U 1941 J. Opt. Soc. Am. **31** 213

-
- | | | |
|---|------|---|
| Fearn H, Cook RJ and Milonni PW | 1995 | Phys. Rev. Lett. 74 1327 |
| Fermi E | 1932 | Rev. Mod. Phys. 4 87 |
| Ford GW and Weber MG | 1984 | Phys. Rep. 113 197 |
| Foresi JS, Villeneuve PR, Ferrera J,
Thoen ER, Steinmeyer G, Fan S,
Joannopoulos JD, Kimmerling LC
Smith HI and Ippen EP | 1997 | Nature 390 143 |
| Franklin B | 1774 | Phil. Trans. Roy. Soc.
London 64 445 |
| Gaines GL | 1966 | <i>Insoluble monolayers at
liquid-gas interfaces</i>
(Interscience, New York) |
| Giergiel J, Reed CE, Hemminger JC
and Ushioda S | 1988 | J. Phys. Chem. 92 5357 |
| Girlando A, Philpott MR, Heitmann D,
Swalen JD and Santo R | 1980 | J. Chem. Phys. 72 5187 |
| Goncher GM, Parsons CA and Harris
CB | 1984 | J. Phys. Chem. 88 4200 |
| Greenler RG | 1977 | Surf. Sci. 69 647 |
| Groeneveld RHM, Sprik R and
Legendijk A | 1990 | Phys. Rev. Lett. 64 784 |
| Haken H and Wolf HC | 1993 | <i>The Physics of Atoms
and Quanta</i> 3 rd ed.
(Springer-Verlag, Berlin) |
| Harris JB | 1996 | Ph.D Thesis, University
of Exeter (Unpublished) |
| Harris JB, Preist TW, Wood EL, and
Sambles JR | 1996 | J. Opt. Soc. Am. A 13
803 |

-
- Heinzen DJ, Childs JJ, Thomas JE 1987 Phys. Rev. Lett. **58** 1320
and Feld MS
- Hinds EA 1991 Adv. Atom. Mol. And
Opt. Phys. **28** 237
- Holland WR and Hall DG 1985 Opt. Lett. **10** 414
- Hulet RG, Hilfer ES and Kleppner D 1981 Phys. Rev. Lett. **55** 2137
- Hunt NEJ, Vredenberg AM, Schubert 1995 *Confined Electrons and*
EF, Becker PC, Jacobson DC, Poate *Photons* eds. E Burstein
JM and Zydzik GJ and C Weisbuch
(Plenum press, New
York)
- Hutley MC 1982 *Diffraction Gratings*
(Academic press, New
York)
- Imbusch GF and Kopelman R 1981 *Laser Spectroscopy of*
Solids eds. WM Yen and
PM Selzer (Springer-
Verlag, Berlin)
- Jhe W, Anderson A, Hinds EA, 1987 Phys. Rev. Lett. **58** 666
Meschede D, Moi L and Haroche S
- John S 1987 Phys. Rev. Lett. **58** 2486
- John S and Wang J 1990 Phys. Rev. Lett. **64** 2418
- Jory MJ, Bradberry GW, Cann PS and 1996 Sensors and. Actuators.
Sambles JR **35** 197
- Kaminow IP, Mammel WL and Weber 1974 Appl. Opt. **13** 396
HP
- Kitson SC 1995 Ph.D Thesis, University
of Exeter (Unpublished)

-
- Kitson SC, Barnes WL and Sambles JR 1995 Phys. Rev. B **52** 11441
- Kitson SC, Barnes WL and Sambles JR and Cotter NPK 1996a J. Mod. Opt. **43** 573
- Kitson SC, Barnes WL, and Sambles JR 1996b Opt. Comm. **122** 147
- Kitson SC, Barnes WL and Sambles JR 1996c Phys. Rev. Lett. **77** 2670
- Kitson SC, Barnes WL and Sambles JR 1996d IEEE Photon. Tech. Lett. **8** 1662
- Kitson SC, Barnes WL and Sambles JR 1998 J. Appl. Phys. **84** 2399
- Knobloch H, Brunner H, Leitner A, Aussenegg F, and Knoll W 1993 J.Chem.Phys. **98** 10093
- Knoll W, Philpott MR and Swalen JD 1981 J. Chem. Phys. **75** 4795
- Koppelmann G 1969 Prog. Opt. **7** 1 ed. E Wolf (North-Holland, Amsterdam)
- Kovacs GJ 1978 Surf. Sci. Lett. **78** L245
- Kretschmann E and R  ther H 1968 Z. Naturf. A **23** 2135
- Kuhn H and M  bius D 1971 Angew. Chem. Int. Ed. Engl. **10** 620
- Kunz RE and Lukosz W 1980 Phys. Rev. B **21** 4814
- Kurizki G and Genack AZ 1988 Phys. Rev. Lett. **61** 2269
- Langmuir IV 1915 J. Am. Chem.Soc. **37** 1139

-
- | | | |
|---|-------|---|
| Langmuir IV | 1920 | Trans. Faraday Soc. 15
62 |
| Langmuir IV and Schaefer VJ | 1938 | J. Am. Chem. Soc. 60
1351 |
| Lavallard P, Rosenbauer M. and
Gacoin, T | 1996 | Phys. Rev. A 54 5450 |
| Lawrence CR and Geddes NJ | 1997 | <i>Handbook of Biosensors
and Electronic Noses</i> ,
ed. E Kress-Rogers
(CRC Press) |
| Leung PT, Wu PC, Jelski DA and
George TF | 1987a | Phys. Rev. B 36 1475 |
| Leung PT, George TF | 1987b | Phys. Rev. B 36 4664 |
| Leung PT, Kim YS and George TF | 1988 | Phys. Rev. B 38 10032 |
| Leung PT, Kim YS and George TF | 1989 | Phys. Rev. B 39 9888 |
| Lukosz W and Kunz RE | 1979 | Opt. Comm. 31 42 |
| Martorell J and Lawandy NM | 1990 | Phys. Rev. Lett. 65 1877 |
| Maystre D | 1980 | <i>Electromagnetic theory
of gratings</i> (Springer-
Verlag, Berlin) |
| Melby LR, Rose NJ, Abramson E and
Caris LC | 1964 | J. Am. Chem. Soc. 80
5517 |
| Míguez H, López C Meseguer F
Blanco A, Vázquez L and Mayoral R | 1997 | Appl. Phys. Lett. 71 1148 |
| Möbius D | 1990 | In <i>Langmuir-Blodgett
films</i> (Chapter 5). ed.
Roberts G (Plenum
Press, New York) |

-
- | | | |
|--|-------|--|
| Nash DN and Sambles JR | 1995 | J. Mod. Opt. 42 1639 |
| Nash DN and Sambles JR | 1996 | J. Mod. Opt. 43 81 |
| Novotny L | 1997 | J. Opt. Soc. Am. A 14 91 |
| Nylander C, Liedberg B and Lind T | 1982 | Sensors and Actuators 3
79 |
| Otto A | 1968 | Z. Phys. 216 398 |
| Owyang GH | 1981 | <i>Foundations of Optical Waveguides</i> (Edward Arnold, London) |
| Peterson IR | 1992. | <i>In Molecular electronics</i> , p117-206. ed. GJ Ashwell (Research Studies Press, Taunton) |
| Petrov EP, Bogomolov VN, Kalosha II and Gaponenko SV | 1998 | Phys. Rev. Lett. 81 77 |
| Petty MC | 1996 | <i>Langmuir Blodgett Films</i> (Cambridge University Press) |
| Philpott MR | 1973 | Chem. Phys. Lett. 19
435 |
| Pockels A | 1891 | Nature 43 437 |
| Pockels A | 1893 | Nature 48 152 |
| Pockrand I | 1974 | Phys. Lett. 49a 249 |
| Pockrand I | 1978 | Surf. Sci. 72 577 |
| Pockrand I, Brillante A and Möbius D | 1980 | Chem. Phys. Lett. 69
499 |
| Preist TW, Cotter NPK and Sambles JR | 1995 | J. Opt. Soc. Am. A 12
1740 |

-
- | | | |
|--|------|---|
| Purcell EM | 1946 | Phys. Rev. 69 681 |
| Ræther H | 1988 | <i>Surface Plasmons</i>
(Springer-Verlag, Berlin) |
| Rayleigh | 1899 | Phil. Mag. 48 321 |
| Rayleigh | 1907 | Phil. Mag. 14 213 |
| Rigneault H, Robert S, Begon C,
Jacquier B and Moretti P | 1997 | Phys. Rev. A 55 1497 |
| Rikken GLJA and Kessener YARR | 1995 | Phys. Rev. Lett. 74 880 |
| Ritchie RH, Arakawa ET, Cowan JJ,
and Hamm RN | 1968 | Phys. Rev. Lett. 21 1530 |
| Robert S, Rigneault H and Lamarque
F | 1998 | J. Opt. Soc. Am. B 15
1773 |
| Roberts G | 1990 | <i>Langmuir-Blodgett Films</i>
(Plenum press, New
York) |
| Rosengart EH and Pockrand I | 1977 | Opt. Lett. 1 194 |
| Russell St. J, Birks TA, Knight JC,
Cregan RF, Mangan B and DeSandro
JP | 1998 | J. Jap. Appl. Phys. 37 45 |
| Sambles JR and Innes R | 1988 | J. Mod. Opt. 35 791 |
| Schmidlin EM and Simon HJ | 1989 | Appl. Opt. 28 3323 |
| Schubert EF, Vredenberg AM, Hunt
NEJ, Wong YH, Becker PC, Poate JM,
Jacobson DC, Feldman LC and Zydzik
GJ | 1992 | Appl. Phys. Lett. 61 1381 |
| Selényi P | 1911 | Ann. Phys. 4 Folge 35
444 |
| Selényi P | 1938 | Z. Phys. 108 401 |

-
- Selényi P 1939 Phys. Rev. **56** 477
- Shih MC, Bohanon TM, Mikrut JM, Zschack P and Dutta P 1992 Phys. Rev. A **45** 5734
- Sievenpiper D, Sickmiller ME and Yablonovitch E 1996 Phys. Rev. Lett. **76** 2480
- Sipe JE 1981 Surf. Sci. **105** 489
- Snoeks E, Lagendijk A and Polman A 1995 Phys. Rev. Lett. **74** 2459
- Sommerfeld A 1949 *Partial Differential Equations of Physics* (Academic Press, New York)
- Stanley RP, Houdre R, Oesterle U, Illegems M and Weisbuch C 1993 Phys. Rev. A **48** 2246
- Sullivan K and Hall DG 1997 J. Opt. Soc. Am. B **14** 1149
- Sullivan KG, King O, Sigg C and Hall DG 1994 Appl. Opt. **33** 2447
- Suzuki M, Yokohama H, Brorsen SD and Ippen EP 1991 Appl. Phys. Lett. **58** 998
- Suzuki T and Yu PKL 1995 J. Opt. Soc. Am. B **12** 570
- Tien PK 1977 Rev. Mod. Phys **49** 361
- Tocci MD, Scalora M, Bloemer MJ, Dowling JP and Bowden CM 1996 Phys. Rev. A **53** 2799
- Tomaš MS and Lenac Z 1993 Opt. Comm. **100** 259
- van Blaaderen A, Ruel R and Wiltzius P 1997 Nature **385** 321
- Vlasov YA, Luterova K, Pelant I, Hönerlage B and Astratov VN 1997 Appl. Phys. Lett. **71** 1616

-
- Vukusic PS, Bradberry GW and Sambles JR 1992a Surf. Sci. Lett. **277** L34
- Vukusic PS, Sambles JR and Wright JD 1992b J. Mater. Chem. **2** 1105
- Waldeck DH, Alivisatos AP and Harris CP 1985 Surf. Sci. **158** 103
- Weber WH and McCarthy SL 1975 Phys. Rev. B **12** 5643
- Weber MG and Mills DL 1986 Phys. Rev. B **34** 2893
- Weber WH and Eagen CF 1979 Opt. Lett. **4** 236
- Weiss S, Ha T, Enderle T, Ogletree DF, Selvin PR and Chemla DS 1996 Proc. QELS '96 **9** 25
- Whitmore PM, Robota HJ and Harris CBJ 1982 J. Chem. Phys. **77** 1560
- Wood EL, Sambles JR, Cotter NPK, and Kitson SC 1995 J. Mod. Opt. **42** 1343
- Wood RW 1902 Phil. Mag. **4** 396
- Worthing PT, Amos RM and Barnes WL 1998 Phys. Rev. A (accepted for publication.)
- Wright JC 1976 *Radiationless Processes in Molecules and Condensed Phases* ed. FK Fong. (Springer-Verlag, Berlin)
- Yablonovitch E 1987 Phys. Rev. Lett. **58** 2059
- Yablonovitch E 1993 J. Opt. Soc. Am. B **10** 283
- Yablonovitch E, Gmitter TJ, Meade RD, Rappe AM, Brommer KD and Joannopoulos JD 1991a Phys. Rev. Lett. **67** 3380

-
- Yablonovitch E, Gmitter TJ and Leung KM 1991b Phys. Rev. Lett. **67** 2295
- Yamazaki I, Tamai N, Yamazaki T, Murakami A, Mimuro M and Yoshihiko F 1988 J. Phys. Chem. **92** 5035
- Yariv A 1991 *Quantum Electronics* 4th ed. (Saunders, New York)
- Yeung MS and Gustafson TK 1996 Phys. Rev. A **54** 1996
- Yonezawa Y, Möbius D and Kuhn H 1987 J. Appl. Phys. **62** 2016
- Zbinden H, Muller A and Gisin N 1995 Quant. Semiclass. Opt. **7** 79
- Zhang RJ, Liu HG, Yang KZ, Si ZK, Zhu GY and Zhang HW 1997 Thin Solid Films **295** 228

Appendix A

Magnetic dipole radiation patterns

In this appendix, the magnetic dipole radiation patterns omitted from chapter 6 are presented. These radiation patterns were measured using the same planar samples as the electric dipole radiation patterns presented in *figure 6.10*. The increased noise level on this data as compared to the 614nm data is a direct result of the considerably lower intensity of the 590nm transition.

The data, which is presented in *figure A1*, displays a similar trend to the electric dipole radiation patterns with increasing ion/mirror separation; the emission maxima split apart, and move to higher angles as the ion/mirror separation increases. Eventually, these peaks pass off beyond the substrate horizon, and a new normal emission peak appears. This is where the similarity ends, however, since comparison of *figure A1* with *figure 6.10* shows the differing form of the electric and magnetic dipole radiation patterns for a given ion/mirror separation. The assignment of magnetic dipole character to the 590nm transition comes from the agreement between the experimentally measured radiation patterns and a suitable theoretical model. This model is identical to that presented in *section 6.5.5*, except that it is based on a magnetic, not electric, dipole source.

The angular dependence of the emission intensity for an isolated magnetic dipole emitter is identical to that of an electric dipole emitter, *i.e.* it is given by $I(\gamma) = I_0 \sin^2 \gamma$, where γ is the angle between the propagation direction and the dipole moment. The difference between the radiation patterns arises from the fact that the electric field and magnetic fields are exchanged for electric and magnetic dipoles.

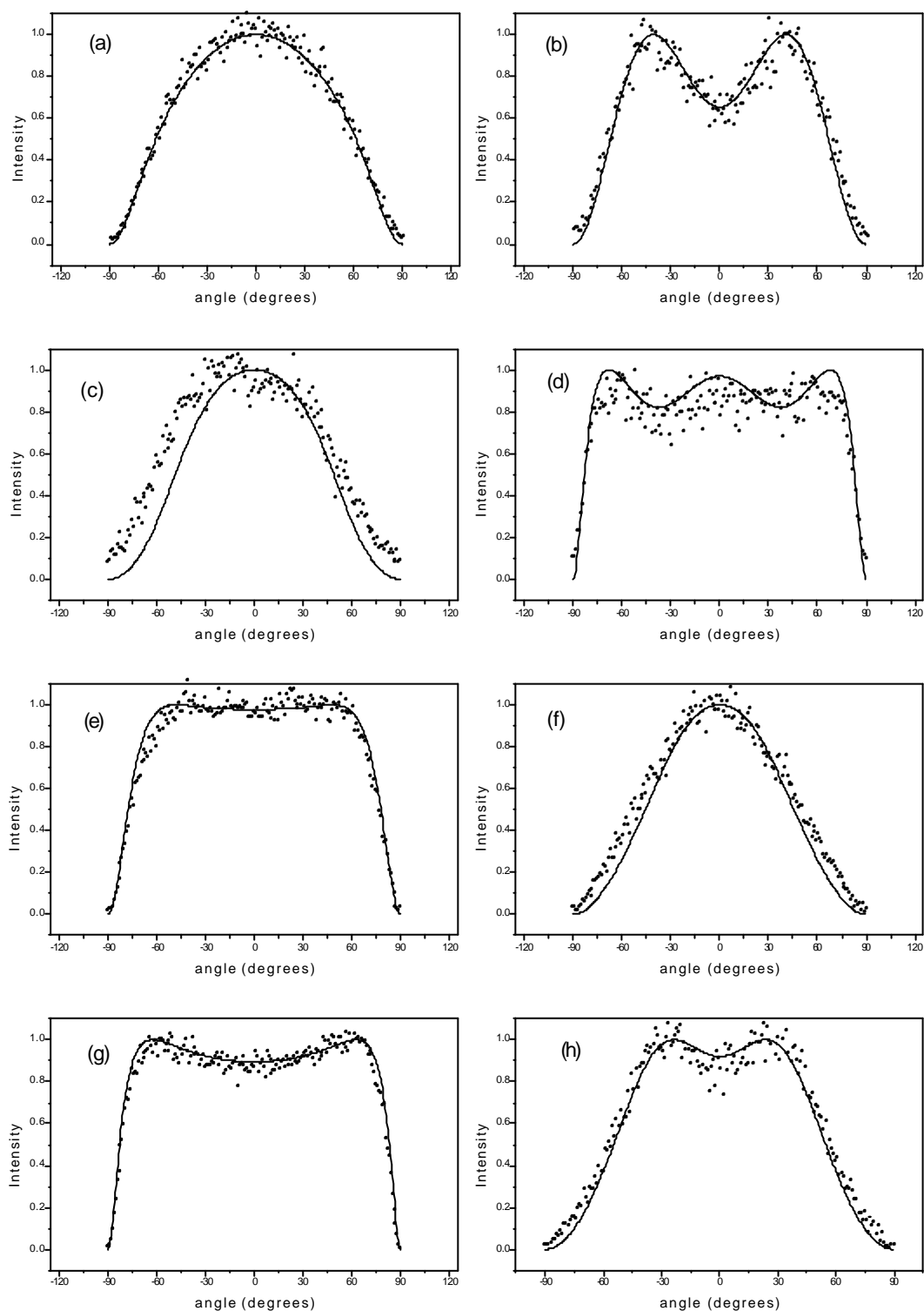


Figure A1 Radiation patterns of the 590nm Eu^{3+} magnetic dipole emission (normalised). The plots in the left column are for p-polarised emission, on the right, s-polarised emission. (a, b) 52nm (c, d) 104nm (e, f) 156nm and (g, h) 208nm . The open circles are experimental data and the solid lines theoretical models.

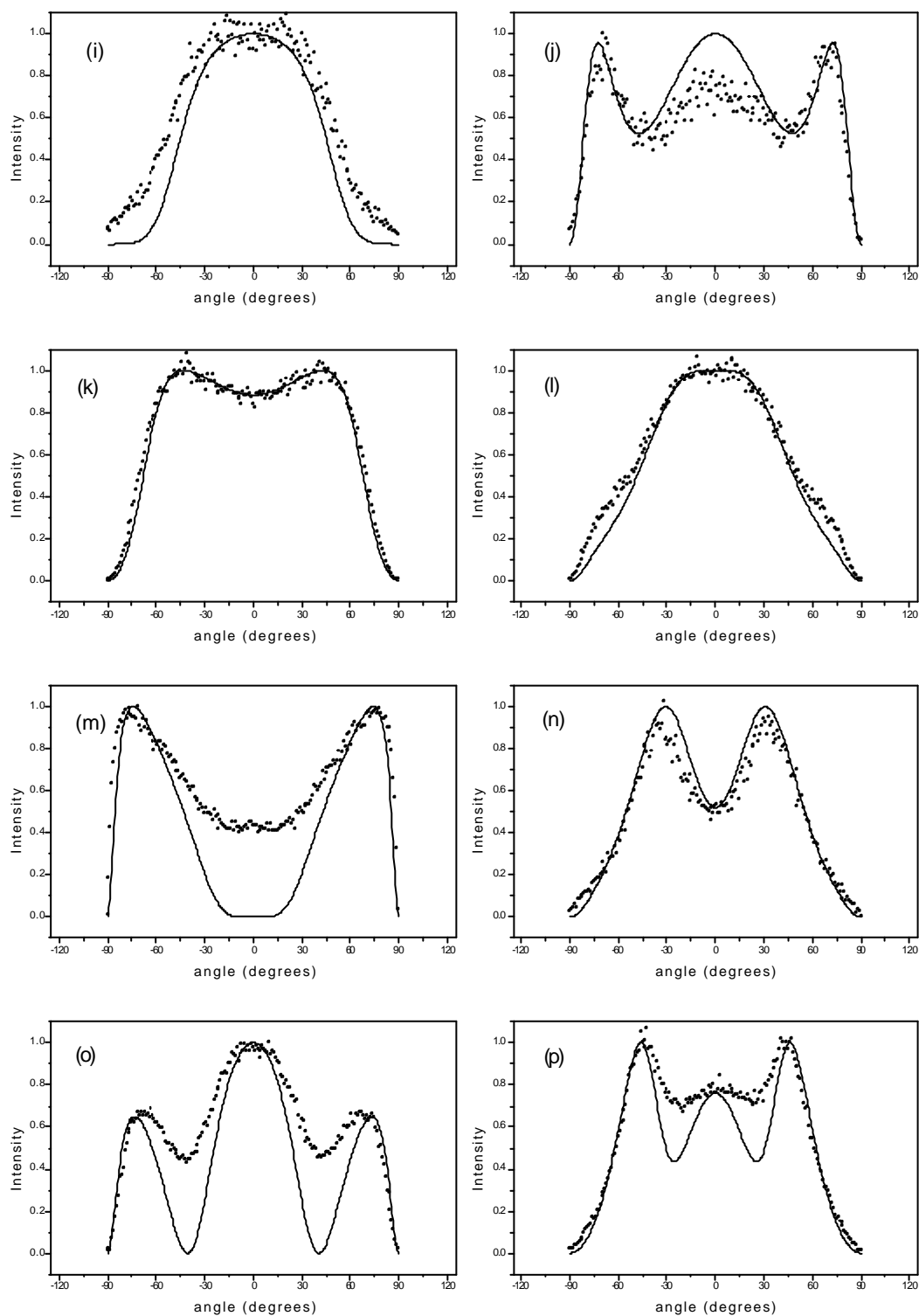


Figure A1 (continued) Radiation patterns of the 590nm Eu^{3+} magnetic dipole emission (normalised). The plots in the left column are for p-polarised emission, on the right s-polarised emission. (i, j) 312nm (k, l) 364nm (m, n) 416nm and (o, p) 468nm. The open circles are experimental data and the solid lines theoretical models.

The angle dependence of the magnetic dipole emission in front of a mirror is calculated in exactly the same manner as that of the electric dipole emission. The important relation is *equation 6.11*, and the relevant values of l_1 , l_2 and δ for a magnetic dipole source are given in *table A1*; cases (a), (b) and (c) refer to the dipole orientations given in *figure 6.12*.

dipole orientation	l_1	l_2	δ
(a)	$\sin^2\alpha$	$\rho_s^2 \sin^2 \alpha$	δ_s
(b)	$\cos^2\alpha$	$\rho_s^2 \cos^2 \alpha$	$\delta_s + \pi$
(c)	1	ρ_p^2	δ_p

Table A1 The values taken by l_1 , l_2 and δ for the three different magnetic dipole orientations. The dipole emission is taken to have a maximum intensity of unity.

The resulting expressions for the single interface angular intensity distributions are as follows (these are for an isotropic distribution of magnetic dipoles, and are equivalent to the electric dipole expressions, *equations 6.16* and *6.17*.)

$$I_p(\alpha) = 1 + \rho_p^2 + 2\rho_p \cos(\varphi - \delta_p) \quad (\text{A1})$$

$$I_s(\alpha) = 1 + \rho_s^2 - 2\rho_s \cos 2\alpha \cos(\varphi - \delta_s) \quad (\text{A2})$$

The emission from the experimental double interface system is then obtained by substituting *equations A1* and *A2* into *equations 4.17* and *4.18* respectively. The parameters used to obtain the theoretical models in *figure A1* are given in *table A2*. The parameters for the LB spacer layer have not been changed from the values used for the 614nm emission, but it was found necessary to adjust the silver permittivity somewhat to obtain reasonable agreement between theory and experiment.

The discrepancies between theory and experiment for the magnetic dipole data are more marked than in the electric dipole case. This may be due, at least in part, to the greater width of the 590nm emission (see *figure 4.10*), which would lead to a “smearing out” of the experimental radiation patterns. The

small ion/mirror separation radiation patterns have slowly varying features with angle and agree quite well with the theory. Any smearing out of these slowly varying features would be barely noticeable. Conversely, the larger ion-mirror separations, which have more, and hence faster varying features, exhibit greater discrepancies with the model, and seem to be more smoothed out than the theoretical dependencies.

Eu ³⁺ emission wavelength, λ_0	592.0 nm
Silver complex permittivity, $\hat{\epsilon}_{Ag}$	-12+0.5i
22-tricosenoic acid complex permittivity, $\hat{\epsilon}_{LB}$	2.49+0.0i
22-tricosenoic acid monolayer thickness, \hat{d}	2.68 nm

Table 6.2 The parameters used to obtain the theoretically modelled radiation pattern dependencies of *figure A1*.